IDENTIFICATION OF THE FLUID INDUCED INSTABILITY PHENOMENON IN JOURNAL BEARINGS

by

Seyed Mohammad Miraskari

B.Sc., Amirkabir University of Technology (Tehran Polytechnic,) 2006
M.Sc., Sharif University of Technology, 2009

A THESIS SUBMITTED IN PARTIAL FULFILLMENT OF
THE REQUIREMENTS FOR THE DEGREE OF

DOCTOR OF PHILOSOPHY

in

THE FACULTY OF GRADUATE AND POSTDOCTORAL STUDIES
(Mechanical Engineering)

THE UNIVERSITY OF BRITISH COLUMBIA
(Vancouver)

April 2017

Abstract

The demand for high pressure injection of natural gas in underground has been an incentive for a growing interest in the design and manufacture of multistage compressors. Many of such compressors suffer from violent sub-synchronous whirl. If the spin-speed of the rotors exceed the "threshold speed of instability," the rotor-bearing system experiences sub-synchronous whirling known as oil whirl/whip. For rotors supported on journal bearings, oil whirl is the most common cause of instability. Existing models fall short in predicting the nature of sub-synchronous instabilities in journal bearings with a finite length. In this thesis, a new nonlinear rotor-bearing model is introduced to characterize the phenomenon of oil whirl for rotors supported on finite length journal bearings.

As a first step in constructing a rotor-bearing model, this research introduces a modified scheme for performance predictions of cavitated journal bearings. The resulting algorithms are then used throughout the thesis to obtain solutions to the Reynolds equation in original and perturbed form in order to calculate journal induced pressure and pressure gradients. The pressure gradients are used as a basis for the calculation of bearing linear and nonlinear dynamic coefficients. Dynamic coefficients are widely used to represent the journal bearing reaction forces exerted on the rotating shaft. These coefficients are implemented to construct mathematical models of the system that are suitable for studying dynamics and stability. Analytical treatments are introduced wherever possible to provide a means for verification purposes.

The linear and nonlinear stability of flexible shafts supported on finite length journal bearings is studied. As linear models are not suitable for bifurcation analysis, a simple yet versatile nonlinear rotor-bearing model is proposed such that the journal force is represented by first and higher order dynamic coefficients. Results show that the implementation of nonlinear coefficients can enable the application of nonlinear analysis methods. Nonlinear stability analysis is carried out by implementing a variety of techniques including the Hopf bifurcation theorem and eigenvalue analysis of the Monodromy matrices. The versatility of the techniques used made it possible to study the existence and directions of Hopf bifurcations for rotors supported on finite length journal bearings.

Preface

Chapter 2 is collected from the data presented in the following article:

Miraskari, M., Hemmati, F., Jalali, A., AlQaradawi, M., and Gadala, M. S., 2016, "A Robust Modification to the Universal Cavitation Algorithm in Journal Bearings," Journal of Tribology.

I discretized and solved the governing equations specific to the problem at hand, generated and extracted the results, and wrote the manuscript in consultation with Mohamed S. Gadala. Some modifications were suggested by Farzad Hemmati, A Jalali, and M.Y AlQaradawi.

Chapter 3 is collected from the data presented in the following article:

Miraskari, M., Hemmati, F., M.Y. AlQaradawi, Mohamed S. Gadala, 2017, "Linear Stability Analysis of Finite Length Journal bearings in Laminar and Turbulent Regimes," accepted for publication in Journal of Engineering Tribology.

I derived the governing equations, solved the appropriate equations, generated and extracted the results, and wrote the manuscript in consultation with Mohamed S. Gadala. Some modifications were suggested by Farzad Hemmati and M.Y. AlQaradawi.

Chapter 4 is collected from the data presented in the following article:

Miraskari, M., and Gadala, M. S., 2017, " Nonlinear Dynamics of Flexible Rotors Supported on Journal Bearings – Part (A): Analytical Bearing Model," submitted – under review.

I derived the governing equations and constructed the appropriate models, solved the equations, generated and extracted the results, and wrote the manuscript in consultation with Mohamed S. Gadala.

Chapter 5 is collected from the data presented in the following article:

Miraskari, M., and Gadala, M. S., 2017, " Nonlinear Dynamics of Flexible Rotors Supported on Journal Bearings – Part (B): Numerical Bearing Model," submitted – under review.

I derived the governing equations and constructed the appropriate models, solved the equations, generated and extracted the results, and wrote the manuscript in consultation with Mohamed S. Gadala.

Table of Contents

List of Tables

List of Figures

List of Symbols

C	Radial clearance, m
$C_{ij}, C_{ijk}, C_{ijkl}$ $\bar{C}_{ij}, \bar{C}_{ijk}, \bar{C}_{ijkl}$	Linear and Nonlinear damping coefficients in global Cartesian coordinates (X-Y): $i, j, k, l = x, y$; and in (R-T) coordinates $i, j, k, l = r, t$ where $\bar{C}_{ij} = \frac{C\,\omega}{\Pi}\, C_{ij}$, $\bar{C}_{ijk} = \frac{C^2\,\omega}{\Pi}\, C_{ijk}$, $\bar{C}_{ijkl} = \frac{C^3\,\omega}{\Pi}\, C_{ijkl}$
$[\bar{C}]_{XY}$, $[\bar{C}]_{RT}$, $[\bar{K}]_{XY}$, $[\bar{K}]_{RT}$	Nondimensional linear stiffness and damping matrices in X-Y and R-T coordinate systems
D	Journal bearing diameter, m
D_x, D_z	Decoupled coefficient matrices of the discretized PDE system in x and z directions
$e_0, e, \dot{e}$	e_0: Journal eccentricity at steady state, and $e, \dot{e}$: instantaneous journal eccentricity and velocity
$\%e_{ext}{}^{21}$, $e_{ext}{}^{21}$	Coarse and fine grid extrapolated relative errors in numerical calculation of the field variable
F_x, F_y, F_R, F_T $f_x, f_y, f_\epsilon, f_\varphi$	Total bearing reaction forces in X, Y, R, T directions and the nondimensional force components where $f = F/\Pi$
f_x, f_y	Bearing dynamic reaction force in excess of bearing steady state force in x and y directions, N
$f(\boldsymbol{X}, t)$	Right hand side of the state space equations of motion
F, $F_{i\pm\frac{1}{2},j}$	x-component of the flux vector and its value at control volume interfaces
$\overrightarrow{FI}$, FI^n	Flux integral vector and control volume average flux integral at time-step n
G, $G_{i,j\pm\frac{1}{2}}$	z-component of the flux vector and its value at control volume interfaces
$GCI_{coarse}{}^{32}, GCI_{fine}{}^{21}$	Coarse and fine grid convergence index
g, $gFactor$	
h	Oil film thickness, $h = C(1 + \epsilon\cos(\theta))$, m
H	Non-dimensional oil thickness $H = \frac{h}{C}$
$\boldsymbol{Imp}, Imp_j$	Imp_j are components of the impedance vector: $\boldsymbol{Imp}$

$K_{ij}, K_{ijk}, K_{ijkl}$ $\overline{K}_{ij}, \overline{\mathrm{K}}_{ijk}, \overline{K}_{ijkl}$	Linear and Nonlinear stiffness coefficients in global Cartesian coordinates (X-Y): $i,j,k,l = x,y$; and in (R-T) coordinates $i,j,k,l = r,t$ where $\overline{K}_{ij} = \frac{C}{\Pi} K_{ij}$, $\overline{K}_{ijk} = \frac{C^2}{\Pi} K_{ijk}$, $\overline{\mathrm{K}}_{ijkl} = \frac{C^3}{\Pi} K_{ijkl}$
$K_s, \bar{k}_s$	Shaft stiffness where $\bar{k}_s = \frac{C}{\Pi} K_s = \frac{1}{S} \frac{C K_s}{W}$
k_θ, k_z	Circumferential and longitudinal turbulent coefficients
K_{num}	Numerical stiffness
L	Journal bearing Length, m
$M, m_u, \bar{m}_u$	Reduced mass of the rotor, and unbalance mass where: $\bar{m}_u = \frac{m_u}{M}$
$\boldsymbol{M}$	Monodromy matrix
m, n	Number of elements in x and z directions
N	Rotating speed, $\frac{rev}{sec}$
O_B, O_{js}, O_{jd}, O_M	O_B: Geometric center of the Bearing chamber, O_{js}, O_{jd}: steady state and instantaneous position of the journal center, instantaneous position of the central disk
OL	Order of the system of ordinary differential equations
$P_\varepsilon(t)$	Periodic solutions due to Hopf bifurcation
$P, \bar{P}$	Bearing induced pressure and its non-dimensional form: $\overline{\mathrm{P}} = \frac{\mathrm{P}}{\mu N \left(\frac{R}{C}\right)^2}$
$P_0, P_R, P_T, P_{\dot{R}}, P_{\dot{T}}$	Steady pressure and its gradients in R-T coordinates
$P_0, P_x, P_y, P_{\dot{x}}, P_{\dot{y}},$ $P_{xy}, P_{xx}, P_{yy},$ $P_{y\dot{x}}, P_{x\dot{y}}, P_{x\dot{x}}, P_{y\dot{y}}$	Steady pressure and its gradients in *X*-*Y* coordinate system
$\bar{P}_{max}, \bar{P}_g$	Non-dimensional maximum pressure and supply groove pressure
Q	Rotation matrix
q_i	Generalized journal bearing position and velocity: $q_1 = e$, $q_2 = \varphi$, $q_3 = \dot{e}$ and $q_4 = \dot{\varphi}$
R	Journal radius, m
$R_u, \bar{R}_u$	Unbalance mass eccentricity radius where: $\bar{R}_u = \frac{R_u}{C}$

$R(U)$, $\|R(U)\|_2$	Residual matrix and the L_2 norm of the residual
Re	Average Reynolds number: $Re = \frac{\rho\, R\, \omega\, C}{\mu}$
Re^*	Local Reynolds number: $Re^* = \frac{\rho\, R\, \omega\, h}{\mu}$
S	Sommerfeld number $S = \frac{L\, D\, \mu\, N}{W}\left(\frac{R}{C}\right)^2$
$\bar{S}$	Source term for the steady and perturbed Reynolds equation
t, τ	Time (sec) and its non-dimensional form: $\tau = \omega\, t$
u, $\bar{u}$	Solution to the governing PDE and its control volume average
$\tilde{u}$, $\tilde{U}$	Axillary control volume solution and its vector representation
$\vec{U}$, $\delta\vec{U}$	Control volumes solution vector and the change in solution vector
$W, \bar{W}$	Bearing load capacity $W = \frac{Mg}{2}\ (N)$ and its non-dimensional form: $\bar{W} = \frac{W}{L\, D\, \mu\, \omega}\left(\frac{C}{R}\right)^2$
x, y, R, T	Cartesian and rotated coordinate systems. The R coordinate is aligned with the line of centers.
$\dot{x}, \dot{y}, \dot{R}, \dot{T}$	Velocity components in Cartesian and rotated coordinate systems
$\ddot{x}, \ddot{y}$	Journal bearing acceleration in (x, y) coordinate system
X_i	State-space variables of the dynamical system. $i = 1,2, \ldots, 6$
X_i	State-space variables of the dynamical system. $i = 1,2, \ldots, 6$
X^n	linearly independent vector solutions of $\dot{\mathbf{X}} = \boldsymbol{A}(t)\, \mathbf{X}$
$\boldsymbol{X}^*$	Fixed point or steady state of the system
$\boldsymbol{X}^n, \boldsymbol{X}^{n+1}$	State-space vector at time-step n and n+1
$\delta\boldsymbol{X}$	Change in solution of the dynamical system from two consecutive time-steps
$\bar{x}, \bar{y}, \bar{X}_{journal}, \bar{Y}_{journal}$	Dimensionless journal center displacement in horizontal and vertical directions
x, z	Circumferential and axial directions in space
$\bar{x}, \bar{z}$	Dimensionless circumferential and axial directions in space
X_i	Coefficients of the linear discretized system in x direction. $i = -2, -1, 0, 1$

Z_j	Coefficients of the linear discretized system in z direction. $j = -1, 0, 1$
$\boldsymbol{A}(\nu), \boldsymbol{B}(\nu)$	Real and imaginary parts of the complex eigenvalues of the Jacobian matrix
α	Fluid density ratio: $\alpha = \frac{\rho}{\rho_c}$
$\beta, \bar{\beta}$	Lubricant bulk modulus (Pa) and its non-dimensional form: $\bar{\beta} = \frac{\beta}{\mu\omega}\left(\frac{C}{R}\right)^2$
γ, Γ	Stability parameter $\gamma = \frac{C\,K_S}{W}\bar{\omega}_{th}^2$ and bearing characteristic number: $\Gamma = \frac{\mu R L^3}{M C^{2.5} g^{0.5}}$
$\epsilon_0,\ \varphi_0$	Steady state eccentricity ratio $\epsilon = \frac{e}{C}$ and attitude angle
$\epsilon, \varphi, \dot{\epsilon}, \dot{\varphi}$	Instantaneous journal position and velocity in rotating frame of reference (ϵ, φ)
$\boldsymbol{\phi}(\mathrm{t})$	T-periodic solution to the system $\dot{\mathbf{X}} = \boldsymbol{A}(t)\,\mathbf{X}$
$\boldsymbol{\Phi}(t)$	fundamental matrix solution for the linearized equation about the periodic orbit
$\boldsymbol{\eta}_0$	Set of initial conditions for the system of equations: $\boldsymbol{\eta}_0 = \boldsymbol{X}(0)$
$\zeta, \vartheta, \xi, \psi$	Attitude angles measured from: ξ: instantaneous line of centers to the load line ϑ: instantaneous line of centers to squeeze velocity vector line ζ: pure squeeze velocity vector to the global *X* coordinate ψ: instantaneous line of centers to the global *X* coordinate
$\theta_0, \theta, \theta_n$	θ_0, θ are circumferential coordinates measured with respect to steady and dynamic line of centers. θ_n is measured from the $-X$ global coordinate.
θ_{cav}	The cavitation boundary
λ	Eigenvalues of the discretized system coefficient matrix
μ	Fluid film (lubricant) viscosity (Pa.s)

μ_j, μ^H, μ_{2i}	Floquet exponents corresponding to the periodic solution of the system where μ^H is the first nonzero exponent of μ_j, and μ_{2i} is the coefficient in the series expansion of the Floquet exponent μ^H
$\nu, \nu_c, \nu^H, \nu_{2i}$	ν is the system tuning parameter, ν_c is the critical system parameter at which a bifurcation occurs, ν^H is the predicted system parameter when Hopf bifurcation occurs; and ν_{2i} is the coefficient in the series expansion of ν^H
$\nu, \bar{\nu}$	Whirl frequency $\nu = \omega\bar{\nu}$
Π	Non-dimensionalizing group: $\Pi = L\ D\ \mu\ N\ \left(\frac{R}{C}\right)^2$
ρ, ρ_c	Fluid film density (kg/m^3) and film viscosity at cavitation pressure
ρ_j	Characteristic (Floquet) multipliers corresponding to the periodic solution of the system
φ	Attitude angle
$\Phi_{ext}{}^{21}$	Extrapolated field variable in fine grid
Φ_1, Φ_2, Φ_3	Numerical estimate of the field variable in fine, medium and coarse mesh
ω,$\bar{\omega}$	Dimensional and non-dimensional Shaft rotating speed (rad/s): $\bar{\omega} = \omega\sqrt{M/K_s}$
ω_r	Under-relaxation parameter
$\bar{\omega}_{th}$	Dimensionless threshold speed of instability

List of Abbreviations

AF	Approximate Factorization
E.A.	Elrod-Adams
FLS	Full Linear System
FVM	Finite Volume Method
HBT	Hopf Bifurcation Theory
ODE	Ordinary Differential Equation
PDE	Partial Differential Equation
SOR	Successive Over Relaxation

Acknowledgements

First and foremost, I would like to thank my supervisor, Dr. Mohamed Gadala, for his continuous support, his kind manners and his professional leadership. It was a pleasure for me to benefit from his guidance and advice through my PhD years. I would also like to thank my supervisory committee for their helpful engagement in this project.

Special thanks to Dr. Mohamed Alqaradawi for his kind support, and to the Qatar National Research Fund (QNRF) for partially funding this research.

I would like to express my thanks to my friends and fellow colleagues, Farzad, Alireza and Shayan for all the fruitful discussions that we had on numerous issues within the past few years. My work benefits from your insights and expertise, and your thoughtful engagement in this research. Also, I give many thanks to my lab mates Arian, Alireza and Mohsen for creating a friendly environment without which my PhD years wouldn't have been as pleasant as they were.

I wish to give my wholehearted thanks to my mother and my sister Galineh. I know that me being away has impacted you in so many ways, yet, you never let that waver your unconditional support, love and care for me. Many thanks to my sister, Melika, for being able to continually love and care for me and to patiently handle the temperament of a PhD student in the final years of his degree.

I wish to thank my dearest uncles, Hashem and Mahmoud. I can't imagine being at this point of my life if it wasn't for your support, both emotionally and financially. You treated me as your own son and I love you and am thankful to you in the same way as I am to my parents.

Finally, I want to thank my dear friends and brothers, Mehdi and Mehdi. The hardships in my life would have been unbearable if it weren't for both of you.

To the memory of my Father,

Who valued education more than anything else in the world; who put forth his children ahead of his own interests every single time; who loved to see this day more than anyone else, even me; whom I miss dearly and truly and will always be in my heart.

Chapter 1: Introduction

1.1 Background

Rotating machines started being manufactured in significant numbers concurrent with the development of waterwheels for hydraulic power in the early 1800s, and steam turbines in the late 1800s. The first type of dynamic problem associated with rotor bearing systems was the critical speed phenomena when the excitation frequency (the spin speed of an unbalanced shaft) coincides with a natural frequency of the system and may lead to excessive vibration amplitudes. The first analysis of the critical speed phenomena was done by Rankine in 1869 [1]. Through his incorrect modeling, he concluded that rotor systems will become unstable if they operate above the first critical speed of the system. This conclusion has been found to be incorrect, and has delayed progress in the field of rotor science by 50 years [2]. It was shown later that Rankine's incorrect predictions was due to a failure to include the Coriolis force in his model [3]. Rankine's over-simplified model of a rotor-bearing system is depicted in Figure 1-1. The first experimental evidence of successful supercritical operation was reported in 1890s by Delaval [2].

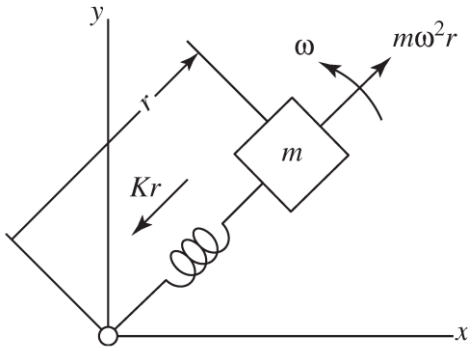

Figure 1-1. The Rankine rotor-bearing model

In the early developments in the field, the importance of bearings was not recognized until the work of Reynolds in 1886 that showed mathematically how a pressure is generated in the oil film to support the shaft. In 1919, Jeffcott [4] has corrected the analysis of the critical speed and showed analytically that rotor systems can operate at supercritical speeds. The Jeffcott model is shown in Figure 1-2. The next major issue to arise was whirl instability, first addressed by Newkirk and Kimball in 1920 [2].

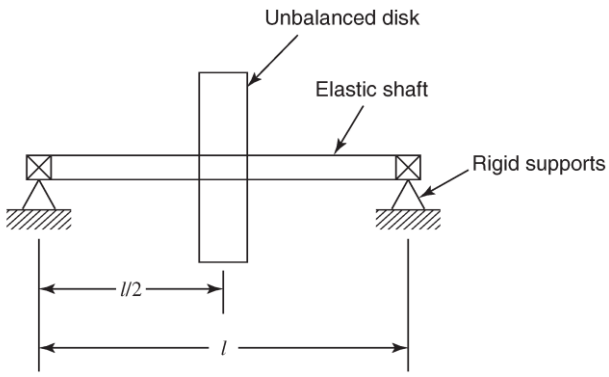

Figure 1-2. The Jeffcott rotor-bearing model

1.1.1 Hydrodynamic Bearings

In the 19th century, it was widely accepted that the oil in bearings simply serves to reduce the sliding friction between the shaft and the bearing. In 1886, Reynolds's mathematical analysis showed that a pressure is generated in the oil film due to the rotation of the shaft within the bearing [5]. A schematic of a journal bearing inside the bearing chamber is shown in Figure 1-3.

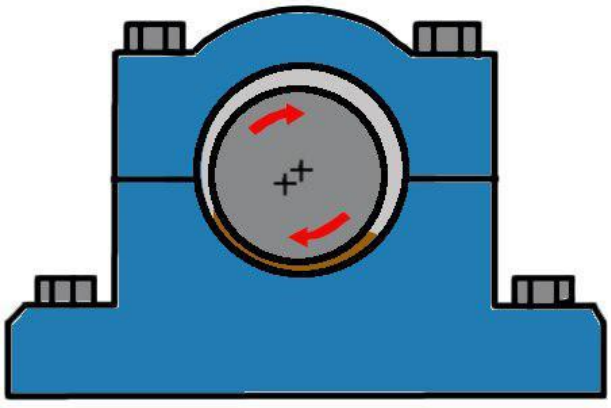

Figure 1-3. The schematic of a journal bearing inside the bearing chamber

At the time, Reynolds's partial differential equation of the oil film was not feasible to solve in two dimensions. The first successful remedy came from the work of Sommerfeld and Harrison [6] who

simplified the problem and were able to solve the Reynolds equation to obtain the induced pressure and bearing forces on the shaft. The most important aspects of their work were firstly, to show that the induced bearing force is enough to support the load of the shaft and to show that this oil film force is not in line with the radial deflection of the shaft from the bearing centerline. As a result, there will be a component of the force normal to the radial deflection which is known as the cross-coupled force, and this force is responsible for the sub-synchronous instability that occurs at supercritical speeds, known as the **oil whirl/whip** effect. The cross coupled terminology comes from the form of the force expressions in a nonrotating X-Y coordinate where a rotor displacement in X direction produces a force in the Y direction [2]. The induced journal forces are shown in Figure 1-4.

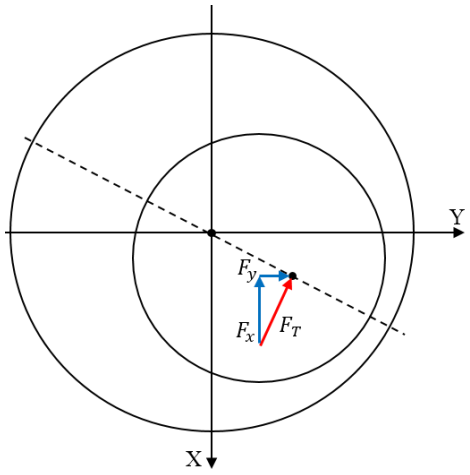

Figure 1-4. The tangential force component exerted from the oil onto the journal

Newkirk and Taylor [7] were among the first to relate the bearing induced instability to the oil film bearings. They found that when the system reaches twice its first critical speed, a sub-synchronous whirl destabilizes the system; however, they could not successfully explain the phenomenon. In 1959, Hori [8] succeeded in explaining various fundamental characteristics of oil whip by studying the stability of shaft motion under the induced pressures of journal bearings.

1.1.2 Rotordynamic Models

A better model of the rotor bearing system was introduced by D.M Smith in 1933 [9]. He went far beyond Jeffcott in his work and successfully concluded that while damping always favors stability

in bearing supports, it can also cause instability in the rotating parts at speeds above the critical speed. A new method for calculating critical speeds of flexible rotors was introduced in 1945 by Prohl [10] for rotors modeled by a series of lumped masses at different stations. His method became known later as the transfer matrix method.

Early researchers modeled flexible rotors as circular, flexible beams with concentrated mass stations being supported at rigid points in the bearing locations. It was not until the work of Hagg and Sankey in 1956 that journal bearings began to be modeled as radial springs and dampers [11]. The very first attempts to solve the Reynolds equation by means of numerical methods goes back to the work of Raimondi and Boyd in 1958 [12]. J.W Lund, in his PhD thesis in 1966, defined the so called linearized force coefficients for oil film bearings [13]. Lund defined the stiffness and damping coefficients for the bearings. His definition also included the cross-coupling effects. A modified Jeffcott model with journal forces modeled as spring and dampers is shown in Figure 1-5.

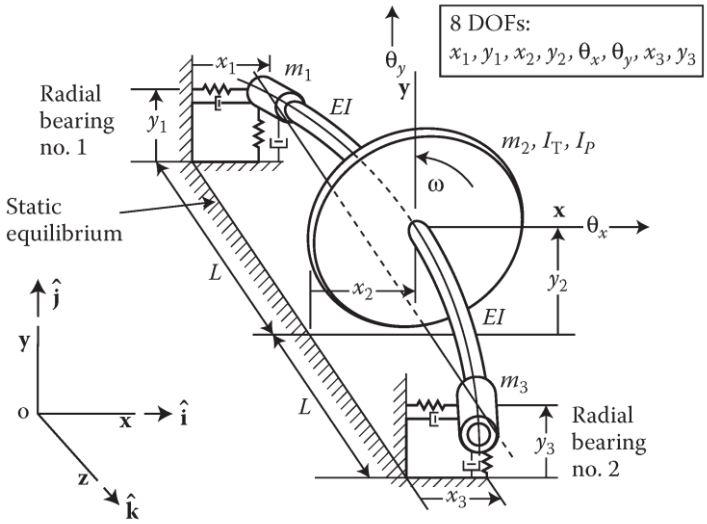

Figure 1-5. A modified rotor-bearing model with 8 DOFs [14]

While most of the rotor systems being used before the 1940s were generally operating at low speeds, the development of gas turbines for aircraft propulsion, as well as the need for centrifugal machines for petrochemical gas compression, brought many more applications at a variety of speeds in turbomachinery. The demand for high pressure injection of natural gas in underground

lead to the design of multistage compressors. In the 1970's many such compressors were suffering from violent sub-synchronous whirl [2], a form of instability in rotordynamics. These very expensive problems arising in industrial compressors were the incentive for the development of computer simulations of rotordynamic instability. The most significant development was an algorithm published by Lund in 1974 as an extension to the Myklestad-Prohl method (which only calculated the critical speeds). His algorithm allowed damping and cross coupled force coefficients to be included in the model, and damped eigenvalues of the system were computed [15].

1.1.3 Rotordynamic Instability

In turbomachinery, instabilities are characterized by whirling of the rotor-bearing systems at frequencies other than the rotating frequency of the shaft. While the most common source of vibrations in rotor-bearing systems is the shaft imbalance, the resulting vibrations are synchronous and they never cause instability. The term instability in rotordynamics is often associated with sub-synchronous vibrations. While large amplitudes of sub-synchronous vibrations do not occur frequently, they can appear at certain operating conditions and can lead to high amplitude and destructive vibrations [16]. Different mechanisms have been identified in the literature to explain rotordynamic instability, such as the hydrodynamic bearings (oil whirl/whip) [7], internal friction in rotating parts [17], dry friction whip [18], labyrinth seals [19] et cetera. For the rotor bearing systems supported on journal bearings, the oil whirl/whip instability is the most frequent source of instability and will be addressed in detail.

In a fully balanced rotor-bearing system and at moderately low rotational speeds, the only mode of motion is the rotor spinning at its designed operating speed. At this equilibrium point, the journal bearing induced pressures can support the weight of the shaft. This point is referred to as the static equilibrium position or the steady state point of the system. If the rotor bearing system is undisturbed, the system remains at its steady state operating point. A small unbalance force however, will push the shaft to orbit around the steady state point. Although any mode of motion beyond the desired spinning is generally unwanted, small orbits are usually tolerated and do not endanger the safe operation of the system. Upon increasing the spin speed of the shaft, and after crossing critical shaft spin speed, high amplitude vibrations can suddenly occur even for a fully balanced rotor. This occurrence of high amplitude vibrations is a bifurcation in the dynamical

system and is known as the *oil whirl* phenomenon in rotor-bearing systems. Oil whirl is a self-induced instability and is a result of the transfer of energy from rotor spinning to rotor lateral motion [20]. As high amplitude vibrations can be extremely hazardous to the operation of the system and the safety of the working personnel, characterizing the mechanisms that can cause excessive whirling motion is of paramount importance. Photos of a catastrophic system failure due to excessive whirling amplitudes in a steam turbine unit are shown in Figure 1-6.

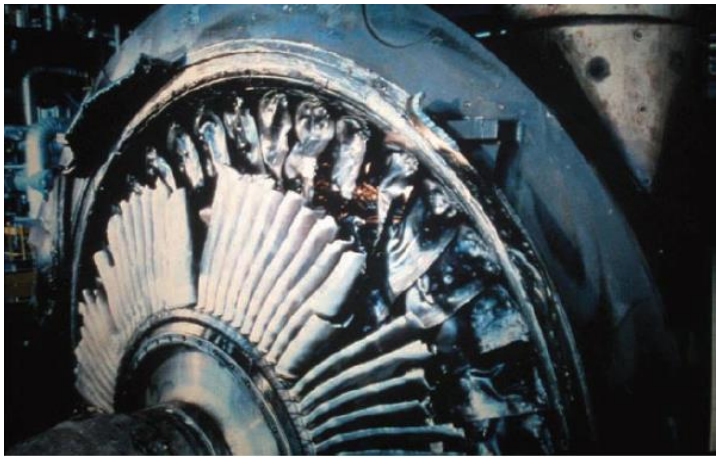

(a)

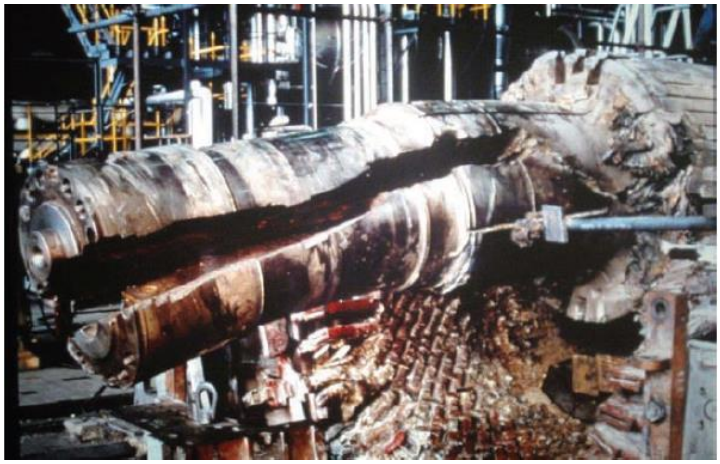

(b)

Figure 1-6. Photos [14] from a 1970s catastrophic failure of a large 600MWsteam turbine-generator set. Failures is potentially traced to the large unbalance forces from loss of one or more large LP turbine blades at running speed, coupled with behavior of journal bearings during large unbalance. (a) LP steam turbine last stage. (b) Generator shaft.

The follower journal bearing forces at a spin speed beyond a critical value, known as the threshold speed of instability, ω_{th}, is responsible for this instability [2, 21]. The follower force can alternatively be expressed as the cross-coupled stiffness coefficient of a journal bearing [16]. In linear stability theory applied to rotor-bearing systems, the equations of motion of the rotor and journal are constructed using the linearized stiffness and damping coefficients around steady state equilibrium points [13]. Eigenvalue analysis of this linearized system of equations of motion are then used to find the speed at which the real part of the eigenvalue of the system becomes positive (indication of instability due to undamped vibrations) for each eccentricity. Stability maps are then obtained to help identify the stable/unstable regions of operation [18].

1.2 Literature Review

1.2.1 Cavitation in Journal Bearings

The first successful mathematical model ever proposed for the lubrication problem was by Osborne Reynolds in 1886. Even Reynolds himself was doubtful that the fluid film can sustain sub-atmospheric pressures and hence he limited his analysis to lower eccentricities. The remarkable analytical solution to the Reynolds Equation by Sommerfeld in 1904 predicted a negative anti-symmetric pressure (tensile stress) in the divergent region of the bearing with magnitudes as large as the predicted positive pressure. Liquids in pure form or with a small amount of dissolved gaseous content were reported to withstand tensile stresses of even up to hundreds of atmospheres [22]. However, in tribological environments with extreme shearing of the lubricant and high rates of heat generation and dissipation, a film rupture is expected when the fluid pressure drops below the saturation pressure of the dissolved gases (gaseous cavitation) or below the vapor pressure (vapor cavitation or boiling) [23]. The onset and extent of liquid cavitation in fluid film bearings is equally important in determining the load capacity of a fluid film bearing as well as largely influencing the rotor-dynamic stability of a rotor-bearing system and its maximum whirl amplitude of vibration [24]. Furthermore, vapor cavitation collapse (implosion) can cause severe surface material damage.

Regardless of the nature of the bubbles that form during cavitation, whether caused by the environment or coming from the lubricant film itself, the bubbles induce a rupture in the continuous lubricant film. This happens in the diverging part of the lubricant film where the original Reynolds theory predicts negative pressures. Although the existence of the cavitated region is well understood, the exact position of the rupture interface and the applied boundary conditions at the interface are subjects for considerable discussion.

The first attempt to account for the film rupture, was made by Gumbel in 1914; he assumed the boundary of the rupture originated in the immediate vicinity of the film at minimum thickness, and neglected the sub-ambient pressure loop completely when calculating bearing performance. His work falls short mainly because it does not respect the mass continuity at the interface and does not account for film reformation. Although the pressure predictions based on the Gumbel condition are at variance with experimental data, the Gumbel boundary condition applied to short and long journal bearings result in closed-form solutions for bearing performance and is still employed in theoretical work [25]. The next major work came from Swift and Stieber in 1932, who assumed a zero pressure gradient at the start of the cavitation zone. The algorithm proposed by Christopherson [26] in 1941 is based on the Swift-Stieber model and has been widely used in numerical analysis due to its ease of implementation. The main disadvantage of the Christopherson algorithm is that it is not mass-conserving and it is not capable of presenting the sub-cavity pressures that occur just upstream from the cavitation boundary. Non mass-conserving schemes are shown to predict incomplete identification of the film rupture and incorrect detection of the film reformation. Analysis of dynamic journal bearings and bearings with textured surfaces revealed that ensuring the mass continuity is necessary to correctly predict film rupture and reformation [27, 28].

The majority of existing mass-conserving algorithms are based on the notable work of Jacobsson-Floberg [29] and Ollson [30], together known as the JFO cavitation model. This model assumes a constant pressure everywhere in the cavitation region ($P = P_{cav}$) and hence, takes the pressure gradient to be zero in the cavitated region. Their model also provides boundary conditions that conserve the mass at the interface between the full film (non-cavitated) and the cavitation zones at rupture and reformation boundaries. The JFO model semi-accurately [31] predicts the onset and shape of the cavitation region in bearings that operate at moderate to high journal eccentricities

(i.e. moderate to large static loads). The main disadvantage of the JFO model is the difficulty of implementation in computer codes, due to the complexity of numerical treatment of the nonlinear boundary conditions. Elrod and Adams [32, 33] developed a finite difference algorithm based on the JFO theory, but in a very simple manner. They introduced a change of variable that is related to the film pressure through the bulk modulus of the lubricant and rewrote the governing equations (in terms of the new variable) assuming constant bulk modulus throughout the lubricant film. They also combined two governing equations into a single equation throughout the lubrication region by proper use of a switch function to suppress the pressure driven terms in the cavitated region. Their ingenious approach was very successful for cavitated journal bearing performance predictions and is usually referred to as the universal cavitation algorithm (also E.A. algorithm). The cavitation algorithm was then mainly solved by means of Gauss-Seidel based relaxation methods [28, 34] or Alternate direction Implicit (ADI) [24, 35].

Vijayaraghavan and Keith [36] addressed a change in the type of PDE at the cavitation boundary, and designed an algorithm that takes this change into consideration to further refine computational efficiency. As relaxation and ADI methods require large computing times to convergence, different algorithms were proposed to enhance the convergence speed of the Elrod algorithm. Vijayaraghavan and Keith [36] proposed the use of the Approximate Factorization (AF) technique. Woods and Brew [37] and Qiu and Khonsari [38] advocated the use of Multigrid techniques to accelerate the convergence speed.

The implementation of the universal cavitation algorithm is generally troubling in a computer code, mainly due to dependency of the numerical efficiency on the chosen values for the lubricant bulk modulus (β). Choosing β values close to its physical value of approximately 2 GPa, can render the system of equations too stiff to obtain accurate solutions, and it can also affect the convergence speed drastically. This difficulty was addressed by choosing artificially low values for β [32, 36], assuming that this particular choice does not affect the final results [39]. Many subsequent studies show that the choice of β indeed affects the performance predictions of the journal bearings [40-43].

Sahlin et al. [43] reported that treating the bulk modulus as a constant in the whole domain can produce accurate results only for a narrow pressure range . They introduced an algorithm mainly based on the Elrod algorithm, but with an arbitrary choice for pressure-density to account for bulk modulus variations with pressure, and noted the importance of the bulk modulus on the final calculations. Bayada and Chupin [41] and Bayada [44] proposed an algorithm similar to Elrod-Adams by directly solving the constitutive equations of the lubricant with detailed descriptions of the mixture characteristics in the cavitated region. They proposed a smooth pressure-density relation similar to Sahlin et al. [43], together with models for viscosity variations with density. Their unified treatment of the cavitated and full film regions eliminate the need for up-winding differencing in the cavitation region and naturally allows for sub-cavitation pressures in the cavitation region, which is in-line with experimental predictions of pressures as low as 0.07 MPa upstream of the rupture interface [45]. They also showed how the choice of the lubricant bulk modulus can change the pressure distribution and the cavitation boundary. However, there was no reference made to how this choice can affect the performance of the numerical scheme itself.

As an alternative approach to the universal cavitation algorithm, Giacopini et al. [46] proposed a mass-conserving linear complementarity formulation for the one dimensional cavitation problem. The major advantage of their complementarity formulation is that it alleviates the problems associated with the need to change the scheme differencing method as a result of a change in the PDE type at the cavitation boundary. Bertocchi et al. [42] extended the original one-dimensional LCP formulation of Giacopini et al. [46] to include the effects of fluid compressibility (pressure-density relationship), piezo-viscosity (variation of viscosity with pressure) and non-Newtonian fluid behavior (shear rate dependence of lubricant viscosity) for 1D and 2D cavitation problems. Almqvist et al. [40] proposed a model starting with the expression of the mass flow that leads directly to the linear complementarity problem (LCP). The linearity is guaranteed by treating β as a constant. They reported on the influence of chosen bulk modulus values (100 MPa up to 10 GPa) on fluid film pressure, and suggested that the load carrying capacity of the bearing increases as the compressibility of the fluid decreases. The LCP based algorithms do offer benefits compared to the Switch function approaches; however, a complete performance analysis of these algorithms is missing in the literature and hence their computational efficiency is unclear and undocumented.

1.2.2 Linear Stability Analysis under Laminar and Turbulent Conditions

Rotor whirling can be caused by a variety of mechanisms such as imbalance and misalignment with whirl frequencies of equal (synchronous) and higher (super-synchronous) than the spin speed of the shaft, respectively. In turbomachinery, an instability is usually referred to rotor whirling at frequencies other than the rotating spin frequency of the shaft. Although sub-synchronous rotor whirling is not the most common type of instability, when it does occur at certain operating conditions, it can lead to high amplitude and potentially destructive lateral vibrations in the system. The necessary condition for the occurrence of such sub-synchronous whirling, known as oil whirl/whip, is an operating spin speed of the shaft that exceeds a threshold speed, known as "threshold speed of instability" [16]. Linearized stiffness and damping coefficients are frequently used as a basis for stability analysis of the rotor bearing systems in an aim to find the threshold speeds of instability for a rotor-bearing system. The linearized coefficients are evaluated at the equilibrium position of the journal and are commonly calculated either by the infinitesimal approach of Lund [47] or the finite perturbation approach as in Qiu and Tieu [48].

The journal bearing force is a strong nonlinear function of its position with respect to the bearing chamber. However, the stability of the rotor-bearing system can be characterized by means of linear analysis with the use of linearized bearing dynamic coefficients. It is widely known that the "local" stability of a non-linear system is essentially the same as the local stability of its linearized form; even though their stability type and global stability could be different [49]. Local stability analysis is valid only if the operating condition of interest is close enough to an operating equilibrium point or a fixed point of the system. Being close to a fixed point of the system is also a requirement for accurately estimating the linearized dynamic coefficients of the system, although there are different reports on the minimum required distance from fixed points to obtain accurate results. Lund [47] used the infinitesimal approach to obtain the dynamical coefficients such that the induced bearing pressure is perturbed by an infinitesimal amount through perturbing the oil film thickness. The operating points arising from this infinitesimal perturbation of the system are by definition very close to the steady state points of the system. He reported that the obtained coefficients are valid up to 40% of the bearing clearance.

As an alternative approach to obtain the dynamic coefficients, finite perturbations of the journal position and velocity are carried out, combined with direct numerical differencing to obtain the linearized coefficients. Qiu and Tieu [48] studied the effect of perturbation amplitudes and concluded that the finite perturbation-based calculated coefficients are within 2.5% of those obtained by the infinitesimal approach, if the perturbations of displacement and velocity are kept lower than 5% and 4%, respectively. Choy et al. [50] calculated nonlinear bearing stiffness coefficients and showed that oil film forces will exhibit nonlinearities when displacements are sufficiently far from the steady state operating point. San-Andres and Santiago [51] obtained the dynamic coefficients under high dynamic loads for which the journal moved in large orbital motions of up to 50% of the bearing clearance, and found good agreement with analytical linearized coefficients. Meruane and Pascual [52] calculated linear and nonlinear bearing coefficients under large orbital motion and showed that the linearized analytical coefficients agree reasonably with numerically obtained linear coefficients. They reported negligible variations between the linear and nonlinear models, provided that the operating speed is kept below the threshold speed of instability. Wang et al. [53] and Yang et al. [54] used an infinitesimal approach to calculate linear and nonlinear bearing coefficients. Their results indicate close similarity between linear and nonlinear coefficients for eccentricity ratios of up to $\epsilon = 0.8$. They reported that linearized results will be incorrect at very high journal loads, especially for $\epsilon > 0.95$.

The majority of stability studies of rotor-bearing systems in the literature are based on the declaration that fluid-film flow remains laminar throughout the operation of the machine. For large and heavy load bearings that run at high spin speeds and utilize low kinematic viscosity lubricants, the oil film flow becomes turbulent. To correctly identify the instability phenomenon and the oil whirl threshold speed of instability, the flow regime (whether laminar or turbulent) needs to be taken into account. This requires the inclusion of the effects of turbulence on the dynamic fluid forces. Hashimoto et al. [55, 56] and Wang et al. [57] investigated turbulent journal bearing performance under dynamic conditions for short bearings. They linearized turbulent coefficients in the Ng-Pan-Elrod model in an attempt to derive analytical expressions for the journal force. However, their implemented linearization can lead to erroneous force predictions at large eccentricity ratios and high Reynolds numbers. Cai-Wan Chang-Jian et al. [58, 59] investigated the dynamics of a flexible rotor bearing system supported by two turbulent journal bearings. They

neglected the spatial gradients of turbulent coefficients to simplify the pressure and force calculations to obtain close form solutions. Their simplifying assumption can also lead to erroneous performance predictions.

1.2.3 Nonlinearity in Rotor-Bearing Systems

Based on the linear stability criterion, it is generally believed that machines should not operate at speeds above the threshold speed of instability. Several cases were reported where machines operated in stable condition much beyond the threshold speed of instability [15].

When nonlinearity exists in a system, a destabilizing force can cause sudden qualitative dynamic change in the system (bifurcation), such as the nonlinear jump phenomenon in rotors in the presence of large unbalance force [60] or the transition from steady state solution of a balanced spinning shaft to limit cycle (rotor whirl) and nonsynchronous and chaotic responses [61, 62]. These types of undesirable motion can endanger the safe operation of the rotor-bearing system. While linearized coefficients are useful in obtaining a stability threshold for the rotor system, stability analysis based on these coefficients cannot reveal the nature of bifurcations (being sub or supercritical) in the system [61-63].

It has been realized that localized nonlinearities can have very significant local and global effects on high speed rotor systems. A very important source of nonlinearities is caused by fluid film forces within journal bearings and seals, which can have significant effects on the dynamic characteristics of rotor systems [21].

In linear systems, response to harmonic excitation (like the imbalance force) can only contain the frequencies of the harmonic driving forces. However, in nonlinear systems, the response to harmonic driving forces can lead to periodic (possibly with sub and super-harmonics), quasi-periodic (non-integer related harmonics), and chaotic motions [14]. Linearized models for studying the dynamic behavior of rotor systems may lead to inaccurate results as a consequence of missing complex phenomena such as transitions to limit cycles, and aperiodic and chaotic responses [63, 64].

Among the very first observations of subharmonic vibrations resulting from nonlinearity in rotor systems is the work done by Ehrich [65]. Ehrich found that when the system is running at speeds near twice the fundamental frequency of the rotor, subharmonic responses are present. Later on, Bently [66] reported experimental observations of second and third order subharmonics by studying a simple horizontal rotor, and concluded that the occurrence of these subharmonics is due to the bearing clearances in the rotor system. Botman [67] reported non-synchronous vibrations at speeds above two times the critical speed of a rigid rotor mounted on dampers, and concluded that the non-synchronous response originates from the effect of the supporting dampers. Assuming the nonlinear effects to be as a result of bearing clearances, Childs [68] used a perturbation technique to study the occurrence of subharmonics. Saito [69] utilized a harmonic balance method (HBM) along with a fast Fourier transform procedure originally proposed by Yamamuchi [70] to explain nonlinear effects of ball bearings on a Jeffcott rotor. The same procedure was used by Choi and Noah [71] to investigate the occurrence of superharmonics and subharmonics in the presence of bearing clearance. Ehrich [72] used a finite difference formulation for numerical integration of the mathematical model and showed that higher order subharmonics, up to the 9^{th} order, exist in a high speed rotor system with bearing clearances.

Aperiodic behavior in journal bearings was reported by Holmes et al. [73], by studying the motion of a symmetric rigid shaft supported on short journal bearings. Nikolajsen and Holmes [74] reported subharmonic vibrations of orders up to four, with operating speeds near three to four times the critical speed of a flexible shaft supported on journal bearings and squeeze film dampers. Muszynska [75] calculated rotor synchronous and sub-synchronous self-excited vibrations (whirl and whip) due to an unbalance force by means of modal analysis of a mathematical model of a symmetric rigid rotor supported on a journal bearing. The fluid film radial stiffness, damping and inertia effects in the model were described by nonlinear functions of the rotor eccentricity. Confirmed by several experiments, it was shown that after a threshold of stability, the pure rotational motion of the shaft becomes unstable, yet, the resulting whirl regime can remain stable [20].

A majority of steady state instabilities occurring in mechanical systems are due to Hopf bifurcations [76]. For the case of rotor systems, a Hopf bifurcation means that energy is transferred

from the rotating motion into periodic whirl motion — a motion that can be referred to as a limit cycle in nonlinear dynamics terminology. In order to understand the nature of the whirling motion, it is necessary to determine the direction of bifurcation and stability of the limit cycle [77]. Many simplified techniques have developed for this analysis [78].

1.2.4 Hopf Bifurcations in Dynamic Response of Journal Bearings

When the rotor operating speed exceeds the threshold speed of instability, the whirl amplitude can become unbounded either gradually (supercritical bifurcation) or suddenly (subcritical bifurcation) [63]. In the case of subcritical bifurcation, a small perturbation from the equilibrium point may lead to instability even when the rotor speed is under the threshold limit. Thus, subcritical bifurcations are more dangerous than supercritical bifurcations, and proper considerations are needed in the design stage to assure operation within the supercritical region [63]. As mentioned before, while linear stability analysis can provide the threshold speed of instability, the nature of bifurcation (being sub or supercritical) cannot be obtained. To predict the existence and type of the bifurcation, a nonlinear analysis of the dynamic response of the rotor bearing system is needed. Once the nonlinear equations of motion are derived, they can be used to predict the existence and type of the bifurcation (sub or supercritical) as well as the instability threshold speed based on the Hopf theorem [76, 79]. The Hopf bifurcation theory (HBT) is concerned with the bifurcation of the periodic orbits from the equilibrium points of a system whose behavior is described by the ordinary differential equations $\dot{X} = f(X, \nu)$ as the system parameter υ crosses a critical value υ_c. The Hopf bifurcation theorem provides appropriate criteria for the prediction of the existence, shape, and period of the periodic solution [76]. Hopf bifurcation theory has been applied to long journal bearings [62], short bearings [61], and finite journal bearings [63].

Subcritical bifurcations in rotor-bearing systems were experimentally observed in the early twentieth century by Newkirk and Taylor [7]. They reported that at running speeds of lower than the threshold speed, violent rotor whipping can occur due to even a small shock applied to the system. This was later confirmed by Hori [8], however, the real cause was not clear at the time. Hori did extensive research on how an earthquake (a shock) can affect the occurrence of the oil whip [80, 81]. As an attempt to explain the effects of a shock on the occurrence of oil whip, Khonsari and Chang [82] introduced the concept of the stability envelope, R_s, such that if the

journal is released from inside the R_s , the orbit will settle into a steady-state equilibrium position. If released from outside the R_s, the orbit will grow larger, extending to the clearance circle of the rotor-bearing system. To find R_s, Khonsari and Chang [82] proposed a trial and error method. An analytic method for estimating the size of R_s was later proposed by Wang and Khonsari [83] for short journal bearings by implementing the HBT.

Myers [62] applied the HBT for stability analysis of a rigid rotor supported on long journal bearings. He identified the existence of three separate regions in the parameter space of the steady state eccentricity ration. These three regions from low to high values are subcritical, supercritical, and again subcritical bifurcations. A similar analysis for short journal bearings was done by Hollis and Taylor in 1986 [61]. They reported that in short journal bearings, the subcritical bifurcation exists if the modified Sommerfeld number is greater than a critical value; otherwise, the supercritical bifurcation exists.

Noah and Sundararajan [63] applied the HBT to a rotor supported on finite length journal bearings. They used impedance descriptions originally proposed by Childs et al. [84, 85] to obtain analytic expressions for the fluid film forces in journal bearings. It was shown that in the case of supercritical bifurcations, there is a gradual transition from stability to instability. On the other hand, in the case of subcritical bifurcation, stable journal orbits may exist above and below the threshold limit, and no gradual transition from stability to instability occurs. The existence of subcritical bifurcation was experimentally verified for a rotor supported on short journal bearings by Deepak and Noah [86].

Ding et al. [77] applied the Hopf bifurcation theory to investigate the balanced and unbalanced dynamics of a symmetric rotor-seal system based on Muszynska's [87] nonlinear seal model. Implementing algebraic criterion proposed by Poor [88], they showed that only supercritical regions exists for perfectly balanced systems. In their analysis of periodically perturbed Hopf bifurcation [89] (due to imbalance), they showed that non-synchronized whirl of the imbalanced rotor can either be a quasi-periodic motion resulting from Hopf bifurcation, or a half-frequency whirl from period doubling bifurcation.

Wang and Khonsari [57] applied the HBT method to dynamic equations of a rotor supported on short journal bearings acting in a turbulent regime. They showed that turbulence tends to deteriorate the stability of the rotor-bearing system; as the Reynolds number increases in the bearing fluid film, the stability threshold speed decreases, especially with small Sommerfeld numbers. Effects of rotor stiffness on the existence and type of bifurcation and the instability threshold speed was studied by Wang and Khonsari [90] based on the application of Hopf bifurcation theory. They reported that rotor stiffness has a profound influence on a system's stability threshold speed and its bifurcation type, and should not be neglected.

The use of closed-form expressions for the journal bearing force is common to all above-mentioned literature studying the nonlinear system response, whether by applying the HBT or by direct time integration of the equations of motion. The closed-form expressions are obtained by approximating the journal force based on the asymptotic *Short*, *Long* and *Finite* bearing theories.

1.2.5 Nonlinear Stability Analysis in Rotor-Bearing Systems

HBT describes the bifurcation of the periodic orbits from the equilibrium points of a system whose behavior is described by the autonomous ordinary differential equations $\dot{\boldsymbol{X}} = \boldsymbol{f}(\boldsymbol{X}, \nu)$ as the system parameter ν crosses a critical value ν_c. In the case of rotor-bearing systems, the parameter is usually the spin speed ω and the critical value is the threshold speed of instability ω_{th}. For the nonlinear system of equations in the form $\dot{\boldsymbol{X}} = \boldsymbol{f}(\boldsymbol{X}, \nu)$, the zeroth order terms in a Taylor expansion of the right hand side is used to find the fixed points of the system. The first order terms as in the Jacobian matrix, $\frac{\partial \boldsymbol{f}}{\partial \boldsymbol{X}}$, are used to determine the linear stability and whirl threshold speed [25, 91]. The second and third order terms are used to identify the type of Hopf bifurcation in the system [61, 63].

As discussed, common among existing literature that applies HBT to a rotor-bearing system, is the use of closed-form expressions for the journal bearing force that is exerted on the shaft [57, 61, 71, 83, 90]. This use of closed-form expressions is mostly needed since distinguishing the type of bifurcation requires estimating the higher order derivatives of the right hand side of the system of equations: $\dot{\boldsymbol{X}} = \boldsymbol{f}(\boldsymbol{X}, \nu)$. Since the nonlinearity in the system is mainly caused by the journal

bearing forces, higher order derivatives of the system reduces down to higher order derivatives of the journal force with respect to journal position and velocity. If the journal force is expressed analytically, calculating the higher order derivatives is not a challenge. Unfortunately, closed-form expressions for the journal force are only available for very limited geometries in the form of asymptotic solutions to the Reynolds equation: namely, *Ocvirk Short bearing* and *Sommerfeld Long bearing* solutions. An approximate solution also exists for Finite length bearings with very simple geometries and limited cavitation models based on a weighted sum of the short and long asymptotic solutions [85].

Linearized stiffness and damping coefficients were proposed by Lund [47, 92] as an alternative way to express the journal force in excess of its equilibrium values. Such treatment can potentially be extended to any journal geometry and desired cavitation model [93], and in that sense is superior to closed-form journal force expressions. However, application of linear coefficients in stability analysis is limited to the calculation of whirl threshold speed. Bifurcation types and directions cannot be found based on just linear coefficients, as they are functions of second and third order derivatives of the force with respect to journal position and velocity.

Hypothesis: higher order coefficients can be used to avoid degenerate cases that are caused in HBT analysis when the journal force is expressed only by linear coefficients.

Although the probable benefits of employing higher order coefficients in bifurcation analysis of rotor-bearing systems is not addressed in the literature, there exists a few attempts to calculate the nonlinear coefficients mainly aimed for better trajectory predictions. Sawicki and Rao [94] used a linear infinitesimal perturbation of the pressure gradients to find the nonlinear coefficients of a finite bearing. Meruane and Pascual [52] used a least mean square to fit the numerically obtained trajectories to a mathematical model with nonlinear coefficients of up to third order. Wang et al. [53] and Yang et al. [54] used a full second order Taylor expansion of bearing induced forces and pressure to find the nonlinear dynamic coefficients for a short, long, and finite journal bearing. However, widespread differences exist in the reported trends and values of the nonlinear dynamic coefficients in the literature. As nonlinear-based analysis is very sensitive to the system parameter inputs, such inconsistency in the reported nonlinear coefficients will yield inaccurate predictions.

Thus, a comprehensive method to obtain the nonlinear dynamic coefficients for finite length journal bearings is needed.

1.3 Objectives

The main objectives of this thesis are as follows:

- To have a robust, fast converging algorithm capable of accurately predicting the performance characteristics of a journal bearing under a wide range of loading conditions

- To construct a simplified, yet realistic, rotor-bearing model (flexible rotors supported on finite length journal bearings) suitable for stability analysis in rotor-bearing systems

- To study the effect of more realistic operating conditions (specifically turbulent flows) on linear stability boundaries of a rotor-bearing system

- To extend the mathematical model of the rotor-bearing system such that the complicated dynamics of the system, including bifurcation types and directions, can be captured with relatively low computational cost

- To predict the safe operating regions for existing rotor-bearing systems and to provide the analysis means necessary for a priori predictions in the design stage

1.4 Outline

In order to achieve the defined objectives, this thesis is divided into four chapters. Chapter 1 starts with the necessary background following with a literature review and objectives of this thesis. Chapter 2 is devoted to the development of a robust cavitation algorithm. The developed algorithm is then used as the basis for performance predictions of journal bearings in the rest of the thesis. Chapter 3 addresses the task of constructing a simplified mathematical model of the rotor-bearing system and the means of obtaining the stability bounds in the system as well as studying the turbulence effects on calculated stability boundaries. Chapters 4 and 5 are designed to test the

validity of the proposed hypothesis and to further demonstrate the capabilities of the proposed enhanced model. The details of the materials in each chapter are as follows:

1.4.1 On Modifying the Cavitation Algorithm

In Chapter 2, the long-lasting problem with the robustness of the universal cavitation algorithm is addressed. Based on the Finite Volume discretization of the governing equations of motion, an alternative solution scheme is proposed as an attempt to accelerate the convergence speed of the mass-conserved Elrod-Adams algorithm, and to eliminate the scheme dependency on chosen values of the lubricant bulk modulus. The cost of artificially decreasing the bulk modulus on computed results is discussed, and recommendations are given for the safe margin for such a reduction in order to stabilize the scheme while maintaining the desired accuracy. The dependence of the scheme stability on various input parameters is systematically studied by means of a thorough eigenvalue analysis of the coefficient matrix of the discretized system of equations.

1.4.2 On the Effect of Flow Regimes on Linear Stability

In Chapter 3, the pressure distributions of turbulent finite length journals are obtained by proper numerical solutions to the modified Reynolds lubrication equation. Two turbulent models of Ng-Pan and Elrod, and Constantinescu are implemented in the modified equation for comparison purposes. The calculated pressures are then used as the basis of the infinitesimal perturbation method to find the turbulent dynamic coefficients for a range of operating conditions. Having the dynamic coefficients, the threshold speed of instability of a flexible shaft supported on end laminar and turbulent journals is found by means of linear stability analysis. Stability bounds are then compared for different shaft stiffness and Reynolds numbers, ranging from laminar to fully turbulent flows; this is done in an attempt to study the range of applicability for the original Reynolds equation and to find the operating conditions for which modified analysis under turbulent conditions is necessary in order to obtain accurate stability bounds. The journal bearing trajectories are also obtained by means of fast and robust implicit integration techniques for laminar and turbulent regimes, solely based on the calculated dynamic coefficients.

1.4.3 On Nonlinear Stability Analysis

To determine the bifurcation types in a rotor-bearing system, finding higher order derivatives of the bearing forces with respect to journal velocity and position is required. As closed-form expressions for journal bearing force is not generally available, Hopf bifurcation studies of rotor-bearing systems have been limited to simple geometries and cavitation models. As a main hypothesis in this thesis, it is postulated that a rotor-dynamic model that benefits from higher order representations of the fluid forces can solve two problems at once. By incorporating the dynamic coefficients, one can potentially calculate them for any bearing geometry and type. By using higher order coefficients, nonlinear analysis such as HBT can be conducted to characterize the bifurcations in the system.

To test the proposed hypothesis, in Chapter 4, a systematic approach is proposed for the calculation of nonlinear dynamic coefficients. First, second and third order Taylor expansion of the journal force is used to find the nonlinear coefficients in the most general form that is useful for short and long journal bearings. The calculated coefficients are then implemented in a mathematical model of a flexible rotor-bearing system. A Hopf bifurcation subroutine is developed to assess the stability of the oil whirl around the threshold speed of instability and to find the governing bifurcation types for a range of operating conditions. System trajectories are also found for the rotor-bearing systems for which journal forces are expressed, based on closed-form or the proposed nonlinear coefficient-based model. The nonlinear coefficient-based model is shown to be capable of revealing the bifurcation types of the system as well as its complicated dynamics in real time.

In Chapter 5, the aim is to generalize the nonlinear analysis given in Chapter 4, for bifurcation analysis in rotor-bearing systems in which the rotor is supported on finite length journal bearings. To do this, nonlinear coefficients for a finite journal are given based on an extended perturbation analysis of the Reynolds lubrication equation. The calculated coefficients are then used to construct a nonlinear coefficient-based model for a flexible shaft supported on end journal bearings. A global nonlinear analysis technique, as an alternative to the local HBT analysis, based on the *Monodromy matrix* of the periodic solutions is conducted. The Monodromy matrix is calculated for operating spin speeds beyond the threshold speed of instability. The eigenvalues of

the Monodromy matrix, i.e. the *Floquet multipliers*, are calculated to assess the bifurcation types and direction for a fully balanced rotor-bearing system. Balanced and unbalanced system trajectories are also studied to further illustrate the benefits of the proposed model in predicting the behavior of the rotor-bearing system under a range of operating speeds.

Chapter 2: A Mass-Conserving Cavitation Algorithm for Journal Bearings

In this chapter, a modified fast converging, mass-conserving, and robust algorithm is proposed in order to calculate the pressure distribution of a cavitated axially grooved journal bearing based on the finite volume discretization of the Elrod-Adams (E.A.) cavitation model. The solution of the cavitation problem is shown to strongly depend on the specific values chosen for the lubricant bulk modulus. Results show that the new proposed scheme can handle the stiff discrete numerical system for any chosen value of the lubricant bulk modulus (β) and hence a significant improvement in the robustness is achieved compared to traditionally implemented schemes in the literature. Enhanced robustness is found to have no effect on the accuracy of the obtained results, and the convergence speed is shown to be considerably faster than in the widely-used techniques in the literature. The effects of bulk modulus, static load, and mesh size on the numerical stability of the system are also studied by means of eigenvalue analysis of the coefficient matrix of the discrete numerical system. It is shown that the impact of static load and mesh size on numerical stability is negligible, compared to the significant impact of varying bulk modulus values.

2.1 Mathematical Model for Mass Converging Cavitation Problem

The E.A. algorithm [32] with Vijayaraghavan [95] treatment is studied here as the underlying mathematical model. The standard J.F.O/E.A. treatment is based on acknowledging the fact that Poiseuille (pressure gradient) terms in the compressible Reynolds equation vanish in the cavitated region where the mass flow is only governed by the Couette (advective) terms. This distinction between the two regions of the flow leads to a mathematical model with two governing equations for full film and cavitated regions [25]:

$$\frac{\partial(\rho h)}{\partial t}+\frac{\partial}{\partial x}\left(\frac{\rho h U}{2}-\frac{\rho h^3}{12\mu}\frac{\partial p}{\partial x}\right)-\frac{\partial}{\partial z}\left(\frac{\rho h^3}{12\mu}\frac{\partial p}{\partial z}\right)=0 \qquad (2.1)$$

$$\frac{\partial(\rho h)}{\partial t}+\frac{\partial}{\partial x}\left(\frac{\rho h U}{2}\right)=0$$

where ρ is fluid density, h is film thickness, $U = R\omega$ is journal surface velocity, p is fluid film pressure, and μ is lubricant viscosity. Several pressure-density relations are proposed in the literature to relate the change of lubricant density to the lubricant pressure. In general, the validity of such relations is a function of induced pressures in the lubricant [96]. The pressure-density relation can be expressed in its most general form [42]:

$$\rho = \rho_c f(p) \tag{2.2}$$

The most widely adopted compressibility relation in lubrication applications is based on the constant bulk modulus (β) of the lubricant:

$$\rho = \rho_c \, exp\left(\frac{p - p_c}{\beta}\right) \tag{2.3}$$

where p_c and ρ_c are the pressure and density in the cavitated region. A generalization of Eq. (2.3) in the form of Eq. (2.2) can be easily adopted [40] in rewriting the compressible Reynolds equation, but is omitted here for simplicity. The constant bulk modulus model is therefore used for the analysis in this chapter.

The J.F.O/E.A. mathematical model is mass converging and can also be derived directly from the continuity equation [40], assuming a homogenous three-dimensional flow [97]. The major difficulty here is that although the governing equations for each region of the flow are simply stated, identifying the cavitation boundary separating the two regions can be challenging. The pioneering work of Elrod and Adams [32] suggested the use of a switch function, g, as well as a change of variable in an effort to unify the two governing equations into one equation:

$$g = \begin{cases} 1, & in\ full\ film\ region \\ 0, & in\ cavitated\ region \end{cases}$$
$$\alpha = \frac{\rho}{\rho_c} \tag{2.4}$$

where α is the density ratio. The switch function permits pressure terms to be retained in the full film region or to be neglected in the cavitation region. Eq. (2.3) can be re-written such that:

$$p = p_c + g\beta\ ln(\alpha) \tag{2.5}$$

The pressure is approximately uniform in the cavitated region and is equal to p_c. Since the typical lubricant bulk modulus β is a large number ($\cong 2\ Gpa$), the density ratio (α) is only slightly greater than unity in the full film region and hence Eq. (2.5) can be approximately expressed in a simpler form [35]:

$$p = p_c + g\beta\ (\alpha - 1) \tag{2.6}$$

And hence the modified compressible Reynolds equation for the new variable α becomes [25]:

$$\frac{\partial(\alpha h)}{\partial t} + \frac{\partial}{\partial x}\left(\frac{Uh\alpha}{2} - \frac{\beta h^3}{12\mu} g \frac{\partial \alpha}{\partial x}\right) - \frac{\partial}{\partial z}\left(\frac{\beta h^3}{12\mu} g \frac{\partial \alpha}{\partial z}\right) = 0 \tag{2.7}$$

The solution to Eq. (2.7) will yield the density ratio, α. The induced pressure then is easily found through Eq. (2.6). In order to solve Eq. (2.7), a finite volume discretization is employed.

2.2 Numerical Treatment of Cavitation based on Finite Volume Method

2.2.1 Discretization

Non-dimensionalizing the governing PDE of Eq. (2.7) is preferred for versatility of the numerical analysis and faster convergence. The non-dimensionalized variables are as follows

$$\bar{x} = \frac{x}{2\pi R}\ , \qquad \bar{z} = \frac{z}{L}\ , \qquad H = \frac{h}{C}\ , \qquad \bar{\beta} = \frac{\beta}{\mu\omega}\left(\frac{C}{R}\right)^2\ , \qquad \bar{t} = \omega t \tag{2.8}$$

where *R*, *L*, *C* and *ω* are journal radius, length, clearance, and rotational velocity, respectively. By substituting the non-dimensional variables of Eq. (2.8) back into Eq. (2.7), the non-dimensional form can be constructed as:

$$\frac{\partial(\alpha H)}{\partial \bar{t}} + \frac{\partial}{\partial \bar{x}}\left(\frac{\alpha H}{4\pi} - \frac{\bar{\beta}}{48\pi^2}\ H^3 g \frac{\partial \alpha}{\partial \bar{x}}\right) - \frac{\partial}{\partial \bar{z}}\left(\frac{\bar{\beta}}{48(L/D)^2} H^3 g \frac{\partial \alpha}{\partial \bar{z}}\right) = 0 \tag{2.9}$$

Inclusion of the switch function in Eq. (2.9) requires some attention. Similar to the treatment in Ref. [35], the pressure induced flow term can be re-arranged such that:

$$g\frac{\partial \alpha}{\partial \bar{x}} = g\frac{\partial(\alpha-1)}{\partial \bar{x}} = \frac{\partial g(\alpha-1)}{\partial \bar{x}} - (\alpha-1)\frac{\partial g}{\partial \bar{x}} \tag{2.10}$$

The term $(\alpha-1)\frac{\partial g}{\partial \bar{x}}$ vanishes for any α since the switch function, g only changes at $\alpha = 1$. And hence:

$$g\frac{\partial \alpha}{\partial \bar{x}} = \frac{\partial g(\alpha-1)}{\partial \bar{x}} \tag{2.11}$$

Similar treatment for the other pressure driven term will simplify Eq. (2.9) to:

$$\frac{\partial(\alpha H)}{\partial \bar{t}} + \frac{\partial}{\partial \bar{x}}\left(\frac{\alpha H}{4\pi} - \frac{\bar{\beta}}{48\pi^2}\, H^3 \frac{\partial g(\alpha-1)}{\partial \bar{x}}\right) - \frac{\partial}{\partial \bar{z}}\left(\frac{\bar{\beta}}{48(L/D)^2} H^3 \frac{\partial g(\alpha-1)}{\partial \bar{z}}\right) = 0 \tag{2.12}$$

Representing Eq. (2.12) in a general form suitable for discretization and dropping all the non-dimensional bars for simplifying notation, we can write:

$$\frac{\partial u}{\partial t} + \frac{\partial F}{\partial x} + \frac{\partial G}{\partial z} = 0 \tag{2.13}$$

where:

$$\begin{aligned} u &= \alpha H \\ F &= \frac{\alpha H}{4\pi} - \frac{\beta}{48\pi^2}\, H^3 \frac{\partial g(\alpha-1)}{\partial x} \\ G &= \frac{\beta}{48(L/D)^2} H^3 \frac{\partial g(\alpha-1)}{\partial z} \end{aligned} \tag{2.14}$$

A finite volume discretization technique is applied for solving Eq. (2.13). Taking the control volume integral (in this case a control surface) of Eq. (2.13) over the volume (surface) of a two-dimensional representative cell with an area of $\Delta x\, \Delta z$ will yield:

$$\iint \frac{\partial u}{\partial t} dA + \iint \left(\frac{\partial F}{\partial x} + \frac{\partial G}{\partial z}\right) dA = 0 \tag{2.15}$$

Applying Gauss's theorem in plane and assuming a fixed control surface with no moving boundaries and defining $\vec{F} = F\,\hat{\imath} + G\,\hat{k}$ will result in:

$$\frac{d}{dt}\iint u\,dA + \oint \vec{F}.n\,dS = 0 \tag{2.16}$$

Defining the control surface average quantity as:

$$\bar{u}_{i,j} = \frac{1}{A_{i,j}}\iint u\,dA = \frac{1}{\Delta x\,\Delta z}\iint u\,dx\,dz \tag{2.17}$$

and performing the contour integral over the boundary of the representative two-dimensional cell for the last two terms in Eq. (2.16) will yield:

$$\frac{d\bar{u}_i}{d\bar{t}} + \frac{F_{i+\frac{1}{2},j} - F_{i-\frac{1}{2},j}}{\Delta x} + \frac{G_{i,j+\frac{1}{2}} - G_{i,j-\frac{1}{2}}}{\Delta z} = 0 \tag{2.18}$$

where the ½ indices correspond to the value of the flux at the cell boundary as compared to the flux values at the cell center. In order to discretize the time dependent term, a first order Implicit Euler method is adopted here. Hence, Eq. (2.18) can be written as:

$$\frac{{\bar{u}_{i,j}}^{n+1} - {\bar{u}_{i,j}}^{n}}{\Delta t} + \frac{{F_{i+\frac{1}{2},j}}^{n+1} - {F_{i-\frac{1}{2},j}}^{n+1}}{\Delta x} + \frac{{G_{i,j+\frac{1}{2}}}^{n+1} - {G_{i,j-\frac{1}{2}}}^{n+1}}{\Delta z} = 0 \tag{2.19}$$

where superscript *n* indicates a variable value at the current time-step, and superscript *n+1* is to represent a variable value at the next time-step. Common to the implicit schemes, the variable value in the next time-step needs to be expressed in terms of the variable and its gradients at the current time-step by means of a Taylor series expansion of the fluxes:

$$\begin{aligned} {F_{i+\frac{1}{2},j}}^{n+1} &= F_{i+\frac{1}{2},j}\left({\bar{u}_{i,j}}^{n+1}, {\bar{u}_{i+1,j}}^{n+1}\right) \\ &= F_{i+\frac{1}{2},j}\left({\bar{u}_{i,j}}^{n} + \delta\bar{u}_{i,j}, {\bar{u}_{i+1,j}}^{n} + \delta\bar{u}_{i+1,j}\right) \\ &= F_{i+\frac{1}{2},j}\Big|^{n} + \left.\frac{\partial F_{i+\frac{1}{2},j}}{\partial\bar{u}_{i,j}}\right|^{n}\delta\bar{u}_{i,j} + \left.\frac{\partial F_{i+\frac{1}{2},j}}{\partial\bar{u}_{i+1,j}}\right|^{n}\delta\bar{u}_{i+1,j} + O(\delta\bar{u}^2) \end{aligned} \tag{2.20}$$

where $\delta\bar{u}_{i,j} = {\bar{u}_{i,j}}^{n+1} - {\bar{u}_{i,j}}^{n}$ and $F_{i+\frac{1}{2},j}\Big|^{n} = F_{i+\frac{1}{2},j}\left({\bar{u}_{i,j}}^{n}, {\bar{u}_{i+1,j}}^{n}\right)$. Other terms in Eq. (2.19) are treated in a similar fashion. Plugging zero and first order Taylor expand terms back into Eq. (2.19) will result in:

$$\delta\bar{u}_{i,j}\left(\frac{1}{\Delta t} + \frac{1}{\Delta x}\frac{\partial F_{i+\frac{1}{2},j}}{\partial\bar{u}_{i,j}}\Big|^{n} - \frac{1}{\Delta x}\frac{\partial F_{i-\frac{1}{2},j}}{\partial\bar{u}_{i,j}}\Big|^{n} + \frac{1}{\Delta z}\frac{\partial G_{i,j+\frac{1}{2}}}{\partial\bar{u}_{i,j}}\Big|^{n} - \frac{1}{\Delta z}\frac{\partial G_{i,j-\frac{1}{2}}}{\partial\bar{u}_{i,j}}\Big|^{n}\right)$$
$$+ \frac{1}{\Delta x}\frac{\partial F_{i+\frac{1}{2},j}}{\partial\bar{u}_{i+1,j}}\Big|^{n}\delta\bar{u}_{i+1,j} - \frac{1}{\Delta x}\frac{\partial F_{i-\frac{1}{2},j}}{\partial\bar{u}_{i-1,j}}\Big|^{n}\delta\bar{u}_{i-1,j} \tag{2.21}$$
$$+ \frac{1}{\Delta z}\frac{\partial G_{i,j+\frac{1}{2}}}{\partial\bar{u}_{i,j+1}}\Big|^{n}\delta\bar{u}_{i,j+1} - \frac{1}{\Delta z}\frac{\partial G_{i,j-\frac{1}{2}}}{\partial\bar{u}_{i,j-1}}\Big|^{n}\delta\bar{u}_{i,j-1} = FI^{n}$$

where $FI^{n} = -\frac{{F_{i+\frac{1}{2},j}}^{n} - {F_{i-\frac{1}{2},j}}^{n}}{\Delta x} - \frac{{G_{i,j+\frac{1}{2}}}^{n} - {G_{i,j-\frac{1}{2}}}^{n}}{\Delta z}$ is the flux integral that is evaluated at the n[th] time-step. As noted by Vijayaraghavan and Keith [36, 95], Eq. (2.9) has different characteristics in the full film and cavitation regions; being an elliptic PDE (similar to the Laplace equation) in the full film region and a hyperbolic PDE (similar to wave equation) in the cavitated region. Since the nature of the governing equation in the full film region is elliptic, the solution is expected to be smooth and hence central differencing schemes are desirable in this region. On the other hand, the hyperbolic nature of the PDE in the cavitated region necessitates the use of upwind flux functions to capture discontinuities and sudden changes in the flow field.

Vijayaraghavan and Keith [36, 95] proposed adding higher order artificial viscosity terms to the shear term in Eq. (2.9) in such a way that pressure induced flow terms exist in the full film region but vanish in the cavitated region. The whole equation can now be centrally differenced such that by substituting $g = 1$ in the full film region, the central differencing remains in effect; and, in the cavitation region, central differencing automatically switches to second order upwind differencing by substituting $g = 0$ [36]. The shear term is then approximately expressed as:

$$\frac{\partial u}{\partial x} = \frac{\partial}{\partial x}\left[u - (1-g)\left(\frac{\partial^2 u}{\partial x^2}\frac{\Delta x^2}{3} - \frac{\partial^3 u}{\partial x^3}\frac{\Delta x^3}{4}\right)\right] \tag{2.22}$$

By adding the artificial viscosity terms of Eq. (2.22), the fluxes in Eq. (2.14) are to be updated such that:

$$
\begin{aligned}
u &= \alpha H \\
F &= \frac{u}{4\pi} - \frac{\beta}{48\pi^2}\, H^3 \frac{\partial g(\alpha-1)}{\partial x} - \frac{(1-g)}{4\pi}\left(\frac{\partial^2 u}{\partial x^2}\,\frac{\Delta x^2}{3} - \frac{\partial^3 u}{\partial x^3}\,\frac{\Delta x^3}{4}\right) \\
G &= \frac{\beta}{48(L/D)^2} H^3 \frac{\partial g(\alpha-1)}{\partial z}
\end{aligned}
\tag{2.23}
$$

Substituting Eq. (2.23) into Eq. (2.21) will yield the discretized form of the governing PDE for the Cavitation problem. Details of the substitution and the final discretized equation are given in Appendix A.

2.2.2 Solution Procedure

The discretized equation as detailed in Appendix A is shown to take the final form of:

$$
\begin{aligned}
LHS = X_{-2}\,\delta u_{i-2,j} + X_{-1}\,\delta u_{i-1,j} + XZ_0\,\delta u_{i,j} + X_{+1}\,\delta u_{i+1,j} + Z_{-1}\,\delta u_{i,j-1} \\
+ Z_{+1}\,\delta u_{i,j+1}
\end{aligned}
\tag{2.24}
$$

The set of linear algebraic equations arisen form the discretized Reynolds equation has been solved in the literature with a variety of different methods such as conventional explicit successive over relaxation (SOR) scheme [28, 34], implicit Successive Line Over Relaxation (SLOR), Alternate Direction Implicit (ADI) [24, 35], Multigrid SOR [37, 38] and Approximate Factorization (AF) technique [36, 95]. Linear systems arisen from implicit time schemes of the Adams/Elrod algorithm has commonly been solved using the AF technique [36, 54, 95, 98].

Eq. (2.24) is a single equation written for a representative cell for which its value depends on its immediate neighbors. By solving Eq. (2.24), the change in solution of the representative cell $\delta u_{i,j}$ at each time step can be found. Writing Eq. (2.24) for all control volumes in the field gives a linear system of equations which takes the form of:

$$
(I + \Delta t\, D_x + \Delta t\, D_z)\delta\vec{U} = \overrightarrow{FI} \tag{2.25}
$$

Assuming a n by m mesh, $\delta\vec{U}$ and $\overrightarrow{FI}$ are column vectors of size $n\times m$. I, D_x, D_y are square matrices with $n\times m$ rows and $n\times m$ columns. The underlying assumption in the approximate factorization technique is that the LHS of Eq. (2.25) can be approximated by:

$$(I + \Delta t\, D_x + \Delta t\, D_z) = (I + \Delta t\, D_x)(I + \Delta t\, D_z) \tag{2.26}$$

An extra term $\Delta t^2\, D_x\, D_z$ is added to the left hand side of Eq. (2.25) as a result of the assumption as in Eq. (2.26). For time accurate solutions, this induced error is tolerable due to the fact that the space discretization was chosen to be second order accurate for both full film and cavitation regions. However, if a higher order space discretization scheme is needed, such approximation will force the whole scheme to be only second order accurate. Hence, for any higher order space discretization, the AF technique cannot be implemented unless the interest is only in finding the steady state solution.

The major benefit from the AF technique is its ability to decouple the two physical dimensions such that the solution can be sought in *x* and *z* directions in a two-step process:

$$\begin{aligned}(I + \Delta t\, D_x)\delta\widetilde{U} &= \overrightarrow{FI} \\ (I + \Delta t\, D_z)\delta\vec{U} &= \delta\widetilde{U}\end{aligned} \tag{2.27}$$

where $\widetilde{U}$ is the axillary solution vector. The tri-diagonal linear systems of Eq. (2.27) can be solved on the domain, row by row and column by column, such that the size of coefficient matrices D_x and D_z can be significantly reduced from a full matrix of $n\times m$ by $n\times m$ for the whole domain to just $m\times m$ and $n\times n$, respectively. Such a reduction can be beneficial whenever computer memory is of concern, but it does not significantly affect the overall computational cost since each linear system of reduced size needs to be repeatedly solved for every row and every column. As an alternative to the existing solution schemes and to enhance the robustness of the solver, a new scheme is proposed in this study.

2.2.3 Proposed Iterative Solver

The proposed scheme is mainly consists of three modifications to the extant and widely used Elrod/Adams algorithm with Vijayaraghavan and Keith treatment [32, 33, 36] such that:

1) The system of linear equations is directly solved via Gaussian elimination in a single step for the full linear system of Eq. (2.24), as shown in Appendix A . Solving the full system as compared to the approximate factorization based schemes, has two immediate benefits: Firstly, the low frequency error is attenuated much more effectively at each iteration and hence considerably fewer iterations are required for convergence. Secondly, it does not introduce an artificial error of second order to the discretization and hence can be used for implicit time-accurate simulations. The scheme that is based on the direct solve of the full linear system of Eq. (2.24) will be referred to as FLS in this chapter. It shall be noted that since the total number of elements is fairly limited in the majority of lubrication problems, obtaining the exact solution to the discretized system is efficiently possible. Hence, implementation of iterative solvers for the linear system is not justified for the lubrication problem.

2) The automatic time stepping method used here is based on an effective optimization scheme recently proposed by Ceze et al. [99] for aerodynamic problems. The update to the time step size and the solution update at each iteration will essentially depend on an under-relaxation parameter ω such that:

$$\vec{U}^{n+1} = \vec{U}^{n} + \omega_r \, \delta\vec{U} \tag{2.28}$$

The updated time-step magnitude is also a function of the under-relaxation parameter:

$$\Delta t^{n+1} = \begin{cases} \gamma \, \Delta t^{n}, & \omega_r = 1 \\ \Delta t^{n}, & 0.01 \leq \omega_r \leq 1 \\ k \, \Delta t^{n}, & \omega_r < 0.01 \end{cases} \tag{2.29}$$

where ω_r is the under-relaxation parameter, k and γ are tunable parameters with default values of 0.1 and 2 respectively. Defining the L_2 norm of the residual $R(U)$ as:

$$\|R(U)\|_2 = \sqrt{\frac{\sum_i \sum_j R(U)_{ij}{}^2}{i_{max}\, j_{max}}} = \sqrt{\frac{\sum_i \sum_j FI_{ij}{}^2}{i_{max}\, j_{max}}} \tag{2.30}$$

Note that the flux integral is a function of the available solution at the current time-step: $FI = FI(U^n)$. Algorithm 1 shows the steps for estimating the value of the under-relaxation parameter ω_r :

Algorithm 1.
$\omega_r = 1$ $\widetilde{U} = \vec{U}^n + \omega_r \, \delta\vec{U}$ while $\left\| \frac{\widetilde{U} - \vec{U}^n}{\Delta t} - R(\widetilde{U}) \right\|_2 > \|R(U)\|_2$ $\omega_r = \frac{\omega_r}{2}$ $\widetilde{U} = \vec{U}^n + \omega_r \, \delta\vec{U}$ End

Note that a line search algorithm is incorporated with the implicit solver to guarantee the reduction of residual norm in the next nonlinear iteration.

3) The switch function is implemented based on the improved scheme of Fesanghari and Khonsari [100] such that while iterating, the switch function exponentially decays toward zero in the cavitation region and exponentially grows towards unity in the full film region unlike the binary switching in the Elrod algorithm. The implementation is shown in Algorithm 2.

Algorithm 2.

If $\alpha_{ij} \geq 1$
  If $gFactor > 0$
  $g_{ij} = \frac{g_{ij}}{gFactor}$
  else
  $g_{ij} = 1$
  end
else
  $g_{ij} = g_{ij} \times gFactor$
End

where $gFactor$ is the switch function multiplier with a reported optimal value of 0.8 in reference [100].

2.3 Numerical Results

The proposed numerical scheme of Section 2.2.3 is to be compared to the traditional scheme based on the approximate factorization as implemented in references [36, 54, 95, 98]. Eq. **(A**.10) is solved over a structured mesh on the surface of a journal bearing as shown in Figure 2-1(a). The computational domain is depicted in Figure 2-1(b). The performance study of the scheme is categorized based on the solver type (AF or Full) and selected bulk modulus value (artificially softened or physical).

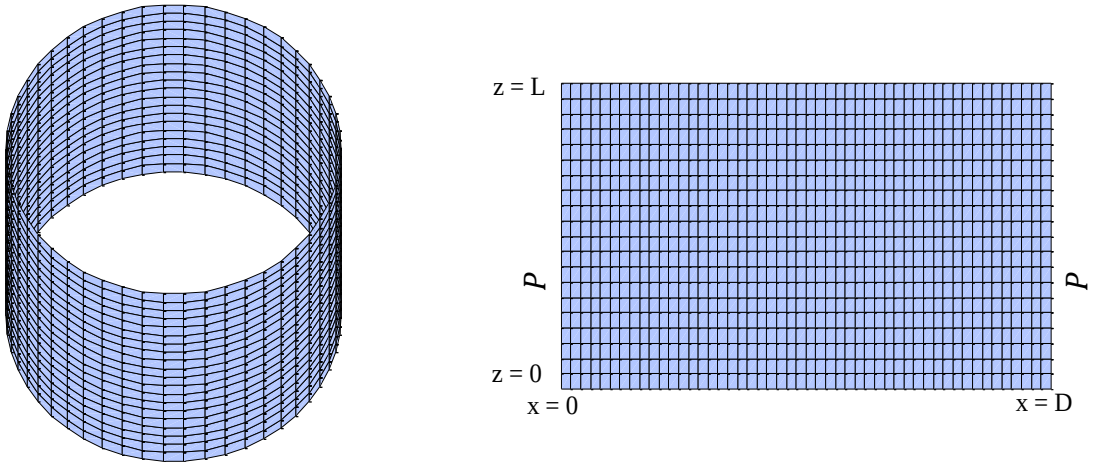

(a) (b)

Figure 2-1 Structured 50×20 mesh (a) and the computational domain (b)

In order to show the performance in each case, three scheme indicators are studied. Firstly, the evolution of the L_2 norm of the residual $\|R(U)\|_2$ as defined in Eq. (2.30) versus number of iterations is reported. The last two scheme indicators are the maximum pressure in the field and the Sommerfeld number (an average quantity) defined as:

$$S = \frac{\mu\, N\, L\, D}{W}\left(\frac{R}{C}\right)^2 \tag{2.31}$$

where $N = \frac{\omega}{2\pi}$ and W is the bearing load capacity defined as:

$$W = \int_0^{\theta_{cav}} \int_{-\frac{L}{2}}^{\frac{L}{2}} p\, R\, d\theta dz \tag{2.32}$$

Although predictions of the cavitation algorithm depend on the magnitudes of the lubricant bulk modulus (β) chosen for the analysis, realistic β magnitudes leads to a very stiff system of equations for which obtaining an accurate solution in a short period of time is considerably difficult. To avoid the accuracy and slow convergence issues, it is customary to choose artificially lower values for the bulk modulus in an attempt to soften the system of equations. Numerically stable algorithms have been proposed and are shown to give acceptable results for β values of 1/100 to 1/10 of the more realistic values of $\beta \approx 2Gpa$ [32, 98, 100]. An ideal scheme is therefore a scheme that can achieve accurate results in a relatively quick manner while the magnitude of the bulk modulus is as close as possible to the realistic physical values. To show the superiority of the numerical scheme proposed in Section 2.2.3, the performance prediction is carried out for the artificially softened and realistic system of equations as follows. All problems were solved with a personal computer on a single core of an Intel i7 chip @ 3.40 GHz and 12 GB memory.

2.3.1 The Softened System of Equations

The boundary condition used for this analysis is the Dirichlet boundary condition for both circumferential (x) and longitudinal (z) directions, as shown in the computational domain in Figure 2-1(b). The axial Dirichlet Boundary condition is based on selecting a grooved journal bearing with the groove located at the maximum film thickness. If the supplied oil pressure at the groove is equal to the cavitation pressure P_{cav}, reformation happens at the groove itself and there will be no reformation boundary to capture. This is the simplest case for the numerical scheme and is initially selected here. The scheme performance indicators for the softened system of equations at the reduced bulk modulus of $\beta = 20\ MPa$ ($\equiv \bar{\beta} = 2.75\times10^{2}$) is shown in Figure 2-2 (a) for AF and Figure 2-2 (b) for the FLS representation.

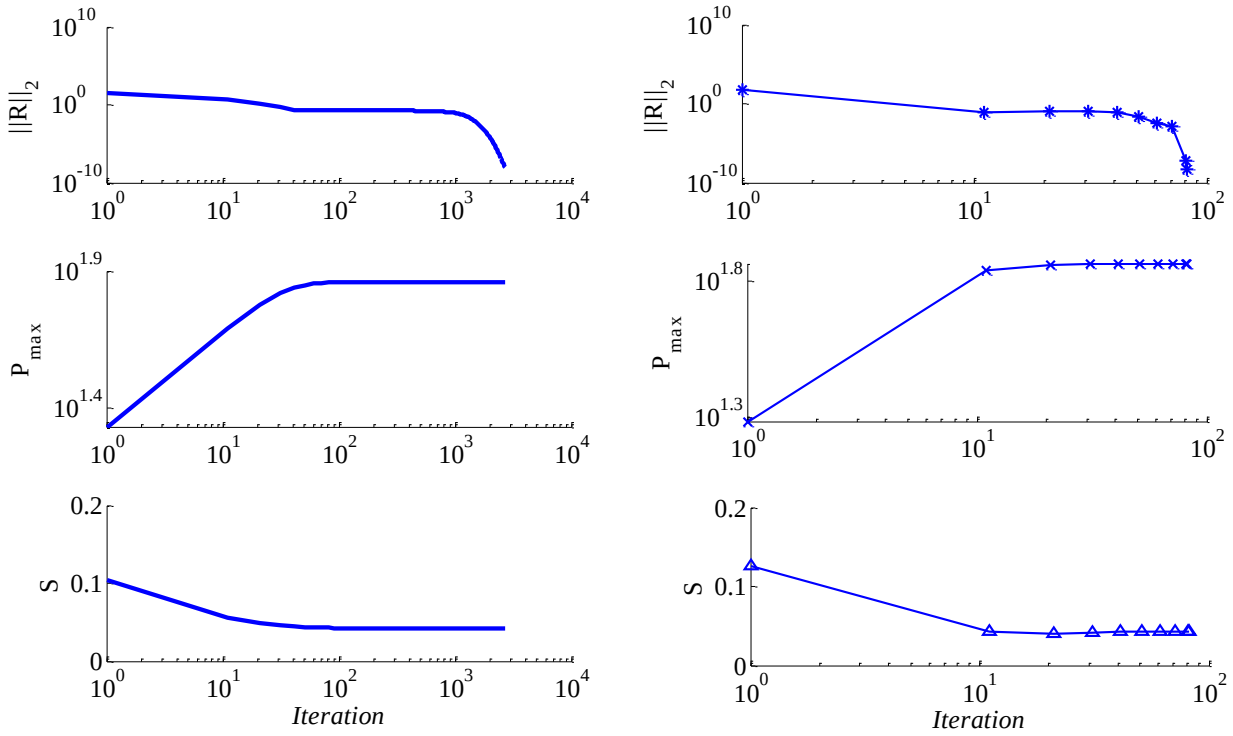

Figure 2-2. Performance study of the softened system of equations at $\beta = 20\ MPa$ for the AF solver (a) and the FLS solver (b).

By direct comparison of the L_2 norm of the residual $\|R(U)\|_2$ for AF scheme in Figure 2-2 (a) and for the FLS scheme in Figure 2-2 (b), it can be seen that both schemes do converge and reach the preset goal of $\|R(U)\|_2 \leq 10^{-8}$. However, the number of required iterations to reach convergence is considerably lower for the full system, being 2,676 for AF versus only 82 iterations for the FLS. As the computation cost per iteration is similar between the two schemes, fewer iterations required for reaching convergence in the FLS scheme also means faster convergence in computation time. To show the similarity of computational cost per iteration, CPU computation time of both schemes for the two selected mesh sizes are compared to each other in Figure 2-3.

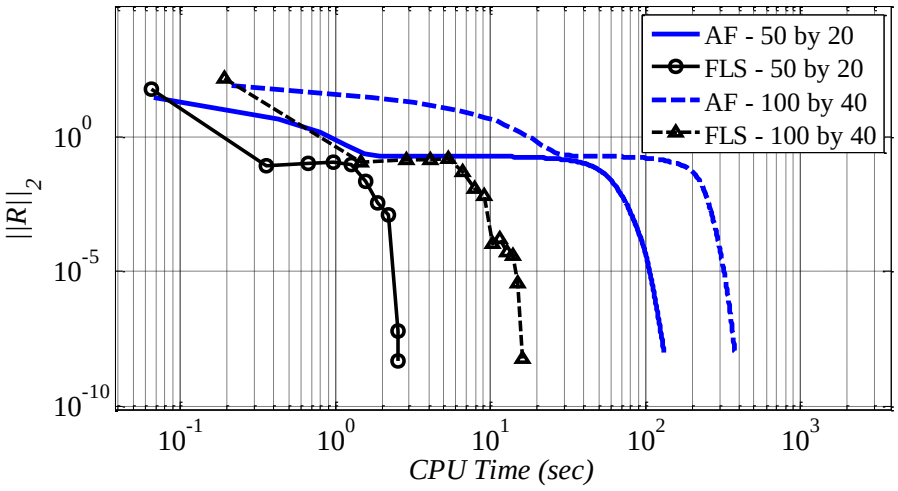

(a)

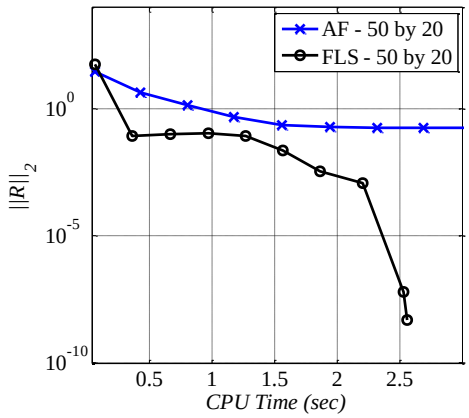

(b)

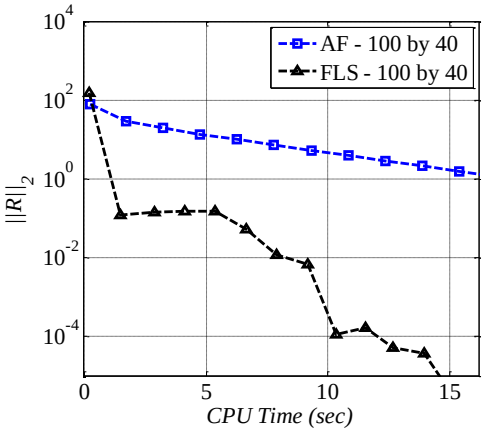

(c)

Figure 2-3. CPU computation time of AF and FLS schemes for a 50 by 20 and a 100 by 40 mesh, total iterations to converge (a) , first 100 iterations for 50 by 20 mesh (b) and first 120 iterations for 100 by 40 mesh (c)

Solution indicators for both schemes reach the values of $\bar{P}_{max} = 72.93$ and $S = 0.0427$ for a predefined eccentricity ratio of $\epsilon = 0.8$. In order to study what proportion in computation time and iterations is due to the effect of the full linear system representation versus approximate factorization, AF and FLS schemes were compared based on two different cases: "Case 1" with traditional binary switching of the switch function and with a constant time-step, and "Case 2" with all the features of the proposed algorithm as outlined in Section 3.3. Convergence plots for both cases versus iterations and CPU time is given in Figure 2-4 (a) and (b), respectively. It is

noteworthy to mention that due to the superior robustness of the FLS based algorithm, the fixed time-step value chosen to perform the time marching can be chosen more than two to three orders of magnitude higher than the biggest time-step for which the AF scheme remains numerically stable. Such an advantage will then result in much faster convergence as can be seen in Figure 2-4 (a) and (b).

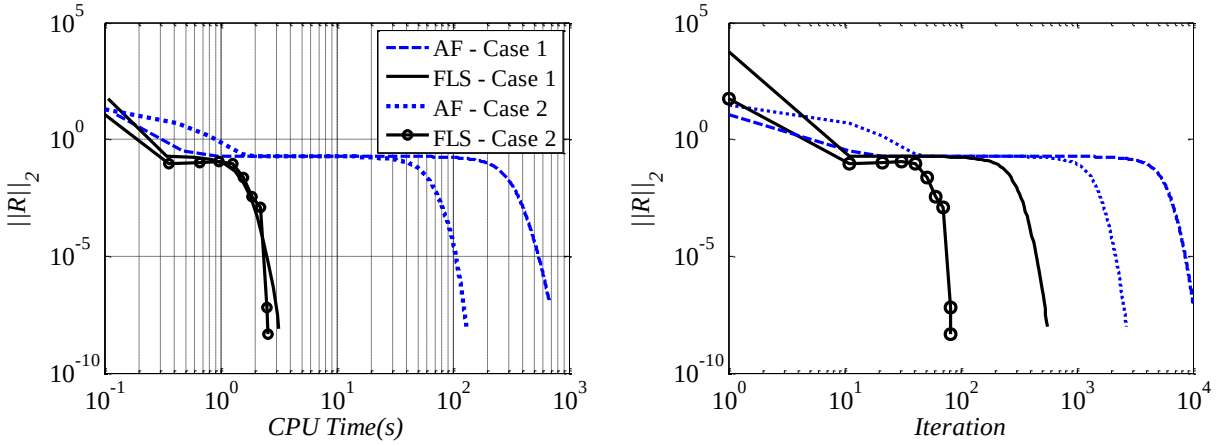

(a) (b)

Figure 2-4. Performance study (a) and CPU computation time (b) of the softened system of equations at $\beta = 20\ MPa$ for AF and FLS schemes with binary switch function and fixed time step.

2.3.2 The Stiff System of Equations

Performance studies for the system of equations with realistic bulk modulus values of $\beta = 2\ GPa$ ($\equiv \bar{\beta} = 2.75\times10^4$) are shown in Figure 2-5.

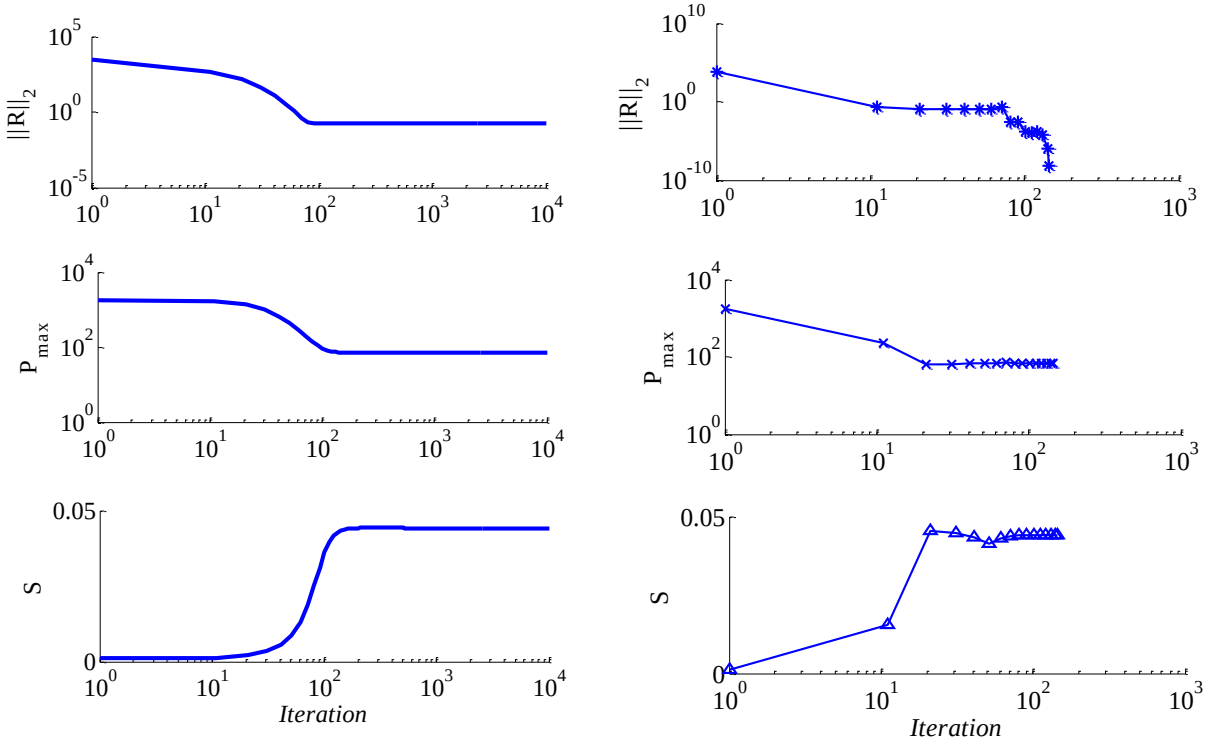

Figure 2-5. Performance study of the stiff system of equations at $\beta = 2\ GPa$ for the AF solver (a) and the Full linear system solver (b).

The AF based method for solving the stiff system shows poor performance as can be marked by lack of convergence in Figure 2-5 (a). The lowest obtained value for $\|R(U)\|_2$ after 10,000 iterations is only 0.018 and hence the predefined goal of 10^{-8} is not achieved. On the contrary, the FLS scheme converges in just 145 iterations, only a few iterations more than what was required for the softened system. The final obtained values for non-dimensional maximum pressure are $\bar{P}_{max} = 70.18$ and $\bar{P}_{max} = 70.21$ for the AF and Full schemes, respectively. The distribution of error in obtaining the non-dimensional pressure ($\overline{dP} = \bar{P}|_{FLS,\beta=2\ GPa} - \bar{P}|_{AF,\beta=2\ GPa}$) over the whole domain is shown in Figure 2-6(a). The error was found to accumulate close to and downstream of the cavitation boundary where there is a switch in the differencing scheme from central to upwind.

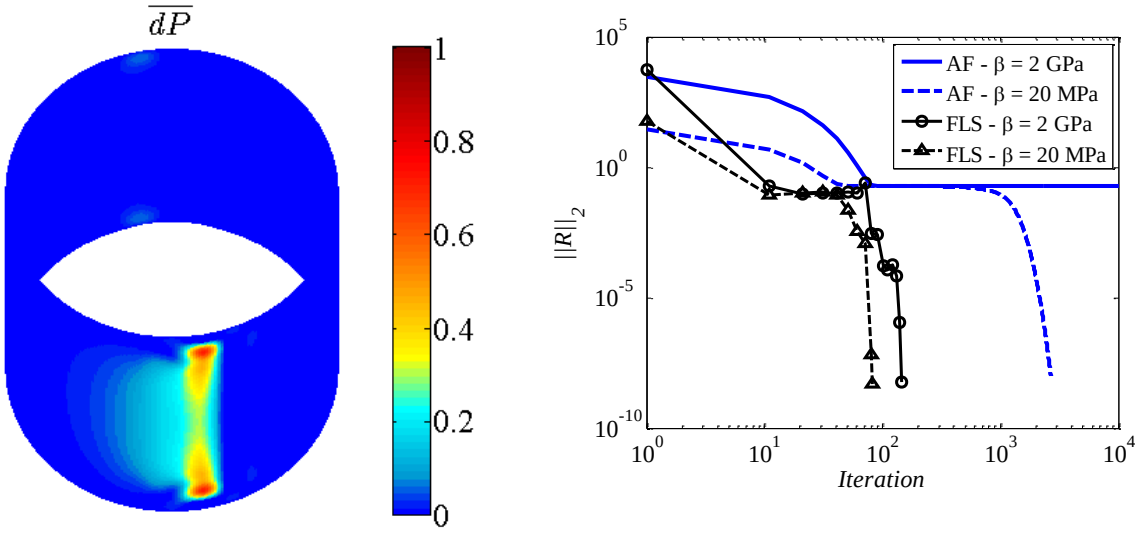

(a) (b)

Figure 2-6. Error distribution $\overline{dP}$ (a) and L_2 norms of the residual ($\|R\|_2$) versus iterations for rigid and softened system based on AF and FLS schemes (b).

It is expected that if the norm of the residuals reaches the predefined goal, the discrepancy between the calculated pressure values vanishes. However, this is not computationally effective since the number of iterations required for such a reduction in residual norms is far more than what is needed for the FLS based scheme and hence its superiority in solving the stiff system of equations is evident. The L_2 norm of the residual of both schemes are superimposed for both the softened and the rigid numerical systems versus iterations and are shown against iteration number in Figure 2-6 (b).

2.3.3 Verification and Comparison of Results

A mesh sensitivity analysis is carried out for the non-pressurized axially grooved bearing at $\beta = 2GPa$ and $\epsilon = 0.8$ in both *x* and *z* directions separately, and are shown in Figure 2-7 . It shall be noted here that unidirectional mesh sensitivity analysis is only helpful to assess the sensitivity of calculated parameters to the mesh size, in either directions of the problem. Once such knowledge is established, the grid study needs to be carried out in both directions, simultaneously. The maximum field pressure as well as the Sommerfeld number and cavitation location at journal centerline along *x*-axis are selected as target variables (φ) of interest for mesh sensitivity analysis.

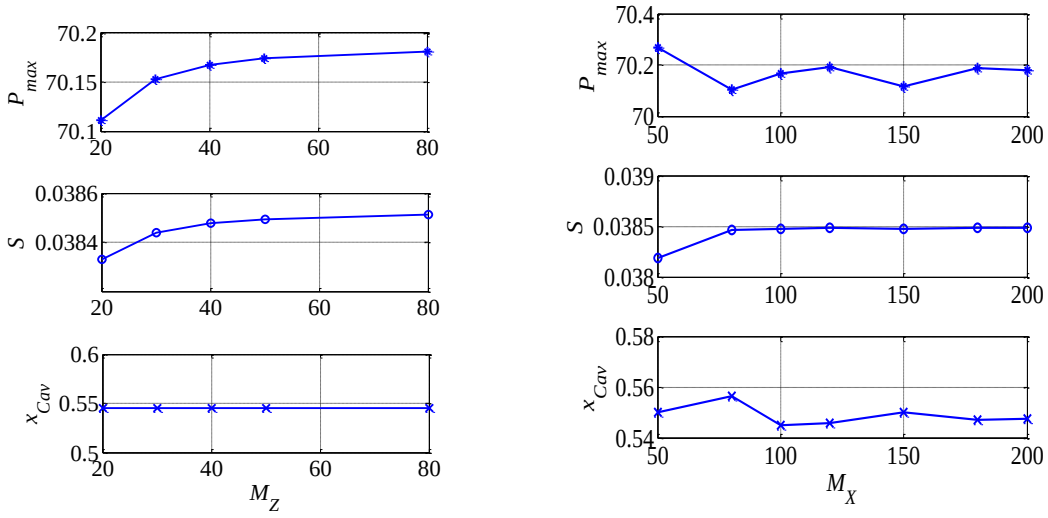

(a) (b)

Figure 2-7. Mesh-Sensitivity analysis in Z (a) and X (b) directions

As can be seen in Figure 2-7, the evolution of solution parameters with increasing mesh-size in both Z and X directions becomes insignificant after 40 and 100 divisions, respectively. To study the effect of increasing mesh-size in both directions simultaneously with estimated uncertainties in obtaining the solution, the fine grid convergence index $GCI_{fine}{}^{21}$ (an indicator of numerical uncertainty in obtaining the solution for a particular mesh) as well as extrapolated target variables Φ_{ext} and corresponding grid error for a selected mesh (50×20, 100×40 and 200×80) are calculated based on [101] and are tabulated in Table 2-1.

Table 2-1. Sample calculations of discretization errors

	$\Phi = P_{max}$	$\Phi = S$	$\Phi = \bar{x}_{cav}$
Φ_1 (fine grid)	70.1928	0.0385	0.5475
Φ_2	70.1674	0.0385	0.5450
Φ_3 (coarse grid)	70.2087	0.0380	0.5500
$\Phi_{ext}{}^{32}$	70.1012	0.0385	0.5400
$\Phi_{ext}{}^{21}$	70.2336	0.0385	0.5500
$\%e_{ext}{}^{32}$	0.0944	0.1332	0.9259
$\%e_{ext}{}^{21}$	0.0581	0.0139	0.4545

	$\Phi = P_{max}$	$\Phi = S$	$\Phi = \bar{x}_{cav}$
$\%GCI_{coarse}{}^{32}$	0.1179	0.1667	1.1468
$\%GCI_{fine}{}^{21}$	0.0726	0.0174	0.5708

As shown in Table 2-1, the coarse grid (50×20 (x, z)) and intermediate grid (100×40) convergence indices $\%GCI_{coarse}{}^{32}$ and $\%GCI_{fine}{}^{21}$, indicating numerical uncertainty in calculating maximum target variables in the coarsest and intermediate grids, do not exceed % 1.2 and % 0.6 for any of the calculated solution indicators of both grids, respectively. Hence both the coarsest and intermediate grids are acceptable and the coarse grid is used in this chapter for scheme performance analysis.

Comparisons and Verification:

Case 1-1, pure sliding motion without reformation:

In this case, the one-dimensional problem of a hydrodynamic bearing with a convergent-divergent sinusoidal profile as shown in Figure 2-8 is studied.

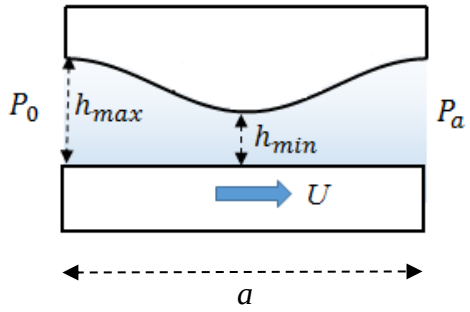

Figure 2-8. Schematic of a convergent-divergent bearing under pure sliding motion as in Giacopini et al. [46]

This particular example is chosen identical to that of Giacopini et al. [46] for comparison of the current proposed algorithm to the LCP-based type algorithms of references [40, 42, 46]. The selected parameters are tabulated in Table 2-2. The external pressures are chosen as $P_0 = P_a = 0$ and hence no film reformation occurs. The pressure curve is calculated by the FLS algorithm at a remarkably high bulk modulus of $\beta = 100\ GPa$ (to mimic incompressibility) on a uniform mesh

of 60 elements and is compared to the incompressible solution of Giacopini et al. [46] in Figure 2-9(a).

Table 2-2. Sliding bearing physical and geometrical parameters as in Giacopini et al. [46]

Case	$h_{max}(mm)$	$h_{min}(mm)$	$a(mm)$	$\mu\ (Pa.S)$	$U(m/s)$	$P_c(MPa)$	$P_0 = P_a(MPa)$
1-1	0.025	0.015	125	0.015	4	0	0
1-2	0.025	0.015	125	0.015	4	0	1

Case 1-2, pure sliding motion with reformation:

If the external pressures are chosen as $P_0 = P_a = 1\ MPa$, reformation takes place in the lubricated film. The obtained pressure distribution is calculated and compared to that of ref [46] and is shown in Figure 2-9(b).

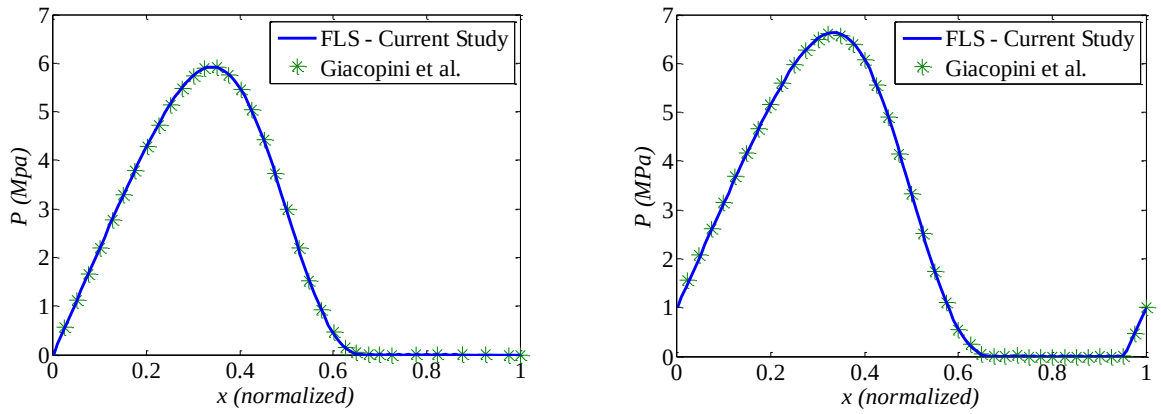

(a) (b)

Figure 2-9. Comparison of the calculated film pressure based on the FLS in the current study versus the LCP based results of Giacopini et al. [46] for Case 1-1, (a) and 1-2, (b)

Pressure distributions obtained by the FLS algorithm agree with the results of Giacopini et al. [46] with and without reformation as depicted in Figure 2-9. This agreement was indeed expected as both algorithms are mass conserving.

Case 2-1, axially grooved journal bearing with non-pressured groove (no reformation):

The scheme indicators as well as the predicted solution indicators of a non-pressured grooved journal bearing ($\bar{P}_g = 0$) for a range of lubricant bulk modulus is given in Table 2-3 at an

eccentricity ratio of $\epsilon = 0.8$, are compared with the reported results of Vijayaraghavan and Keith [39] for a 150×8 grid.

Table 2-3. Comparison of predicted parameters of a non-pressurized grooved journal bearing

	Current study		Current study		Current study	Ref [39]
β	20 *MPa*		30 *MPa*		2 *GPa*	≡30 *MPa*
Solution Method	AF	FLS	AF	FLS	FLS	AF
$\bar{P}_{max}$	72.2759	72.4370	71.4976	71.4976	69.6741	70.18
S	0.0364	0.0362	0.0366	0.0366	0.0374	-
$\bar{W}$	7.5823	7.6081	7.5265	7.5265	7.3645	7.14
Cav. Location ($\bar{x}$)	0.5433	0.5500	0.5500	0.5500	0.5500	0.553
Ref. Location ($\bar{x}$)	-	-	-	-	-	-
Time steps to steady state	2108	93	3104	94	144	2354

Case 2-2, axially grooved journal bearing with pressured groove (with reformation):

If the supplied oil pressure at the groove is greater than the atmospheric pressure, a reformation boundary appears at a location other than the groove. In this case, locating the reformation boundary is difficult since the reformation front changes position with solution evolution and hence makes it a more challenging problem to be numerically solved and to reach the desired convergence. Similar performance analysis was carried out for a journal bearing with pressurized grooves at $\bar{P}_g = 2\,\pi$ and are tabulated in Table 2-4 against results of Vijayaraghavan and Keith [39].

Table 2-4. Comparison of predicted parameters of a pressurized grooved journal bearing

	Current study		Current study		Current study	Ref [39]
β	20 *MPa*		30 *MPa*		2 *GPa*	≡30 *MPa*
Solution Method	AF	FLS	AF	FLS	FLS	AF
$\bar{P}_{max}$	73.0067	73.1731	72.2094	72.2094	70.3793	70.81
S	0.0324	0.0323	0.0326	0.0326	0.0333	-
$\bar{W}$	7.3145	7.3394	7.2597	7.2598	7.1018	6.87
Cav. Location ($\bar{x}$)	0.5433	0.5500	0.5500	0.5500	0.5500	0.553
Ref. Location ($\bar{x}$)	0.9100	0.9100	0.9100	0.9100	0.9100	0.900
Time steps to steady state	4950	235	7429	264	428	10,380

The pressure distribution on journal surface for both the non-pressured groove and pressured grooved journal bearings are shown in Figure 2-10 for a Mesh size of 50 by 20.

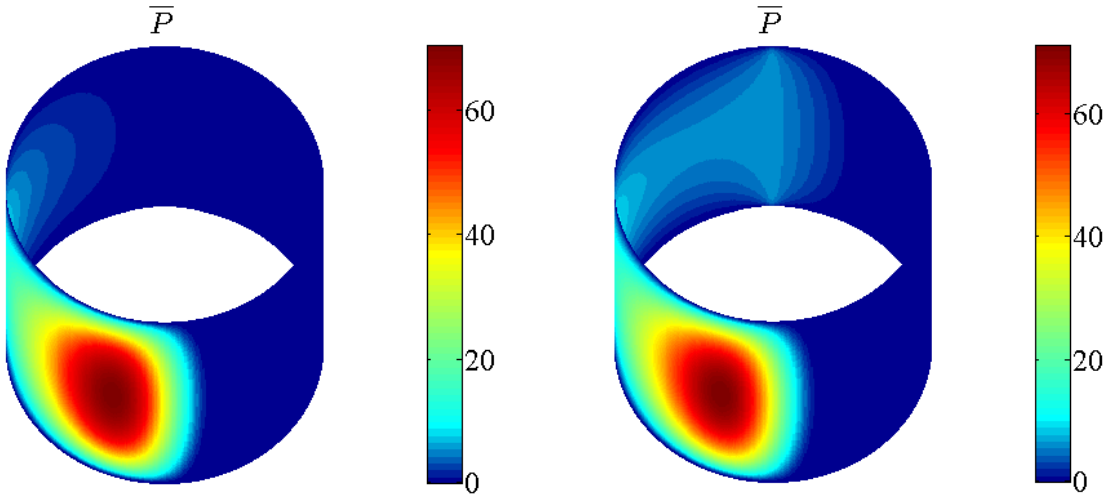

(a) (b)

Figure 2-10. Pressure distribution of a non-pressured supply groove journal bearing of Case 2-1 (a) and for a pressurized supply groove with $\bar{P}_g = 2\,\pi$ of Case 2-2 (b) both at $\epsilon = 0.8$ with a physical choice of bulk modulus $\beta = 2GPa$

Direct comparison of the predicted parameters for both non-pressured and pressured supply groove journal bearings as in Table 2-3 and Table 2-4 can reveal the significant importance of the chosen values for the lubricant bulk modulus on reported results. Such a dependency has been denied [39], or not much attention has been paid to this dependency, and it has therefore been ignored [35, 98] or fully acknowledged [40, 41, 43] in the literature. To better illustrate this, two solution parameters that are most sensitive to the chosen value of the bulk modulus are chosen (P_{max} *and* S) and the error in obtaining them for a range of applied lubricant bulk modulus is calculated and shown in Figure 2-11. The reference value for error estimation was chosen to be the converged values at physical lubricant bulk modulus of $\beta = 2GPa$ such that:

$$Error = \frac{u|_{\beta^*} - u|_{\beta_{physical}}}{u|_{\beta_{physical}}} \tag{2.33}$$

where β^* is the bulk modulus value used for analysis. The converged values of pressure distribution at journal mid-span against lubricant bulk modulus are shown in Figure 2-11.

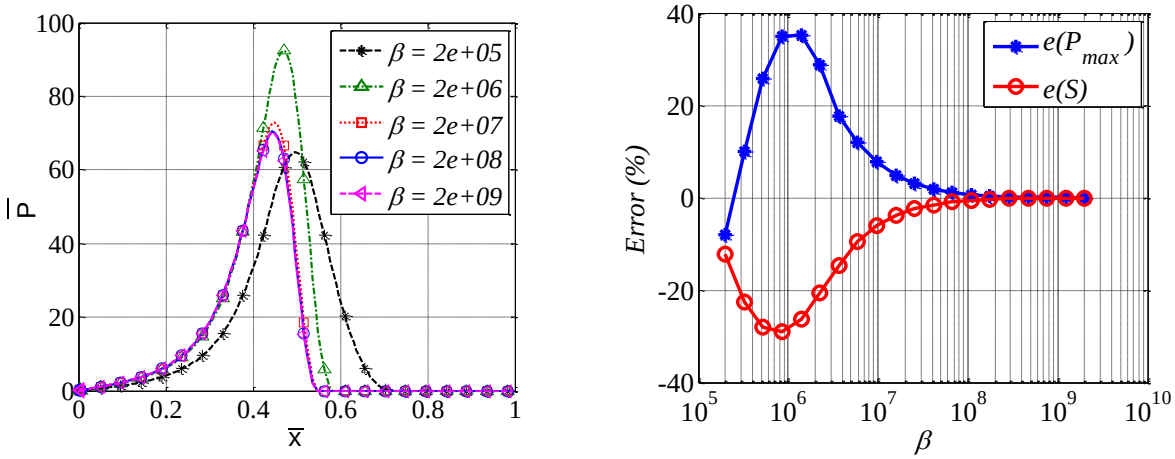

(a) (b)

Figure 2-11. Error in obtaining solution parameters vs. choice of bulk modulus, β (a) and Pressure variation at mid-span with β (b)

The variation of calculated error in solution parameters versus the bulk modulus as in Figure 2-11(a) suggests that the β dependency is significant for very low values of β ($\sim 2\times10^6$), and that by increasing the lubricant bulk modulus towards $\beta = 2\times10^7$ and beyond, the error in obtaining the solution drops below 3% in magnitude. As increasing β is crucial in obtaining the correct solution, the inherit numerical difficulty associated with higher β values becomes problematic for the AF based scheme, while it has almost no effect on the proposed full linear system based scheme (FLS), and hence is a good indicator for the robustness of the proposed numerical scheme.

Although β dependency for the cavitation solution from the Elrod algorithm has been previously addressed [40, 41, 43], a thorough quantitative stability analysis is missing in the literature. Implementing the FLS scheme has a second advantage over the AF schemes since the full coefficient matrices that are constructed during the solution procedure represent the numerical scheme as a whole and are ideal for eigenvalue analysis [102] which is required to assess the stability of a numerical scheme. This is further addressed in Section 2.3.4.

Case 3, high eccentric journal bearing with pressurized groove

The ultimate test for the efficacy and robustness of the FLS based algorithm is to solve for the combination of stiff numerical system with physical bulk modulus of $\beta = 2\ GPa$ under high

eccentricity ratios of $\epsilon = 0.9{\sim}0.99$ with a pressurized groove of $\bar{P}_g = 20\,\pi$ where the cavitation reformation boundary is to be captured. Calculated pressure contours and corresponding convergence plots for a range of eccentricity ratios are given in Figure 2-12. Results of Figure 2-12 are all obtained for a finer mesh of 100 by 40. This particular choice of mesh was indeed required to accurately capture the high pressure gradients in high eccentric devices. Based on the convergence plots of Figure 2-12 (b), it can be easily inferred that the performance of FLS based algorithm is not affected by the choice of eccentricity ratio. However, the difficulty in resolving the reformation boundary demands more iterations to reach convergence compared to the unpressurized cases of Figure 2-5.

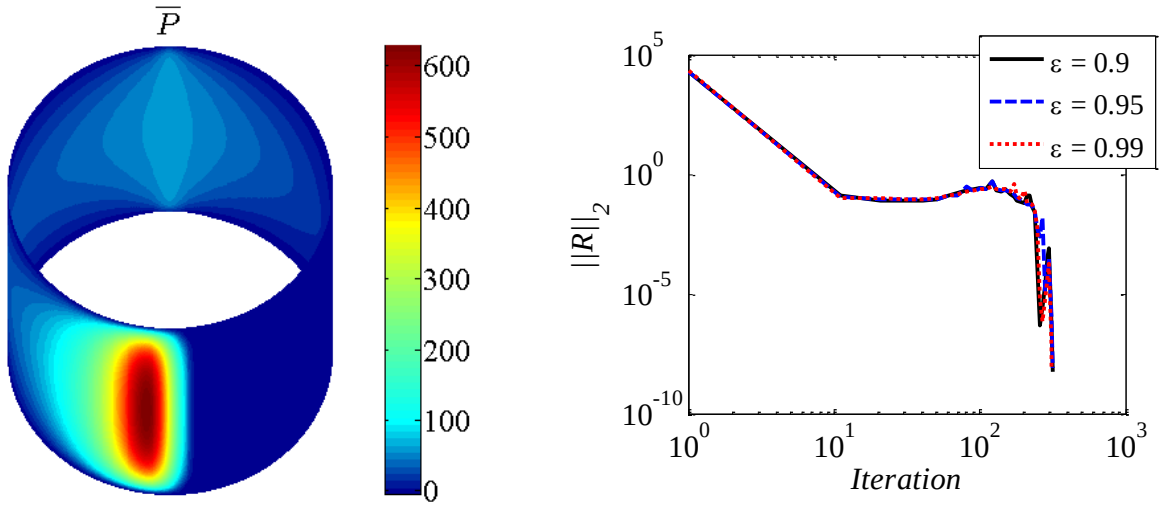

(a) (b)

Figure 2-12. Pressure contours for a high eccentric journal bearing at $\epsilon = 0.95$ with pressurized groove at $\bar{P}_g = 20\,\pi$ and physical bulk modulus of $\beta = 2\ GPa$ (a) and the corresponding convergence plots for a range of eccentricity ratios (b)

2.3.4 Numerical Stability of the Cavitation Algorithm

A numerical stability analysis is performed based on the eigenvalue analysis of the coefficient matrix for a pressurized grooved Journal bearing at a range of lubricant bulk modulus values as low as $\beta = 2{\times}10^{5}$ ($\equiv \bar{\beta} = 2.75$) up to $\beta = 2{\times}10^{9}$ ($\equiv \bar{\beta} = 2.75{\times}10^{4}$). The coefficient matrix used for analysis needs to be in the form of Eq. **(A**.11) for the eigenvalues to represent the numerical system as a whole. The calculated eigenvalues are depicted in Figure 2-13.

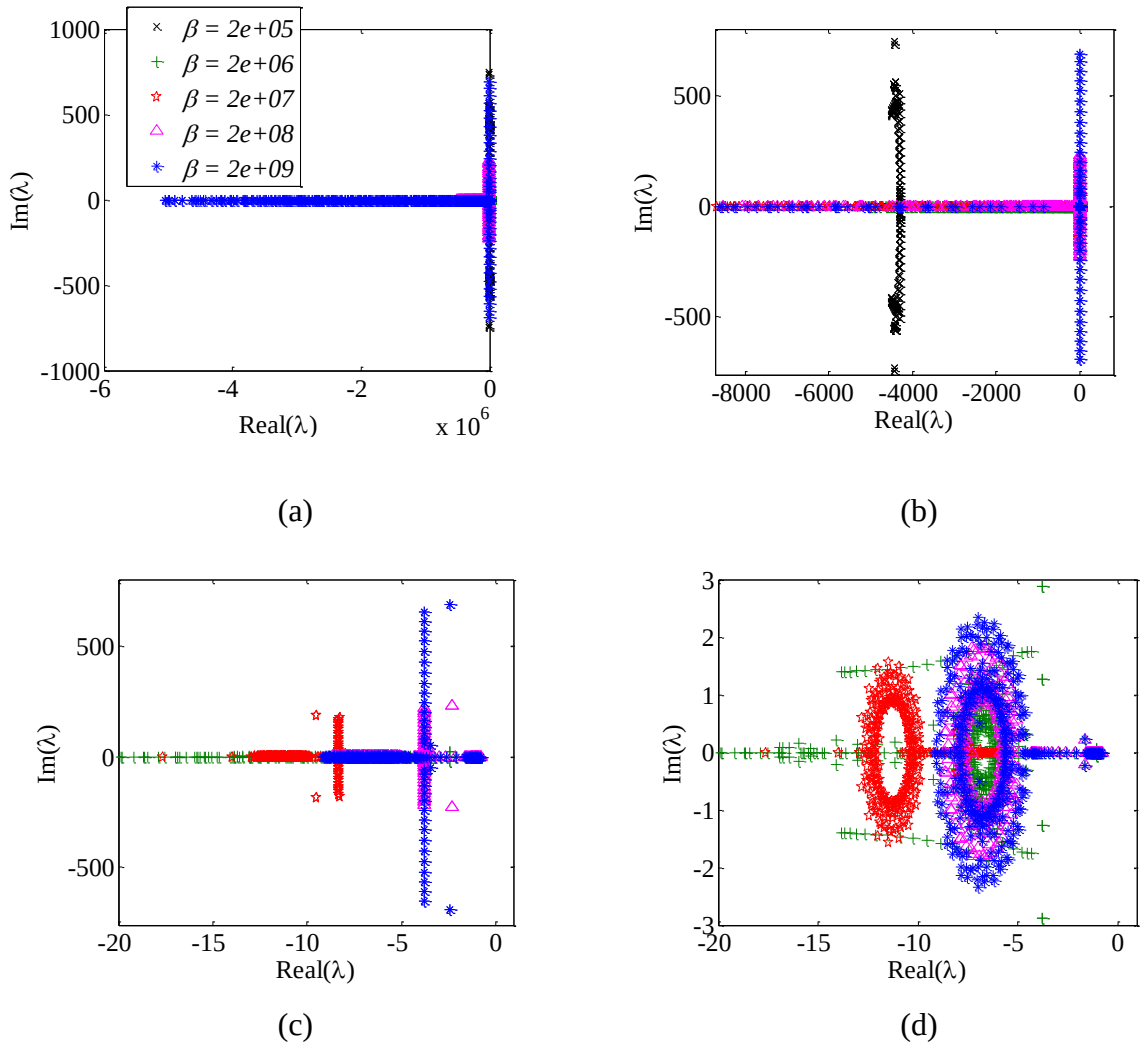

Figure 2-13. Eigenvalues of the Full linear system for a range of lubricant bulk modulus

By analysing the eigenvalues λ of Figure 2-13, it is evident that there is a space structure to the calculated eigenvalues, being spread on both real and imaginary axes as in Figure 2-13 (a) to (c) and yet maintaining a structure close to the origin as shown in Figure 2-13 (d). It can be also seen that as the bulk modulus increases in magnitude, the space span of the eigenvalues expands on both real and imaginary axes and shifts leftward towards the origin on the real axis. An increase in the real part of the eigenvalues concurrent with an increase in their imaginary part , is associated with the coexistence of lower and higher frequency harmonics with higher amplitudes in the solution i.e., increased difficulty to resolve the errors. As a result, schemes that are inherently problematic in dealing with low frequency errors like Approximate Factorization are not suitable

for the cavitation problem. Another indicator for numerical difficulty in obtaining the solution is high values of numerical stiffness.

Defining stiffness of a numerical scheme as $K_{num} = \frac{max(|Re(\lambda)|)}{min(|Re(\lambda)|)}$, it can be shown how stiffness increases exponentially with increasing bulk modulus as shown in Figure 2-14 (a) for a range of eccentricity ratios. The effect of the applied load, i.e. eccentricity ratio, on numerical stiffness for a range of selected bulk moduli is shown in Figure 2-14 (b) as well as the choice of number of elements in both x and z directions in Figure 2-14 (c) and (d). A 100×40 mesh was used to calculate the results of Figure 2-14 (a) and (b) and a bulk modulus of $\beta = 2\ GPa$ was used for the calculations in Figure 2-14 (c) and (d). Since Figure 2-14 (c) and (d) are designed to study the change of numerical stiffness versus M_x and M_z, the number of mesh divisions in the alternate direction is to be kept constant and was set to $M_z = 40$ and $M_x = 100$ for Figure 2-14 (c) and (d), respectively.

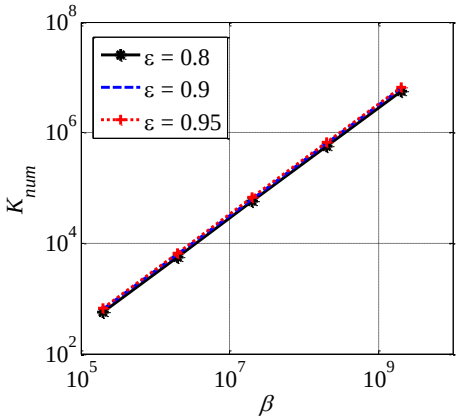

(a)

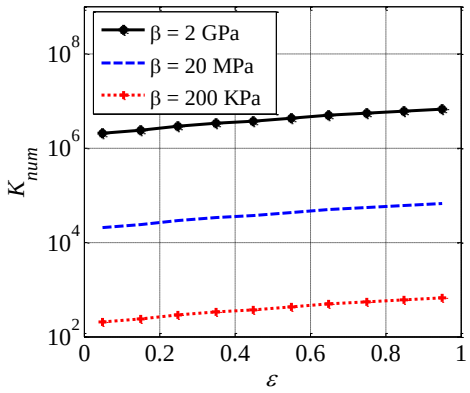

(b)

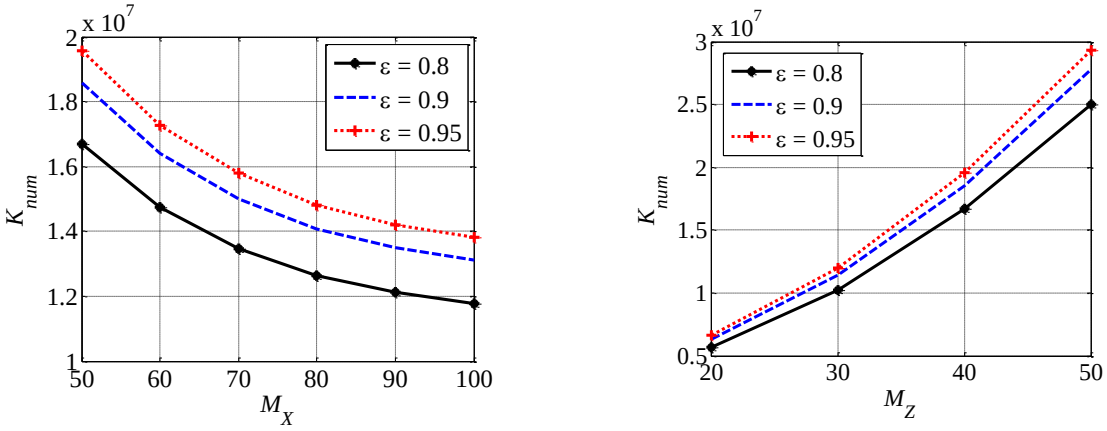

(c) (d)

Figure 2-14. Numerical stiffness versus the lubricant bulk modulus (a), eccentricity ratios (b) and number of mesh elements in *x* (c) and *z* directions *x* (d).

The numerical stiffness results of Figure 2-14 demonstrate that increasing static load renders the numerical system slightly stiffer but not with a great margin. It can also be seen from Figure 2-14(c) and (d) that the choice of mesh size in both directions is insignificant to numerical stiffness. However, as expected, an order of magnitude increase in lubricant bulk modulus significantly increases the stiffness of the numerical system regardless of the static load (i.e. eccentricity ratio). In order to maintain the stability of such a stiff numerical system, solvers are usually forced to choose unreasonably small time-steps, which lead to very slow convergence. In the lubrication problem, where accuracy of results depend on the physical choice of the bulk modulus, the inevitable stiff discretized numerical system needs to be solved efficiently by means of well adopted schemes, such as the one proposed in this chapter.

Chapter 3: Linear Stability of Finite Length Journal Bearings in Turbulent Regimes

In this chapter, dynamic coefficients of a finite length journal bearing are numerically calculated under laminar and turbulent regimes, based on Ng-Pan-Elrod's and Constantinescu's turbulent models. Linear stability charts of a flexible rotor supported on laminar and turbulent journal bearings are found by calculating the threshold speed of instability associated with the start of the unstable oil whirl phenomenon. Local journal trajectories of the rotor-bearing system are found at different operating conditions solely based on the calculated dynamic coefficients in laminar and turbulent flow.

3.1 Governing Equations

Figure 3-1(a) shows a schematic of a journal bearing inside the bearing clearance. A simple rotor-bearing system can be represented as a concentrated mass supported on journal bearings modeled as direct and cross coupled spring and dampers as shown in Figure 3-1(b) (cross coupled not showing).

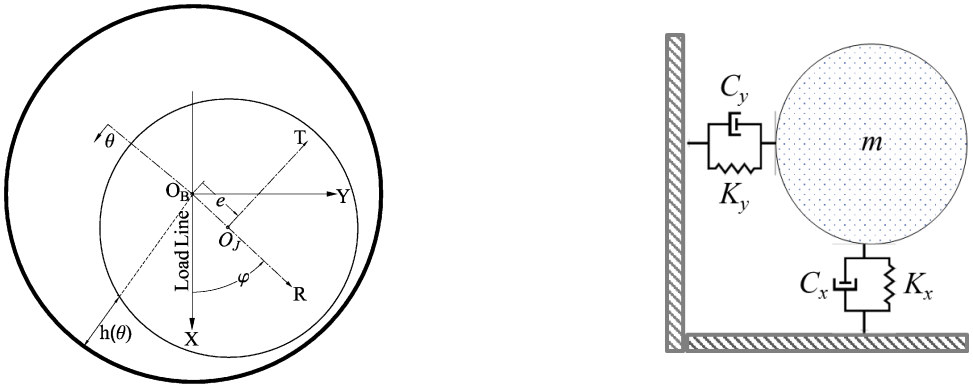

(a) (b)

Figure 3-1. the schematic of a journal inside bearing (a) and modeling the effect of journal bearings with linear stiffness and damping coefficients (b)

Under static equilibrium, the weight of the rotor and journal is in balance with the bearing force such that $\vec{F} + \overrightarrow{W} = 0$, and hence relative to the static equilibrium state, the x and y components of the dynamic deviation of bearing force upon the rotor can be expressed as follows:

$$F_x + W_x = f_x = \frac{\partial F_x}{\partial x}dx + \frac{\partial F_x}{\partial \dot{x}}d\dot{x} + \frac{\partial F_x}{\partial y}dy + \frac{\partial F_x}{\partial \dot{y}}d\dot{y} + (higher\ order\ terms)$$
$$F_y + W_y = f_y = \frac{\partial F_y}{\partial x}dx + \frac{\partial F_y}{\partial \dot{x}}d\dot{x} + \frac{\partial F_y}{\partial y}dy + \frac{\partial F_y}{\partial \dot{y}}d\dot{y} + (higher\ order\ terms) \quad (3.1)$$

It is convenient to write Equation (3.1) in the following matrix form:

$$\begin{Bmatrix} f_x \\ f_y \end{Bmatrix} = -\begin{bmatrix} K_{xx} & K_{xy} \\ K_{yx} & K_{yy} \end{bmatrix}\begin{Bmatrix} x \\ y \end{Bmatrix} - \begin{bmatrix} C_{xx} & C_{xy} \\ C_{yx} & C_{yy} \end{bmatrix}\begin{Bmatrix} \dot{x} \\ \dot{y} \end{Bmatrix} \quad (3.2)$$

where $K_{ij} \equiv -\left(\partial F_i/\partial x_j\right)$ and $C_{ij} \equiv -\left(\partial F_i/\partial \dot{x}_j\right)$ are the eight bearing stiffness and damping coefficients as proposed by Lund [13] . The bearing reaction force can be calculated by integrating the oil induced pressure over the surface of the journal:

$$F_R = \int_0^{\theta_{cav}} Rd\theta \int_{-\frac{L}{2}}^{\frac{L}{2}} PCos(\theta)dz\ ,\quad F_T = \int_0^{\theta_{cav}} Rd\theta \int_{-\frac{L}{2}}^{\frac{L}{2}} PSin(\theta)dz \quad (3.3)$$

In order to calculate the oil induced pressure, one needs to solve the Reynolds partial differential equation for laminar flow:

$$\frac{1}{R^2}\frac{\partial}{\partial\theta}\left(\frac{h^3}{12\,\mu}\frac{\partial P}{\partial\theta}\right) + \frac{\partial}{\partial z}\left(\frac{h^3}{12\,\mu}\frac{\partial P}{\partial z}\right) = \frac{1}{2}\omega\frac{\partial h}{\partial\theta} + \frac{\partial h}{\partial t} \quad (3.4)$$

Equation (3.4) does not have an analytical solution and either needs to be simplified or to be solved numerically. For long journal bearings with length to diameter ratio of $\frac{L}{D} > 2$, it is assumed that the variation in the induced pressure is more important in the circumferential direction compared to the change in the pressure along the axial direction. In such cases, only the first term in the LHS of Eq. (3.4) is retained, and solving the resulting ODE yields the *long bearing* approximation pressures. Retaining the second term in the LHS of Eq. (3.4) only, which holds for $\frac{L}{D} < 0.5$, will yield the pressure based on the *short bearing* approximation. In short bearings, the abrupt pressure change in the axial direction outweighs the pressure variations along the circumferential direction. Despite the relative ease in characterizing the bearing performance based on approximate short and long bearings solutions, the application of these approximations can be far from reality since

most of the real journal bearings used in the industry have length to diameter ratios of around unity and hence, accurate characterization of bearing performance is only possible by obtaining the solution to the Reynolds equation in its complete form as in Eq. (3.4).

In relatively large diameter ($d > 0.4m$) journal bearings, the flow state becomes turbulent at low rotating speeds ($\omega < 400\,rpm$), when using low-viscosity lubricants, or when operating with large clearances. The state of the flow in fluid-film journal bearings can be judged by its Reynolds number. It is unanimously agreed in the literature that turbulence makes its first appearance in journal bearings at a Reynolds number of approximately 2000 [103]. Once the flow becomes turbulent, the importance of the instability mechanism and transitioning that resulted in the turbulence flow diminishes [25]. Even though existing turbulent models for thin-film flows do not account for transitioning to turbulent from laminar flow, they are shown to predict the velocity profile and pressures with substantial agreement to the near isothermal bearing experiments in the fully turbulent region [25, 104]. For unsteady, incompressible turbulent flows in the oil film journal bearings as shown in Figure 1, the Reynolds equation can be written as:

$$\frac{1}{R^2}\frac{\partial}{\partial\theta}\left(\frac{h^3}{k_\theta\mu}\frac{\partial P}{\partial\theta}\right)+\frac{\partial}{\partial z}\left(\frac{h^3}{k_z\mu}\frac{\partial P}{\partial z}\right)=\frac{\omega}{2}\frac{\partial h}{\partial\theta}+\frac{\partial h}{\partial t} \tag{3.5}$$

where k_θ and k_z are the turbulence coefficients in circumferential and longitudinal directions, respectively. In this Chapter, two turbulence methods are employed. First is the Constantinescu's model based on the Prandtl mixing length hypothesis [104, 105]; second, is the Ng-Pan-Elrod model based on eddy viscosity [104, 106]. The turbulence coefficients along with their constants for both employed models are presented in Equation (3.6) and Table 3-1.

$$\begin{cases} k_z = 12 + a_1(Re^*)^{a_2} \\ k_\theta = 12 + a_3(Re^*)^{a_4} \end{cases} \tag{3.6}$$

where Re^* is the local Reynolds number which varies with θ.

Table 3-1. Turbulent constants of Constantinescu and Ng-Pan-Elrod model

Constants	Turbulence Models	
	Constantinescu	Ng-Pan-Elrod
a_1	0.0198	0.0044
a_2	0.741	0.96
a_3	0.026	0.0136
a_4	0.8265	0.9

From Equation (3.5) and (3.6) the turbulent Reynolds equation can be written as:

$$\frac{1}{R^2}\frac{\partial}{\partial\theta}\left(\frac{h^3}{k_\theta\mu}\frac{\partial P}{\partial\theta}\right)+\frac{\partial}{\partial z}\left(\frac{h^3}{k_z\mu}\frac{\partial P}{\partial z}\right)=-\frac{C\epsilon\omega}{2}Sin(\theta)+C\dot{\epsilon}Cos(\theta)+C\epsilon\dot{\varphi}Sin(\theta) \tag{3.7}$$

As mentioned previously, if only the second term in the LHS of Equation (3.4) is retained, solving the resulting ODE will yield the pressure in turbulent short bearings. It can be easily shown that the resulting pressure can be written as:

$$P_{short}=\frac{k_z\mu}{h^3}\left[-\frac{C\varepsilon\omega}{2}Sin(\theta)+C\dot{\varepsilon}Cos(\theta)+C\varepsilon\dot{\varphi}Sin(\theta)\right]\left(\frac{z^2}{2}-\frac{L^2}{8}\right) \tag{3.8}$$

3.2 Identification of Bearing Dynamic Coefficients

A direct solution to Equation (3.4) for laminar flow will yield the corresponding laminar pressure field. In order to obtain the journal bearing dynamic coefficients, the force derivatives with respect to displacement and velocity of the journal center are to be obtained such that $k_{ij}\equiv-\left(\partial F_i/\partial x_j\right)$ and $c_{ij}\equiv-\left(\partial F_i/\partial\dot{x}_j\right)$. The coefficients can now be directly calculated by first exerting some external finite perturbation at each steady state point following direct numerical differentiation [14, 25, 48]. While a finite perturbation approach may be adequate for practical purposes, the inherent numerical inaccuracy of the method can be eliminated by employing a perturbation solution known as the infinitesimal perturbation approach [47]. It is reported that provided the perturbation amplitudes are kept lower than *0.02C* (displacement) or *0.02ωC* (velocity) for normal bearing eccentricities, the calculated dynamic coefficients will be within 0.1% of the infinitesimal approach [48]. An infinitesimal perturbation method is used in this work. Following [47, 94], the

lubricant thickness in steady state h_0 is perturbed in R and T directions (as in Figure 3-1.a) in the form:

$$\begin{aligned} h &= h_0 + dh = h_0 + dR\cos\theta + dT\sin\theta \\ \frac{\partial h}{\partial t} &= d\dot{R}\cos\theta + d\dot{T}\sin\theta \end{aligned} \tag{3.9}$$

This perturbation in film thickness will result in a perturbation of the pressure film as

$$P = P_0 + dP = P_0 + \frac{\partial P}{\partial R}dR + \frac{\partial P}{\partial T}dT + \frac{\partial P}{\partial \dot{R}}d\dot{R} + \frac{\partial P}{\partial \dot{T}}d\dot{T} \tag{3.10}$$

Equations (3.9) and (3.10) are substituted back into the modified Reynolds Equation for turbulent flow (3.5), and keeping only zeroth and first order terms will omit the time-dependent terms and will yield five steady pressure and pressure gradient equations:

$$\frac{1}{R^2}\frac{\partial}{\partial\theta}\left(\frac{{h_0}^3}{k_\theta\mu}\frac{\partial P_0}{\partial\theta}\right) + \frac{\partial}{\partial z}\left(\frac{{h_0}^3}{k_z\mu}\frac{\partial P_0}{\partial z}\right) = \frac{\omega}{2}\frac{\partial h_0}{\partial\theta} \tag{3.11}$$

$$\frac{1}{R^2}\frac{\partial}{\partial\theta}\left(\frac{{h_0}^3}{k_\theta\mu}\frac{\partial P_R}{\partial\theta}\right) + \frac{\partial}{\partial z}\left(\frac{{h_0}^3}{k_z\mu}\frac{\partial P_R}{\partial z}\right) = -\frac{\omega}{2}\sin\theta - \frac{1}{R^2}\frac{\partial}{\partial\theta}\left(\frac{3\,{h_0}^2}{k_\theta\mu}\cos\theta\frac{\partial P_0}{\partial\theta}\right) - \frac{\partial}{\partial z}\left(\frac{3\,{h_0}^2}{k_z\mu}\cos\theta\frac{\partial P_0}{\partial z}\right) \tag{3.12}$$

$$\frac{1}{R^2}\frac{\partial}{\partial\theta}\left(\frac{{h_0}^3}{k_\theta\mu}\frac{\partial P_T}{\partial\theta}\right) + \frac{\partial}{\partial z}\left(\frac{{h_0}^3}{k_z\mu}\frac{\partial P_T}{\partial z}\right) = \frac{\omega}{2}\cos\theta - \frac{1}{R^2}\frac{\partial}{\partial\theta}\left(\frac{3\,{h_0}^2}{k_\theta\mu}\sin\theta\frac{\partial P_0}{\partial\theta}\right) - \frac{\partial}{\partial z}\left(\frac{3\,{h_0}^2}{k_z\mu}\sin\theta\frac{\partial P_0}{\partial z}\right) \tag{3.13}$$

$$\frac{1}{R^2}\frac{\partial}{\partial\theta}\left(\frac{{h_0}^3}{k_\theta\mu}\frac{\partial P_{\dot{R}}}{\partial\theta}\right) + \frac{\partial}{\partial z}\left(\frac{{h_0}^3}{k_z\mu}\frac{\partial P_{\dot{R}}}{\partial z}\right) = \cos\theta \tag{3.14}$$

$$\frac{1}{R^2}\frac{\partial}{\partial\theta}\left(\frac{{h_0}^3}{k_\theta\mu}\frac{\partial P_{\dot{T}}}{\partial\theta}\right) + \frac{\partial}{\partial z}\left(\frac{{h_0}^3}{k_z\mu}\frac{\partial P_{\dot{T}}}{\partial z}\right) = \sin\theta \tag{3.15}$$

A solution of the modified Reynolds differential equation for steady pressure (Eq. (3.11)) has been obtained numerically using a finite volume method with successive over-relaxation scheme (point Gauss–Seidel with over relaxation parameter $\omega = 1.4$). A sample mesh of 100×30 (θ, z) was

selected to calculate the pressure field for a low Reynolds number operating point at eccentricity ratio of $\epsilon = 0.8$. The calculated pressure is non-dimensionalized and is shown along with the mesh in Figure 3-2. The pressure boundary condition is the commonly used Swift-Stieber boundary condition for a fully cavitated journal bearing such that $P = \frac{\partial P}{\partial \theta} = 0 \; at \; \theta = \theta_{cav}$ for the cavitated zone and zero pressure at the journal edges $P_0 = dP = 0 \; at \; Z = \pm\frac{L}{2}$ [25].

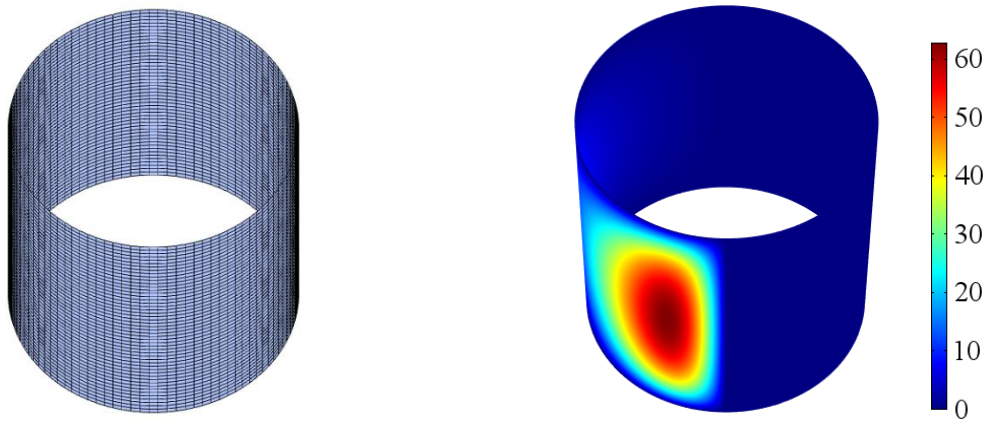

(a) (b)

Figure 3-2. The selected mesh (a) and non-dimensional pressure distribution, $\bar{P}$, on the journal surface for a cavitated journal bearing (b).

The pressure distributions (non-dimensionalized) of the finite length journal for laminar and both available turbulent models are calculated at the journal mid-span and are compared to available analytical solutions of a short bearing in Figure 3-3. The corresponding pressure distributions are evaluated for two different cases at $\varepsilon = 0.6$. First at a low Reynolds number of $Re = 1000$ (well into the laminar region) Figure 3-3 (a), and then for a relatively high Reynolds number of $Re = 10000$ (fully turbulent) as shown in Figure 3-3 (b). Results indicate that as the Reynolds number increases, the predicted pressure distributions of the modified Reynolds equation deviates increasingly from the pressures as predicted by the classical Reynolds equation. The predicted pressures of a turbulent bearing for both turbulent models are sufficiently close at low Reynolds numbers but pressure predictions of the Ng-Pan method become increasingly different from the pressure predictions based on the Constantinescu model at higher Reynolds numbers.

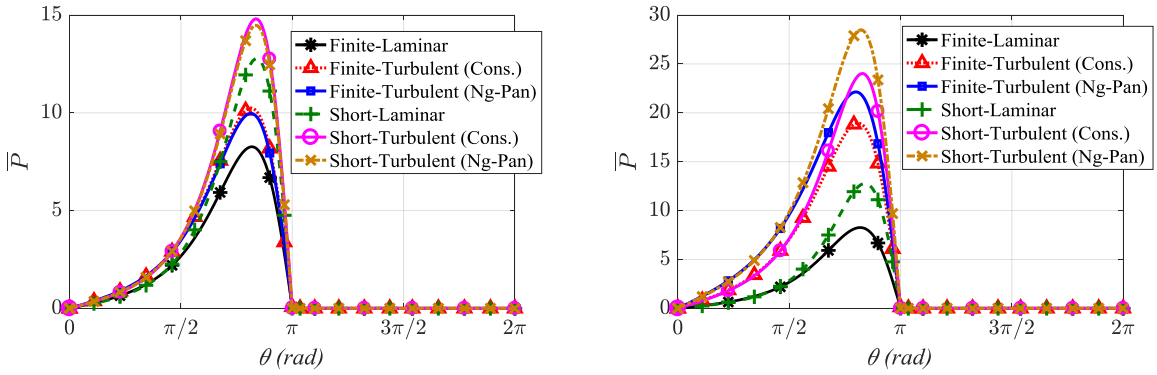

(a) (b)

Figure 3-3. The comparison of numerically and analytically obtained pressure (non-dimensional) distributions at mid-span of a finite length journal bearing with $L/D = 1/2$ for laminar and turbulent flow at $\varepsilon = 0.6$ and Re = 1000 (a) and Re = 10000 (b).

The obtained pressure field is then used as a basis for calculation of the pressure field gradients according to Equations (3.12) to (3.15). Having all the pressure gradients calculated in the *R*-*T* coordinate system, the dynamic coefficients can be simply found by integrating the pressure gradients over the non-cavitated flow region [47] on the journal surface according to the Swift-Stieber boundary condition:

$$\begin{Bmatrix} K_{rr} \\ K_{tr} \end{Bmatrix} = -\int_0^{\theta_{cav}} \int_{-\frac{L}{2}}^{\frac{L}{2}} P_R \begin{Bmatrix} \cos\theta \\ \sin\theta \end{Bmatrix} R d\theta dz \,, \begin{Bmatrix} K_{rt} \\ K_{tt} \end{Bmatrix} = -\int_0^{\theta_{cav}} \int_{-\frac{L}{2}}^{\frac{L}{2}} P_T \begin{Bmatrix} \cos\theta \\ \sin\theta \end{Bmatrix} R d\theta dz$$
$$\begin{Bmatrix} C_{rr} \\ C_{tr} \end{Bmatrix} = -\int_0^{\theta_{cav}} \int_{-\frac{L}{2}}^{\frac{L}{2}} P_{\dot{R}} \begin{Bmatrix} \cos\theta \\ \sin\theta \end{Bmatrix} R d\theta dz \,, \begin{Bmatrix} C_{rt} \\ C_{tt} \end{Bmatrix} = -\int_0^{\theta_{cav}} \int_{-\frac{L}{2}}^{\frac{L}{2}} P_{\dot{T}} \begin{Bmatrix} \cos\theta \\ \sin\theta \end{Bmatrix} R d\theta dz \quad (3.16)$$

Having the dynamic coefficients matrices $\boldsymbol{k}$ and $\boldsymbol{c}$ in *R*-*T* coordinates, a simple coordinate transformation with the angle of rotation being the attitude angle φ, will yield the bearing coefficients in the *x*-*y* coordinate system:

$$Q = \begin{pmatrix} \cos\varphi & -\sin\varphi \\ \sin\varphi & \cos\varphi \end{pmatrix}, \; [\bar{K}]_{x-y} = -Q[\bar{K}]_{R-T}\, Q^T \,, [\bar{C}]_{x-y} = -Q[\bar{C}]_{R-T} Q^T \quad \textbf{(3.17)}$$

Based on sensitivity analysis of the maximum pressure as a function of the number of divisions in the circumferential (θ) and axial (z) directions, it is reported in the literature that the solution is more sensitive to the circumferential mesh density [52, 107]. A mesh density sensitivity analysis was carried out for four representative mesh sizes of 30×12, 50×20, 100×30 and 150×40 (θ, z). The maximum field pressure as well as all stiffness and damping coefficients were selected as target variables (φ) of interest for mesh sensitivity analysis and are calculated at an eccentricity ratio of $\epsilon = 0.8$ for a finite length journal bearing with $\frac{L}{D} = 1$. Plots of stiffness and damping coefficients vs total number of elements are shown in Figure 3-4.

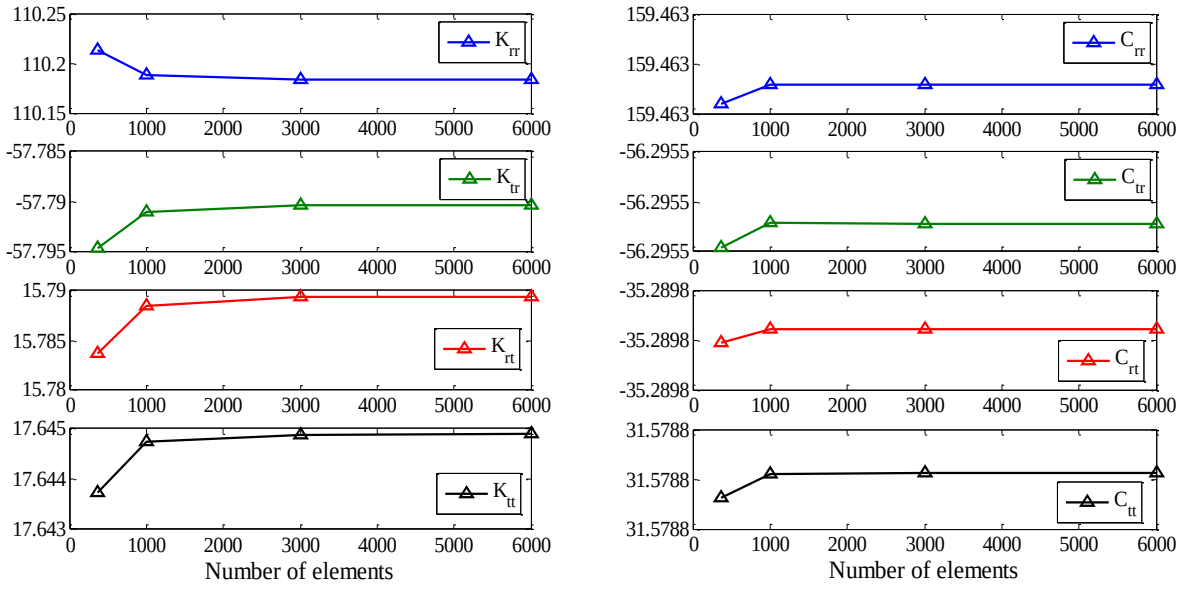

(a) (b)

Figure 3-4. Non-dimensional Stiffness (a) and damping (b) coefficients as target variables for mesh sensitivity analysis

The fine grid convergence index ${GCI_{fine}}^{21}$ (an indicator of mesh numerical uncertainty) as well as extrapolated target variables and corresponding grid error for a subset of selected mesh (30×12, 50×20 and 100×30) were calculated based on [101]. The fine grid convergence calculations for dynamic stiffness as target variables are tabulated in Table 3-2. The fine grid (100×30 (θ, z)) convergence index ${GCI_{fine}}^{21}$ indicating numerical uncertainty in calculating the

maximum target variable does not exceed % 0.4 for maximum field pressure and does not exceed % 0.0012 for any of the calculated dynamic coefficients; hence, the final fluid model was selected with 100 ×30 (θ, z) divisions with a total of 3000 2D fluid elements.

Table 3-2. Sample calculations of discretization errors

	$\phi = P_{max}$	$\phi = K_{rr}$	$\phi = K_{tr}$	$\phi = K_{rt}$	$\phi = K_{tt}$
Φ_1 (fine grid)	61.6153	110.1834	-57.7904	15.7893	17.6449
Φ_2	61.4949	110.1880	-57.7910	15.7884	17.6447
Φ_3 (coarse grid)	61.5675	110.2128	-57.7946	15.7837	17.6437
${\Phi_{ext}}^{21}$	61.7984	110.1823	-57.7902	15.7895	17.6449
${\%e_a}^{21}$	0.1953	4.24E-03	1.15E-03	5.55E-03	8.29E-04
${\%e_{ext}}^{21}$	0.2963	9.83E-04	2.59E-04	1.26E-03	1.42E-04
${\%GCI_{fine}}^{21}$	0.3715	1.23E-03	3.24E-04	1.57E-03	1.78E-04

The calculated values for stiffness and damping of a finite length journal bearing in laminar flow are compared to the analytically available coefficients of a short bearing for a length to diameter ratio $\frac{L}{D} = 1$ when plotted against the Sommerfeld number and are shown in Figure 3-5.

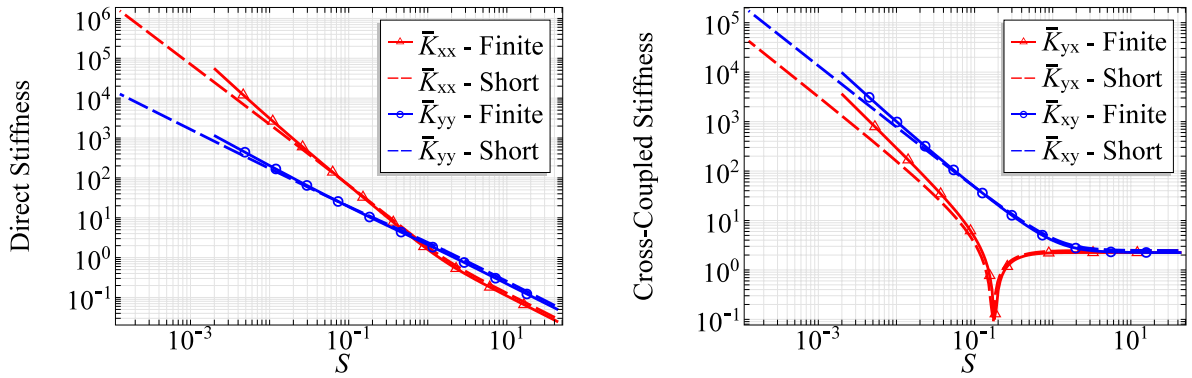

(a) (b)

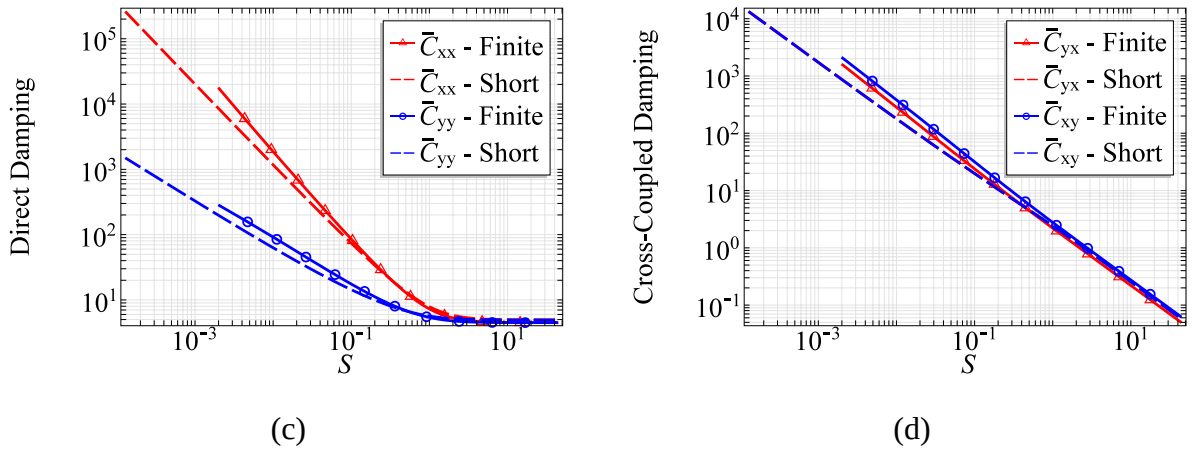

(c) (d)

Figure 3-5. The comparison of numerically calculated laminar dynamic coefficients of a finite length journal bearing ($L/D = 1/2$) with analytical short bearing results. Direct stiffness (a), Cross-coupled stiffness (b), Direct damping (c) and Cross-coupled damping (d).

As can be seen from Figure 3-5, at high Sommerfeld numbers (lower static load on shaft and hence smaller eccentricity ratios), the numerically obtained coefficients from direct solution to the Reynolds equations will become increasingly closer to the analytically obtained short bearing values unlike the big deviations in the low Sommerfeld region (high load and or higher eccentricity ratios). This is of course expected because of the higher pressure relief of the short bearing compared to a finite length journal bearing especially at high static loads.

3.3 Mathematical Model of the Rotor-Bearing System

In an ideal and fully balanced rotor-bearing system, the shaft spins at its designed operating speed while the induced pressures inside the end journals can support the weight of the shaft; hence, there exists an equilibrium point where the journal center finds and stays during the operation. This point is referred to as the static equilibrium position. If the rotor bearing system is undisturbed, the rotor will remain in its equilibrium position. For small disturbances, for instance a small unbalance force, the shaft will no longer stay at the static equilibrium point. Instead, it orbits via a closed elliptic curve around its equilibrium point. These are the harmonic solutions to a stable dynamic system operating in its stable region. If the operating speed of the shaft exceeds the so called threshold speed of instability ω_{th}, no stable harmonic solution exists and the journal orbit will spiral outward towards either a bounded stable limit cycle (with orbits generally much greater than the stable closed harmonic orbits) or towards the point where metal to metal contact occurs.

This change of the dynamical behavior of the system is called a bifurcation and is known in rotor dynamics terminology as the oil whirl-whip phenomenon. It should be noted that oil whirl and rotor whirling will happen for both fully balanced and unbalanced rotors, though the threshold speed of a balanced system is higher than the threshold speed of an unbalanced system.

The transition (bifurcation) to high amplitude vibration, whether to a stable limit cycle or towards the bearing clearance, can be either gradual (supercritical bifurcation) or sudden (subcritical bifurcation). Bifurcation towards the limit cycle is generally considered as an unstable operating condition while it is not necessarily unstable. The reason for this is that the majority of the stability analyses available in the literature are based on linear analysis. From the viewpoint of linear analysis, there is no difference between unstable and stable limit cycles (they are both considered as unstable). Even though the bifurcation type cannot be evaluated via linear analysis, the stability margin can indeed be identified by simple linear analysis. This is because that local stability of nonlinear and linearized systems are essentially the same. Linearized analysis will be used here to identify the stability margins of the system. To do this, one needs to find the threshold speed of instability for a given rotor-bearing system at any applied static load to the shaft. If the operating speed of the rotor is kept below this threshold speed, the system remains in its stable region and hence the operation is considered safe. The analysis here follows from [25, 91].

Referring to Figure 3-6, to analyze a flexible, center-loaded and perfectly balanced rotor symmetrically supported by two identical fluid-film journal bearings, the following assumptions are made:

- Deflection of the flexible shaft is small to allow the use of linear beam theory.
- The mass of the shaft and rotor torque of the midpoint mass are negligible.
- The rotor mass is lumped at the midpoint.
- Axial and torsional vibrations of the lumped mass are negligible.
- Gyroscopic effect of the shaft, disk and journal bearings are negligible.

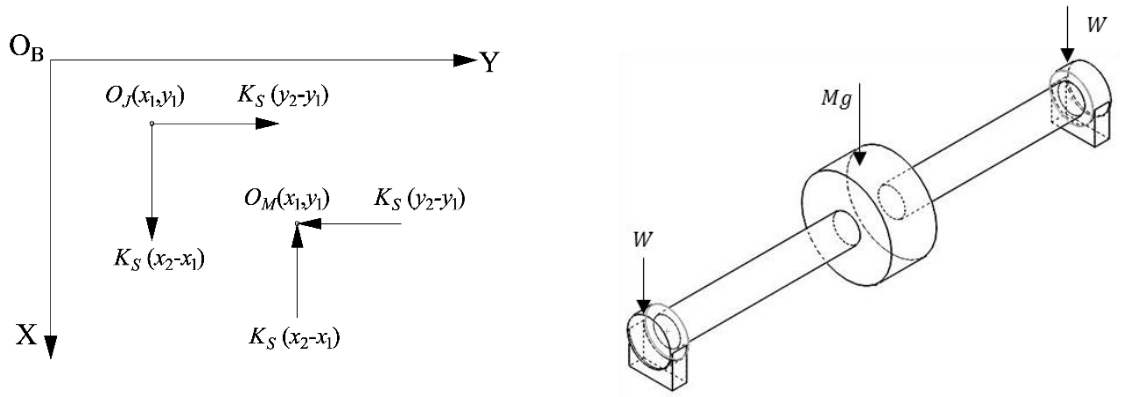

Figure 3-6. Schematic of a flexible rotor supported on journal bearings. O_J and O_M correspond to the geometric center of the journal and the central disc respectively.

The equations of motion for the central disk and journal bearings may be written as follows:

$$\begin{aligned} Central\ Disk: &\begin{cases} M\ddot{x}_2 + K_s(x_2 - x_1) = 0 \\ M\ddot{y}_2 + K_s(y_2 - y_1) = 0 \end{cases} \\ Journal\ Bearings: &\begin{cases} -2dF_x + K_s(x_2 - x_1) = 0 \\ -2dF_y + K_s(y_2 - y_1) = 0 \end{cases} \end{aligned} \quad , \tag{3.18}$$

where K_s is the shaft stiffness, dF_x and dF_y are the components of the force due to induced bearing pressure in excess of the equilibrium forces, and are calculated based on Equation (3.2). Assuming harmonic motion of the central disc and journals with frequency $\nu = Re(\nu) + i\ Im(\nu)$:

$$\begin{pmatrix} x_1 \\ x_2 \end{pmatrix} = \begin{pmatrix} X_1 \\ X_2 \end{pmatrix} e^{\nu t}\ , \begin{pmatrix} y_1 \\ y_2 \end{pmatrix} = \begin{pmatrix} Y_1 \\ Y_2 \end{pmatrix} e^{\nu t} \tag{3.19}$$

By substituting Equation (3.19) into Equation (3.18), the following expression may be obtained:

$$\begin{bmatrix} \dfrac{-K_s M\nu^2}{K_s + M\nu^2} + 2K_{xx} + 2\nu C_{xx} & 2K_{xy} + 2\nu C_{xy} \\ 2K_{yx} + 2\nu C_{yx} & \dfrac{-K_s M\nu^2}{K_s + M\nu^2} + 2K_{yy} + 2\nu C_{yy} \end{bmatrix} \begin{pmatrix} X_1 \\ X_2 \end{pmatrix} = \begin{pmatrix} 0 \\ 0 \end{pmatrix} \tag{3.20}$$

Non-dimensionalizing according to [25] for shaft and bearing stiffness and bearing damping, and also having $\begin{pmatrix} \bar{X}_1 \\ \bar{X}_2 \end{pmatrix} = \frac{1}{C}\begin{pmatrix} X_1 \\ X_2 \end{pmatrix}$, $\omega = \bar{\omega}\sqrt{K_s/M}, \nu = \omega\bar{\nu}, \alpha = \frac{-\bar{K}_s\bar{\nu}^2\bar{\omega}^2}{1+\bar{\nu}^2\bar{\omega}^2}$, the non-dimensional from of Equation (3.20):

$$\begin{bmatrix} \alpha + 2\bar{K}_{xx} + 2\bar{\nu}\bar{C}_{xx} & 2\bar{K}_{xy} + 2\bar{\nu}\bar{C}_{xy} \\ 2\bar{K}_{yx} + 2\bar{\nu}\bar{C}_{yx} & \alpha + 2\bar{K}_{yy} + 2\bar{\nu}\bar{C}_{yy} \end{bmatrix} \begin{pmatrix} \bar{X}_1 \\ \bar{X}_2 \end{pmatrix} = \begin{pmatrix} 0 \\ 0 \end{pmatrix} \tag{3.21}$$

The condition of non-trivial (non-zero) solution requires that the determinant of the characteristic matrix be set to zero. By setting the imaginary part of the determinant of Equation (3.21) to zero:

$$\alpha = \frac{2(\bar{K}_{xy}\bar{C}_{yx} + \bar{K}_{yx}\bar{C}_{xy} - \bar{K}_{yy}\bar{C}_{xx} - \bar{K}_{xx}\bar{C}_{yy})}{\bar{C}_{xx} + \bar{C}_{yy}} \tag{3.22}$$

By setting the real part of the determinant of Equation (3.21) to zero:

$$\bar{\nu}^2 = \frac{\alpha^2 + 2(\bar{K}_{xx} + \bar{K}_{yy})\alpha + 4(\bar{K}_{xx}\bar{K}_{yy} - \bar{K}_{xy}\bar{K}_{yx})}{4(\bar{C}_{xy}\bar{C}_{yx} - \bar{C}_{xx}\bar{C}_{yy})} \tag{3.23}$$

In the state of neutral stability, $\bar{\nu}$ is purely imaginary and $\frac{\nu_{whirl}}{\omega} = \sqrt{-\bar{\nu}^2}$. Having $\bar{K}_s = \frac{C}{L\,D\,\mu\,N\left(\frac{R}{C}\right)^2} K_s = \frac{1}{S}\frac{C\,K_s}{W}$ and using the definition of α, the instability threshold value can be found as:

$$\bar{\omega}_{th}^2 = \frac{\alpha}{\bar{\nu}^2(\bar{K}_s - \alpha)} \tag{3.24}$$

3.4 Results and Discussions

3.4.1 Laminar and Turbulent Dynamic Coefficients

The finite length journal bearing pressure and pressure gradients in turbulent flow can be calculated by solving the steady and perturbed modified Reynolds equation, Eq. (3.11) to (3.15). The Coefficients in *R-T* coordinate system are then calculated by integrating the pressure gradients as in Eq. (3.16). A coordinate transformation as in Eq. (3.17) from *R-T* to *X-Y* is then necessary to find the coefficients in the *X-Y* coordinate system, which is suitable for stability analysis. This is done for a range of Reynolds numbers (10000, 20000 and 30000) and for both the Constantinescu and Ng-Pan Elrod turbulent models, and are compared to the calculated coefficients in the laminar region against the Sommerfeld number in Figure 3-7.

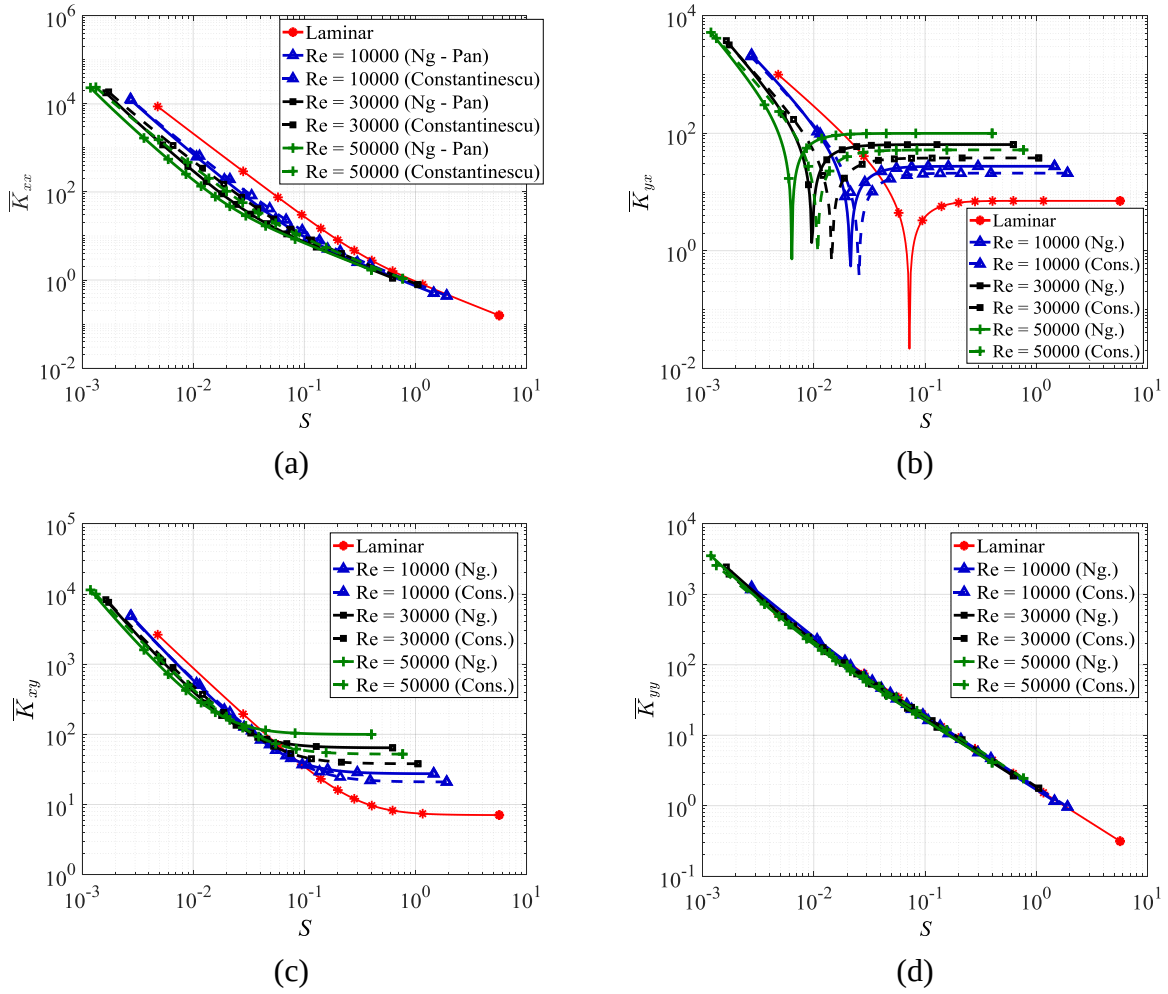

Figure 3-7. Comparison of the stiffness coefficients of a fully turbulent finite length journal bearing with the laminar (Reynolds independent) stiffness coefficients, $\overline{K}_{xx}$ (a), $\overline{K}_{yx}$ (b), $\overline{K}_{xy}$ (c) and $\overline{K}_{yy}$ (d).

Similar treatment was carried out to calculate the damping coefficients of turbulent journal bearings. The calculated bearing damping coefficients in turbulent flow are compared to the previously calculated coefficients in the laminar region and are plotted against the corresponding Sommerfeld number in Figure 3-8.

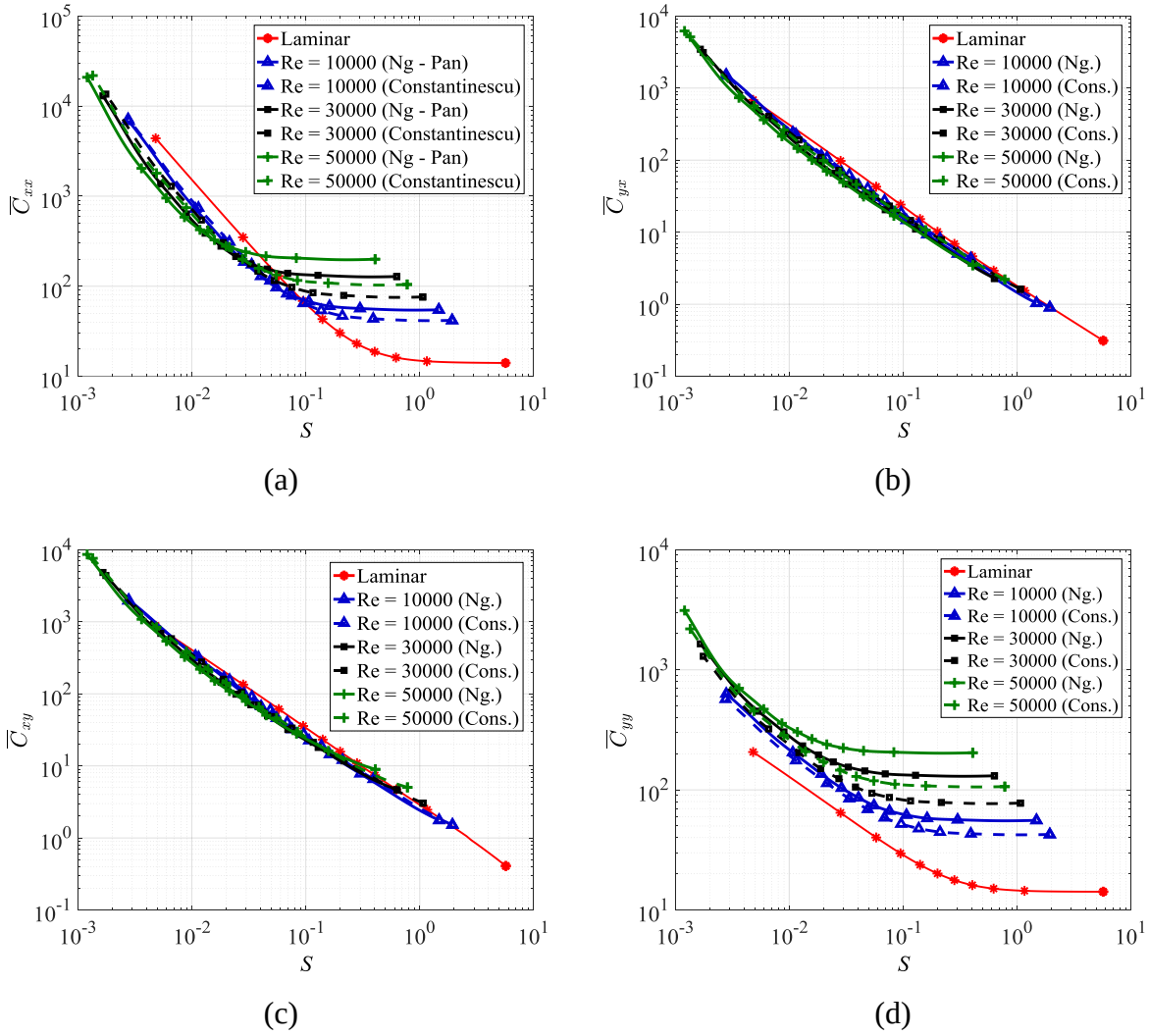

Figure 3-8. Comparison of the damping coefficients of a fully turbulent finite length journal bearing with the laminar (Reynolds independent) damping coefficients, $\overline{C}_{xx}$ (a), $\overline{C}_{yx}$ (b), $\overline{C}_{xy}$ (c) and $\overline{C}_{yy}$ (d).

By substituting laminar and turbulent coefficients obtained based on the two different turbulent models (as shown in Figure 3-7 and Figure 3-8) into Equations (3.22) to (3.24), one can obtain the stability margins of a flexible shaft supported by laminar and turbulent finite length journal bearings.

3.4.2 Identification of Threshold Speed of Instability

The non-dimensional threshold speed of instability $\overline{\omega}_{th}$ is calculated to find the corresponding stability parameter $\gamma = \frac{C K_s}{W} \overline{\omega}_{th}^2$ for laminar and turbulent bearings at a range of Reynolds numbers. The stability parameter γ is plotted against the Sommerfeld number for different non-dimensional

shaft stiffness parameter values, as shown in Figure 3-9. Stable and unstable regions are indicated in the Figure 3-9 (a).

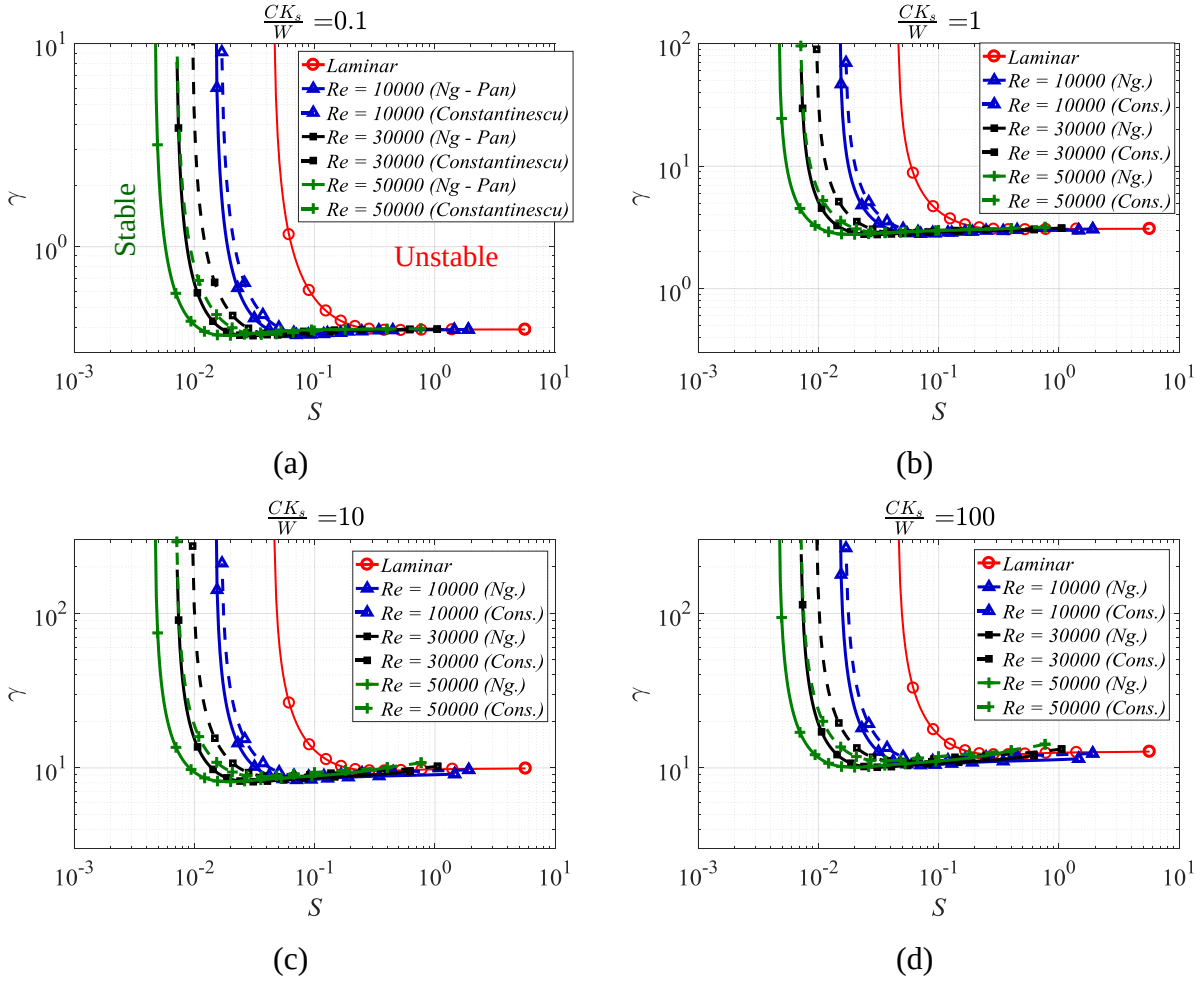

Figure 3-9. Linear stability curves of a flexible shaft supported on laminar and turbulent finite length journal bearings at ends against the Sommerfeld number for a range of non-dimensional shaft stiffness $CK_s/W = 0.1$ (a), $CK_s/W = 1$ (b), $CK_s/W = 10$ (c) and $CK_s/W = 100$ (d).

By comparing the stability of turbulent bearings to the laminar bearings and holding the non-dimensional shaft stiffness constant as in Figure 3-9 (a-d), it is clear that the turbulent curves are shifted to the left of the laminar curve for all of the shaft stiffness values, indicating that the unstable region expands at higher Reynolds numbers. The expanded unstable region due to turbulent bearings is in the low Sommerfeld $S \leq 0.05$ (high loading) region. This suggests that as the static loading increases on the shaft, the turbulent bearings become progressively less stable compared to the bearing which is operating in the laminar region of oil film flow. In the high Sommerfeld region $S \geq 0.2$ (low load), the stability curves of laminar and turbulent bearings are

very much alike. This destabilizing effect of turbulent bearings increases with the Reynolds number. At each Reynolds and at each non-dimensional shaft stiffness value, the stability curves of Constantinescu's turbulent model are positioned above the curves obtained based on the Ng-Pan Elrod turbulent model, suggesting that the Ng-Pan Elrod turbulent treatment is more conservative when used as a basis for design of the rotor-bearing system.

3.4.3 Rotor-Bearing System Trajectories

To illustrate the expansion of the unstable operating region and the shortcomings of the laminar theory in predicting the stable regions of the rotor-bearing system, the journal trajectories at different operating points should be calculated. To do this, the set of governing equations of motion for the journal and the shaft are to be numerically calculated to obtain the trajectory of the journal center. This is done first by transforming the linear ODE system of Equation (3.18) into a state-space representation of the form $\dot{\boldsymbol{X}} = f(\boldsymbol{X}, t)$ as follows:

$$\dot{X}_1 = \frac{C_{xy}\left(K_s X_2 - K_s X_4 + 2\ K_{yx} X_1 + 2\ K_{yy} X_2\right)}{2C_{xx}C_{yy} - 2C_{xy}C_{yx}} - \frac{C_{yy}\left(K_s X_1 - K_s X_3 + 2\ K_{xx} X_1 + 2\ K_{xy} X_2\right)}{2C_{xx}C_{yy} - 2C_{xy}C_{yx}}$$

$$\dot{X}_2 = \frac{C_{yx}\left(K_s X_1 - K_s X_3 + 2\ K_{xx} X_1 + 2\ K_{xy} X_2\right)}{2C_{xx}C_{yy} - 2C_{xy}C_{yx}} - \frac{C_{xx}\left(K_s X_2 - K_s X_4 + 2\ K_{yx} X_1 + 2\ K_{yy} X_2\right)}{2C_{xx}C_{yy} - 2C_{xy}C_{yx}} \qquad (3.25)$$

$$\dot{X}_3 = X_5\ ,\ \dot{X}_4 = X_6\ ,\ \dot{X}_5 = \frac{-K_s(X_3 - X_1)}{M}\ ,\ \dot{X}_6 = \frac{-K_s(X_4 - X_2)}{M}$$

where (X_1, X_2) and (X_3, X_4) are (x, y) position coordinates of the journal center and the mass disk center, respectively. The journal bearing coefficients in Equation (3.18) are time varying functions of the journal center (X_1, X_2). It shall be noted that trajectories can be solely obtained based on the linearized coefficients, provided that the journal position remains close to its steady state position. The system of Equations (3.25) can be used as a basis for calculation of the journal trajectories for much more complicated systems, provided that the dynamic coefficients are available (either previously calculated or experimentally obtained).

The system of coupled linear ODEs of Equation (3.25) is integrated numerically by an implicit scheme to obtain the trajectories of the journal and the disk center. When the journal force is expressed in terms of dynamic coefficients, the Jacobian of the linear ODE system can be easily

calculated and hence can be used effectively in an implicit time integration scheme. A first order Implicit Euler method is adopted here:

$$\dot{\boldsymbol{X}} = \frac{\boldsymbol{X}^{n+1} - \boldsymbol{X}^{n}}{\delta t} = \frac{\delta \boldsymbol{X}}{\delta t} = f^{n+1}(\boldsymbol{X}, t) \tag{3.26}$$

where superscripts *n* and *n+1* are to represent a variable value at the current and the next time-step, respectively. The next step is to express the right hand side of Eq. (3.26), $f^{n+1}(\boldsymbol{X}, t)$, in terms of the functions of the variable and its gradients at the current time-step, through a Taylor series expansion:

$$f^{n+1}(\boldsymbol{X}, t) = f(\boldsymbol{X}^{n+1}) = f(\boldsymbol{X}^{n} + \delta \boldsymbol{X}) = f(\boldsymbol{X}^{n}) + \left.\frac{\partial f}{\partial \boldsymbol{X}}\right|^{n} \delta \boldsymbol{X} + H.O.T \tag{3.27}$$

where $\left.\frac{\partial f}{\partial \boldsymbol{X}}\right|^{n}$ is the Jacobian matrix of the linear ODE system evaluated at the current time-step, taking the following form:

$$J(\boldsymbol{X}) = \frac{\partial f}{\partial \boldsymbol{X}} =$$

$$\begin{pmatrix} \frac{C_{yy}K_s + 2C_{yy}K_{xx} - 2C_{xy}K_{yx}}{2C_{xy}C_{yx} - 2C_{xx}C_{yy}} & \frac{2C_{yy}K_{xy} - \mathrm{Cxy}(K_s + 2K_{yy})}{2C_{xy}C_{yx} - 2C_{xx}C_{yy}} & \frac{C_{yy}K_s}{2C_{xx}C_{yy} - 2C_{xy}C_{yx}} & \frac{C_{xy}K_s}{2C_{xy}C_{yx} - 2C_{xx}C_{yy}} & 0 & 0 \\ \frac{C_{yx}(K_s + 2K_{xx}) - 2C_{xx}K_{yx}}{2C_{xx}C_{yy} - 2C_{xy}C_{yx}} & \frac{C_{xx}K_s - 2C_{yx}K_{xy} + 2C_{xx}K_{yy}}{2C_{xy}C_{yx} - 2C_{xx}C_{yy}} & \frac{C_{yx}K_s}{2C_{xy}C_{yx} - 2C_{xx}C_{yy}} & \frac{C_{xx}K_s}{2C_{xx}C_{yy} - 2C_{xy}C_{yx}} & 0 & 0 \\ 0 & 0 & 0 & 0 & 1 & 0 \\ 0 & 0 & 0 & 0 & 0 & 1 \\ \frac{K_s}{M} & 0 & -\frac{K_s}{M} & 0 & 0 & 0 \\ 0 & \frac{K_s}{M} & 0 & -\frac{K_s}{M} & 0 & 0 \end{pmatrix} \tag{3.28}$$

Having the Jacobian matrix of the system, we can write the system of coupled linear ODEs as:

$$\dot{\boldsymbol{X}} = \frac{\delta \boldsymbol{X}}{\delta t} \cong f(\boldsymbol{X}^{n}) + J(x)\delta \boldsymbol{X} \tag{3.29}$$

the change in solution $\delta \boldsymbol{X}$ can now be found via solving a linear system such that:

$$\left(\frac{I}{\delta t} - J(\boldsymbol{x})\right)\delta \boldsymbol{X} = f(\boldsymbol{X}^{n}) \tag{3.30}$$

where $I, \delta \boldsymbol{X}$ and $f(\boldsymbol{X}^n)$ are $N \times 1$ matrices and $J(\boldsymbol{X})$ is a $N \times N$ matrix for a coupled system of N ordinary differential equations of first order. A direct solve of the linear system of Eq. (3.30) by Gaussian elimination will yield the change in solution $\delta \boldsymbol{X}$ from time-step n to $n+1$. The calculated change in solution can then be used as a basis for first order or second order accurate implicit time integration schemes. The major benefit of implicit schemes is that their stability has minor to negligible sensitivity to chosen time steps and are therefore ideal for studying stiff dynamical systems as in the case of journal bearing supported shafts. As was explained above, a key step in implicit calculations is finding the Jacobian matrix at each time step, which is inherently efficient if the Jacobian matrix can be found explicitly as in Eq. (3.28).

Non-dimensional journal trajectories in laminar and turbulent conditions, plot of $\bar{X}_{journal}$ vs $\bar{Y}_{journal}$ $\left(\bar{X} = \frac{X}{C}\right)$, at three different operating points were calculated by means of the detailed implicit time integration method of Equations (3.25) to (3.30). The turbulent journal trajectory was based on the Ng-Pan Elrod model at $Re = 10000$. The selected operating points (marked with circles) and calculated trajectories are shown in Figure 3-10.

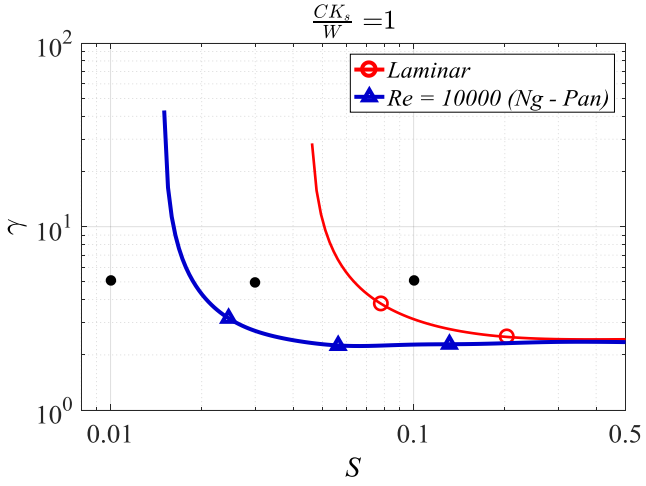

(a)

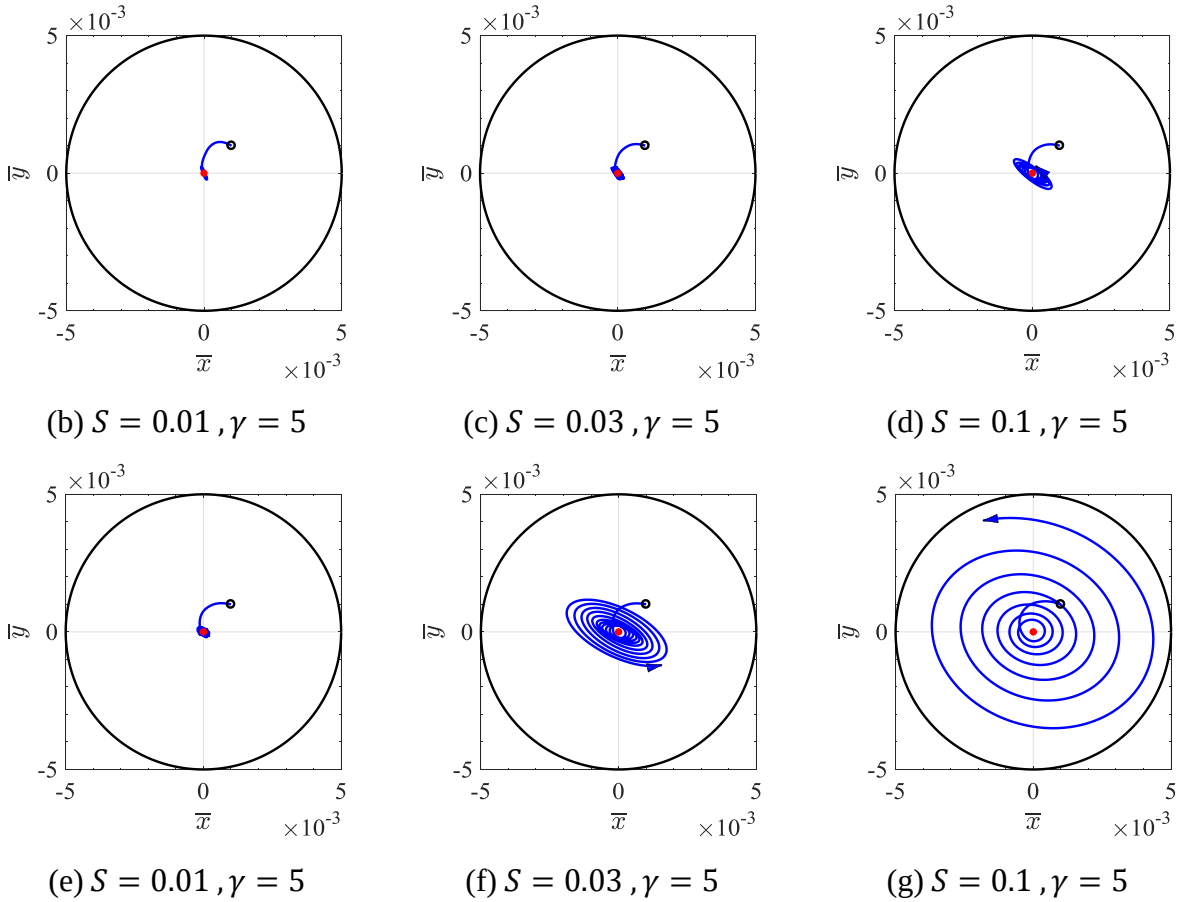

Figure 3-10. Journal bearing trajectory at three operating points (stars in (a)) under laminar (b, c and d) and turbulent (e, f and g) regimes of flow.

For all cases shown in Figure 3-10, the journal center is released from a point very close to its steady state point (within the radius of 0.1% of the journal clearance around the steady state point), and its trajectory is followed in time. The first operating point is selected such that it lies in the stable region of both laminar and turbulent curves at $S = 0.01\,, \gamma = 5$. Similar results were obtained where the journal finds its steady state point and remains there, Figure 3-10(b) and (e). The next operating point $S = 0.03\,, \gamma = 5$ lies between the laminar and turbulent curves. As expected, the laminar based trajectories, Figure 3-10(c), can still find the steady state point while the turbulent based trajectories, Figure 3-10(f), start to grow and hence become unstable. This again indicates that stable regions obtained based on the laminar theory can become unstable at higher Reynolds numbers. Both laminar and turbulent trajectories grow in the third selected operating point of $S = 0.1\,, \gamma = 5$ though with different speeds, as shown in Figure 3-10(d) and (g).

Chapter 4: Nonlinear Dynamics of a Rotor-Bearing System using an Analytical Bearing Model

To test the proposed hypothesis, a nonlinear coefficient based method for representing the bearing force is presented in this chapter as a versatile technique for characterizing the bearing force in a rotor-bearing system. Linear and nonlinear dynamic coefficients of a journal bearing are calculated in different coordinates with a systematic approach that can be applied to both short and long journal bearings. A flexible rotor-bearing system is presented for which bearing force is modeled with linear and nonlinear dynamic coefficients. A Hopf bifurcation analysis is then carried out to determine whether the proposed model can be used for characterizing the bifurcations in the system.

4.1 Nonlinear Bearing Model with Dynamic Coefficients

Figure 4-1 shows the adopted coordinate system for a journal bearing inside the bearing clearance.

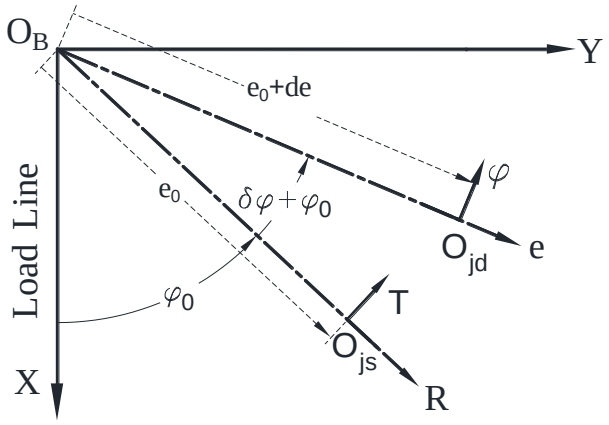

Figure 4-1. the adopted coordinate systems for a journal in bearing clearance

The geometric center of the bearing is represented by O_B in Figure 4-1 and is chosen as the center of the Fixed and inertial *X*-*Y* coordinate system. At steady state and under static equilibrium, the weight of the rotor and journal is in balance with the bearing force such that $\boldsymbol{F} + \boldsymbol{W} = 0$. The steady state position is marked as O_{J_S} with the associated eccentricity of e_0, and the attitude angle

of φ_0. The components of the lubricant force along the fixed directions *(R, T)*, are F_R and F_T. If the journal is perturbed around its resting point (for instance due to a small imbalance force), at a particular instant it will occupy position O_J. At this instant, the eccentricity is $e = e_0 + \delta e$, and the attitude angle is $\varphi = \varphi_0 + \delta\varphi$, with journal instantaneous velocities $\dot{e}$ and $e\,\dot{\varphi}$. The instantaneous lubricant force now has components F_ϵ and F_φ, relative to the instantaneous radial and tangential coordinates ϵ and φ, respectively. A $\delta\varphi$ clockwise rotation can be used to express the instantaneous forces in the Fixed *R-T* coordinate system:

$$\begin{pmatrix} F_R \\ F_T \end{pmatrix} = \begin{pmatrix} \cos\delta\varphi & -\sin\delta\varphi \\ \sin\delta\varphi & \cos\delta\varphi \end{pmatrix} \begin{pmatrix} F_\epsilon \\ F_\varphi \end{pmatrix} \tag{4.1}$$

assuming $\delta\varphi$ is small:

$$\cos\delta\varphi \approx \left(1 - \frac{\delta\varphi^2}{2}\right) \text{ and } \sin\delta\varphi \approx \left(\delta\varphi - \frac{\delta\varphi^3}{6}\right) \tag{4.2}$$

The total change in the radial force component ΔF_R in excess of its equilibrium value F_{R0} can now be written as:

$$\Delta F_R = F_\epsilon \left(1 - \frac{\delta\varphi^2}{2}\right) - F_\varphi \left(\delta\varphi - \frac{\delta\varphi^3}{6}\right) - F_{\epsilon 0}\,, \tag{4.3}$$

And similarly for the change in the tangential force component in excess of its equilibrium value F_{T0} we have: $\Delta F_T = F_T - F_{\varphi 0}$. Note that the steady state value of the instantaneous force components $F_{\epsilon 0}$ and $F_{\varphi 0}$ is essentially F_{R0} and F_{T0}, respectively. A Taylor expansion of the scalar force component functions F_ξ, $\xi = \epsilon, \varphi$ about the equilibrium point up to the third order can be written as:

$$\begin{aligned} F_\xi \cong F_{\xi 0} + \sum_{i=1}^{4} \frac{\partial F_\xi}{\partial q_i}\delta q_i + \frac{1}{2}\sum_{i,j=1}^{4} \frac{\partial^2 F_\xi}{\partial q_i \partial q_j}\delta q_i \delta q_j \\ + \frac{1}{6}\sum_{i,j,k=1}^{4} \frac{\partial^3 F_\xi}{\partial q_i \partial q_j \partial q_k}\delta q_i \delta q_j \delta q_k \end{aligned} \tag{4.4}$$

with $q_1 = e, q_2 = \varphi, q_3 = \dot{e}$ and $q_4 = \dot{\varphi}$. All the derivatives in Eq. (4.4) are evaluated at the steady state point where $\dot{e} = \dot{\varphi} = 0$. It is customary to write the change in force due to the perturbation, $\Delta F_\eta\ , \eta = r, t$, in the form of stiffness and damping dynamic coefficients such that:

$$\begin{aligned}\Delta F_\eta = {} & K_{\eta r}\delta e + K_{\eta t}\delta\varphi + C_{\eta r}\delta\dot{e} + C_{\eta t}\delta\dot{\varphi} + K_{\eta rr}\delta e^2 + K_{\eta tt}\delta\varphi^2 + K_{\eta rt}\delta e\delta\varphi \\ & + C_{\eta rr}\delta\dot{e}\delta e + C_{\eta rt}\delta\dot{e}\delta\varphi + C_{\eta tr}\delta\dot{\varphi}\delta e + C_{\eta tt}\delta\dot{\varphi}\delta\varphi + K_{\eta rrr}\delta e^3 \\ & + K_{\eta ttt}\delta\varphi^3 + K_{\eta rtt}\delta e\delta\varphi^2 + K_{\eta trr}\delta e^2\delta\varphi + C_{\eta rrr}\delta\dot{e}\delta e^2 \\ & + C_{\eta ttt}\delta\dot{\varphi}\delta\varphi^2 + C_{\eta rtt}\delta\dot{e}\delta\varphi^2 + C_{\eta trr}\delta\dot{\varphi}\delta e^2\end{aligned} \tag{4.5}$$

The dynamic coefficients in the *R-T* coordinate system can be found by substituting Eq. (4.4) back into Eq. (4.3) and conducting a one-to-one comparison to the form of Eq. (4.5).

4.2 Bearing Dynamic Coefficients in the *R-T* Coordinate System

The non-dimensional induced forces of a short journal bearing for a fully cavitated π-film (Gumbel Boundary Condition) bearing are given in the literature [25] as:

$$\begin{aligned} f_\epsilon &= \left(\frac{L}{D}\right)^2\left(1-\frac{2\dot{\varphi}}{\omega}\right)\left(-\frac{2\pi^2(2\epsilon^2+1)\dot{\epsilon}}{\omega(1-\epsilon^2)^{5/2}\left(1-\frac{2\dot{\varphi}}{\omega}\right)}-\frac{4\pi\epsilon^2}{(1-\epsilon^2)^2}\right) \\ f_\varphi &= \left(\frac{L}{D}\right)^2\left(1-\frac{2\dot{\varphi}}{\omega}\right)\left(\frac{\pi^2\epsilon}{(1-\epsilon^2)^{3/2}}+\frac{8\pi\epsilon\dot{\epsilon}}{\omega(1-\epsilon^2)^2\left(1-\frac{2\dot{\varphi}}{\omega}\right)}\right)\end{aligned} \tag{4.6}$$

where the non-dimensional forces and dynamic coefficients are related such that:

$$\begin{aligned} & f = \frac{F}{\Pi}, \bar{K}_{ij} = \frac{C}{\Pi}\,K_{ij}\ , \bar{C}_{ij} = \frac{C\,\omega}{\Pi}\,C_{ij}\ , \bar{K}_{ijk} = \frac{C^2}{\Pi}\,K_{ijk}\ , \bar{C}_{ij} = \frac{C^2\,\omega}{\Pi}\,C_{ij}\ , \bar{K}_{ijkl} = \\ & \frac{C^3}{\Pi}\,K_{ijkl}\ , \bar{C}_{ijkl} = \frac{C^3\,\omega}{\Pi}\,C_{ijkl} \text{ with } \Pi = L\,D\,\mu\,N\left(\frac{R}{C}\right)^2\end{aligned} \tag{4.7}$$

It shall be noted that since the dynamic bearing forces for both short and long journal bearings (for which an analytical expression exists) are not explicit functions of higher powers of $\dot{e}$ and $\dot{\varphi}$, therefore $\frac{\partial^2 F_\epsilon}{\partial\dot{e}^2} = \frac{\partial^2 F_\epsilon}{\partial\dot{\varphi}^2} = \frac{\partial^2 F_\epsilon}{\partial\dot{e}\partial\dot{\varphi}} = \frac{\partial^2 F_\varphi}{\partial\dot{e}^2} = \frac{\partial^2 F_\varphi}{\partial\dot{\varphi}^2} = \frac{\partial^2 F_\varphi}{\partial\dot{e}\partial\dot{\varphi}} = 0$ (similarly for third order terms), and the corresponding dynamic coefficients are zero and are omitted from the form given in Eq. (4.5).

The non-dimensional linear and nonlinear (second order) bearing dynamic coefficients are calculated and given in Table 4-1, Table 4-2 and Table 4-3. The third order coefficients are calculated in a similar fashion.

Table 4-1. Linear dynamic coefficients in R-T coordinate

Linear Stiffness Coefficients	General Form	Short Bearing (π film)	Linear Damping Coefficients	General Form	Short Bearing (π film)
$\bar{K}_{rr}$	$\frac{\partial f_\epsilon}{\partial \epsilon}$	$\left(\frac{L}{D}\right)^2 \frac{-8\pi\epsilon(\epsilon^2+1)}{(1-\epsilon^2)^3}$	$\bar{C}_{rr}$	$\omega \frac{\partial f_\epsilon}{\partial \dot{\epsilon}}$	$\left(\frac{L}{D}\right)^2 \frac{-2\pi^2(2\epsilon^2+1)}{(1-\epsilon^2)^{5/2}}$
$\bar{K}_{rt}$	$\frac{1}{\epsilon}\left(-f_{\varphi 0}+\frac{\partial f_\epsilon}{\partial \varphi}\right)$	$\left(\frac{L}{D}\right)^2 \frac{-\pi^2}{(1-\epsilon^2)^{3/2}}$	$\bar{C}_{rt}$	$\frac{\omega}{\epsilon}\frac{\partial f_\epsilon}{\partial \dot{\varphi}}$	$\left(\frac{L}{D}\right)^2 \frac{8\pi\epsilon}{(1-\epsilon^2)^2}$
$\bar{K}_{tr}$	$\frac{\partial f_\varphi}{\partial \epsilon}$	$\left(\frac{L}{D}\right)^2 \frac{\pi^2(2\epsilon^2+1)}{(1-\epsilon^2)^{5/2}}$	$\bar{C}_{tr}$	$\omega \frac{\partial f_\varphi}{\partial \dot{\epsilon}}$	$\left(\frac{L}{D}\right)^2 \frac{8\pi\epsilon}{(1-\epsilon^2)^2}$
$\bar{K}_{tt}$	$\frac{1}{\epsilon}\left(f_{\epsilon 0}+\frac{\partial f_\varphi}{\partial \varphi}\right)$	$\left(\frac{L}{D}\right)^2 \frac{-4\pi\epsilon}{(1-\epsilon^2)^2}$	$\bar{C}_{tt}$	$\frac{\omega}{\epsilon}\frac{\partial f_\varphi}{\partial \dot{\varphi}}$	$\left(\frac{L}{D}\right)^2 \frac{-2\pi^2}{(1-\epsilon^2)^{3/2}}$

Table 4-2. Nonlinear (second order) stiffness coefficients in R-T

Nonlinear Stiffness Coefficients	General Form	Short Bearing (π film)
$\bar{K}_{rrr}$	$\frac{1}{2}\frac{\partial^2 f_\epsilon}{\partial \epsilon^2}$	$\left(\frac{L}{D}\right)^2 \frac{-4\pi(3\epsilon^4+8\epsilon^2+1)}{(1-\epsilon^2)^4}$
$\bar{K}_{trr}$	$\frac{1}{2}\frac{\partial^2 f_\varphi}{\partial \epsilon^2}$	$\left(\frac{L}{D}\right)^2 \frac{3\pi^2\epsilon(2\epsilon^2+3)}{2(1-\epsilon^2)^{7/2}}$
$\bar{K}_{rtt}$	$\frac{1}{2\epsilon^2}\left(-f_{\epsilon 0}-2\frac{\partial f_\varphi}{\partial \varphi}+\frac{\partial^2 f_\epsilon}{\partial \varphi^2}\right)$	$\left(\frac{L}{D}\right)^2 \frac{2\pi}{(1-\epsilon^2)^2}$
$\bar{K}_{ttt}$	$\frac{1}{2\epsilon^2}\left(-f_{\varphi 0}+2\frac{\partial f_\epsilon}{\partial \varphi}+\frac{\partial^2 f_\varphi}{\partial \varphi^2}\right)$	$\left(\frac{L}{D}\right)^2 \frac{-\pi^2}{2\epsilon(1-\epsilon^2)^{3/2}}$
$\bar{K}_{rrt}$	$\frac{1}{\epsilon}\left(-\frac{\partial f_\varphi}{\partial \epsilon}+\frac{\partial^2 f_\epsilon}{\partial \epsilon \partial \varphi}\right)$	$\left(\frac{L}{D}\right)^2 \frac{-\pi^2(2\epsilon^2+1)}{\epsilon(1-\epsilon^2)^{5/2}}$
$\bar{K}_{trt}$	$\frac{1}{\epsilon}\left(\frac{\partial f_\epsilon}{\partial \epsilon}+\frac{\partial^2 f_\varphi}{\partial \epsilon \partial \varphi}\right)$	$\left(\frac{L}{D}\right)^2 \frac{-8\pi(\epsilon^2+1)}{(1-\epsilon^2)^3}$

Table 4-3. Nonlinear (second order) damping coefficients in R-T

Nonlinear Damping Coefficients	General Form	Short Bearing (π film)
$\bar{C}_{rrr}$	$\omega \frac{\partial^2 f_\epsilon}{\partial \dot{\epsilon} \partial \epsilon}$	$\left(\frac{L}{D}\right)^2 \frac{-6\pi^2 \epsilon (2\epsilon^2+3)}{(1-\epsilon^2)^{7/2}}$
$\bar{C}_{trr}$	$\omega \frac{\partial^2 f_\varphi}{\partial \dot{\epsilon} \partial \epsilon}$	$\left(\frac{L}{D}\right)^2 \frac{8\pi(3\epsilon^2+1)}{(1-\epsilon^2)^3}$
$\bar{C}_{rtt}$	$\frac{\omega}{\epsilon^2}\left(-\frac{\partial f_\varphi}{\partial \dot{\varphi}} + \frac{\partial^2 f_\epsilon}{\partial \dot{\varphi} \partial \varphi}\right)$	$\left(\frac{L}{D}\right)^2 \frac{2\pi^2}{\epsilon(1-\epsilon^2)^{3/2}}$
$\bar{C}_{ttt}$	$\frac{\omega}{\epsilon^2}\left(\frac{\partial f_\epsilon}{\partial \dot{\varphi}} + \frac{\partial^2 f_\varphi}{\partial \dot{\varphi} \partial \varphi}\right)$	$\left(\frac{L}{D}\right)^2 \frac{8\pi}{(1-\epsilon^2)^2}$
$\bar{C}_{rrt}$	$\frac{\omega}{\epsilon}\left(-\frac{\partial f_\varphi}{\partial \dot{\epsilon}} + \frac{\partial^2 f_\epsilon}{\partial \dot{\epsilon} \partial \varphi}\right)$	$\left(\frac{L}{D}\right)^2 \frac{-8\pi}{(1-\epsilon^2)^2}$
$\bar{C}_{trt}$	$\frac{\omega}{\epsilon}\left(\frac{\partial f_\epsilon}{\partial \dot{\epsilon}} + \frac{\partial^2 f_\varphi}{\partial \dot{\epsilon} \partial \varphi}\right)$	$\left(\frac{L}{D}\right)^2 \frac{-2\pi^2(2\epsilon^2+1)}{\epsilon(1-\epsilon^2)^{5/2}}$
$\bar{C}_{rtr}$	$\omega \frac{\partial^2 f_\epsilon}{\partial \dot{\varphi} \partial \epsilon}$	$\left(\frac{L}{D}\right)^2 \frac{16\pi(\epsilon^2+1)}{(1-\epsilon^2)^3}$
$\bar{C}_{ttr}$	$\omega \frac{\partial^2 f_\varphi}{\partial \dot{\varphi} \partial \epsilon}$	$\left(\frac{L}{D}\right)^2 \frac{-2\pi^2(2\epsilon^2+1)}{\epsilon(1-\epsilon^2)^{5/2}}$

4.3 Bearing Dynamic Coefficients in the *X-Y* Coordinate System

Once the linear coefficients are calculated in the *R-T* coordinate, a simple coordinate transformation can transfer them to any rotated frame of reference through a simple rotation transformation. For instance, the following clockwise transformation will yield the dynamic coefficients in the fixed *X-Y* coordinate of Figure 3-1:

$$Q_0 = \begin{pmatrix} \cos\varphi_0 & -\sin\varphi_0 \\ \sin\varphi_0 & \cos\varphi_0 \end{pmatrix}, \; [\bar{K}]_{xy} = -Q_0 [\bar{K}]_{RT} {Q_0}^T \, , [\bar{C}]_{xy} = -Q_0 [\bar{C}]_{RT} {Q_0}^T \tag{4.8}$$

where $[\bar{K}]_{RT}$ and $[\bar{C}]_{RT}$ are linear stiffness and damping matrices in the *R-T* coordinate system. Although such transformation is easily carried out for linear dynamic coefficients, the nonlinear coefficients cannot be transformed in a similar fashion and therefore an alternative approach is

needed to calculate the nonlinear dynamic coefficients for any desired rotated frame of reference. To do this, the following counter-clockwise transformation is adopted here:

$$\begin{pmatrix} \delta e \\ e_0 \delta\varphi \end{pmatrix} = Q \begin{pmatrix} \delta x \\ \delta y \end{pmatrix} \text{ and } \begin{pmatrix} \delta \dot{e} \\ e_0 \delta\dot{\varphi} \end{pmatrix} = Q \begin{pmatrix} \delta \dot{x} \\ \delta \dot{y} \end{pmatrix} \text{ where } Q = \begin{pmatrix} \cos\varphi & \sin\varphi \\ -\sin\varphi & \cos\varphi \end{pmatrix} \tag{4.9}$$

Note that the angle of rotation in Eq. (4.9) is the instantaneous position angle φ. At this point, change in the bearing forces in excess of the equilibrium can be written in the *X*-*Y* coordinate, analogous to the *R*-*T* coordinate expression of Eq. (4.5), such that:

$$\begin{aligned} \Delta F_\zeta = {} & K_{\zeta x}\delta x + K_{\zeta y}\delta y + C_{\zeta x}\delta\dot{x} + C_{\zeta y}\delta\dot{y} + K_{\zeta xx}\delta x^2 + K_{\zeta yy}\delta y^2 + K_{\zeta xy}\delta x\delta y \\ & + C_{\zeta xx}\delta\dot{x}\delta x + C_{\zeta xy}\delta\dot{x}\delta y + C_{\zeta yx}\delta\dot{y}\delta x + C_{\zeta yy}\delta\dot{y}\delta y + K_{\zeta xxx}\delta x^3 \\ & + K_{\zeta yyy}\delta y^3 + K_{\zeta xyy}\delta x\delta y^2 + K_{\zeta yxx}\delta x^2\delta y + C_{\zeta xxx}\delta\dot{x}\delta x^2 \\ & + C_{\zeta yyy}\delta\dot{y}\delta y^2 + C_{\zeta xyy}\delta\dot{x}\delta y^2 + C_{\zeta yxx}\delta\dot{y}\delta x^2 \end{aligned} \tag{4.10}$$

where $\zeta = x, y$. Substituting Eq. (4.9) back into the Equations (4.4) and (4.3) and conducting a one to one comparison with Eq. (4.10) will yield the dynamic coefficients in the *X*-*Y* coordinate system.

4.4 Mathematical Model of the Rotor-Bearing System

The simplified rotor-bearing system consists of a flexible, center-loaded rotor that is symmetrically supported by two identical fluid-film journal bearings. The schematic of the rotor-bearing system is given in Figure 3-6. The equations of motion for the central disk and journal bearings can be written as follows:

$$\begin{aligned} Central\ Disk: & \begin{cases} M\ddot{x}_2 + K_s(x_2 - x_1) = +m_u R_u \omega^2 \cos\omega t \\ M\ddot{y}_2 + K_s(y_2 - y_1) = +m_u R_u \omega^2 \sin\omega t \end{cases}, \\ Journal\ Bearings: & \begin{cases} -2\Delta F_x + K_s(x_2 - x_1) = 0 \\ -2\Delta F_y + K_s(y_2 - y_1) = 0 \end{cases} \end{aligned} \tag{4.11}$$

where x and y are components of the journal displacement vector $\boldsymbol{x}$, K_s is the shaft stiffness, M is the total mass of the fully balanced rotor-bearing system, m_u is the unbalance mass at the disc location, R_u is the unbalance mass eccentricity radius, and ΔF_x and ΔF_y are the components of the

force due to induced bearing pressure in excess of the equilibrium forces and are calculated based on Eq. (4.10). The equations of motion of Eq. (4.11) can be non-dimensionalized through the following non-dimensional variables:

$$\boldsymbol{X} = \frac{\boldsymbol{x}}{C}, \tau = \omega t\,, \bar{\omega} = \omega\sqrt{M/K_s}\,, \bar{R}_u = \frac{R_u}{C}\,, \bar{m}_u = \frac{m_u}{M}\,, \bar{k}_s = \frac{C}{L\,D\,\mu\,N\left(\frac{R}{C}\right)^2}\,K_s \tag{4.12}$$

The non-dimensional equations of motion in the state-space form can be written as:

$$\begin{cases} -2\delta f_x + \bar{k}_s(X_3 - X_1) = 0 \\ -2\delta f_y + \bar{k}_s(X_4 - X_2) = 0 \\ \dot{X}_3 = X_5 \\ \dot{X}_4 = X_6 \\ \bar{\omega}^2\dot{X}_5 + (X_3 - X_1) = +\,\bar{m}_u\,\bar{R}_u\,\bar{\omega}^2\cos\tau \\ \bar{\omega}^2\dot{X}_6 + (X_4 - X_2) = +\,\bar{m}_u\,\bar{R}_u\,\bar{\omega}^2\sin\tau \end{cases} \tag{4.13}$$

where (X_1, X_2) and (X_3, X_4) are (x, y) coordinates of the journal center and the mass disk center position, respectively, and $\delta f_\zeta\,, \zeta = x, y$ is the non-dimensional journal bearing force components vector in excess of the equilibrium journal force and is expressed such that:

$$\begin{aligned} \delta f_\zeta = {} & \bar{K}_{\zeta x}\delta X_1 + \bar{K}_{\zeta y}\delta X_2 + \bar{C}_{\zeta x}\dot{X}_1 + \bar{C}_{\zeta y}\dot{X}_2 + \bar{K}_{\zeta xx}\delta {X_1}^2 + \bar{K}_{\zeta yy}\delta {X_2}^2 \\ & + \bar{K}_{\zeta xy}\delta X_1\delta X_2 + \bar{C}_{\zeta xx}\dot{X}_1\delta X_1 + \bar{C}_{\zeta xy}\dot{X}_1\delta X_2 + \bar{C}_{\zeta yx}\dot{X}_2\delta X_1 \\ & + \bar{C}_{\zeta yy}\dot{X}_2\delta X_2 + \bar{K}_{\zeta xxx}\delta {X_1}^3 + \bar{K}_{\zeta yyy}\delta {X_2}^3 + \bar{K}_{\zeta xyy}\delta X_1\delta {X_2}^2 \\ & + \bar{K}_{\zeta yxx}\delta {X_1}^2\delta X_2 + \bar{C}_{\zeta xxx}\dot{X}_1\delta {X_2}^2 + \bar{C}_{\zeta yyy}\dot{X}_2\delta {X_2}^2 \\ & + \bar{C}_{\zeta xyy}\dot{X}_1\delta {X_2}^2 + \bar{C}_{\zeta yxx}\dot{X}_2\delta {X_1}^2 \end{aligned} \tag{4.14}$$

where δX_1 and δX_2 are the position of the journal center in excess of the equilibrium position and $\dot{X}_1$and $\dot{X}_2$ are instantaneous journal center velocities. Non-dimensional equations of motion of Eq. (4.13) may now be used to study the stability of the rotor-bearing system as well as its dynamical response at any operating point of the system.

4.5 Nonlinear Stability Analysis of the Flexible Rotor-Bearing System

4.5.1 Application of the Hopf Bifurcation Theory in Stability Analysis

The term Hopf bifurcation refers to the local birth or death of a periodic solution (self-excited oscillation) from an equilibrium state, as a parameter crosses a critical value [108, 109]. In an autonomous system of ordinary differential equations $\dot{\boldsymbol{X}} = \boldsymbol{f}(\boldsymbol{X}, \nu)$, a Hopf bifurcation occurs when the system of equations has an isolated stationary point (fixed point or steady state of the system) $\boldsymbol{X} = \boldsymbol{X}^*$ such that $\boldsymbol{f}(\boldsymbol{X}^*, \nu) = 0$, and the Jacobian matrix of the system of equations defined as:

$$\boldsymbol{J}(\nu) = \frac{\partial \boldsymbol{f}}{\partial \boldsymbol{X}}(\boldsymbol{X}^*, \nu) \tag{4.15}$$

has a pair of complex conjugate eigenvalues $\lambda_{1,2} = A(\nu) \pm i\boldsymbol{B}(\nu)$ such that at a critical parameter value $\nu = \nu_c$ the complex pair becomes purely imaginary:

$$\boldsymbol{B}(\nu_c) > 0\ ,\ A(\nu_c) = 0 \text{ and } A'(\nu_c) \neq 0 \tag{4.16}$$

As a result, there is a loss of linear stability of the fixed point $\boldsymbol{X}^*$ as ν crosses ν_c and provided that the remaining eigenvalues of $\boldsymbol{J}(\nu_c)$ have strictly negative real parts, the system will have a family of periodic solutions (i.e. *limit cycle*) $P_\varepsilon(t)$ for $0 < \varepsilon < \varepsilon_H$. The amplitude of the limit cycle is proportional to $(\nu - \nu_c)^{\frac{1}{2}}$ and the system parameter is given by a C^{L+1}function of ε [110]:

$$\nu^H(\varepsilon) = \sum_{i=1}^{\frac{OL}{2}} \nu_{2i}\varepsilon^{2i} \text{ for } 0 < \varepsilon < \varepsilon_H \tag{4.17}$$

where *OL* is the order of the system of ordinary differential equations. Exactly two of the *Floquet (characteristic) exponents* of $P_\varepsilon(t)$ approach 0 as $\varepsilon \to 0$. One of them is zero and the other one is a C^{L+1} function:

$$\mu^H(\varepsilon) = \sum_{i=1}^{\frac{OL}{2}} \mu_{2i}\varepsilon^{2i} \text{ for } 0 < \varepsilon < \varepsilon_H \tag{4.18}$$

The periodic solution is orbitally asymptotically stable with asymptotic phase if $\mu^H < 0$ and is unstable for $\mu^H > 0$. The role of characteristic exponents of the periodic solution in assessing limit cycle stability is given by the *Floquet* theorem.

4.5.2 Floquet Theorem

For the system of equations of the form $\dot{\mathbf{X}} = \boldsymbol{A}(t)\,\mathbf{X}$ where $\boldsymbol{A}(t)$ is periodic with period *T*, then x need not be periodic, however it must be of the form:

$$\boldsymbol{X}(t) = e^{\mu T}\boldsymbol{P}(t) \tag{4.19}$$

where $\boldsymbol{P}(t)$ is *T*-periodic.

A fundamental solution matrix for the set of ordinary differential equations $\dot{\mathbf{X}} = \boldsymbol{A}(t)\,\mathbf{X}$ can be obtained by

$$\boldsymbol{\Phi}(t) = \begin{bmatrix}\begin{bmatrix} X^1 \end{bmatrix} & \ldots & \begin{bmatrix} X^n \end{bmatrix}\end{bmatrix} \tag{4.20}$$

where $X^1 \ldots X^n$ are a set of *n* linearly independent solutions of $\dot{\mathbf{X}} = \boldsymbol{A}(t)\,\mathbf{X}$ and thus the fundamental solution satisfies:

$$\dot{\boldsymbol{\Phi}} = \boldsymbol{A}(t)\,\boldsymbol{\Phi} \tag{4.21}$$

Now, if $\boldsymbol{\Phi}(t)$ is a fundamental solution, then it easily follows that $\boldsymbol{\Phi}(t+T)$ is also a fundamental solution. Hence, there exists a constant nonsingular matrix $\boldsymbol{M}$ such that:

$$\boldsymbol{\Phi}(t+T) \;=\; \boldsymbol{\Phi}(t)\boldsymbol{M} \;\text{ with } det(\boldsymbol{M}) = exp\left(\int_0^T tr(\boldsymbol{A}(t))dt\right) \tag{4.22}$$

The eigenvalues $\rho_1, \ldots, \rho_n$ of $\boldsymbol{M}$ are called the *characteristic multipliers* for $\dot{\mathbf{X}} = \boldsymbol{A}(t)\,\mathbf{X}$. The *characteristic exponents* or *Floquet exponents* are $\mu_1, \ldots, \mu_n$ satisfying:

$$\rho_1 = e^{\mu_1 T}, \rho_2 = e^{\mu_2 T}, \ldots \rho_n = e^{\mu_n T} \tag{4.23}$$

The entire solution is stable if all the characteristic multipliers satisfy $|\rho_j| \leq 1$. $\boldsymbol{M} = \boldsymbol{\Phi}(T)$ can be obtained by generating a set of *n* linearly independent solutions to form $\boldsymbol{\Phi}(t)$. Except for special cases, this is generally difficult and a numerical perturbation method is needed to find an approximate solution to the periodic orbit before performing a numerical differentiation to obtain $\boldsymbol{\Phi}(T)$.

4.5.3 Limit Cycle Stability

In terms of stability, the fixed point $\boldsymbol{X}^*$ is a stable *spiral* for $\nu < \nu_c$ and becomes an unstable spiral with phase-plane orbits spiraling out: after the system parameter ν crosses the critical value ν_c. But this change of stability is a local change and the global behavior of the solution sufficiently far from the fixed point can be qualitatively unaffected to this change of stability. If the nonlinearity makes the far flow contracting then orbits will still be coming in and we expect a periodic orbit, a limit cycle, to appear where the near and far flow find a balance. If the periodic solution is stable, it will replace the unstable stationary solution as the long-term behavior of the system. In this case, for almost all initial conditions in the neighborhood of the unstable stationary solution, the system will settle in a controlled state of motion: a stable limit cycle and in the case of rotor-bearing stability, stable and low amplitude whirling of the rotor. It is then said that the system has undergone a *supercritical Hopf bifurcation*. However, if the periodic solution is unstable, solutions that used to remain near the origin are now forced to grow into large-amplitude oscillations and the system is said to have undergone a *subcritical bifurcation*. In this case, there are unstable periodic solutions coexisting with the stationary state even before crossing the critical system parameter ν_c. These unstable solutions represent a mechanism which certain small but finite amplitude perturbations from the stationary solution may grow to high amplitude vibrations at a domain that linear stability analysis has identified as "stable". Subcritical bifurcations are hazardous for the safe operation of majority of systems and are to be identified and avoided, if possible.

Assessing the stability of the resulting limit cycle (i.e. periodic solution upon crossing the critical threshold) is essential in characterizing the dynamic response of the system, and also in identifying whether a supercritical or subcritical bifurcation is to occur near the critical parameter of the system. The linearization does not provide a distinction since in both cases, a pair of eigenvalues moves from the left to the right half-plane; thus, a nonlinear analysis is required for accurate identification of the bifurcation in the system. As previously mentioned, the stability of the limit cycle can be identified by the sign of its characteristic exponents μ^H. Determining the characteristic exponents of linear periodic systems, analytically, is an extremely difficult task except for simple second order systems. It is known [111] that for a second order system:

$$\dot{x} = f(x, y, \nu)$$
$$\dot{y} = g(x, y, \nu) \tag{4.24}$$

with a fixed point $(x, y) = (x_0, y_0)$, the characteristic exponent can be given by:

$$\mu_j = \frac{1}{16}\left(f_{xxx} + f_{xyy} + g_{xxy} + g_{yyy}\right) + \frac{1}{16\gamma(\nu_c)}\left[f_{xy}\left(f_{xx} + f_{yy}\right) - g_{xy}\left(g_{xx} + g_{yy}\right) - f_{xx}g_{xx} + f_{yy}g_{yy}\right] \tag{4.25}$$

where $f_{xy} = \left.\frac{\partial^2 f}{\partial x \partial y}\right|_{\nu=\nu_c}(x_0, y_0)$ and etc. A generalization of Eq. (4.25) for higher order systems is given by Hassard and Wan [110] and is included in Appendix B . The corresponding numerical recipe provided by Hassard et al. [76] is used in this chapter as a basis for a Hopf bifurcation subroutine. The subroutine is then used for the purpose of analyzing the stability of the oil whirl phenomenon in the dynamical system of Eq. (4.13) applied to a fully balanced system with $\bar{m}_u = 0$ that can be written in the autonomous form of $\dot{\boldsymbol{X}} = \boldsymbol{f}(\boldsymbol{X}, \nu)$. As is evident form Eq. (4.25), the stability of the limit cycle is a function of higher order derivatives of the $\boldsymbol{f}(\boldsymbol{X}, \nu)$ as compared to the linear analysis, for which only the Jacobean matrix is sufficient to characterize the stability of the system. The common practice in the literature is to represent the journal forces only by the linear dynamic coefficients. This linear representation results in a degenerate case in which all the higher derivatives in Eq. (4.25) turn to zero and thus the stability of the limit cycle cannot be identified. The nonlinear representation of journal forces as functions of journal position and velocity as in Eq. (4.10) is suitable for nonlinear analysis, for implementation of the Hopf bifurcation theory, and for studying the limit cycle stability.

4.6 Results and Discussions

4.6.1 Bearing Dynamic Coefficients in the *X*-*Y* Coordinate System

The coefficients in the *X*-*Y* coordinate, in their general form, and for a π-film short bearing are calculated and given in Appendix C . The absolute values of linear and nonlinear dynamic

coefficients of a π-film short bearing are plotted against the eccentricity ratio in Figure 4-2, Figure 4-3, and Figure 4-4.

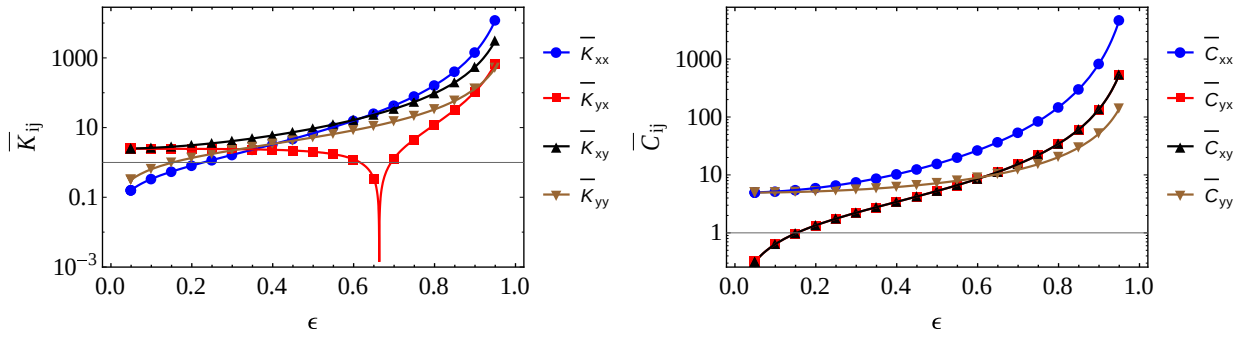

(a) (b)

Figure 4-2. Linear dynamic coefficients in *X*-*Y* coordinate system for a π-film short bearing with $L/D = 1/2$

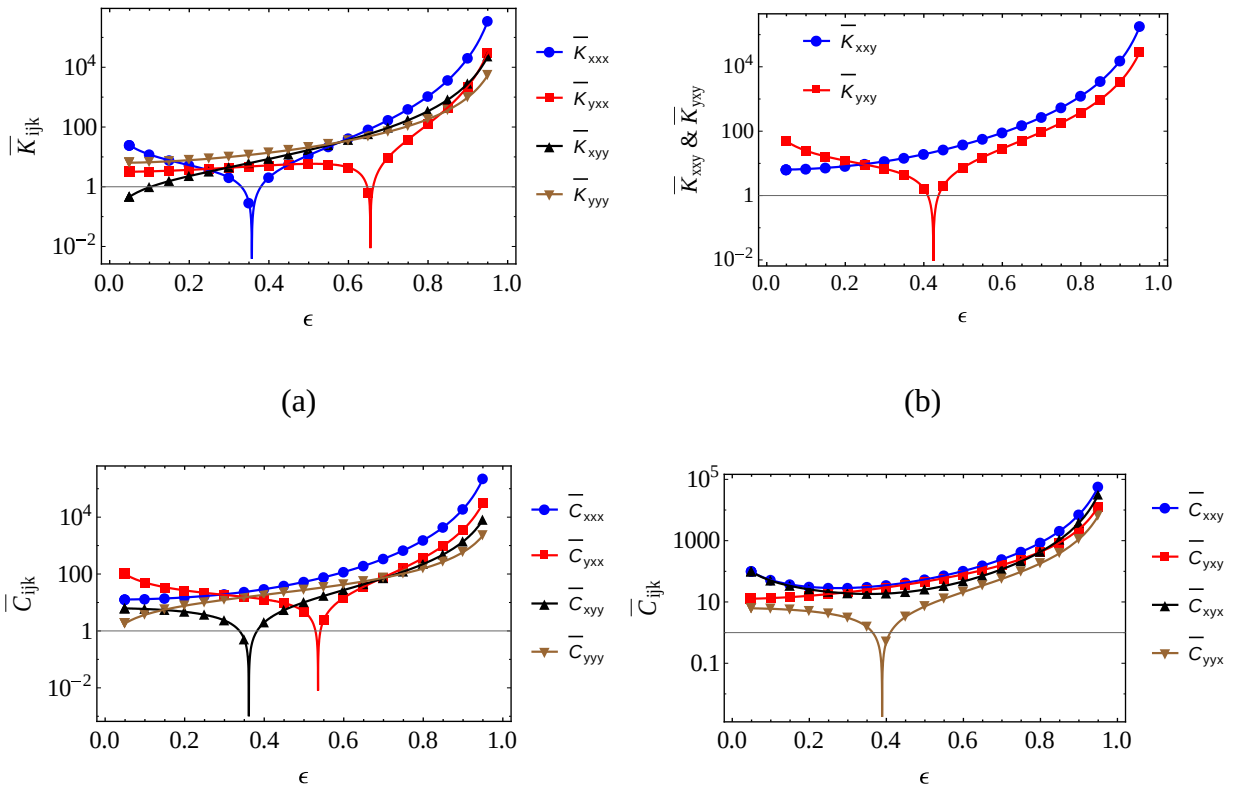

(a) (b)

(c) (d)

Figure 4-3. Nonlinear (second order) dynamic coefficients (absolute values) in X-Y coordinate system

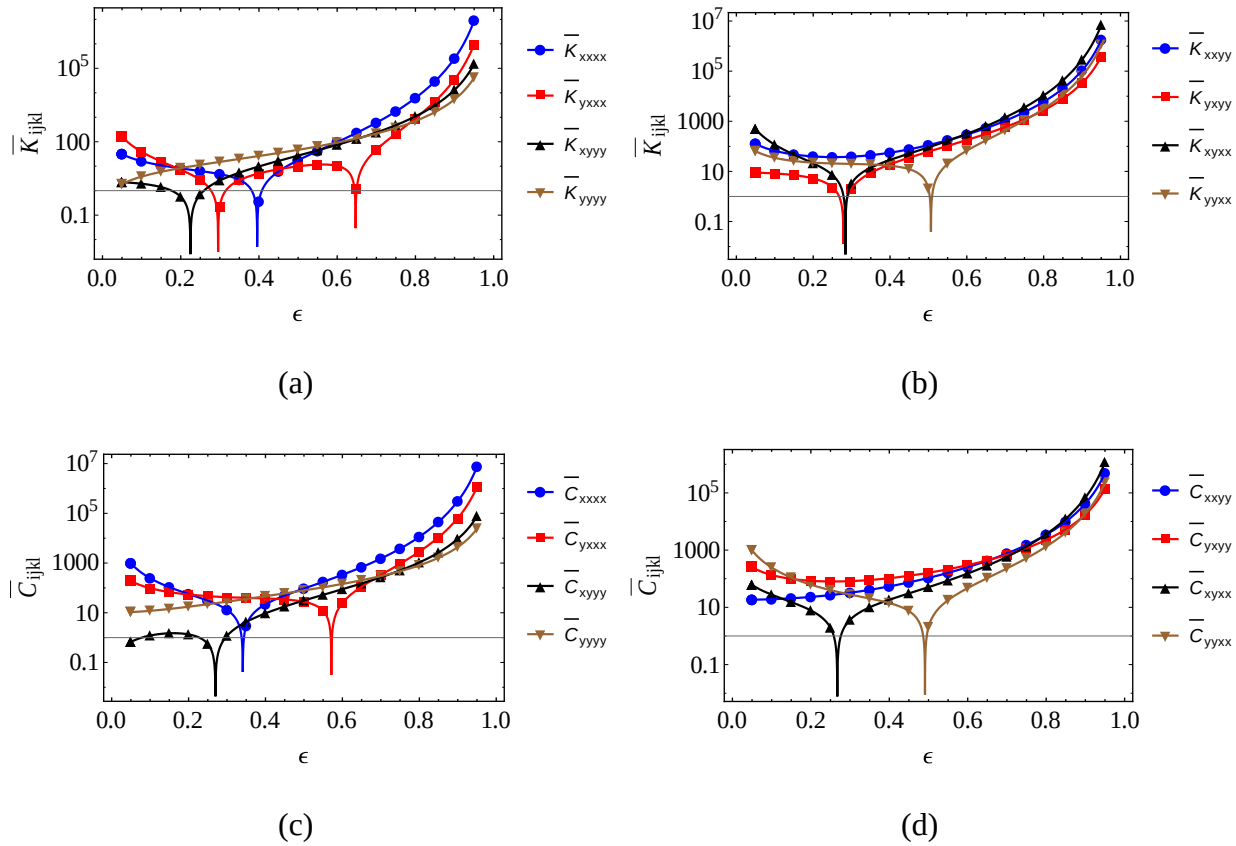

Figure 4-4. Nonlinear (third order) dynamic coefficients (absolute values) in X-Y coordinate system

Having all the linear and nonlinear dynamic coefficients of the journal bearings, the mathematic model of the rotor-bearing system can be constructed and the stability of the system can be assessed.

4.6.2 Identification of the Stability Bounds of the Rotor-Bearing System by Hopf Bifurcation Algorithm

In the absence of other nonlinear effects such as Reynolds number dependence in modified Reynolds equation for Turbulent flow, the operating condition of the rotor-bearing system can be identified solely based on the applied static load on the system. This is usually done by representing the system characteristics as functions of either the eccentricity ratio or the Sommerfeld number. Linear stability bounds (threshold speed of instability $\bar{\omega}_{th}$) of the system of Eq. (4.13) were calculated in Section 3.3 in a similar fashion to Ref [25, 91] and are given as:

$$\bar{\omega}_{th}^2 = \frac{\alpha}{\bar{\nu}^2(\bar{K}_s - \alpha)}$$
$$\alpha = \frac{2(\bar{K}_{xy}\bar{C}_{yx} + \bar{K}_{yx}\bar{C}_{xy} - \bar{K}_{yy}\bar{C}_{xx} - \bar{K}_{xx}\bar{C}_{yy})}{\bar{C}_{xx} + \bar{C}_{yy}} \quad (4.26)$$
$$\bar{\nu}^2 = \frac{\alpha^2 + 2(\bar{K}_{xx} + \bar{K}_{yy})\alpha + 4(\bar{K}_{xx}\bar{K}_{yy} - \bar{K}_{xy}\bar{K}_{yx})}{4(\bar{C}_{xy}\bar{C}_{yx} - \bar{C}_{xx}\bar{C}_{yy})}$$

The calculated threshold speeds are used as an initial guess for the Hopf bifurcation algorithm. The algorithm is, however, independent of the analytical expression for $\bar{\omega}_{th}$ as long as the initial guess is close enough to the threshold values. The Floquet exponents, μ^H, are then found and their sign at each operating point is used to identify whether the bifurcation at the threshold speed is sub or supercritical. Calculated results of stability parameter $\gamma = \frac{C K_s}{W}\bar{\omega}_{th}^2$ for a range of non-dimensional shaft stiffness are plotted against the Sommerfeld number and are shown in Figure 4-5 (a).

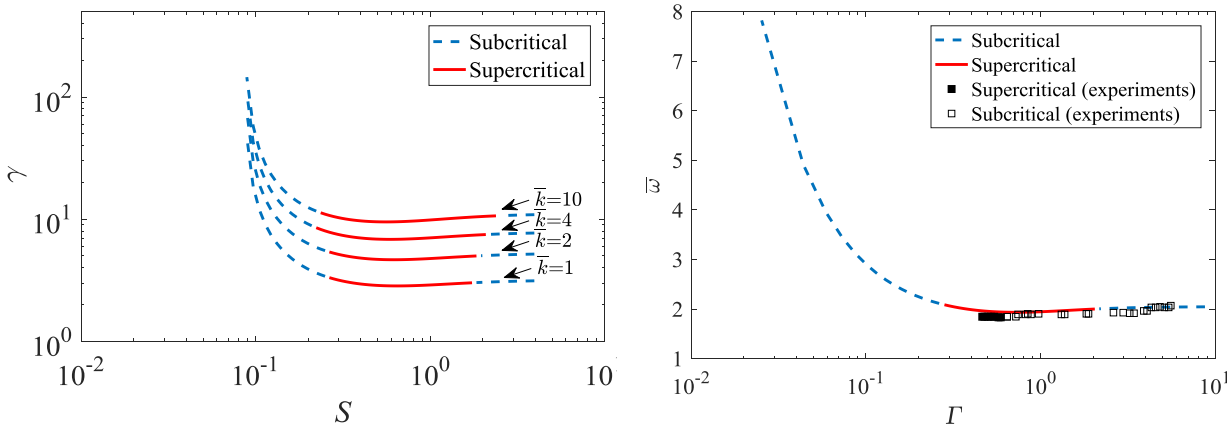

(a) (b)

Figure 4-5. stability bounds of the flexible rotor-bearing system for a range of non-dimensional shaft stiffness values (a) and comparison to experimental results of Wang and Khonsari [90] (b)

Khonsari and Wang [90] designed and tested an experimental set-up for a flexible shaft supported on end journal bearings and identified the threshold speed of instability and bifurcation types for a range of bearing parameter Γ defined as:

$$\Gamma = \frac{\mu R L^3}{M C^{2.5} g^{0.5}} = 2\pi \left(\frac{L}{D}\right)^2 \frac{S}{\omega}\sqrt{\frac{g}{C}} \quad (4.27)$$

where S is the Sommerfeld number. Their experimental results for a flexible shaft with non-dimensional half-shaft stiffness of $\bar{k}_{wang} \equiv 2\bar{k} = 2.9$ is plotted with the numerical predictions based on the mathematical model of this chapter as shown in Figure 4-5 (b). As it can be seen from Figure 4-5 (b), there is good agreement in threshold speed calculation as well as a qualitative agreement on bifurcation types between the numerical predictions and the experimental results. Both results suggest a transition from supercritical to subcritical bifurcation as the bearing parameter increases. The difference between the numerical estimates and the experiments is due to simplifications in the mathematical model such as assuming a perfectly balanced rotor and neglecting the fluid inertial and shaft gyroscopic effects, as well as the simplifying assumption of concentrated mass at the shaft center.

Results of Figure 4-5 show that the bifurcation types in the dynamic system of Eq. (4.13) can be successfully identified by the Hopf bifurcation analysis. The Hopf bifurcation algorithm will yield the Floquet exponents provided that the bearing dynamic forces are represented with nonlinear terms as in Eq. (4.10). If linear bearing coefficients are used to represent the bearing forces, Hopf bifurcation algorithm cannot differentiate the bifurcation type at the threshold speed of instability. The nonlinear force representation of Eq. (4.10) is beneficial not only in the current study of short journal bearings, but also makes it possible to study Hopf bifurcations in more realistic systems with finite length journal bearings for which a journal force representation is generally not available. The underlying dynamics of the system of nonlinear ordinary differential equations of Eq. (4.13) can also be studied through direct time integration of the system to obtain journal trajectories evolving with time. Such trajectories can further illustrate how the bifurcation type can affect physical stability in a rotor-bearing system.

4.6.3 Rotor-Bearing Dynamic Response

Numerical integration of the non-dimensional equations of motion as in Eq. (4.13) will yield the dynamical response of the system at any instance in time. Four operating points are chosen to illustrate the journal trajectories as shown in Figure 4-6.

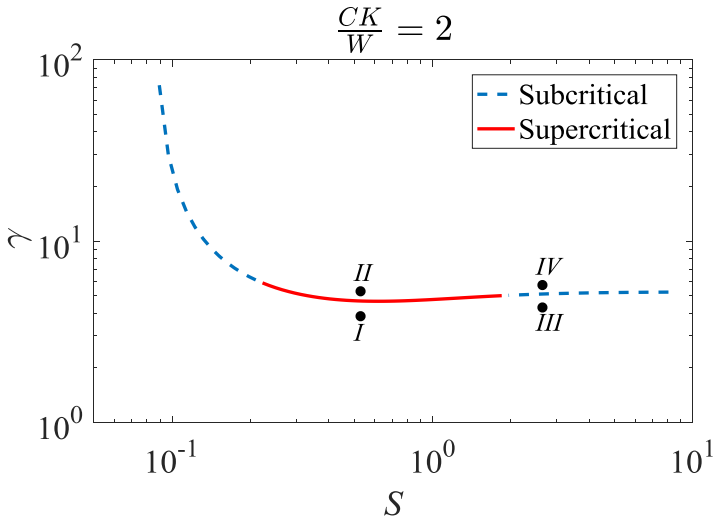

Figure 4-6. Selected operating points of a fully balanced rotor-bearing system in stable and unstable regions for time integration

The operating points *I, II, III* and *IV* as marked in Figure 4-6, are selected in an attempt to demonstrate the system dynamics before and after crossing the threshold speed of instability for both super and subcritical regions of the system. The calculated trajectories for supercritical operating points (*I* and *II*) and subcritical operating points (*III* and *IV*) are shown in Figure 4-7. The line of centers is plotted with a dashed line in and the steady state point is marked with a bullet in Figure 4-7 (a-d).

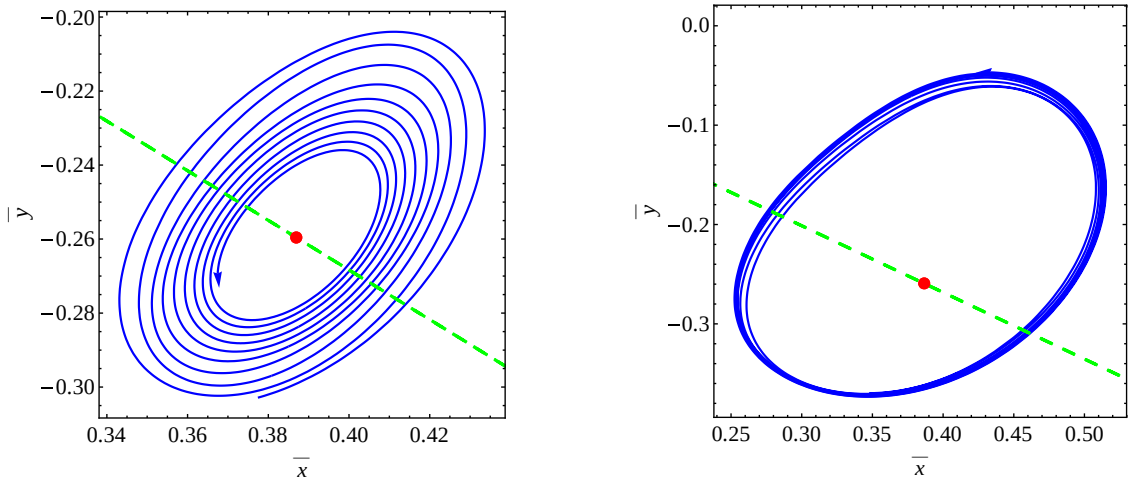

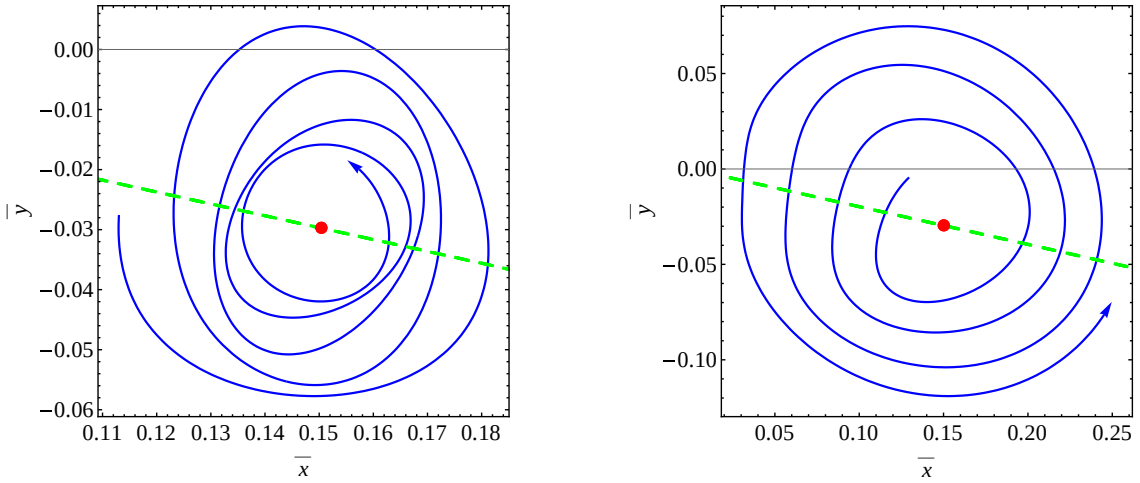

(c) (d)

Figure 4-7. Journal trajectories for the operating points within the supercritical region; Point *I* ($S = 0.5, \gamma = 4$), before crossing the threshold speed (a), point *II* ($S = 0.5, \gamma = 5.5$), after crossing the threshold speed (b), and the subcritical region; Point *III* ($S = 2.5, \gamma = 4.5$), before crossing the threshold speed (c) and point *IV* ($S = 2.5, \gamma = 6$), after crossing the threshold speed (d)

The calculated journal trajectory for operating point *I* where $\omega < \omega_{th}$ is depicted in Figure 4-7 (a). The trajectory is spiraling inward to find the steady state point of the system. If enough time is given to the system, the trajectory will settle into a single point where the vertical component of the journal force is equal to the rotor weight and the system is in equilibrium. Upon increasing the shaft spin speed and crossing the threshold speed of instability, operating point *II* with $> \omega_{th}$, the system will no longer settle into a steady state point. However, since the operating region lies within the supercritical bifurcation region as identified by Hopf bifurcation analysis, the trajectory settles into a stable limit cycle as shown in Figure 4-7 (b). At and around the subcritical region, the situation is different in the sense that after crossing the threshold speed (operating point *IV*), there is no stable limit cycle and the trajectory rapidly grows; therefore journal position cannot be traced if the journal force is represented with dynamic coefficients. This is shown in Figure 4-7 (c-d).

An alternative approach to finding the trajectories of the system of Eq. (4.13) and Eq. (4.14) is to replace the coefficient-based force representation of Eq. (4.14) with the closed-form forces in excess of the equilibrium:

$$\delta f_\epsilon = f_\epsilon - f_{\epsilon 0}$$
$$\delta f_\phi = f_\phi - f_{\phi 0} \tag{4.28}$$

where f_ϵ and f_ϕ are given in Eq. (4.6) and $f_{\epsilon 0}$ and $f_{\phi 0}$ are steady state journal forces. Although using the analytical forces does enable one to calculate the trajectories with any desired time-span and any bifurcation region when other methods fail to do so, the disadvantage is that the closed-form journal forces are available for very limited and simple cases that are far from industrial bearings that are used in practice. The main benefit from a trajectory analysis that is based on closed-form journal forces is to have a basis of comparison for how other models behave relative to the exact journal forces and to show how closely they can mimic the forces and dynamics of the system. The last alternative for finding the trajectories is to only retain the linear dynamic coefficients from Eq. (4.14) and thus calculate the trajectories based on a linear bearing model. The closed-form and linear bearing models are implemented and the resulting trajectories are found and are plotted against the nonlinear bearing model of this chapter as shown in Figure 4-8. The clearance circle is shown in black.

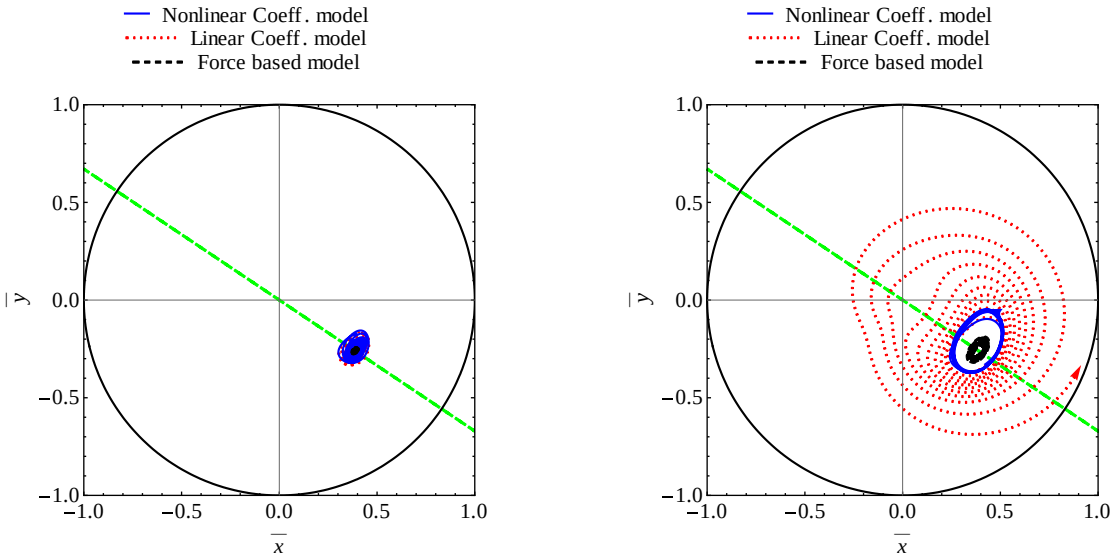

(a) (b)

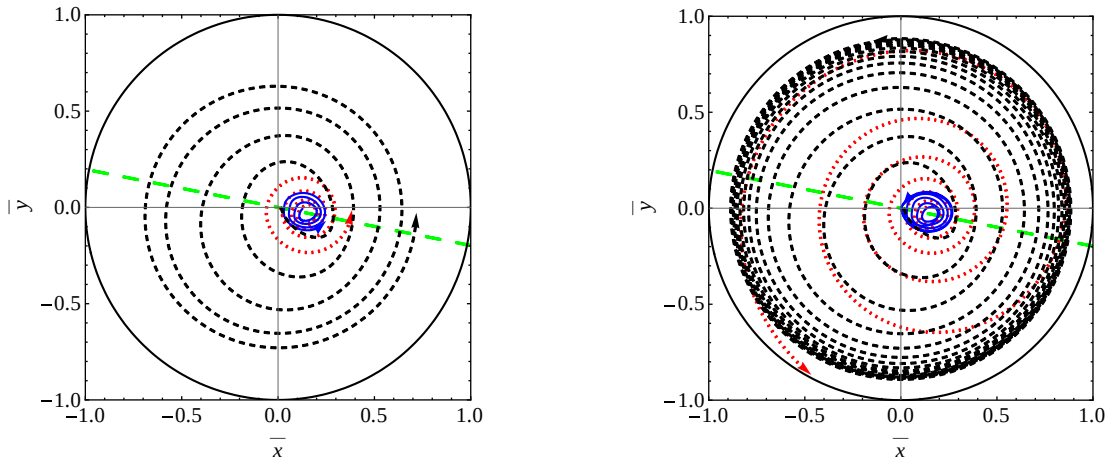

(c) (d)

Figure 4-8. Comparison of the obtained journal trajectory based on linear and nonlinear coefficient models and the force based model for operating points *I* (a), *II* (b), *IV*(c) and (d).

At operating point *I*, within the stable boundaries, there is no difference in obtained journal trajectories as in Figure 4-8(a). In the supercritical bifurcation region of point *II*, the trajectories are expected to find a limit cycle. While both force-based and nonlinear coefficient models do find a stable limit cycle, the linear coefficient model fails to do so and its trajectories grow unbounded, as shown in Figure 4-8(b). It shall be noted that the predicted size of the limit cycle in Figure 4-8(b) is different for the force and nonlinear models. Since the predictions of the force-based model are generally more accurate, this difference in predicted results can be attributed to the approximating nature of any coefficient-based model and indicates the limitations of the adopted model.

Despite the limitations, the nonlinear-based model is shown to successfully predict the existence of a stable limit cycle, which is indeed the main goal of the current study, unlike the inaccurate predictions of the linear bearing coefficient model. The superiority of the force-based model is again manifested in Figure 4-8(c-d) where the trajectories are predicted with no difficulty both at an early stage, Figure 4-8 (c), and also further ahead in time, Figure 4-8 (d). On the other hand, the linear-based model experiences uncontrolled growth, and the nonlinear-based model becomes very stiff with minimum required dynamic time increments approaching zero, and thus it fails to predict the evolution of trajectories with time. Further time integration as in Figure 4-8(d) shows that the force-based predictions are within the clearance cycle despite the asymptotically unstable nature of the solution in which the system response becomes only physically bounded. As manifested in

the results of Figure 4-8, one can conclude that journal forces are best expressed with closed-from expressions. However, the lack of existing analytical expressions for the journal forces limits the adaptability of the force-based model to very simple bearing geometries with less realistic cavitation models. Thus, the use of nonlinear bearing coefficients in predicting the journal force appears promising, not only for the purpose of predicting the stability boundaries and bifurcation types, but also for use with any bearing geometry with any desired cavitation model. Hence, the nonlinear coefficient-based model is the most versatile between the models discussed in this chapter.

Chapter 5: Nonlinear Dynamics of a Rotor-Bearing System using a Numerical Bearing Model

In the previous chapter, it was shown that higher order coefficients can be used to avoid degenerate cases that are caused when the journal force is expressed only by linear coefficients. Although the nonlinear coefficient-based model given in the previous chapter was shown to be capable of revealing the bifurcation types of the system, the nonlinear coefficients were only given for when analytic expressions exist. The treatment can be generalized to any bearing provided that nonlinear coefficients can be given for finite bearings with a desired geometry.

In this chapter, the nonlinear stability of a flexible rotor-bearing system supported on finite length journal bearings is addressed. A perturbation method of the Reynolds lubrication equation is presented to calculate the bearing nonlinear dynamic coefficients, a treatment that is suitable to any bearing geometry. A mathematical model, *nonlinear coefficient-based model*, is proposed for the flexible rotor bearing system for which the journal forces are represented through linear and nonlinear dynamic coefficients. The proposed model is then used for nonlinear stability analysis in the system. A shooting method is implemented to find the periodic solutions due to Hopf bifurcations. The *Monodromy* matrix associated to the periodic solution is found at any operating point as a by-product of the shooting method. The eigenvalue analysis of the Monodromy matrix is then carried out to assess the bifurcation types and directions due to Hopf bifurcation in the system for speeds beyond the threshold speed of instability.

5.1 Nonlinear Bearing Model with Dynamic Coefficients

Figure 5-1 shows a schematic of a journal bearing inside the bearing clearance.

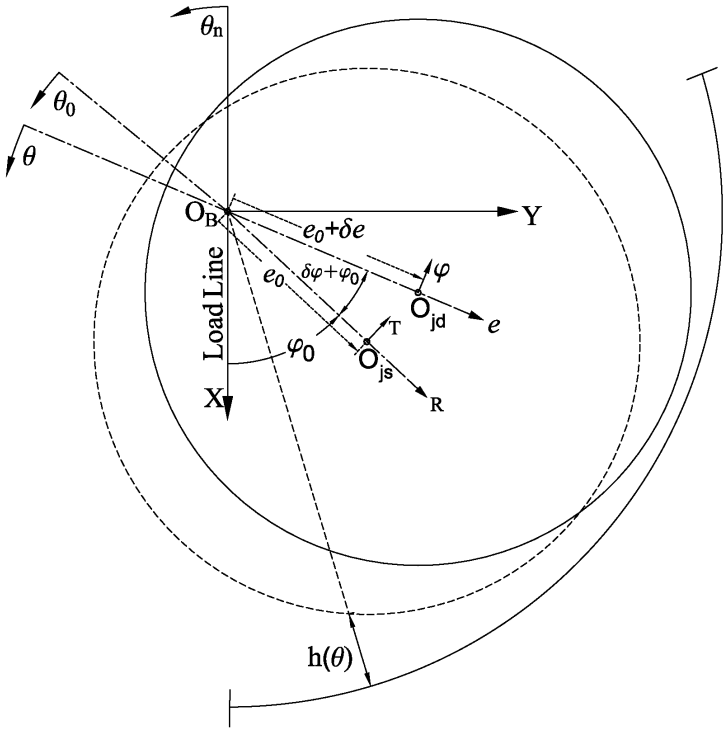

Figure 5-1. the schematic of a journal inside bearing with the adopted coordinate systems

The geometric center of the bearing is given by O_B in Figure 5-1 and is selected as the center of the fixed and inertial *X*-*Y* coordinate system. Under steady state conditions, the weight of the rotor and journal, $\boldsymbol{W}$, is balanced by the induced bearing force, $\boldsymbol{F}$, such that $\boldsymbol{F} + \boldsymbol{W} = 0$. At the steady state, the journal is located at O_{J_S} with the eccentricity e_0 and an attitude angle of φ_0. The steady oil induced force components along the fixed directions *(R, T),* are F_{R0} and F_{T0}. The bearing reaction force, $\boldsymbol{F}$, can be calculated by integrating the oil induced pressure over the surface of the journal:

$$F_R = \int_0^{\theta_{cav}} R_j \, d\theta \int_{-\frac{L}{2}}^{\frac{L}{2}} P \cos(\theta) \, dz \,, \quad F_T = \int_0^{\theta_{cav}} R_j \, d\theta \int_{-\frac{L}{2}}^{\frac{L}{2}} P \sin(\theta) \, dz \tag{5.1}$$

where θ_{cav} is the circumferential cavitation boundary and *P* is lubricant induced pressure. In order to calculate the oil induced pressure, the Reynolds partial differential equation needs to be solved [25]:

$$\frac{1}{R_j^2}\frac{\partial}{\partial\theta}\left(\frac{h^3}{12\,\mu}\frac{\partial P}{\partial\theta}\right) + \frac{\partial}{\partial z}\left(\frac{h^3}{12\,\mu}\frac{\partial P}{\partial z}\right) = \frac{1}{2}\omega\frac{\partial h}{\partial\theta} + \frac{\partial h}{\partial t} \tag{5.2}$$

where R_j is the journal radius, μ is lubricant viscosity, (θ, z) are basis of the coordinate system given in Figure 5-1, ω is the spin speed of the journal, and h is the oil film thickness given as [25]:

$$h = C + R_j + e\cos(\theta) - R_j\sqrt{1 - \left(\frac{e}{R_j}\right)^2 \sin^2(\theta)} \tag{5.3}$$

where C is the bearing clearance and e is the journal eccentricity. In journal bearings with typical clearance to radius values of $\frac{C}{R_j} \approx 0.002$, the oil thickness can be given with sufficient accuracy by the approximate equation which is accurate to order $\left(\frac{e}{R_j}\right)$ as [112]:

$$h \equiv C\ H \cong C(1 + \epsilon\ \cos(\theta)) \tag{5.4}$$

where $\epsilon = \frac{e}{C}$ is the eccentricity ratio and $H = \frac{h}{C}$ is the non-dimensional film thickness. At steady state, the film thickness h_0 is given as:

$$h_0 = C(1 + \epsilon_0\ \cos(\theta_0)) \equiv C\ H_0 \tag{5.5}$$

where the steady circumferential angle θ_0 at any point on the journal surface is measured from the steady line of centers $\overline{O_B O_{Js}}$. If the journal is perturbed, it will occupy the instantaneous position O_J with eccentricity $e = e_0 + \delta e$ and the attitude angle of $\varphi = \varphi_0 + \delta\varphi$ as shown in Figure 5-1. Note that the circumferential angle θ is now measured from the instantaneous line of centers $\overline{O_B O_J}$. This change in the position of the journal results in a change in the oil film thickness. The dynamic non-dimensional oil thickness can be written as:

$$H \cong 1 + (\epsilon_0 + \delta\epsilon)\cos(\theta) = 1 + (\epsilon_0 + \delta\epsilon)\cos(\theta_0 - \delta\varphi) \tag{5.6}$$

Expanding the argument of the cosine and assuming $\delta\varphi$ is small such that $\cos(\delta\varphi) \approx 1$ and $\sin(\delta\varphi) \approx \delta\varphi$, we will have:

$$H \cong H_0 + \delta\epsilon\cos(\theta_0) + \epsilon_0\delta\varphi\sin(\theta_0) + \delta\epsilon\ \delta\varphi\sin(\theta_0) \tag{5.7}$$

5.1.1 Linear Dynamic Coefficients in *X*-*Y* Coordinate System

It is beneficial for numerical integration to write the Reynolds equation (5.2) in a non-dimensional form:

$$\frac{\partial}{\partial\theta}\left(\frac{H^3}{12}\frac{\partial\bar{P}}{\partial\theta}\right)+\frac{1}{4}\left(\frac{D}{L}\right)^2\frac{\partial}{\partial\bar{z}}\left(\frac{H^3}{12}\frac{\partial\bar{P}}{\partial\bar{z}}\right)=\pi\frac{\partial H}{\partial\theta}+2\pi\frac{\partial H}{\partial\tau} \tag{5.8}$$

where,

$$z=L\,\bar{z}\,,h=C\,H\,,P=\Pi_{\mathrm{p}}\,\bar{P},\tau=\omega t\,,\Pi_{\mathrm{p}}=\frac{\Pi}{\mathrm{L\,D}}\text{ with }\Pi=L\,D\,\mu\,N\,\left(\frac{R}{C}\right)^2\text{ and }N=\frac{\omega}{2\pi} \tag{5.9}$$

A linear approximation for the perturbed film thickness can be obtained by setting the higher order terms in Eq.(5.7) to zero:

$$H_l=H_0+\delta\epsilon\cos(\theta_0)+\epsilon_0\delta\varphi\sin(\theta_0) \tag{5.10}$$

We now define a new circumferential angle, θ_n, measured from $-X$ axis such that $\theta_n=\theta_0+\varphi_0$ as shown in Figure 5-1. Thus:

$$\begin{aligned}H_l&=H_0+\delta\epsilon\cos(\theta_n-\varphi_0)+\epsilon_0\delta\varphi\sin(\theta_n-\varphi_0)\\&=H_0+\delta\epsilon\cos(\theta_n)\cos(\varphi_0)+\delta\epsilon\sin(\theta_n)\sin(\varphi_0)\\&\quad+\epsilon_0\delta\varphi\sin(\theta_n)\cos(\varphi_0)-\epsilon_0\delta\varphi\cos(\theta_n)\sin(\varphi_0)\end{aligned} \tag{5.11}$$

by adopting a counter-clockwise (CCW) transformation:

$$\begin{pmatrix}\delta\epsilon\\\epsilon_0\delta\varphi\end{pmatrix}=Q\begin{pmatrix}\delta\bar{x}\\\delta\bar{y}\end{pmatrix}\text{ where }Q=\begin{pmatrix}\cos\varphi_0&\sin\varphi_0\\-\sin\varphi_0&\cos\varphi_0\end{pmatrix} \tag{5.12}$$

where $\bar{x}=\frac{x}{C}$ is the non-dimensional *x*-coordinate in the fixed *X*-*Y* coordinate system, the linearized film thickness can be represented as:

$$H_l=H_0+\delta\bar{x}\cos(\theta_n)+\delta\bar{y}\sin(\theta_n) \tag{5.13}$$

and is identical to the expression given by Lund [47] for the perturbed oil film thickness. A perturbation in the film thickness results in a perturbation in the induced fluid pressure. The induced journal pressure is a function of journal position and velocity and thus the perturbed pressure can be given as a series expansion such that:

$$\bar{P} = \bar{P}_0 + \delta\bar{P} \approx \bar{P}_0 + \frac{\partial \bar{P}}{\partial \bar{x}}\delta\bar{x} + \frac{\partial \bar{P}}{\partial \bar{y}}\delta\bar{y} + \frac{\partial \bar{P}}{\partial \dot{\bar{x}}}\delta\dot{\bar{x}} + \frac{\partial \bar{P}}{\partial \dot{\bar{y}}}\delta\dot{\bar{y}} \tag{5.14}$$

where $\dot{\bar{x}} = \frac{d\bar{x}}{d\tau}$ and etc. Upon substituting the perturbed pressure of Eq.(5.14) and the perturbed film thickness of Eq.(5.13) into the non-dimensional Reynolds equation (5.8) and performing an order analysis, one can obtain partial differential equations in pressure and pressure gradients by retaining the first order terms only:

$$\begin{aligned}
&\mathcal{O}(1): \mathcal{R}\{\bar{P}_0\} = -\pi \frac{\partial H_0}{\partial \theta} \\
&\mathcal{O}(\delta x): \mathcal{R}\{\bar{P}_x\} = -\pi \sin(\theta_n) - \frac{\partial}{\partial \theta}\left(\frac{3\,{H_0}^2}{12}\cos(\theta_n)\frac{\partial \bar{P}_0}{\partial \theta}\right) - \\
&\frac{1}{4}\left(\frac{D}{L}\right)^2 \frac{\partial}{\partial \bar{z}}\left(\frac{3\,{H_0}^2}{12}\cos(\theta_n)\frac{\partial \bar{P}_0}{\partial \bar{z}}\right) \\
&\mathcal{O}(\delta y): \mathcal{R}\{\bar{P}_y\} = \pi \cos(\theta_n) - \frac{\partial}{\partial \theta}\left(\frac{3\,{H_0}^2}{12}\sin(\theta_n)\frac{\partial \bar{P}_0}{\partial \theta}\right) - \\
&\frac{1}{4}\left(\frac{D}{L}\right)^2 \frac{\partial}{\partial \bar{z}}\left(\frac{3\,{H_0}^2}{12}\sin(\theta_n)\frac{\partial \bar{P}_0}{\partial \bar{z}}\right) \\
&\mathcal{O}(\delta \dot{x}): \mathcal{R}\{\bar{P}_{\dot{x}}\} = 2\pi \cos(\theta_n) \\
&\mathcal{O}(\delta \dot{y}): \mathcal{R}\{\bar{P}_{\dot{y}}\} = 2\pi \sin(\theta_n) \\
&\text{where } \mathcal{R}\{\,\} = \frac{\partial}{\partial \theta}\left(\frac{{H_0}^3}{12}\frac{\partial\{\,\}}{\partial \theta}\right) + \frac{1}{4}\left(\frac{D}{L}\right)^2 \frac{\partial}{\partial \bar{z}}\left(\frac{{H_0}^3}{12}\frac{\partial\{\,\}}{\partial \bar{z}}\right)
\end{aligned} \tag{5.15}$$

where $\bar{P}_{\dot{x}} = \frac{\partial \bar{P}}{\partial \dot{\bar{x}}}$ and etc. Journal bearing force components can be expressed in a series expansion about the steady state point such that:

$$f_\zeta \cong f_{\zeta 0} + \frac{\partial f_\zeta}{\partial \bar{x}}d\bar{x} + \frac{\partial f_\zeta}{\partial \dot{\bar{x}}}d\dot{\bar{x}} + \frac{\partial f_\zeta}{\partial \bar{y}}d\bar{y} + \frac{\partial f_\zeta}{\partial \dot{\bar{y}}}d\dot{\bar{y}} \tag{5.16}$$

where $\zeta = x, y$ and $f_i = \frac{F_i}{\Pi}$ is the non-dimensional journal bearing force. $\left(f_{x0}, f_{y0}\right)$ are components of the bearing force at equilibrium. The eight bearing stiffness and damping coefficients were proposed by Lund [13] in the form,

$$\bar{K}_{ij} \equiv -\left(\frac{\partial f_i}{\partial \bar{x}_j}\right) \text{ and } \bar{C}_{ij} \equiv -\left(\frac{\partial f_i}{\partial \dot{\bar{x}}_j}\right) \text{ with } i, j = x, y \tag{5.17}$$

The components of the journal force can be directly given in the *X-Y* coordinate by adopting the new circumferential coordinate, θ_n, in the force descriptions of Eq. (5.1):

$$f_x = \frac{1}{2}\int_0^{\theta_{cav}} \int_{-\frac{1}{2}}^{\frac{1}{2}} \bar{P}\cos(\theta_n)\ d\theta d\bar{z}\ ,\quad f_y = \frac{1}{2}\int_0^{\theta_{cav}} \int_{-\frac{1}{2}}^{\frac{1}{2}} \bar{P}\sin(\theta_n)\ d\theta d\bar{z} \tag{5.18}$$

By substituting the perturbed pressure of Eq.(5.14) and the series expansion of bearing force as in Eq.(5.16) into Eq.(5.18) and performing an order analysis, the linear dynamic coefficients of the journal bearing can be given as functions of the induced pressure gradients:

$$\begin{Bmatrix}\bar{K}_{xx}\\ \bar{K}_{yx}\end{Bmatrix} = -\frac{1}{2}\int_0^{\theta_{cav}} \int_{-\frac{1}{2}}^{\frac{1}{2}} \bar{P}_x \begin{Bmatrix}\cos\theta_n\\ \sin\theta_n\end{Bmatrix} d\theta d\bar{z}\ ,\ \begin{Bmatrix}\bar{K}_{xy}\\ \bar{K}_{yy}\end{Bmatrix} = -\frac{1}{2}\int_0^{\theta_{cav}} \int_{-\frac{1}{2}}^{\frac{1}{2}} \bar{P}_y \begin{Bmatrix}\cos\theta_n\\ \sin\theta_n\end{Bmatrix} d\theta d\bar{z}$$
$$\begin{Bmatrix}\bar{C}_{xx}\\ \bar{C}_{yx}\end{Bmatrix} = -\frac{1}{2}\int_0^{\theta_{cav}} \int_{-\frac{1}{2}}^{\frac{1}{2}} \bar{P}_{\dot{x}} \begin{Bmatrix}\cos\theta_n\\ \sin\theta_n\end{Bmatrix} d\theta d\bar{z}\ ,\ \begin{Bmatrix}\bar{C}_{xy}\\ \bar{C}_{yy}\end{Bmatrix} = -\frac{1}{2}\int_0^{\theta_{cav}} \int_{-\frac{1}{2}}^{\frac{1}{2}} \bar{P}_{\dot{y}} \begin{Bmatrix}\cos\theta_n\\ \sin\theta_n\end{Bmatrix} d\theta d\bar{z} \tag{5.19}$$

where $\bar{K}_{ij}$, $\bar{C}_{ij}$ are non-dimensional dynamic coefficients and $\bar{P}_i$ are non-dimensional pressure gradients:

$$\bar{K}_{ij} = \frac{C}{\Pi}\ K_{ij}\ ,\ \bar{C}_{ij} = \frac{C\,\omega}{\Pi}\ C_{ij}\ ,\ \bar{P}_x = \frac{C}{\Pi_p} P_x\ ,\ \bar{P}_{\dot{x}} \equiv \frac{\partial \bar{P}}{\partial \frac{\dot{x}}{}} = \frac{C\,\omega}{\Pi_p} P_{\dot{x}} \tag{5.20}$$

The pressure gradients of Eq. (5.15) are numerically solved for and then are integrated according to Eq.(5.19) to find the journal bearing linear dynamic coefficients.

5.1.2 Nonlinear Dynamic Coefficients in *X-Y* Coordinate System

A nonlinear approximation to the perturbed film thickness, H_{nl}, can be obtained by expanding Eq.(5.6):

$$H_{nl} = 1 + \delta\epsilon\cos(\theta_0) + \epsilon_0\cos(\theta_0) + \epsilon_0\,\delta\phi\sin(\theta_0) - \frac{1}{2}\delta\epsilon\,\delta\phi^2\cos(\theta_0) + \delta\epsilon\,\delta\phi\,\sin(\theta_0) - \frac{1}{2}\delta\phi^2\,\epsilon_0\cos(\theta_0) \tag{5.21}$$

In calculating the film thickness in Eq.(5.21), it is assumed that for small $\delta\varphi$:

$$\cos(\delta\varphi) \approx \left(1 - \frac{\delta\varphi^2}{2}\right), \text{ and } \sin(\delta\varphi) \approx \delta\varphi \tag{5.22}$$

Substituting θ_0 in Eq.(5.21) by $\theta_n - \varphi_0$ and again adopting the counter-clockwise transformation of Eq. (5.12), the nonlinear perturbed film thickness in the *X*-*Y* coordinate can be written as:

$$H_{nl} = H_0 + \delta\bar{x}\cos(\theta n) + \delta\bar{y}\sin(\theta n) + \frac{1}{8\epsilon_0}[-\cos(\theta n - 3\varphi_0) - 2\cos(\theta n - \varphi_0) + 3\cos(\theta n + \varphi_0)]\delta\bar{x}^2 + \frac{1}{4\epsilon_0}[\sin(\theta n - 3\varphi_0) + 3\sin(\theta n + \varphi_0)]\delta\bar{x}\delta\bar{y} + \frac{1}{8\epsilon_0}[\cos(\theta n - 3\varphi_0) - 2\cos(\theta n - \varphi_0) - 3\cos(\theta n + \varphi_0)]\delta\bar{y}^2 \quad (5.23)$$

The nonlinear perturbed film thickness of Eq.(5.23) will result in a nonlinear perturbed pressure. This perturbed pressure can again be expressed in a Taylor series expansion that is an extension to higher order terms from the pressure perturbation of Eq. (5.14) such that:

$$\bar{P} \approx \bar{P}_0 + \frac{\partial\bar{P}}{\partial\bar{x}}\delta\bar{x} + \frac{\partial\bar{P}}{\partial\bar{y}}\delta\bar{y} + \frac{\partial\bar{P}}{\partial\dot{x}}\delta\dot{x} + \frac{\partial\bar{P}}{\partial\dot{y}}\delta\dot{y} + \frac{1}{2}\frac{\partial^2\bar{P}}{\partial\bar{x}^2}\delta\bar{x}^2 + \frac{1}{2}\frac{\partial^2\bar{P}}{\partial\bar{y}^2}\delta\bar{y}^2 + \frac{1}{2}\frac{\partial^2\bar{P}}{\partial\dot{x}^2}\delta\dot{x}^2 + \frac{1}{2}\frac{\partial^2\bar{P}}{\partial\dot{y}^2}\delta\dot{y}^2 + \frac{\partial^2\bar{P}}{\partial\bar{x}\partial\bar{y}}\delta\bar{x}\delta\bar{y} + \frac{\partial^2\bar{P}}{\partial\dot{x}\partial\bar{x}}\delta\dot{x}\delta\bar{x} + \frac{\partial^2\bar{P}}{\partial\dot{x}\partial\bar{y}}\delta\dot{x}\delta\bar{y} + \frac{\partial^2\bar{P}}{\partial\dot{y}\partial\bar{x}}\delta\dot{y}\delta\bar{x} + \frac{\partial^2\bar{P}}{\partial\dot{y}\partial\bar{y}}\delta\dot{y}\delta\bar{y} + \frac{\partial^2\bar{P}}{\partial\dot{x}\partial\dot{y}}\delta\dot{x}\delta\dot{y} \quad (5.24)$$

Similar to the linear analysis performed in the previous section, the perturbed pressure of Eq.(5.24) and the perturbed film thickness of Eq.(5.23) are to be substituted into the non-dimensional Reynolds equation (5.8). An order analysis (of second order terms) will then yield the partial differential equations in higher order pressure gradients:

$$\mathcal{O}(\delta x^2): \mathcal{R}\{\bar{P}_{xx}\} = \cos(\theta_n - 3\varphi_0)\left[\partial_\theta\left(\frac{{H_0}^2}{16\epsilon_0}\partial_\theta\bar{P}_0\right) + \left(\frac{D}{L}\right)^2\frac{{H_0}^2}{64\,\epsilon_0}\partial_{zz}\bar{P}_0\right] + \cos(\theta_n - \varphi_0)\left[\partial_\theta\left(\frac{{H_0}^2}{8\epsilon_0}\partial_\theta\bar{P}_0\right) + \left(\frac{D}{L}\right)^2\frac{{H_0}^2}{32\,\epsilon_0}\partial_{zz}\bar{P}_0\right] - \cos(\theta_n + \varphi_0)\left[\partial_\theta\left(\frac{3{H_0}^2}{16\epsilon_0}\partial_\theta\bar{P}_0\right) + \left(\frac{D}{L}\right)^2\frac{3{H_0}^2}{64\,\epsilon_0}\partial_{zz}\bar{P}_0\right] - \cos^2(\theta_n)\left[\partial_\theta\left(\frac{H_0}{2}\,\partial_\theta\bar{P}_0\right) + \left(\frac{D}{L}\right)^2\frac{H_0}{8}\,\partial_{zz}\bar{P}_0\right] - \cos(\theta_n)\left[\partial_\theta\left(\frac{{H_0}^2}{2}\partial_\theta\bar{P}_x\right) + \left(\frac{D}{L}\right)^2\frac{{H_0}^2}{8}\partial_{zz}\bar{P}_x\right] \quad (5.25)$$

$$\mathcal{O}(\delta y^2): \mathcal{R}\{\bar{P}_{yy}\} = -\cos(\theta_n - 3\varphi_0)\left[\partial_\theta\left(\frac{{H_0}^2}{16\epsilon_0}\partial_\theta\bar{P}_0\right) + \left(\frac{D}{L}\right)^2\frac{{H_0}^2}{64\,\epsilon_0}\partial_{zz}\bar{P}_0\right] + \cos(\theta_n - \varphi_0)\left[\partial_\theta\left(\frac{{H_0}^2}{8\epsilon_0}\partial_\theta\bar{P}_0\right) + \left(\frac{D}{L}\right)^2\frac{{H_0}^2}{32\,\epsilon_0}\partial_{zz}\bar{P}_0\right] + \cos(\theta_n + \varphi_0)\left[\partial_\theta\left(\frac{3{H_0}^2}{16\epsilon_0}\partial_\theta\bar{P}_0\right) + \left(\frac{D}{L}\right)^2\frac{3{H_0}^2}{64\,\epsilon_0}\partial_{zz}\bar{P}_0\right] - \sin^2(\theta_n)\left[\partial_\theta\left(\frac{H_0}{2}\,\partial_\theta\bar{P}_0\right) + \left(\frac{D}{L}\right)^2\frac{H_0}{8}\,\partial_{zz}\bar{P}_0\right] - \sin(\theta_n)\left[\partial_\theta\left(\frac{{H_0}^2}{2}\partial_\theta\bar{P}_y\right) + \left(\frac{D}{L}\right)^2\frac{{H_0}^2}{8}\partial_{zz}\bar{P}_y\right] \tag{5.26}$$

$$\mathcal{O}(\delta x\,\delta y): \mathcal{R}\{\bar{P}_{xy}\} = -\sin(\theta_n - 3\varphi_0)\left[\partial_\theta\left(\frac{{H_0}^2}{16\epsilon_0}\partial_\theta\bar{P}_0\right) + \left(\frac{D}{L}\right)^2\frac{{H_0}^2}{64\,\epsilon_0}\partial_{zz}\bar{P}_0\right] - \sin(\theta_n + \varphi_0)\left[\partial_\theta\left(\frac{3{H_0}^2}{16\epsilon_0}\partial_\theta\bar{P}_0\right) + \left(\frac{D}{L}\right)^2\frac{3{H_0}^2}{64\,\epsilon_0}\partial_{zz}\bar{P}_0\right] - \sin(2\theta_n)\left[\partial_\theta\left(\frac{H_0}{4}\,\partial_\theta\bar{P}_0\right) + \left(\frac{D}{L}\right)^2\frac{H_0}{16}\,\partial_{zz}\bar{P}_0\right] - \sin(\theta_n)\left[\partial_\theta\left(\frac{{H_0}^2}{4}\partial_\theta\bar{P}_x\right) + \left(\frac{D}{L}\right)^2\frac{{H_0}^2}{16}\partial_{zz}\bar{P}_x\right] - \cos(\theta_n)\left[\partial_\theta\left(\frac{{H_0}^2}{4}\partial_\theta\bar{P}_y\right) + \left(\frac{D}{L}\right)^2\frac{{H_0}^2}{16}\partial_{zz}\bar{P}_y\right] \tag{5.27}$$

$$\mathcal{O}(\delta x\,\delta\dot{x}): \mathcal{R}\{\bar{P}_{x\dot{x}}\} = -\frac{\pi}{2\epsilon_0}\cos(\theta_n - 3\varphi_0) - \frac{\pi}{\epsilon_0}\cos(\theta_n - \varphi_0) + \frac{3\pi}{2\epsilon_0}\cos(\theta_n + \varphi_0) - \cos(\theta_n)\left[\partial_\theta\left(\frac{{H_0}^2}{4}\partial_\theta\bar{P}_{\dot{x}}\right) + \left(\frac{D}{L}\right)^2\frac{{H_0}^2}{16}\partial_{zz}\bar{P}_{\dot{x}}\right] \tag{5.28}$$

$$\mathcal{O}(\delta x\,\delta\dot{y}): \mathcal{R}\{\bar{P}_{x\dot{y}}\} = \frac{\pi}{2\epsilon_0}\sin(\theta_n - 3\varphi_0) + \frac{3\pi}{2\epsilon_0}\sin(\theta_n + \varphi_0) - \cos(\theta_n)\left[\partial_\theta\left(\frac{{H_0}^2}{4}\partial_\theta\bar{P}_{\dot{y}}\right) + \left(\frac{D}{L}\right)^2\frac{{H_0}^2}{16}\partial_{zz}\bar{P}_{\dot{y}}\right] \tag{5.29}$$

$$\mathcal{O}(\delta y\,\delta\dot{x}): \mathcal{R}\{\bar{P}_{y\dot{x}}\} = \frac{\pi}{2\epsilon_0}\sin(\theta_n - 3\varphi_0) + \frac{3\pi}{2\epsilon_0}\sin(\theta_n + \varphi_0) - \sin(\theta_n)\left[\partial_\theta\left(\frac{{H_0}^2}{4}\partial_\theta\bar{P}_{\dot{x}}\right) + \left(\frac{D}{L}\right)^2\frac{{H_0}^2}{16}\partial_{zz}\bar{P}_{\dot{x}}\right] \tag{5.30}$$

$$\mathcal{O}(\delta y\,\delta\dot{y}): \mathcal{R}\{\bar{P}_{y\dot{y}}\} = \frac{\pi}{2\epsilon_0}\cos(\theta_n - 3\varphi_0) + \frac{\pi}{\epsilon_0}\cos(\theta_n - \varphi_0) - \frac{3\pi}{2\epsilon_0}\cos(\theta_n + \varphi_0) - \sin(\theta_n)\left[\partial_\theta\left(\frac{{H_0}^2}{4}\partial_\theta\bar{P}_{\dot{y}}\right) + \left(\frac{D}{L}\right)^2\frac{{H_0}^2}{16}\partial_{zz}\bar{P}_{\dot{y}}\right] \tag{5.31}$$

$$\mathcal{O}(\delta\dot{y}\,\delta\dot{y}) = \mathcal{O}(\,\delta\dot{x}\,\delta\dot{x}) = \mathcal{O}(\,\delta\dot{x}\,\delta\dot{y}) = 0 \tag{5.32}$$

where $\mathcal{R}\{\}$ is given in Eq.(5.15). Analogous to the induced pressure, bearing force components can be written in a series expansion as:

$$f_{\xi} \cong f_{\xi 0} + \sum_{i=1}^{4} \frac{\partial f_{\xi}}{\partial q_i}\delta q_i + \frac{1}{2}\sum_{i,j=1}^{4} \frac{\partial^2 f_{\xi}}{\partial q_i \partial q_j}\delta q_i \delta q_j \tag{5.33}$$

with $\xi = \bar{x}, \bar{y}$ and $q_1 = \bar{x}$, $q_2 = \bar{y}$, $q_3 = \dot{\bar{x}}$ and $q_4 = \dot{\bar{y}}$. The bearing force expansion of Eq.(5.33) can be written in terms of bearing dynamic coefficients:

$$\begin{aligned} f_{\xi} = f_{\xi 0} &+ \bar{K}_{\xi x}\delta\bar{x} + \bar{K}_{\xi y}\delta\bar{y} + \bar{C}_{\xi x}\delta\dot{\bar{x}} + \bar{C}_{\xi y}\delta\dot{\bar{y}} + \bar{K}_{\xi xx}\delta\bar{x}^2 + \bar{K}_{\xi yy}\delta\bar{y}^2 \\ &+ \bar{K}_{\xi xy}\delta\bar{x}\delta\bar{y} + \bar{C}_{\xi xx}\delta\dot{\bar{x}}\delta\bar{x} + \bar{C}_{\xi xy}\delta\dot{\bar{x}}\delta\bar{y} + \bar{C}_{\xi yx}\delta\dot{\bar{y}}\delta\bar{x} \\ &+ \bar{C}_{\xi yy}\delta\dot{\bar{y}}\delta\bar{y} \end{aligned} \tag{5.34}$$

where $\xi = \bar{x}, \bar{y}$, and $\bar{K}_{ijk} = \frac{C^2}{\Pi}\,K_{ijk}$, $\bar{C}_{ijk} = \frac{C^2\,\omega}{\Pi}\,C_{ijk}$ are non-dimensional second order nonlinear dynamic coefficients of the journal bearing. Note that in force expansion of Eq.(5.34), there are no coefficients defined as multiplying factors for $\delta\dot{x}\,\delta\dot{x}$, $\delta\dot{y}\,\delta\dot{y}$ and $\delta\dot{x}\,\delta\dot{y}$. This is because the order analysis for pressure gradients $\bar{P}_{\dot{x}\dot{x}}$, $\bar{P}_{\dot{y}\dot{y}}$, and $\bar{P}_{\dot{x}\dot{y}}$ resulted in a zero right hand side, as was given in Eq.(5.32). Thus, these pressure gradients are all zero and therefore the corresponding dynamic coefficients are zero as well.

By substituting the perturbed pressure of Eq.(5.24) and the series expansion of bearing force as in Eq.(5.34) into Eq.(5.18) and performing an order analysis, the nonlinear dynamic coefficients of the journal bearing can be given as functions of the second order pressure gradients:

$$\begin{aligned} &\begin{Bmatrix}\bar{K}_{xxx}\\ \bar{K}_{yxx}\end{Bmatrix} = -\tfrac{1}{2}\int_0^{\theta_{cav}}\int_{-\frac{1}{2}}^{\frac{1}{2}} \bar{P}_{xx}\begin{Bmatrix}\cos\theta_n\\ \sin\theta_n\end{Bmatrix} d\theta d\bar{z}\,, \begin{Bmatrix}\bar{K}_{xyy}\\ \bar{K}_{yyy}\end{Bmatrix} = -\tfrac{1}{2}\int_0^{\theta_{cav}}\int_{-\frac{1}{2}}^{\frac{1}{2}} \bar{P}_{yy}\begin{Bmatrix}\cos\theta_n\\ \sin\theta_n\end{Bmatrix} d\theta d\bar{z}\,, \\ &\begin{Bmatrix}\bar{K}_{xxy}\\ \bar{K}_{yxy}\end{Bmatrix} = -\tfrac{1}{2}\int_0^{\theta_{cav}}\int_{-\frac{1}{2}}^{\frac{1}{2}} \bar{P}_{xy}\begin{Bmatrix}\cos\theta_n\\ \sin\theta_n\end{Bmatrix} d\theta d\bar{z} \end{aligned} \tag{5.35}$$

and,

$$\begin{Bmatrix}\bar{C}_{xxx}\\ \bar{C}_{yxx}\end{Bmatrix} = -\frac{1}{2}\int_0^{\theta_{cav}}\int_{-\frac{1}{2}}^{\frac{1}{2}} \bar{P}_{x\dot{x}}\begin{Bmatrix}\cos\theta_n\\ \sin\theta_n\end{Bmatrix} d\theta d\bar{z}\ ,\ \begin{Bmatrix}\bar{C}_{xyx}\\ \bar{C}_{yyx}\end{Bmatrix} = -\frac{1}{2}\int_0^{\theta_{cav}}\int_{-\frac{1}{2}}^{\frac{1}{2}} \bar{P}_{x\dot{y}}\begin{Bmatrix}\cos\theta_n\\ \sin\theta_n\end{Bmatrix} d\theta d\bar{z},$$
$$\begin{Bmatrix}\bar{C}_{xxy}\\ \bar{C}_{yxy}\end{Bmatrix} = -\frac{1}{2}\int_0^{\theta_{cav}}\int_{-\frac{1}{2}}^{\frac{1}{2}} \bar{P}_{y\dot{x}}\begin{Bmatrix}\cos\theta_n\\ \sin\theta_n\end{Bmatrix} d\theta d\bar{z}\ ,\ \begin{Bmatrix}\bar{C}_{xyy}\\ \bar{C}_{yyy}\end{Bmatrix} = -\frac{1}{2}\int_0^{\theta_{cav}}\int_{-\frac{1}{2}}^{\frac{1}{2}} \bar{P}_{y\dot{y}}\begin{Bmatrix}\cos\theta_n\\ \sin\theta_n\end{Bmatrix} d\theta d\bar{z} \quad (5.36)$$

The nonlinear pressure gradients of Eq.(5.25) to (5.31) are numerically solved for and are then integrated according to Eq.(5.35) and (5.36) to find the journal bearing nonlinear dynamic coefficients.

5.1.3 Remarks

I) As was explained in the previous section, to find the pressure gradients for the nonlinear case, a perturbed expression for the film thickness is needed. The perturbed film will give rise to a perturbed pressure that is then expressed as a series expansion of up to second order. Although the necessity of a higher order pressure expansion is realized in the previous attempts to find nonlinear coefficients in the literature, the film thickness is generally expanded only to include the linear terms [53, 54, 94] as in Eq.(5.13). The resulting pressure gradients and nonlinear coefficients would then fail to follow the same trends for nonlinear short bearing coefficients [113], and this is the major source for variance in previously reported nonlinear coefficients in the literature. Thus, it is essential to include the higher order terms in the film thickness expansion as in Eq. (5.23) to ensure the resulting pressure gradients are accurately calculated.

II) In this chapter, the expressions for pressure gradients are directly calculated the in *X*-*Y* coordinate system by utilizing the circumferential angle θ_n. This was done to facilitate the bearing trajectory and stability analysis that are based on dynamic motion equations, normally expressed in the global *X*-*Y* coordinate. Alternatively, the dynamic coefficients can be represented as functions of pressure gradients in the *R*-*T* coordinate. To do this, the relation between the space derivatives in the two coordinate systems is needed:

$$\frac{\partial}{\partial\xi} = \frac{\partial}{\partial R}\frac{\partial R}{\partial\xi} + \frac{\partial}{\partial T}\frac{\partial T}{\partial\xi} \text{ with } \xi = x, y \quad (5.37)$$

From Eq.(5.12) we will have:

$$\frac{\partial R}{\partial x} = \cos\varphi_0 \, , \frac{\partial T}{\partial x} = -\sin\varphi_0 \, , \frac{\partial R}{\partial y} = \sin\varphi_0 \, , \frac{\partial T}{\partial x} = \cos\varphi_0 \tag{5.38}$$

It then follows:

$$\bar{P}_x = \bar{P}_R \cos\varphi_0 - \bar{P}_T \sin\varphi_0 \, , \bar{P}_y = \bar{P}_R \sin\varphi_0 - \bar{P}_T \cos\varphi_0 \tag{5.39}$$

and similarly for the higher order pressure gradients:

$$\begin{aligned} \bar{P}_{xx} &= \partial_R(\bar{P}_x)\cos\varphi_0 - \partial_T(\bar{P}_x)\sin\varphi_0 = \\ &\partial_R(\bar{P}_R\cos\varphi_0 - \bar{P}_T\sin\varphi_0)\cos\varphi_0 - \partial_T(\bar{P}_R\cos\varphi_0 - \bar{P}_T\sin\varphi_0)\sin\varphi_0 = \\ &\cos^2\varphi_0\,\partial_{RR}\bar{P} - \sin 2\varphi_0\,\partial_{RT}\bar{P} + \sin^2\varphi_0\,\partial_{TT}\bar{P} \end{aligned} \tag{5.40}$$

Integrating the pressure gradients of Eq.(5.39) and Eq.(5.40) according to Eq.(5.19) and Eq.(5.35) will result in similar expressions than those of Wang et al. [53] and Yang et al. [54].

5.2 Discretization

The Reynolds equation for steady pressure and the governing equations for pressure gradients as given in Eq. (5.15) and Eq.(5.25) to (5.31) are discretized based on the Finite Volume Method (FVM) in a similar fashion to the algorithm developed in Chapter 2. The non-dimensional Reynolds equation of Eq. (5.15) for steady pressure, $\bar{P}_0$, can be written in the following form:

$$-\frac{\partial \bar{P}_0}{\partial \tau} + \frac{1}{2\pi}\frac{\partial}{\partial\theta}\left(\frac{-{H_0}^3}{12}\frac{\partial \bar{P}_0}{\partial\theta}\right) + \frac{1}{8\pi}\left(\frac{D}{L}\right)^2\frac{\partial}{\partial\bar{z}}\left(\frac{-{H_0}^3}{12}\frac{\partial \bar{P}_0}{\partial\bar{z}}\right) = \frac{1}{2}\frac{\partial H_0}{\partial\theta} \tag{5.41}$$

Note that the leading term in the left-hand side of Eq.(5.41), $-\frac{\partial \bar{P}}{\partial\tau}$, is artificially added to the original steady equation to facilitate the implementation of robust implicit time-advance schemes. This technique is known as *pseudo-transient continuation* [114]. The solution to the original differential equation for $\bar{P}_0$ is now found as a steady state solution to the pseudo-time-dependent problem of Eq.(5.41) [36, 93].

A first order Implicit Euler discretization in time, and a second order finite volume space discretization of the Eq.(5.41) can be written for a representative two-dimensional cell in the mesh as:

$$\frac{\bar{u}_{i,j}{}^{n+1} - \bar{u}_{i,j}{}^{n}}{\Delta\tau} + \frac{F_{i+\frac{1}{2},j}{}^{n+1} - F_{i-\frac{1}{2},j}{}^{n+1}}{\Delta\theta} + \frac{G_{i,j+\frac{1}{2}}{}^{n+1} - G_{i,j-\frac{1}{2}}{}^{n+1}}{\Delta\bar{z}} = \bar{S}_{i,j} \tag{5.42}$$

with:

$$F = \frac{-H_0{}^3}{24\pi}\frac{\partial\bar{u}}{\partial\theta} \ , G = \left(\frac{D}{L}\right)^2 \frac{-H_0{}^3}{96\pi}\frac{\partial\bar{u}}{\partial\bar{z}} \tag{5.43}$$

where $\bar{u}_{i,j}$ and $\bar{S}_{i,j}$ are the control volume average of steady pressure, $\bar{P}_0$, and the source term, $\frac{1}{2}\frac{\partial H_0}{\partial\theta}$, for a representative surface element of the journal. In Eq. (5.42), superscript *n* indicates a variable value at the current time-step, and superscript *n+1* represents a variable value at the next time-step. The ½ indices in Eq. (5.42) correspond to the value of the flux at the cell boundary as compared to the flux values at the cell center. For instance, at a control surface boundary using a central differencing formulation we will have:

$$F_{i+\frac{1}{2},j} = -\frac{1}{24\pi}\left(\frac{H_{i+1,j} + H_{i,j}}{2}\right)^3 \left(\frac{\bar{u}_{i+1,j} - \bar{u}_{i,j}}{\Delta\theta}\right) \tag{5.44}$$

$F_{i-\frac{1}{2},j}$ can be found by replacing the indice i with $i-1$ in Eq.(5.44). The remaining fluxes in Eq. (5.42) can be found in a similar fashion. To express the flux in the next time-step as in Eq. (5.42), in terms of the flux and its gradients at the current time-step we can have:

$$\begin{aligned} F_{i+\frac{1}{2},j}{}^{n+1} &= F_{i+\frac{1}{2},j}\left(\bar{u}_{i,j}{}^{n+1}, \bar{u}_{i+1,j}{}^{n+1}\right) \\ &= F_{i+\frac{1}{2},j}\left(\bar{u}_{i,j}{}^{n} + \delta\bar{u}_{i,j}, \bar{u}_{i+1,j}{}^{n} + \delta\bar{u}_{i+1,j}\right) \\ &= F_{i+\frac{1}{2},j}\Big|^n + \frac{\partial F_{i+\frac{1}{2},j}}{\partial\bar{u}_{i,j}}\Big|^n \delta\bar{u}_{i,j} + \frac{\partial F_{i+\frac{1}{2},j}}{\partial\bar{u}_{i+1,j}}\Big|^n \delta\bar{u}_{i+1,j} + O(\delta\bar{u}^2) \end{aligned} \tag{5.45}$$

where $\delta\bar{u}_{i,j} = \bar{u}_{i,j}{}^{n+1} - \bar{u}_{i,j}{}^{n}$ and $F_{i+\frac{1}{2},j}\Big|^n = F_{i+\frac{1}{2},j}\left(\bar{u}_{i,j}{}^{n}, \bar{u}_{i+1,j}{}^{n}\right)$. Other terms in Eq. (5.42) are found similarly and are substituted back into Eq. (5.42) to obtain the discretized equation as:

$$\delta\bar{u}_{i,j}\left(\frac{1}{\Delta\tau}+\frac{1}{\Delta\theta}\frac{\partial F_{i+\frac{1}{2},j}}{\partial\bar{u}_{i,j}}-\frac{1}{\Delta\theta}\frac{\partial F_{i-\frac{1}{2},j}}{\partial\bar{u}_{i,j}}+\frac{1}{\Delta\bar{z}}\frac{\partial G_{i,j+\frac{1}{2}}}{\partial\bar{u}_{i,j}}-\frac{1}{\Delta\bar{z}}\frac{\partial G_{i,j-\frac{1}{2}}}{\partial\bar{u}_{i,j}}\right)$$
$$+\frac{1}{\Delta\theta}\frac{\partial F_{i+\frac{1}{2},j}}{\partial\bar{u}_{i+1,j}}\delta\bar{u}_{i+1,j}-\frac{1}{\Delta\theta}\frac{\partial F_{i-\frac{1}{2},j}}{\partial\bar{u}_{i-1,j}}\delta\bar{u}_{i-1,j}+\frac{1}{\Delta\bar{z}}\frac{\partial G_{i,j+\frac{1}{2}}}{\partial\bar{u}_{i,j+1}}\delta\bar{u}_{i,j+1} \tag{5.46}$$
$$-\frac{1}{\Delta\bar{z}}\frac{\partial G_{i,j-\frac{1}{2}}}{\partial\bar{u}_{i,j-1}}\delta\bar{u}_{i,j-1}=-\frac{F_{i+\frac{1}{2},j}-F_{i-\frac{1}{2},j}}{\Delta\theta}-\frac{G_{i,j+\frac{1}{2}}-G_{i,j-\frac{1}{2}}}{\Delta\bar{z}}+\bar{S}_{i,j}$$

Note that all the superscripts in Eq.(5.46) are dropped, knowing that all the terms are evaluated at the current time-step. Generalizing the individual element discretization of Eq. (5.46) to include all the cells within the meshed journal surface, one can write the resulting system of equations in the general form of a linear system in change in solution δu [93]:

$$[A][\delta u]=[B] \tag{5.47}$$

Where $[A]$ is a coefficient matrix and is a function of the derivative of fluxes at the cell boundaries in both directions, and matrix $[B]$ is the sum of the flux integral and the source term. The solution to the linear system of Eq.(5.46) will then yield the change in solution at every iteration (pseudo time-step) and thus the solution can be integrated until the asymptotic steady state is reached.

5.3 Dynamics and Stability of a Rotor-Bearing System

5.3.1 Mathematical Model for Rotor-Bearing Dynamics

The simplified model of a flexible rotor-bearing system of Figure 3-6 is adopted here. The non-dimensional equations of motion can be written in the state-space form as:

$$\begin{cases} -2\delta f_x+\bar{k}_s(X_3-X_1)=0 \\ -2\delta f_y+\bar{k}_s(X_4-X_2)=0 \\ \dot{X}_3=X_5 \\ \dot{X}_4=X_6 \\ \bar{\omega}^2\dot{X}_5+(X_3-X_1)=+\bar{m}_u\,\bar{R}_u\,\bar{\omega}^2\cos\tau \\ \bar{\omega}^2\dot{X}_6+(X_4-X_2)=+\bar{m}_u\,\bar{R}_u\,\bar{\omega}^2\sin\tau \end{cases} \tag{5.48}$$

where (X_1, X_2) and (X_3, X_4) are (x, y) coordinates of the journal center and the mass disk center position, respectively. In Eq.(5.48), $\bar{k}_s$ is the non-dimensional shaft stiffness, $\bar{m}_u$ is the non-dim unbalance mass at the disc location, $\bar{R}_u$ is the non-dim unbalance mass eccentricity radius:

$$\bar{\omega} = \omega\sqrt{M/K_s}\,, \bar{R}_u = \frac{R_u}{C}\,, \bar{m}_u = \frac{m_u}{M}\,, \bar{k}_s = \frac{C}{\Pi}\,K_s \tag{5.49}$$

where M is the total mass of the balanced system rotating at spin speed of ω. In Eq.(5.48), δf_x and δf_y are the non-dimensional journal bearing force components in excess of the equilibrium journal force, and are expressed in this chapter based on either of the following cases:

1) Linear and nonlinear dynamic coefficients; Case 1:

$$\begin{aligned}
\delta f_x = {} & \bar{K}_{xx}\delta X_1 + \bar{K}_{xy}\delta X_2 + \bar{C}_{xx}\dot{X}_1 + \bar{C}_{xy}\dot{X}_2 + \bar{K}_{xxx}\delta {X_1}^2 + \bar{K}_{xyy}\delta {X_2}^2 \\
& + \bar{K}_{xxy}\delta X_1\delta X_2 + \bar{C}_{xxx}\dot{X}_1\delta X_1 + \bar{C}_{xxy}\dot{X}_1\delta X_2 + \bar{C}_{xyx}\dot{X}_2\delta X_1 \\
& + \bar{C}_{xyy}\dot{X}_2\delta X_2 \\
\delta f_y = {} & \bar{K}_{yx}\delta X_1 + \bar{K}_{yy}\delta X_2 + \bar{C}_{yx}\dot{X}_1 + \bar{C}_{yy}\dot{X}_2 + \bar{K}_{yxx}\delta {X_1}^2 + \bar{K}_{yyy}\delta {X_2}^2 \\
& + \bar{K}_{yxy}\delta X_1\delta X_2 + \bar{C}_{yxx}\dot{X}_1\delta X_1 + \bar{C}_{yxy}\dot{X}_1\delta X_2 + \bar{C}_{yyx}\dot{X}_2\delta X_1 \\
& + \bar{C}_{yyy}\dot{X}_2\delta X_2
\end{aligned} \tag{5.50}$$

where δX_1 and δX_2 are the position of the journal center in excess of the equilibrium position and $\dot{X}_1$and $\dot{X}_2$ are instantaneous journal center velocities.

- Linear coefficient-based model; Case 1(a):
  - In this case, all the second order coefficients in Eq. (5.50) are set to zero.
- Nonlinear coefficient-based model; Case 1(b):
  - In this case, all the coefficients in Eq. (5.50) are retained.

2) Closed-form short bearing approximation; Case 2:

The journal forces can be expressed based on the short bearing Ocvirk solution [25] for a fully cavitated π-film (Gumbel Boundary Condition) short journal bearing:

$$\delta f_\epsilon = f_\epsilon - f_{\epsilon_0} \text{ with } f_\epsilon = \left(\frac{L}{D}\right)^2\left(1 - \frac{2\dot{\varphi}}{\omega}\right)\left(-\frac{2\pi^2(2\epsilon^2+1)\dot{\epsilon}}{\omega(1-\epsilon^2)^{5/2}\left(1-\frac{2\dot{\varphi}}{\omega}\right)} - \frac{4\pi\epsilon^2}{(1-\epsilon^2)^2}\right) \tag{5.51}$$

$$\delta f_\varphi = f_\varphi - f_{\varphi_0} \text{ with } f_\varphi = \left(\frac{L}{D}\right)^2 \left(1 - \frac{2\dot{\varphi}}{\omega}\right)\left(\frac{\pi^2 \epsilon}{(1-\epsilon^2)^{3/2}} + \frac{8\pi\epsilon\dot{\epsilon}}{\omega(1-\epsilon^2)^2\left(1-\frac{2\dot{\varphi}}{\omega}\right)}\right)$$

$$\begin{pmatrix}\delta f_x \\ \delta f_y\end{pmatrix} = Q^T \begin{pmatrix}\delta f_\epsilon \\ \delta f_\varphi\end{pmatrix}$$

where $f_{\epsilon_0} = f_\epsilon|_{(\dot{\epsilon},\dot{\varphi})=0}$ is the steady state journal force and Q is the CCW rotation matrix given in Eq.(5.12).

3) Closed-form finite bearing approximation; Case 3:

A closed-form approx. was given by Childs [84, 115] based on a weighted sum of the short and long bearing asymptotic solutions. The resulting bearing forces were given as:

$$\begin{pmatrix}F_x \\ F_y\end{pmatrix} = -2\,\mu\, L \left(\frac{R_j}{C}\right)^3 V_s \begin{pmatrix}Imp_x \\ Imp_y\end{pmatrix} \tag{5.52}$$

where V_s is the amplitude of the pure squeeze-velocity vector $\boldsymbol{V}_s$:

$$V_s = \left(\left(\dot{x} + \frac{\omega}{2} y\right)^2 + \left(\dot{y} - \frac{\omega}{2} x\right)^2\right)^{\frac{1}{2}} \tag{5.53}$$

with (x, y) and $(\dot{x}, \dot{y})$ being the instantaneous journal position and velocity in the global *X-Y* coordinate system. In Eq.(5.52) , Imp_j are components of the impedance vector, $\boldsymbol{Imp}$, with amplitude Imp:

$$\begin{aligned} &Imp_x = Imp\cos(\vartheta - \xi + \zeta)\ , Imp_y = Imp\sin(\vartheta - \xi + \zeta) \\ &Imp = \left(0.15(E^2 + G^2)^{\frac{1}{2}}(1 - \epsilon\cos\xi)^{\frac{3}{2}}\right)^{-1} \\ &E = 1 + 2.12\,Q\ , G = 3(\epsilon\sin\xi)\left(\frac{1 + 3.6\,Q}{4\,(1 - \epsilon\cos\xi)}\right), Q = (1 - \epsilon\cos\xi)\left(\frac{L}{D}\right)^{-2} \end{aligned} \tag{5.54}$$

where the attitude angle, ξ, is given as:

$$\xi = \left(1 - p(1-q^2)^{\frac{-1}{2}}\right)\left[\tan^{-1}\left(\frac{4\,(1+2.12\,B)\,(1-q^2)^{\frac{1}{2}}}{3(1+3.6\,B)\,q}\right) - \frac{\pi}{2}\frac{q}{|q|} + \sin^{-1} q\right] + \vartheta - \sin^{-1} q \tag{5.55}$$

with $p = \epsilon\cos\vartheta$, $q = \epsilon\sin\vartheta$ and $B = (1-\epsilon^2)\left(\frac{L}{D}\right)^{-2}$

ξ, ϑ are attitude angles measured from the instantaneous line of centers to the load line and squeeze velocity vector line, respectively. ζ, ψ are the attitude angles measure from the pure squeeze velocity vector and the line of centers to the global X coordinate, respectively. ξ, ϑ, ζ and ψ are shown in Figure 5-2 and can be expressed as:

$$\zeta = \tan^{-1}\left(\frac{\dot{y} - \frac{\omega}{2}x}{\dot{x} + \frac{\omega}{2}y}\right), \qquad \psi = \tan^{-1}\left(\frac{y}{x}\right), \qquad \vartheta = \psi - \zeta \tag{5.56}$$

The dynamic force expression of Eq.(5.52) is then used to form:

$$\begin{pmatrix}\delta f_x \\ \delta f_y\end{pmatrix} = \frac{1}{\Pi}\begin{pmatrix}F_x - F_{x_0} \\ F_y - F_{y_0}\end{pmatrix} \tag{5.57}$$

where F_{x_0} and F_{y_0} are steady state force components of the finite journal bearing of Eq.(5.52).

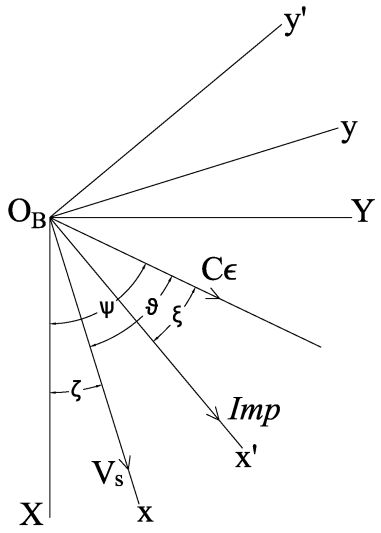

Figure 5-2. The attitudes angles as defined by Childs [84, 115]

5.3.2 Rotor-Bearing Stability: Linear Stability Analysis

Linear stability analysis for a dynamic system is carried out through a simple eigenvalue analysis. The threshold of instability is a critical value for the system parameter beyond which, the eigenvalues of the system will have positive real parts. For the simplified flexible rotor-bearing system of Eq.(5.48), the closed-form expression for the threshold speed of instability ω_{th} is given in Section 3.3 as:

$$\begin{aligned}
\bar{\omega}_{th}^2 &= \frac{\alpha}{\bar{\nu}^2(\bar{K}_s - \alpha)} \\
\alpha &= \frac{2(\bar{K}_{xy}\bar{C}_{yx} + \bar{K}_{yx}\bar{C}_{xy} - \bar{K}_{yy}\bar{C}_{xx} - \bar{K}_{xx}\bar{C}_{yy})}{\bar{C}_{xx} + \bar{C}_{yy}} \\
\bar{\nu}^2 &= \frac{\alpha^2 + 2(\bar{K}_{xx} + \bar{K}_{yy})\alpha + 4(\bar{K}_{xx}\bar{K}_{yy} - \bar{K}_{xy}\bar{K}_{yx})}{4(\bar{C}_{xy}\bar{C}_{yx} - \bar{C}_{xx}\bar{C}_{yy})}
\end{aligned} \tag{5.58}$$

Since the expression for ω_{th} in Eq.(5.58) is limited to the flexible rotor-bearing system of Eq.(5.48) with six general degrees of freedom, a more general approach is used in this chapter following Hassard et al. [76]; this approach is suitable for systems with any degrees of freedom. The method consists of a secant method to solve the equation $A(\nu) = 0$ and a Newton method to

find the fixed points of the system $\boldsymbol{X} = \boldsymbol{X}^*$ such that $\boldsymbol{f}(\boldsymbol{X}^*, \nu) = 0$. The algorithm is given in Appendix D .

5.3.3 Rotor-Bearing Stability: Nonlinear Stability Analysis

The stability of a rotor-bearing system before and after crossing the threshold speed of instability, as characterized by linear analysis, is the focus of the nonlinear stability analysis. As the system parameter crosses the critical parameter value, periodic solutions can exist before (subcritical) and after (supercritical) the crossing. While the mere existence of a larger amplitude periodic solution is considered as an unstable operating condition in the context of linear stability, systems can generally continue operating safely provided that the resulting periodic solution is stable. This occurs in a supercritical bifurcation where after crossing the threshold speed, phase portrait gradually spiral towards an isolated and stable limit cycle (i.e. isolated periodic solution). Assessing the stability of isolated periodic solutions, i.e. limit cycles, and characterizing the bifurcation types is not feasible with linear stability analysis.

Consider $\dot{\boldsymbol{X}} = \boldsymbol{f}(\boldsymbol{X}, \omega)$ has a T-periodic solution $\boldsymbol{\phi}(t)$. Stability of a periodic solution manifests itself in the way neighboring trajectories behave. If $\boldsymbol{X}(t, \boldsymbol{\eta}_0) \equiv \boldsymbol{\phi}(t, \boldsymbol{\eta_0})$ is a solution to $\dot{\boldsymbol{X}} = \boldsymbol{f}(\boldsymbol{X}, \omega)$ where $\boldsymbol{X}(0) = \boldsymbol{\eta}_0$ and $\boldsymbol{\phi}(t, \boldsymbol{\eta}_0 + \delta\boldsymbol{\eta})$ is a solution subject to the initial condition $\boldsymbol{X}(0) = \boldsymbol{\eta}_0 + \delta\boldsymbol{\eta}$, then at time $t = T$ the separation between the solutions is

$$\delta\boldsymbol{\phi}(T) = \boldsymbol{\phi}(T, \boldsymbol{\eta}_0 + \delta\boldsymbol{\eta}) - \boldsymbol{\phi}(T, \boldsymbol{\eta}_0) \cong \frac{\partial \boldsymbol{\phi}}{\partial \boldsymbol{\eta}}(T, \boldsymbol{\eta}_0).\delta\boldsymbol{\eta} = \boldsymbol{M}.\delta\boldsymbol{\eta} \tag{5.59}$$

therefore the matrix $\boldsymbol{M}$ (i.e. its eigenvalues) determines whether initial perturbations from the periodic orbit decay or grow. This matrix is called the *Monodromy* matrix [116]. At $t = 0$, any initial condition is also a solution and satisfies the differential equations of motion, thus $\boldsymbol{\phi}(0, \boldsymbol{\eta}) = \boldsymbol{\eta}$. It immediately follows that $\frac{\partial \boldsymbol{\phi}}{\partial \boldsymbol{\eta}}(0) = \boldsymbol{I}$. Since $\boldsymbol{\phi}(t, \boldsymbol{\eta}_0)$ also satisfies the system of equations $\dot{\boldsymbol{X}} = \boldsymbol{f}(\boldsymbol{X}, \omega)$, we have that:

$$\frac{d}{dt}\boldsymbol{\phi}(t, \boldsymbol{\eta}_0) = \boldsymbol{f}(\boldsymbol{\phi}(t, \boldsymbol{\eta}_0)) \text{ with } \boldsymbol{\phi}(0, \boldsymbol{\eta}_0) = \boldsymbol{\eta}_0 \tag{5.60}$$

Differentiating Eq. (5.60) with respect to $\boldsymbol{\eta}$ will yield:

$$\frac{d}{dt}\frac{\partial \boldsymbol{\phi}(t,\boldsymbol{\eta_0})}{\partial \boldsymbol{\eta}} = \frac{\partial \boldsymbol{f}(\boldsymbol{\phi})}{\partial \boldsymbol{\phi}}\frac{\partial \boldsymbol{\phi}(t,\boldsymbol{\eta_0})}{\partial \boldsymbol{\eta}} = D\boldsymbol{f}(\boldsymbol{\phi})\frac{\partial \boldsymbol{\phi}(t,\boldsymbol{\eta_0})}{\partial \boldsymbol{\eta}} \text{ with } \frac{\partial \boldsymbol{\phi}}{\partial \boldsymbol{\eta}}(0) = \boldsymbol{I} \tag{5.61}$$

Hence, the Monodromy matrix $\boldsymbol{M}$ is the same as $\boldsymbol{\Phi}(T)$ where $\boldsymbol{\Phi}(t) = \frac{\partial \boldsymbol{\phi}(t,\boldsymbol{\eta_0})}{\partial \boldsymbol{\eta}}$ is the *fundamental matrix solution* for the linearized equation about the periodic orbit:

$$\dot{\boldsymbol{\Phi}} = D\boldsymbol{f}(\boldsymbol{\phi})\,\boldsymbol{\Phi} \text{ with } \boldsymbol{\Phi}(0) = \boldsymbol{I} \tag{5.62}$$

$\boldsymbol{\phi}$(t) is periodic by definition, and hence $D\boldsymbol{f}(\boldsymbol{\phi})$ is also periodic; Eq. (5.62) takes the general form appropriate for the *Floquet theorem*. The eigenvalues of the Monodromy matrix are *characteristic multipliers,* $\rho_j = e^{\mu_j T}$, with *characteristic (Floquet) exponents* , μ_j, for the Eq. (5.62) and it is shown [116-118] that the periodic solution is stable if all the characteristic multipliers satisfy $|\rho_j| \leq 1$. The task is then reduced to calculating the Monodromy matrix, $\boldsymbol{M} = \frac{\partial \boldsymbol{\phi}(T,\boldsymbol{\eta}_0)}{\partial \boldsymbol{\eta}}$, and its eigenvalues. Except for special cases, this is generally difficult and a numerical perturbation method is needed to find an approximate solution of the periodic orbit before performing numerical differentiation to obtain $\boldsymbol{\Phi}(T)$.

5.3.4 Calculation of the Monodromy Matrix as a By-Product of Shooting Method

The underlying assumption here is that the system, $\dot{\boldsymbol{X}} = \boldsymbol{f}(\boldsymbol{X}, \omega)$, has a periodic solution, $\boldsymbol{\phi}(t)$, that exists due to a bifurcation in the system (particularly here, due to a Hopf bifurcation). The aim is, then, to identify the stability of the periodic solution based on the corresponding Monodromy matrix. The analysis here is based on the implementation of the shooting method to calculate the periodic solutions as given by Seydel [116, 119] and is implemented to be used for the system of equations given in Eq.(5.48).

Since $\boldsymbol{\phi}(t)$ is periodic, there exists a period T such that $\boldsymbol{\phi}(t) = \boldsymbol{\phi}(t+T)$. To find the periodic solution, the following boundary value problem needs to be solved:

$$\dot{\boldsymbol{X}} = \boldsymbol{f}(\boldsymbol{X}, \omega)\ ,\ \boldsymbol{X}(0) = \boldsymbol{\eta}\ ,\ \boldsymbol{X}(T) = \boldsymbol{\eta} \tag{5.63}$$

where $\boldsymbol{\eta}$ is a vector of initial values. Both $\boldsymbol{\eta}$ and T are unknown at this point. An initial guess of $\boldsymbol{\eta} = \boldsymbol{\eta}_0$ and $T = T_0$ is deviated from the actual values by $\Delta\boldsymbol{\eta} = \boldsymbol{\eta} - \boldsymbol{\eta}_0$ and $\Delta T = T - T_0$. An initial guess is acceptable provided that:

$$\boldsymbol{\phi}(T_0 + \Delta T, \boldsymbol{\eta}_0 + \Delta\boldsymbol{\eta}) - (\boldsymbol{\eta}_0 + \Delta\boldsymbol{\eta}) \approx \mathbf{0} \tag{5.64}$$

By Taylor expanding the first term on left hand side of Eq. (5.64) to the first order around $(T_0, \boldsymbol{\eta}_0)$, and back-substituting in Eq. (5.64) we can have:

$$\left(\frac{\partial\boldsymbol{\phi}}{\partial\boldsymbol{\eta}}(T_0, \boldsymbol{\eta}_0) - \boldsymbol{I}\right)\Delta\boldsymbol{\eta} + \frac{\partial\boldsymbol{\phi}}{\partial T}(T_0, \boldsymbol{\eta}_0)\,\Delta T \approx \boldsymbol{\eta}_0 - \boldsymbol{\phi}(T_0, \boldsymbol{\eta}_0) \tag{5.65}$$

In Eq. (5.65), the term $\frac{\partial\boldsymbol{\phi}}{\partial T}(T_0, \boldsymbol{\eta_0})$ is the slope of trajectories at $T = T_0$ and thus:

$$\frac{\partial\boldsymbol{\phi}}{\partial T}(T_0, \boldsymbol{\eta}_0) = \left.\frac{d\boldsymbol{\phi}(t, \boldsymbol{\eta}_0)}{dt}\right|_{T=T_0} = \boldsymbol{f}(\boldsymbol{\phi}(T_0, \boldsymbol{\eta}_0)) \approx \boldsymbol{f}(\boldsymbol{\phi}(0, \boldsymbol{\eta}_0)) = \boldsymbol{f}(\boldsymbol{\eta}_0) \tag{5.66}$$

The other term in Eq. (5.65), $\frac{\partial\boldsymbol{\phi}}{\partial\boldsymbol{\eta}}(T_0, \boldsymbol{\eta}_0)$, can be found by solving the system of ODEs as given in Eq. (5.62). The system of equations that are to be solved then consists of the set of ODEs in Eq. (5.60) simultaneously with that of Eq. (5.62). This will give a set of 42 coupled ODEs for the 6 *by* 6 system of Eq.(5.48). These coupled ODEs are to be integrated to $t = T_0$ and subsequently all the terms in Eq. (5.65) are found, which then enables us to calculate $\Delta\boldsymbol{\eta}$ and ΔT. Since Eq. (5.65) is a vector equation of order 6, but the total number of unknowns is 7 (being 6 unknowns in $\Delta\boldsymbol{\eta}$ and the extra unknown: ΔT), we need an additional equation to close the set. This can be achieved by imposing an orthogonality condition by enforcing the perturbations to be normal to the vector field: $\boldsymbol{f}^T.\Delta\boldsymbol{\eta} = \mathbf{0}$**.** Thus, the complete set can be written as:

$$\begin{pmatrix} \frac{\partial\boldsymbol{\phi}}{\partial\boldsymbol{\eta}}(T_0, \boldsymbol{\eta}_0) - \boldsymbol{I} & \boldsymbol{f}(\boldsymbol{\eta}_0) \\ \boldsymbol{f}^T(\boldsymbol{\eta}_0) & 0 \end{pmatrix}\begin{pmatrix}\Delta\boldsymbol{\eta} \\ \Delta T\end{pmatrix} = \begin{pmatrix}\boldsymbol{\eta}_0 - \boldsymbol{\phi}(T_0, \boldsymbol{\eta}_0) \\ 0\end{pmatrix} \tag{5.67}$$

The complete set of Eq.(5.67) can be written as a Newton iteration scheme:

$$\begin{pmatrix} \frac{\partial \boldsymbol{\phi}}{\partial \boldsymbol{\eta}}(T_k, \boldsymbol{\eta}_k) - \boldsymbol{I} & \boldsymbol{f}(\boldsymbol{\eta}_k) \\ \boldsymbol{f}^T(\boldsymbol{\eta}_k) & 0 \end{pmatrix}^k \begin{pmatrix} \Delta\boldsymbol{\eta}^{k+1} \\ \Delta T^{k+1} \end{pmatrix} = \begin{pmatrix} \boldsymbol{\eta}_k - \boldsymbol{\phi}(T_k, \boldsymbol{\eta}_k) \\ 0 \end{pmatrix}^k \tag{5.68}$$

All the coefficient matrices in Eq. (5.68) are to be re-calculated at each iteration. The final solution is converged when the second norm of the *change in solution vector* meets a certain tolerance: $\left\| \begin{pmatrix} \Delta\boldsymbol{\eta} \\ \Delta T \end{pmatrix} \right\|_2 \leq 10^{-6}$. As it is clear from the from Eq. (5.68) , $\boldsymbol{M} = \frac{\partial \boldsymbol{\phi}(T, \boldsymbol{\eta}_0)}{\partial \boldsymbol{\eta}}$, is calculated as the by-product of the shooting method. Finally, the eigenvalues of the Monodromy matrix are calculated to assess the stability of the periodic solution. The periodic solution is stable if the modulus of the calculated eigenvalues satisfy $|\rho_j| \leq 1$.

5.4 Results and Discussions

5.4.1 Finite Length Journal Bearing Dynamic Coefficients

The Reynolds Equation (5.8) is discretized for a structured mesh, similar to the method developed in Chapter 2 and Ref [93], and the resulting linear system of Eq.(5.46) is solved with the proposed Full Linear System (FLS) scheme. Alternatively, the Approximate Factorization (AF) scheme, in a similar fashion to the references [36, 93, 98], is also suitable and can be adopted for the discretized system of Eq.(5.46). In the detailed mesh sensitivity analysis of Chapter 2, a coarse grid (50×20 (θ, z)) and intermediate grid (100×40) were studied. It was shown that numerical uncertainty in calculating maximum target variables in the coarsest and intermediate grids, do not exceed % 1.2 and % 0.6 % for any of the calculated solution indicators of both grids, respectively. In the detailed grid study of Chapter 3 for calculation of linear bearing coefficients, it was shown that obtaining the solution for the first-order perturbations to the steady state Reynolds equation require no more restriction on the grid (compared to the steady state case) to produce accurate and mesh-independent results. This was indeed expected since the perturbations of the Reynolds equation are, by definition, tiny variations from the original steady state un-perturbed form. Thus, the grid that is sufficient for obtaining accurate results in the steady state case can be used for the perturbed equations as well. In light of this argument, further grid study for the higher order perturbations in this chapter is omitted and the finer grid of 100×40 is used for the analysis of this chapter. Similarly, the first order pressure gradients of Eq. (5.15), and the nonlinear second

order pressure gradients of Eq.(5.25) to (5.31) are discretized and solved for accordingly. The first and second order pressure gradients for a finite length journal bearing with $\frac{L}{D} = 1$ at eccentricity ratio of $\epsilon = 0.8$ are plotted in Figure 5-3.

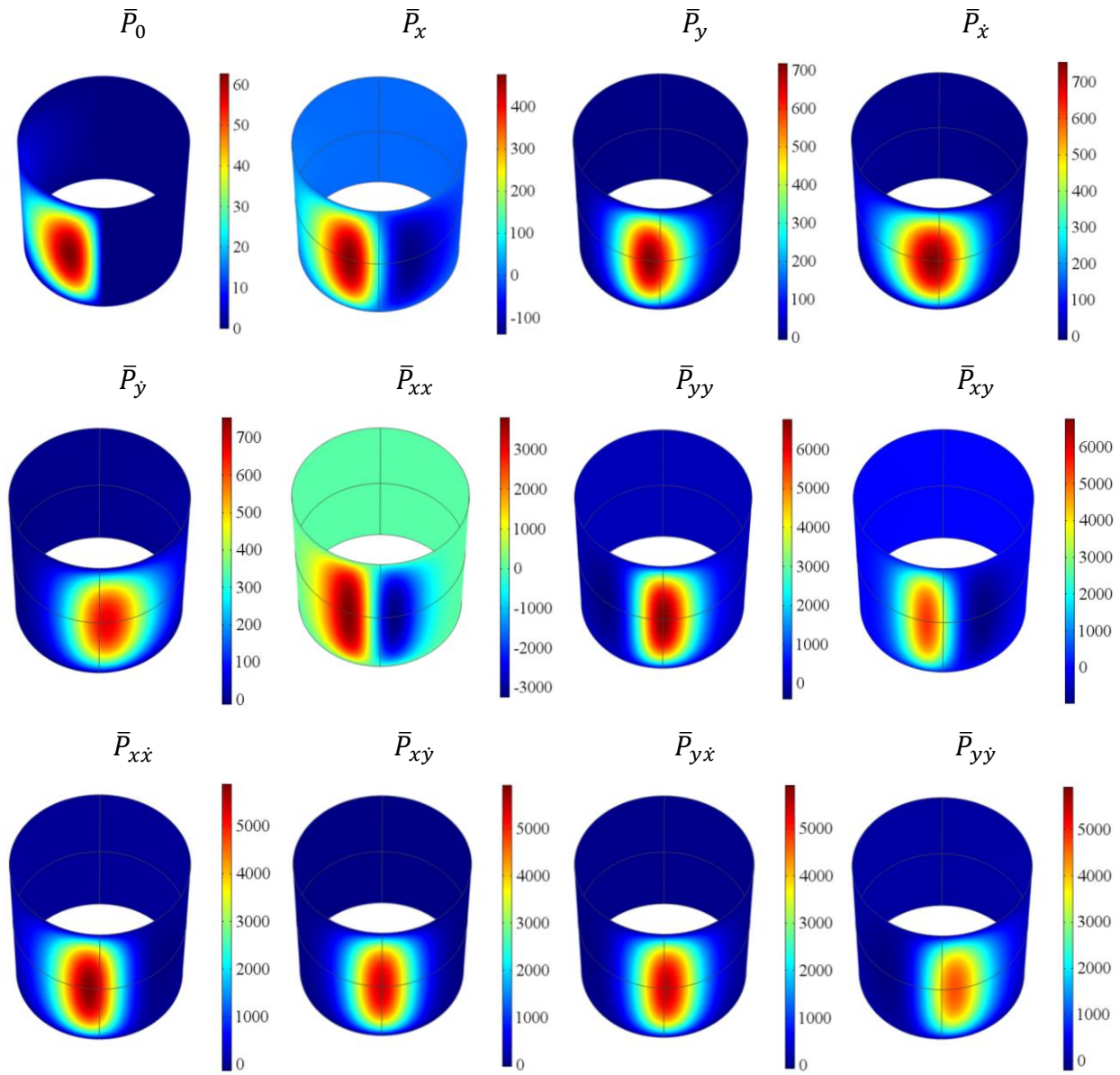

Figure 5-3. Journal bearing steady pressure and pressure gradients with $L/D = 1$ at $\epsilon = 0.8$

The linear pressure gradients of Eq. (5.15) and nonlinear pressure gradients of Eq.(5.25) to (5.31) are numerically solved for a range of journal eccentricity ratios, and are integrated according to Eq.(5.19), Eq.(5.35) and (5.36), to find the linear and nonlinear dynamic coefficients. The linear and nonlinear calculated dynamic coefficients for a finite journal bearing with $\frac{L}{D} = 1$ are shown in Figure 5-4 and Figure 5-5, respectively.

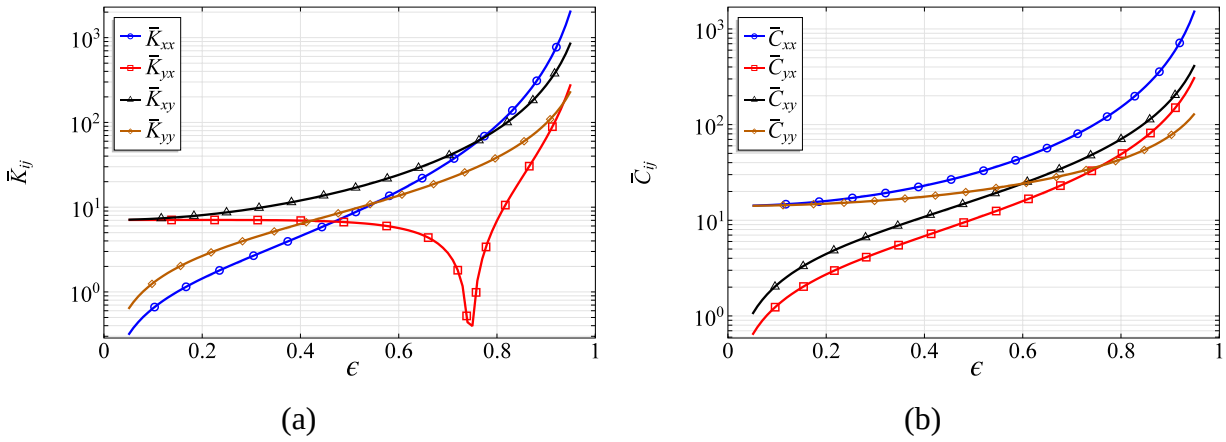

Figure 5-4. Linear stiffness coefficients (a), and damping coefficients (c), for a finite journal bearing with $L/D = 1$.

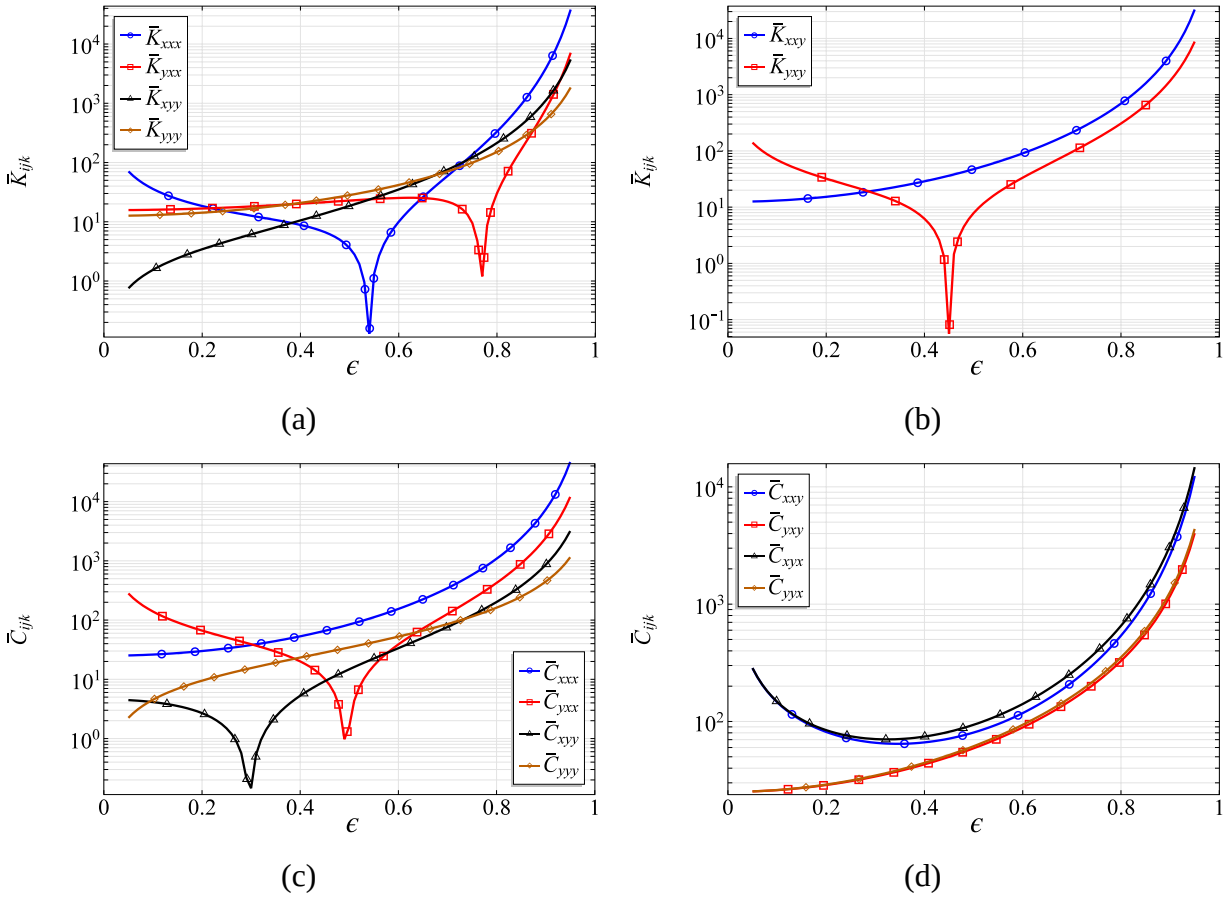

Figure 5-5. Nonlinear second order stiffness coefficients, (a) and (b), and damping coefficients, (c) and (d), for a finite journal bearing with $L/D = 1$.

The calculated coefficients are then used for linear and nonlinear stability analysis and to obtain the trajectories of the coefficient-based model of the rotor-baring system.

5.4.2 Comparison to Analytical Short Bearing Coefficients

The linear coefficients of a finite-length journal bearing, as given in Figure 5-4, can be compared with available analytical results for a π-film short bearing. The linear short bearing coefficients are reported in many previous studies [16, 25, 47, 48, 84, 92]. However, there is a significant shortage of available data for higher order coefficients. Nonlinear bearing coefficients of up to the third order were given in Chapter 4 for a π-film short bearing, and are used here as a basis for comparison for the calculated finite bearing results of Figure 5-5. $\bar{K}_{xx}, \bar{K}_{yx}, \bar{C}_{xx}, \bar{C}_{yx}, \bar{K}_{xxx}, \bar{K}_{yxx}, \bar{C}_{xxx}$ and $\bar{C}_{yxx}$ are selected as a subset, out of the total 22 coefficients, for comparison between the numerical finite bearing and analytical short bearing results. The curves are calculated for $\frac{L}{D} = 1$ and are plotted in Figure 5-6.

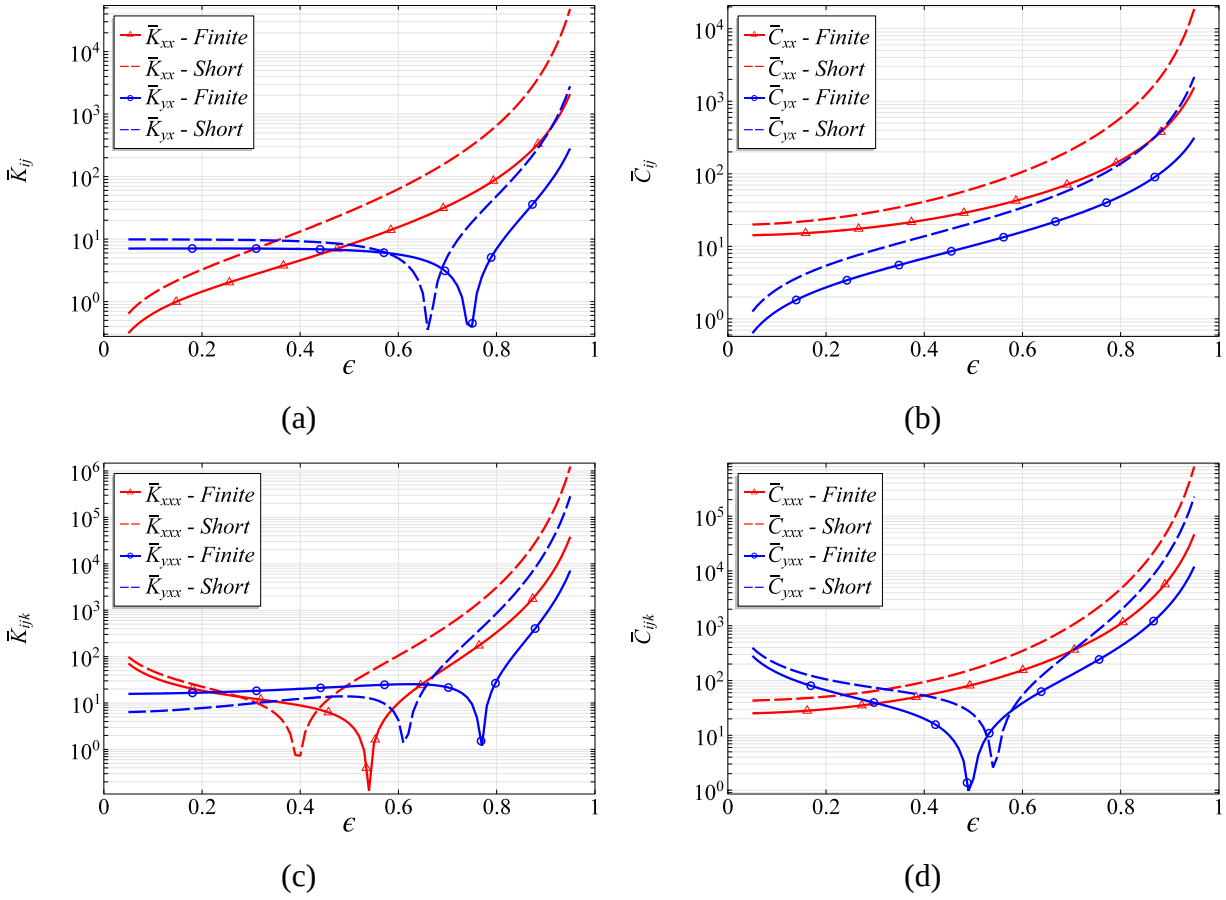

Figure 5-6. Comparison of linear and nonlinear dynamic coefficients for a journal bearing with $L/D = 1$ calculated based on analytic Short bearing coefficients given in Chapter 4 and proposed Finite coefficients given in this Chapter.

As can be seen in Figure 5-6 (a to d), the general trend for short and finite bearing coefficients are similar. This is indeed expected since the short bearing coefficients can be seen as an asymptotic limit of the finite bearing coefficients. Such qualitative agreement can also be used for verification purposes. This is specifically important for nonlinear coefficients, since essentially no useful experimental results are available in the literature. Also, the existing reported analytical coefficients (nonlinear) in the literature are too widespread to be used as a coherent basis for comparison and verification.

5.4.3 Stability Bounds and Bifurcation Types of the Rotor-Bearing System

The linear stability bounds of the flexible rotor-bearing system of Case 1 (Section 5.3) is calculated according to Algorithm 1 for a range of shaft non-dimensional stiffness values, and are plotted in Figure 5-7. The curves of the stability parameter, $\gamma = \frac{C\,K_s}{W}\bar{\omega}_{th}^2$, versus the Sommerfeld number, S, are marked by solid and/or dashed lines to differentiate the regions of sub and supercritical bifurcations. These regions are identified by the eigenvalue analysis of the Monodromy matrix as was discussed in Section 5.3.4. If the calculated Monodromy matrix at any given operating condition (for speeds beyond the threshold speed) has eigenvalues with a modulus of greater than unity, $\rho > 1$, the trajectories that start near the periodic solution will grow and thus the Hopf bifurcation is identified as subcritical. For $\rho \leq 1$ the region is considered supercritical. As expected, results presented in Figure 5-7 (a) show that the extent of the desired supercritical region is expanded by increasing the shaft stiffness.

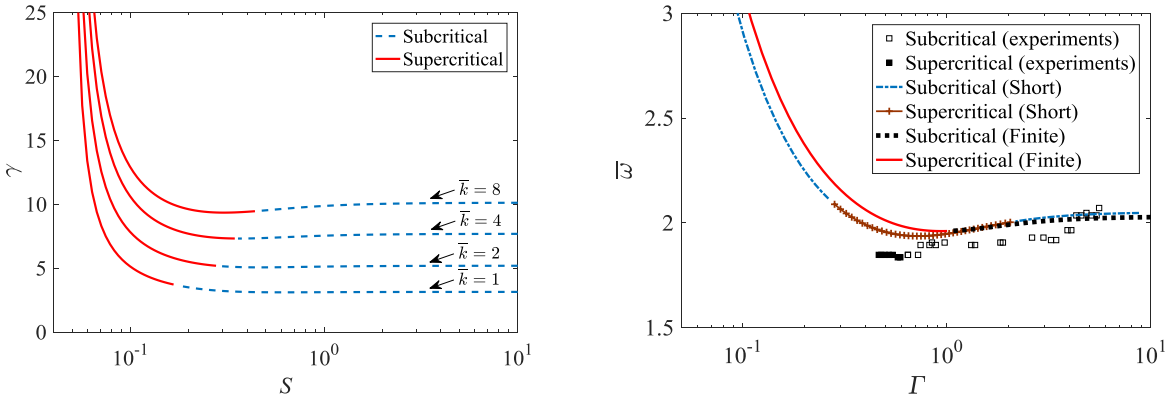

(a) (b)

Figure 5-7. Stability bounds of the flexible rotor-bearing system for a range of non-dimensional shaft stiffness values (a) and comparison to experimental results of Wang and Khonsari [90] (b)

The stability bounds and bifurcation regions of a flexible rotor-bearing system are also calculated with identical system parameters as in the experimental test rig of Wang and Khonsari [90], and are presented alongside their results in Figure 5-7 (b). The selected parameters are given in Table 5-1.

Table 5-1. System parameters for comparison to experimental results of Ref. [90]

Journal bearing length to diameter ratio,	$L/D = 1/2$
Journal Radius,	$R = 0.0127\ m$
Rotor Mass,	$M = 5.4523\ kg$
Radial Clearance,	$C = 50.8\times10^{-6}\ m$
Shaft non-dimensional stiffness,	$\bar{k} = 1.45$
Lubricant viscosity,	$\mu = 0.0274\ Pa.s$

The numerically calculated curves of Figure 5-7 (b) are given for two mathematical models:

- The "Short" bearing model given in Chapter 4 that is based upon a mathematical model of a rotor-bearing system with the bearing forces modeled as analytically obtained nonlinear dynamic coefficients of a short bearing.

- And the "Finite" model that is the proposed nonlinear coefficient-based model in this chapter, as in Case 1(a), Section 5.3.

For both numerical models, the calculated linear stability bound is sufficiently close to the reported experimental results of Wang and Khonsari [90]. However, the predicted boundary between the subcritical and supercritical regions is noticeably different. For all the curves in Figure 5-7 (b), the high Sommerfeld region is consistently marked as subcritical. As the static load on the shaft increases, i.e. lower Sommerfeld, the system becomes more stable until the bifurcation type changes to supercritical. This happens around $S = 0.6$ in the experiments and $S = 2.046$ for the short bearing model, whereas the prediction for the Finite model is $S = 1.003$. Thus, it is evident that the predicted results of the Finite bearing model are in much better agreement with the reported experimental results of Ref. [90].

Another difference between the short and finite models is seen in the very low Sommerfeld region, i.e. large static loads. While the prediction for the Finite model is a continuous supercritical region all the way to high eccentricity ratios, the short bearing model suggests another change in the

bifurcation type. The short bearing models do predict a continuous supercritical region in the low Sommerfeld region for higher shaft stiffness, as reported by Wang and Khonsari [90]; however, their predictions for short bearings, in line with HBT-based predictions of Chapter 4, suggest a change of bifurcation region at low Sommerfeld values for more flexible shafts. As no experimental results are available for these operating regions, it is not possible to conclusively comment on the accuracy of either models.

5.4.4 Rotor-Bearing Trajectories: Balanced Response

A direct time integration of the equations of motion, Eq.(5.48), for the four model cases of Section 5.3 is given here: The linear coefficient-based model, Case 1(a); the nonlinear coefficient-based model, Case 1(b); the short bearing force-based model, Case 2; and, the Finite bearing force-based model of Case 3. Journal bearing trajectories are calculated for all the model cases at four operating points. The selected operating points are marked with bullet-points in Figure 5-8.

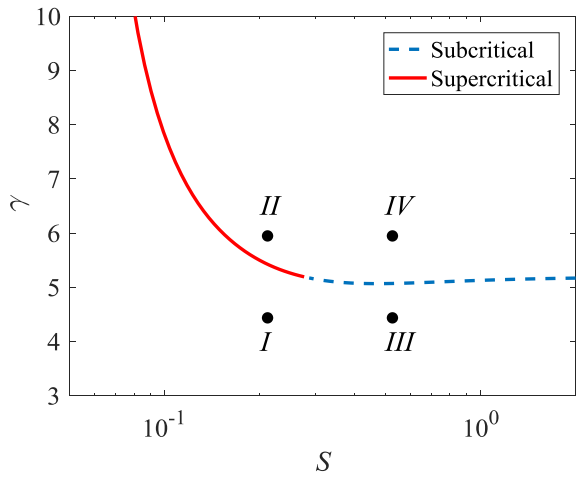

Figure 5-8. Selected operating points for a fully balanced flexible rotor-bearing system with $\bar{k} = CK_s/W = 2$ in stable and unstable regions for time integration

The operating points *I*, *II*, *III* and *IV*, as marked in Figure 5-8, are selected to demonstrate the system dynamics before crossing the threshold speed of instability (points *I*, *III*), and after crossing (points *II*, *IV*). The crossing from point *I* to *II* is in the supercritical region, whereas the crossing from point *III* to *IV* is governed by a subcritical Hopf bifurcation. The system parameters for selected operating points of Figure 5-8 is given in Table 5-2.

Table 5-2. System parameters for operating points *I, II, III* and *IV* of Figure 5-8

Operating point:	Stability parameter, γ:	Sommerfeld, S:	Shaft non-dimensional stiffness, $\bar{k}$:	$\frac{L}{D}$	Unbalance mass, m:	Bifurcation type:
I	4.4	0.2	2	1	N/A	super
II	6	0.2	2	1	N/A	super
III	4.4	0.5	2	1	N/A	sub
IV	6	0.5	2	1	N/A	sub

The calculated trajectories are given in Figure 5-9.

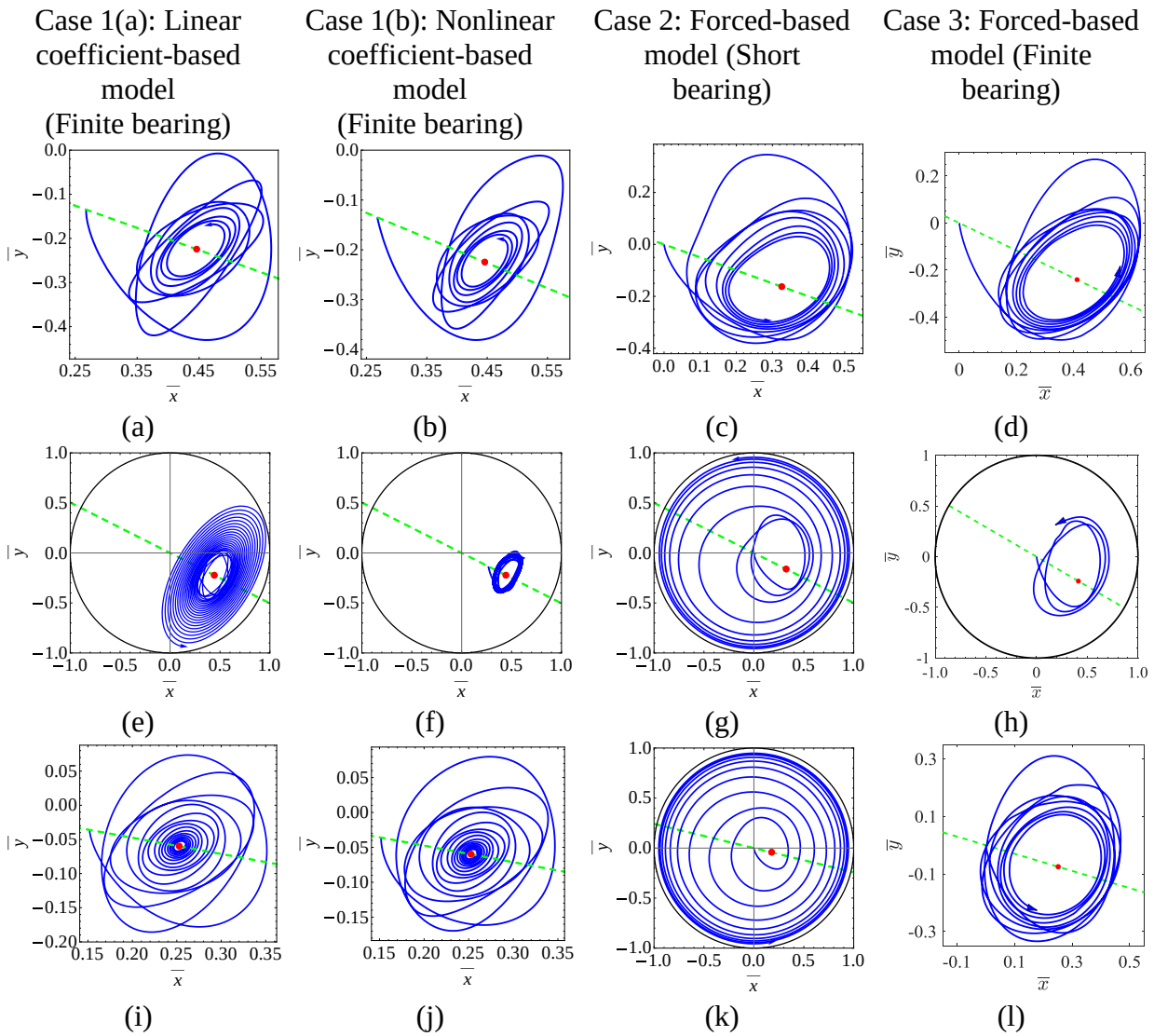

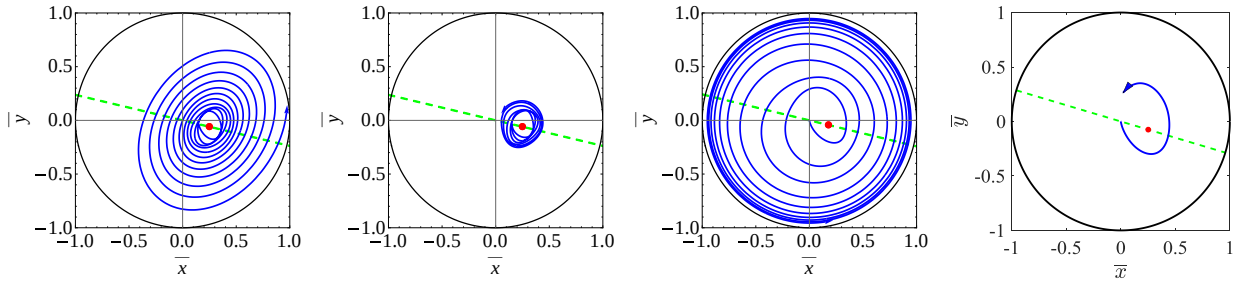

(m) (n) (o) (p)

Figure 5-9. Journal bearing trajectories of a balanced rotor-bearing system at different operating points: point *I* (a to d); point *II*: (e to h); point *III*: (i to l), and point *IV*: (m to p) for the case models of section 5.3: linear coefficient-based model (a, e, i and m); nonlinear coefficient-based model (b, f, j and n); short bearing force-based model (c, g, k and o); and finite bearing force-based model (d, h, l and p).

For operating point *I* in the stable supercritical region, all four model cases, Case 1 (a), (b) and Case 2 and 3, settle into the steady state point (marked by a bullet). This is shown in the trajectory plots of Figure 5-9 (a to d). After crossing the threshold speed, for operating point *II* in the supercritical region, it is expected for the system to have a stable periodic solution (limit cycle) due to a supercritical Hopf bifurcation. The calculated trajectories for operating point *II*, for all case models, is given in Figure 5-9 (e to h). However, the only case model that predicts the existence of the limit cycle is the nonlinear coefficient-base model, Case 1(b), as shown in Figure 5-9 (f). The linear coefficient-based model, Case 1 (a), is insensitive to bifurcation types and shows a gradual increase in the amplitude of the trajectories towards the boundary of the clearance circle marked by a solid circle as shown in Figure 5-9 (e).

For the operating point *III* in the stable subcritical region, the trajectory is expected to again settle into the stable fixed point of the system (i.e. steady state point). This is confirmed by the predictions of Case 1 (a), (b), and Case 3, as shown in Figure 5-9 (i), (j) and (l). However, the short bearing force-based model of Figure 5-9 (k), Case 2, incorrectly predicts an unstable behavior. The operating point *IV* lies in the unstable subcritical region, and thus the trajectory is expected to rapidly grow until only physically bounded by the bearing clearance circle. As shown in Figure 5-9 (n), (o) and (p), all the trajectories show growth to the clearance circle, or to the point where the numerical system is too stiff and further integration is not possible. The only exception is the predictions of the linear coefficient-model, Case 1(a), which is again insensitive to the bifurcation type and only predicts a gradual growth as shown in Figure 5-9 (m).

5.4.5 Rotor-Bearing Trajectories: Unbalanced Response

The balanced results in the previous section show the superiority of the nonlinear coefficient-based model in predicting the dynamics of the rotor-bearing system. In this section, the system response to unbalance excitations is studied, and linear and nonlinear-based model predictions, Case 1 (a) and (b), are compared to each other. The calculated trajectories at $S = 0.2$ and $\bar{k} = 2$ for four different rotational speeds are shown in Figure 5-10. In all cases, the unbalance mass is set to $m =$ 0.07 % of the total mass of the system.

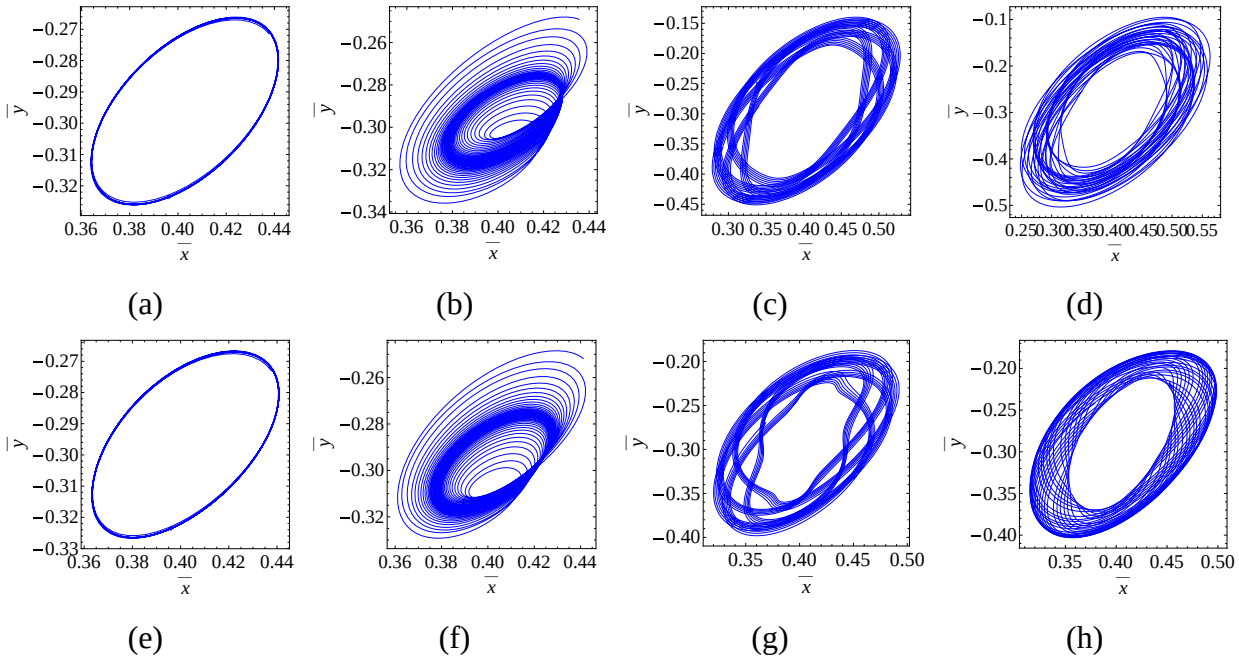

Figure 5-10. Journal bearing trajectories for the unbalanced rotor-bearing system, the linear coefficient-based model (a to d) and nonlinear coefficient-based model (e to h) at different stability parameters: $\gamma = 3.0$ (a and e), $\gamma = 4.40$ (b and f), $\gamma = 5.53$ (c and g) and $\gamma = 5.60$ (d and h).

From the one to one comparison of the unbalance trajectories of the linear and nonlinear system, it is evident that at low rotational speeds there is very good agreement between the predicted results, as shown in Figure 5-10 (a) and (e). By increasing the rotational speed, the trajectories start to deviate increasingly until, at high speeds, even the qualitative pattern in the obtained trajectories is not similar to each other, as shown in Figure 5-10 (d) and (h). Although the extent of the oil whirl amplitudes and space-span of journal trajectories is similar for both models, as portrayed in Figure 5-10 (c), (d), (g) and (h), the difference in the details of the patterns suggests the existence of higher harmonics in the journal response. The frequency content of the journal response at

different rotational speeds can be studied by means of Fourier analysis. Waterfall and contour diagrams of the journal vibrational signal in frequency domain is a common tool in rotor-dynamics, and are employed here for model Cases 1(a) and (b) as presented in Figure 5-11.

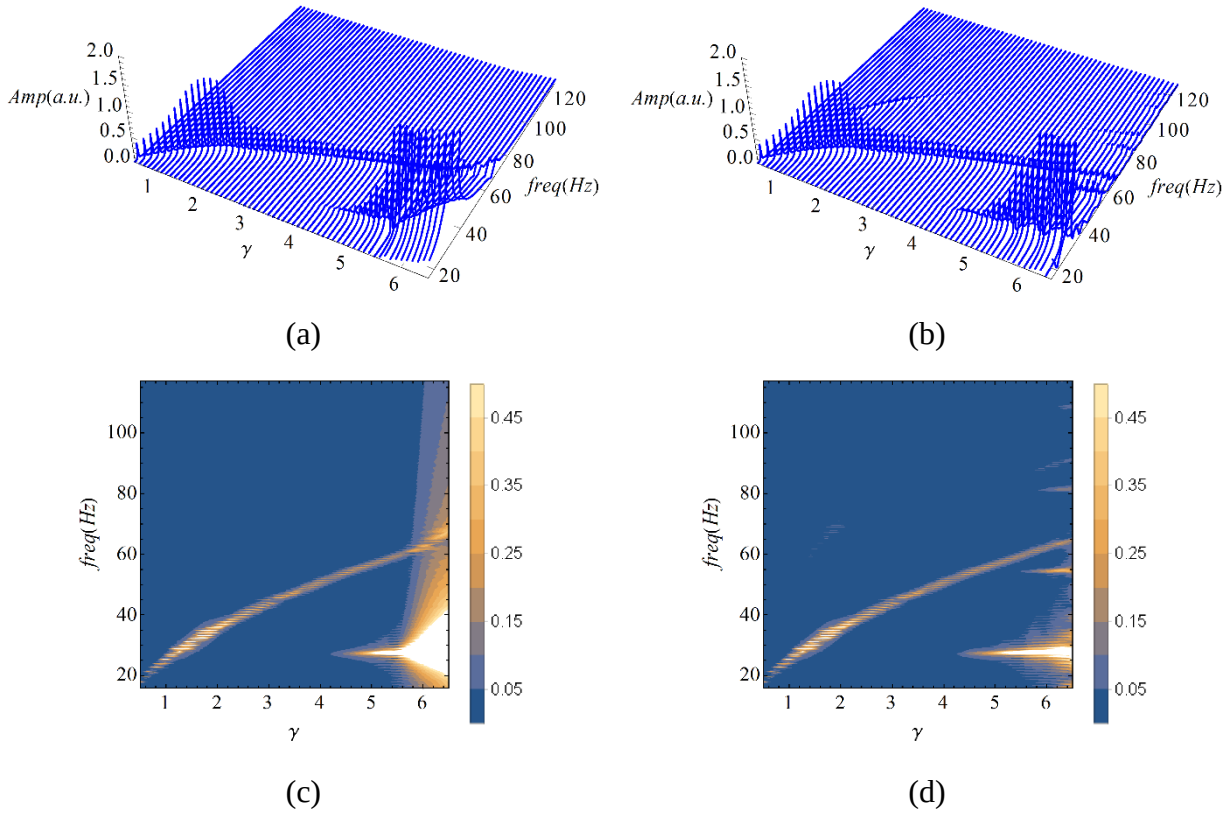

Figure 5-11. Waterfall plots (a-b) and contour plots (c-d) of the frequency content of the journal bearing unbalance response in x-direction for linear coefficient based model, (a) and (c), and for the nonlinear coefficient based model, (b) and (d).

The waterfall diagrams of Figure 5-11 (a) and (b) show the synchronous frequency component starting at lowest rotational speeds and extending to the highest spin speeds. This is expected, since an unbalance response is synchronized with rotational frequency of the rotor and its frequency increases by increasing the rotor spin speed. Since stability parameter $\gamma \propto \omega^2$, a parabola type dependency (instead of a linear dependence) in the frequency domain is expected. This is easily detected in all the subplots of Figure 5-11.

By increasing the stability parameter (and thus the rotational speed), there is an increase in the journal vibration amplitude, and it peaks around $\gamma = 1.6$ for both models. This is the first critical speed for the lateral vibrations of the shaft. Upon further increase of the stability parameter, the

first sign of sub-synchronous whirl appears at about $\gamma = 4.1$ in both models. After this threshold speed, the sub-synchronous whirl amplitude grows increasingly; however, its frequency remains approximately constant, with the constant being the first critical speed of the system. This "locking" of the whirl frequency to the critical speed is usually referred to as *oil whip*. Large oil whip amplitudes are very destructive for the safe operations of the rotor-bearing system. Although both models predict the onset of whipping similarly, the frequency band in the linear model is convoluted, and distinct narrow frequency bands are not detected beyond $\gamma = 5$. On the other hand, the whipping frequency bands in the nonlinear model, as in Figure 5-11 (d), are sufficiently narrow and the locking mechanism is properly identified.

Another shortcoming of the linear coefficient-based model is the absence of super-harmonics and other sub-harmonics (besides the whipping frequency) in the predicted journal frequency response. The nonlinear coefficient-based model, however, has predicted a range of super-harmonics; an extra subharmonic in the journal response as can be identified by narrow and low amplitude frequency bands beyond and below the synchronous parabola in Figure 5-11 (b) and (d). Predictions of higher harmonics is important not only since its existence is supported in experimental data [20, 120], but also for fault detection in rotor-bearing systems. Many fault detection criteria depend on the detection of sub and super-harmonics in vibration data to identify the existence and type of certain faults, such as shaft cracks [121], misalignment and radial loads [120], rotor to stator rubbing [120, 122], dry whip [123], etc. Thus, accurate prediction of such harmonics caused by the oil bearings is vital for successful fault detection and isolation in rotor-bearing systems.

Chapter 6: Conclusions and Future Work

6.1 Summary and Conclusions

The purpose of this thesis is to identify and characterize the oil whirl phenomenon — a destructive form of instability in rotor-bearing systems. To do so, the rotor-bearing system must be represented with a mathematical model that encapsulates the physics of the problem. The most significant step in constructing such a model is to represent the bearing forces that are caused by the shearing of oil in the bearing chamber. This is done by means of modeling the oil-induced forces through journal bearing dynamic coefficients that act as hypothetical springs and dampers in the dynamical model of the system. In order to calculate the dynamic coefficients, the simplified form of the Navier-Stokes equations for thin-film flows, the Reynolds equation, is solved in its original and perturbed form to find journal induced pressure and its gradients. Proper integration of the calculated pressure gradients can then reveal the sought-after dynamic coefficients.

Once the mathematical model of the system is constructed, linear and nonlinear stability analyses are carried out to find the bifurcation boundary (i.e. the stability boundary or the threshold speed after-which oil whirl occurs) and its directions/types. It was shown that identifying the bifurcation types for rotors supported on realistic journal bearings with finite length (for which analytical solutions cannot correctly predict the performance) is possible despite its absence in the literature. The proposed method was to construct the bearing induced forces, not only using the linear dynamic coefficients as is widely adopted in the literature, but also by including higher order nonlinear coefficients. The dependency of the Floquet exponents on higher order derivatives of the journal force was used as the basis for this hypothesis, primarily because bifurcation types are known to be identifiable if Floquet exponents can be found for periodic solutions (i.e. oil whirl trajectories) of the system.

Thorough analytical and numerical analysis is proposed for the calculation of the higher order dynamic coefficients. In the case of short bearings (also applicable to long bearings) with available closed-form expressions for the journal force, analytical coefficients were calculated based on a Taylor expansion of the journal force around the steady state points of the system. The numerical

coefficients were also found based on a perturbation analysis of the Reynolds equation. Numerically obtained coefficients are of ultimate interest since they can be found for any geometry and cavitation model, and thus are applicable to the finite length journal bearings that are of main interest in this thesis. As the analytical method is independent of the numerical approach, the calculated coefficients from the two methods were then compared against each other to verify the validity of the numerical/analytical results. Linear and nonlinear rotor-bearing models were then constructed based on the calculated linear and nonlinear coefficients for both finite-length and asymptotically short/long journal bearings. Both nonlinear models were shown to be suitable (and thus superior) for the calculation of bifurcation types while their linear counterparts fell short in providing a distinction between the bifurcations of the system.

More detailed findings are presented in the following subsections:

6.1.1 Conclusions on the Development of a Robust Algorithm for Cavitated Journal Bearings

A modified fast-converging and robust algorithm was proposed to solve the cavitation problem in axially grooved journal bearings based on the Finite Volume Method (FVM). Detailed discretization of the Adams/Elrod cavitation algorithm with the Vijayaraghavan and Keith treatment was derived and presented based on the FVM. The numerical stability of the fully discretized system was also analyzed by means of eigenvalue analysis of the coefficient matrix of the full linear system.

- The solution of the cavitation problem was shown to strongly depend on the specific values chosen for the bulk modulus of the lubricant.

- It was shown that by increasing the bulk modulus, the space span of the eigenvalues of the system both expands and shifts towards the right half plane, as a clear indicator for difficulty in the convergence of the discretized numerical system.

- Effects of static load and mesh size on the stability of the system were also studied. It was found that their impact is negligible compared to the dominant significance of varying bulk modulus values.

- It was shown how the new proposed scheme that is based on the direct solve of the full linear system is capable of handling the stiff system for any chosen value of the bulk modulus β.

- The new scheme showed a significant improvement in robustness compared to traditionally used Approximate Factorization based schemes.

6.1.2 Conclusions on The Effects of Turbulence on the Linear Stability of Rotor-Bearing Systems

The stability bounds of a rotor-bearing system was presented for a range of operating conditions based on a simplified mathematical model of the system. The simplification is mainly achieved by means of reducing the complicated fluid-solid interaction problem in the rotor-bearing system to the oscillation problem of a mass supported on a flexible and isolated support. Such reduction is made possible by replacing the fluid effects of the bearings by the so-called dynamic bearing coefficients. The proposed simplified model is based on a flexible shaft supported on identical finite length journal bearings. Dynamic coefficients of the journal bearing were calculated based on the Reynolds equation that is modified for turbulent flows. Two turbulent models were used for stability analysis and the corresponding stability boundaries were compared.

- Predicted threshold speeds of instability based on Constantinescu's model were found to be higher than the threshold speeds predicted by the Ng-Pan Elrod turbulent model, and hence the latter model proves to be more conservative in design.

- The stable region of flexible shafts supported on both turbulent and laminar journal bearings were shown to grow by increasing the shaft non-dimensional parameter.

- It was found that at low load and high Sommerfeld region ≥ 0.2 , the stability is not affected by the type of flow within the bearing chamber; hence, a laminar analysis that is based on a non-modified Reynolds equation is sufficient at these operating ranges.

- As the loading increases, the unstable operating region grows. This will result in the occurrence of unstable oil whirl, at even higher static loads, a region that the laminar-based stability analysis would consider a safe operating condition. Hence, modified stability analysis for turbulent flows needs to be implemented whenever the system is operating under high static load.

6.1.3 Conclusions on Nonlinear Stability Analysis Based on a Theoretical Higher Order Coefficient-Based Rotor-Bearing Model

The nonlinear second and third order dynamic coefficients of a journal bearing were presented based on higher order Taylor expansion of the journal forces around the steady state point of the rotor-bearing system. Dynamic coefficients were given in a general form, and for π-film short bearings, coefficients were given as functions of eccentricity ratio. The obtained nonlinear coefficients were then used jointly with linear coefficients in an attempt to express the induced journal force as higher order functions of journal position and velocity. A Hopf bifurcation subroutine was developed to study the birth and stability of limit cycles (oil whirl) in a flexible rotor-bearing system. Journal trajectories were obtained for four rotor-bearing models to further study the true dynamics of the system. In each model, the journal force is represented with either an available closed-form expression, linear dynamic coefficients, or nonlinear coefficients of up to second and third order.

- The proposed nonlinear coefficient model can potentially be extended to any journal bearing with a desired geometry while still revealing the true dynamics of the system.

- The higher order representation was shown to be particularly useful in the study of Hopf bifurcations and stability of oil whirl phenomenon in a flexible rotor-bearing system.

- Little qualitative difference was found between the nonlinear coefficient-based models of second and third order.

- The more simplified second order model was found to be capable of predicting the bifurcations and nonlinear dynamics of the rotor-baring system.

- The second order nonlinear coefficient-based model can be used as a simplified alternative to the third order model when calculating all the higher order coefficients is not practically feasible, especially for finite length journal bearings.

6.1.4 Conclusions on Nonlinear Stability Analysis based on a Numerical Higher Order Coefficient-Based Rotor-Bearing Model

Nonlinear dynamic coefficients for a finite length journal bearing were found by means of an extended perturbation analysis on the Reynolds lubrication equation. The governing equations for steady pressure and its gradients were then discretized and solved by means of a Finite Volume scheme.

- It was shown how a proper higher order perturbation of the film thickness can be used to derive governing equations for first and second order pressure gradients.

The calculated gradients were then used to obtain linear and nonlinear stiffness and damping coefficients for a finite length journal bearing. Numerically obtained dynamic coefficients for a finite bearing were compared to previously calculated analytical short bearing coefficients.

- A qualitative agreement was observed between the coefficients.

- As short bearing results are in fact an asymptotic limit for finite coefficients, such agreements were used as verification for the proposed finite bearing coefficients.

Linear and nonlinear stability of a flexible rotor-bearing system supported on end journal bearings was studied. A mathematical model, *nonlinear coefficient-based model*, was presented based on the calculated linear and nonlinear finite bearing dynamic coefficients. Alternative models based on available closed-form solutions for journal force were also presented for comparison purposes. A numerical algorithm was used to calculate the linear stability bounds (threshold speed of instability) of the given dynamical systems. At spin speeds beyond the threshold speed, the system undergoes a Hopf bifurcation and periodic solutions are born. A nonlinear analysis based on the Shooting method was presented to calculate the Monodromy matrix associated with the existing periodic solutions of the system. The stability of the periodic orbits was then assessed based on the eigenvalue analysis of the calculated Monodromy matrix at any given operating condition.

- Curves of stability were shown to have two general bifurcation regions: the sub and supercritical bifurcation.

- The predicted boundary between the bifurcation regions for the proposed model were found to be in good agreement with the existing experimental results and was shown to be a particularly better estimate compared to the results of the short bearing analysis.

- It was also found that the desired supercritical region expands by increasing the shaft stiffness.

Journal bearing trajectories were also obtained for the proposed mathematical models of the rotor-bearing system. This was done by time-integration of the governing dynamical equations of motion for linear and nonlinear coefficient-based models, as well as the short and finite bearing force-based models. Trajectories were initially obtained for a fully balanced system. The unbalance trajectories were also obtained for the linear and nonlinear coefficient-based models.

- The balanced results suggested the superiority of the proposed nonlinear coefficient-based model, as it was the only model to properly predict the existence of stable limit cycles beyond the threshold speed of instability in supercritical bifurcation regions.

- Results indicate that although both models have qualitatively similar trajectories, there are noticeable differences in both the patterns and frequency content of the calculated vibration signals.

- A complete frequency analysis of the system for a wide range of operating speeds (waterfall diagram) showed that the nonlinear model is better at modelling the lock-in oil whip mechanism as well as capturing sub and super harmonics in the vibration signal.

- The linear model fell short in detecting these harmonics.

- As super and subharmonic signals are widely used as signatures for rotor-bearing fault detection, the ability of the proposed nonlinear model in resolving such frequencies was found to be critically important.

6.2 Limitations and Future Work

At high spin speeds of the shaft, the induced pressure increases; however, the shearing of oil in the bearing chamber can produce excessive heat that can then result in the reduction of oil viscosity; however, the oil viscosity is assumed to be constant in this thesis. Since a reduction in lubricant viscosity also reduces the bearing induced pressures, it counteracts the increase in the pressure at high spin speeds and thus affects bearing performance. Consequently, including the effect of heat generation in the journal bearings and the temperature dependence of oil viscosity is the next important step for modifying the stability boundaries and identifying the bifurcation types of the system. Another assumption throughout this thesis was that the oil dynamics is governed by properties of Newtonian fluids. Shear-thinning at high rotational speeds can affect the stability boundaries of the system and its effects should be included in future studies.

The proposed cavitation algorithm is very well behaved in steady state analysis, yet, difficulties arise if the time dependent solution is of interest. Such difficulty is shared between all the existing cavitation models and thus needs to be addressed. The proper use of pre-conditioners in solving the discretized system of equations, and the use of more advanced iterative solvers can serve as a potential remedy for the time dependent problems and can be studied in the future.

Although the proposed coefficient-based models in this thesis can generally be extended to any bearing geometry and a variety of cavitation boundary conditions, the extension is not necessarily carried out easily. Journal bearings are made in a variety of shapes and incorporating these shapes and cavitation boundaries can introduce convergence difficulties for the perturbed Reynolds equation. Independent research should be devoted to study such effects on linear and nonlinear stability of rotor-bearing systems.

References

[1] Rankine, W., 1869, "On the centrifugal force of rotating shafts," Engineer, 27, pp. 249-249.

[2] Vance, J. M., Zeidan, F. Y., and Murphy, B., 2010, Machinery vibration and rotordynamics, John Wiley & Sons.

[3] Gunter, E. J., Center, L. R., and Laboratories, F. I. R., 1966, Dynamic stability of rotor-bearing systems, Scientific and Technical Information Division, National Aeronautics and Space Administration.

[4] Jeffcott, H., 1919, "XXVII. The lateral vibration of loaded shafts in the neighbourhood of a whirling speed.—The effect of want of balance," The London, Edinburgh, and Dublin Philosophical Magazine and Journal of Science, 37(219), pp. 304-314.

[5] Reynolds, O., 1886, "On the Theory of Lubrication and Its Application to Mr. Beauchamp Tower's Experiments, Including an Experimental Determination of the Viscosity of Olive Oil," Proceedings of the Royal Society of London, 40(242-245), pp. 191-203.

[6] Harrison, W., 1913, The hydrodynamical theory of lubrication with special reference to air as a lubricant, Univ. press.

[7] Newkirk, B. L., and Taylor, H. D., 1925, "Shaft whipping due to oil action in journal bearing," General Electric Review, 28, pp. 559–568.

[8] Hori, Y., 1959, "A theory of oil whip," ASME J. Appl. Mech, 26, pp. 189-198.

[9] Smith, D., 1933, "The motion of a rotor carried by a flexible shaft in flexible bearings," Proceedings of the Royal Society of London. Series A, 142(846), pp. 92-118.

[10] Prohl, M., 1945, "A general method for calculating critical speeds of flexible rotors," Journal of Applied Mechanics, 12(3), pp. 142-148.

[11] Hagg, A., and Sankey, G., 1956, "Some dynamic properties of oil-film journal bearings with reference to the unbalance vibration of rotors," J Appl Mech, 78, pp. 302-306.

[12] Raimondi, A., and Boyd, J., 1958, "A Solution for the Finite Journal Bearing and its Application to Analysis and Design: I," ASLE Transactions, 1(1), pp. 159-174.

[13] Lund, J. W., 1966, "Self-excited Stationary Whirl Orbits of a Journal in a Sleeve Bearing," Rensselaer Polytechnic Institute, PhD Thesis.

[14] Adams, M. L., 2009, Rotating machinery vibration: from analysis to troubleshooting, CRC Press.

[15] Lund, J., 1987, "Stability and damped critical speeds of a flexible rotor in fluid-film bearings," Rotating machinery dynamics, pp. 1-9.
[16] Vance, J. M., 1988, Rotordynamics of turbomachinery, John Wiley & Sons.
[17] Ehrich, F., 1964, "Shaft whirl induced by rotor internal damping," Journal of Applied Mechanics, 31, p. 279.
[18] Ehrich, F. F., 1969, "The dynamic stability of rotor/stator radial rubs in rotating machinery," Journal of Engineering for Industry, 91, p. 1025.
[19] Benckert, H., and Wachter, J., 1980, "Flow induced spring coefficients of labyrinth seals for application in rotor dynamics," NASA. Lewis Res. Center Rotodyn. Instability Probl. in High-Performance Turbomachinery p 189-212(SEE N 80-29706 20-37).
[20] Muszynska, A., 1988, "Stability of whirl and whip in rotor/bearing systems," Journal of Sound and Vibration, 127(1), pp. 49-64.
[21] Ehrich, F., 1991, "Some observations of chaotic vibration phenomena in high-speed rotordynamics," Journal of vibration, acoustics, stress, and reliability in design, 113(1), pp. 50-57.
[22] Temperley, H., and Trevena, D., 1977, "Metastability of phase transitions and the tensile strength of liquids," Proc. Proceedings of the Royal Society of London A: Mathematical, Physical and Engineering Sciences, The Royal Society, pp. 395-402.
[23] Braun, M., and Hannon, W., 2010, "Cavitation formation and modelling for fluid film bearings: a review," Proceedings of the Institution of Mechanical Engineers, Part J: Journal of Engineering Tribology, 224(9), pp. 839-863.
[24] Brewe, D. E., 1986, "Theoretical modeling of the vapor cavitation in dynamically loaded journal bearings," Journal of tribology, 108(4), pp. 628-637.
[25] Szeri, A. Z., 2011, Fluid film lubrication, Cambridge University Press Cambridge.
[26] Christopherson, D. G., 1941, "A new mathematical method for the solution of film lubrication problems," Proceedings of the Institution of Mechanical Engineers, 146(1), pp. 126-135.
[27] Ausas, R., Ragot, P., Leiva, J., Jai, M., Bayada, G., and Buscaglia, G. C., 2007, "The impact of the cavitation model in the analysis of microtextured lubricated journal bearings," Journal of tribology, 129(4), pp. 868-875.
[28] Ausas, R. F., Jai, M., and Buscaglia, G. C., 2009, "A mass-conserving algorithm for dynamical lubrication problems with cavitation," Journal of tribology, 131(3), p. 031702.

[29] Jakobsson, B. a. F., L., 1957, "The finite Journal bearing considering vaporization," Transactions of Chalmers University of Technology, Guthenberg, Sweden, 190, p. 308.
[30] Olsson, K. O., 1965, "Cavitation in dynamically loaded bearing," Trans. Chalmers University of Technology, Guthenberg, Sweden 308, p. 308.
[31] Etsion, I., and Ludwig, L., 1982, "Observation of pressure variation in the cavitation region of submerged journal bearings," Journal of Lubrication Technology, 104(2), pp. 157-163.
[32] Elrod, H., and Adams, M., "A computer program for cavitation and starvation problems," Proc. First LEEDS LYON Symposium on Cavitation and Related Phenomena in Lubrication, Mechanical Engineering Publications for the Institute of Tribology, New York, pp. 37-41.
[33] Elrod, H. G., 1981, "A cavitation algorithm," Journal of tribology, 103(3), pp. 350-354.
[34] Miranda, A., 1983, "Oil flow, cavitation and film reformation in journal bearings, including an interactive computer-aided design study," University of Leeds.
[35] Hirani, H., Athre, K., and Biswas, S., 2001, "A simplified mass conserving algorithm for journal bearing under large dynamic loads," International Journal of Rotating Machinery, 7(1), pp. 41-51.
[36] Vijayaraghavan, D., and Keith, T., 1990, "An efficient, robust, and time accurate numerical scheme applied to a cavitation algorithm," Journal of tribology, 112(1), pp. 44-51.
[37] Woods, C. M., and Brewe, D. E., 1989, "The solution of the Elrod algorithm for a dynamically loaded journal bearing using multigrid techniques," Journal of tribology, 111(2), pp. 302-308.
[38] Qiu, Y., and Khonsari, M., 2009, "On the prediction of cavitation in dimples using a mass-conservative algorithm," Journal of tribology, 131(4), p. 041702.
[39] Vijayaraghavan, D., and Keith, T., 1990, "Grid transformation and adaption techniques applied in the analysis of cavitated journal bearings," Journal of tribology, 112(1), pp. 52-59.
[40] Almqvist, A., Fabricius, J., Larsson, R., and Wall, P., 2014, "A new approach for studying cavitation in lubrication," Journal of tribology, 136(1), p. 011706.
[41] Bayada, G., and Chupin, L., 2013, "Compressible fluid model for hydrodynamic lubrication cavitation," Journal of tribology, 135(4), p. 041702.
[42] Bertocchi, L., Dini, D., Giacopini, M., Fowell, M. T., and Baldini, A., 2013, "Fluid film lubrication in the presence of cavitation: a mass-conserving two-dimensional formulation for compressible, piezoviscous and non-Newtonian fluids," Tribology International, 67, pp. 61-71.

[43] Sahlin, F., Almqvist, A., Larsson, R., and Glavatskih, S., 2007, "A cavitation algorithm for arbitrary lubricant compressibility," Tribology International, 40(8), pp. 1294-1300.
[44] Bayada, G., 2014, "From a compressible fluid model to new mass conserving cavitation algorithms," Tribology International, 71, pp. 38-49.
[45] Braun, M., and Hendricks, R., 1984, "An experimental investigation of the vaporous/gaseous cavity characteristics of an eccentric journal bearing," ASLE transactions, 27(1), pp. 1-14.
[46] Giacopini, M., Fowell, M. T., Dini, D., and Strozzi, A., 2010, "A mass-conserving complementarity formulation to study lubricant films in the presence of cavitation," Journal of tribology, 132(4), p. 041702.
[47] Lund, J., 1987, "Review of the concept of dynamic coefficients for fluid film journal bearings," Journal of tribology, 109(1), pp. 37-41.
[48] Qiu, Z., and Tieu, A., 1996, "The effect of perturbation amplitudes on eight force coefficients of journal bearings," Tribology Transactions, 39(2), pp. 469-475.
[49] Strogatz, S. H., 2014, Nonlinear dynamics and chaos: with applications to physics, biology, chemistry, and engineering, Westview press.
[50] Choy, F. K., Braun, M. J., and Hu, Y., 1991, "Nonlinear Effects in a Plain Journal Bearing: Part 1—Analytical Study," Journal of tribology, 113(3), pp. 555-561.
[51] Andréas, L. S., and De Santiago, O., 2005, "Identification of journal bearing force coefficients under high dynamic loading centered static operation," Tribology Transactions, 48(1), pp. 9-17.
[52] Meruane, V., and Pascual, R., 2008, "Identification of nonlinear dynamic coefficients in plain journal bearings," Tribology International, 41(8), pp. 743-754.
[53] Weimin, W., Lihua, Y., Tiejun, W., and Lie, Y., 2012, "Nonlinear dynamic coefficients prediction of journal bearings using partial derivative method," Proceedings of the Institution of Mechanical Engineers, Part J: Journal of Engineering Tribology, 226(4), pp. 328-339.
[54] Yang, L.-H., Wang, W.-M., Zhao, S.-Q., Sun, Y.-H., and Yu, L., 2014, "A new nonlinear dynamic analysis method of rotor system supported by oil-film journal bearings," Applied Mathematical Modelling, 38(21), pp. 5239-5255.
[55] HASHIMOTO, H., and WADA, S., 1982, "An influence of inertia forces on stability of turbulent journal bearings," Bulletin of JSME, 25(202), pp. 653-662.

[56] Hashimoto, H., Wada, S., and Ito, J.-i., 1987, "An application of short bearing theory to dynamic characteristic problems of turbulent journal bearings," Journal of tribology, 109(2), pp. 307-314.
[57] Wang, J., and Khonsari, M., 2006, "Application of Hopf bifurcation theory to rotor-bearing systems with consideration of turbulent effects," Tribology international, 39(7), pp. 701-714.
[58] Chang-Jian, C.-W., and Chen, C. o.-K., 2006, "Bifurcation and chaos of a flexible rotor supported by turbulent journal bearings with non-linear suspension," Proceedings of the Institution of Mechanical Engineers, Part J: Journal of Engineering Tribology, 220(6), pp. 549-561.
[59] Chang-Jian, C.-W., and Chen, C.-K., 2007, "Bifurcation and chaos analysis of a flexible rotor supported by turbulent long journal bearings," Chaos, Solitons & Fractals, 34(4), pp. 1160-1179.
[60] Adams, M., and McCloskey, T., "Large unbalance vibration in steam turbine-generator sets."
[61] Hollis, P., and Taylor, D., 1986, "Hopf bifurcation to limit cycles in fluid film bearings," Journal of tribology, 108(2), pp. 184-189.
[62] Myers, C., 1984, "Bifurcation theory applied to oil whirl in plain cylindrical journal bearings," Journal of Applied Mechanics, 51, p. 244.
[63] Noah, S. T., and Sundararajan, P., 1995, "Significance of considering nonlinear effects in predicting the dynamic behavior of rotating machinery," Journal of Vibration and Control, 1(4), pp. 431-458.
[64] Adams, M., 1980, "Non-linear dynamics of flexible multi-bearing rotors," Journal of Sound and Vibration, 71(1), pp. 129-144.
[65] Ehrich, F. F., "Subharmonic vibration of rotors in bearing clearance," ASME.
[66] Bently, D., 1974, "Forced subrotative speed dynamic action of rotating machinery," ASME paper(74-PET), p. 16.
[67] Botman, M., "Experiments on oil-film dampers for turbomachinery."
[68] Childs, D. W., "Fractional-frequency rotor motion due to nonsymmetric clearance effects," p. 1981.
[69] Saito, S., 1985, "Calculation of nonlinear unbalance response of horizontal Jeffcott rotors supported by ball bearings with radial clearances," Journal of Vibration Acoustics Stress and Reliability in Design, 107, p. 416.
[70] Yamauchi, S., 1983, "The nonlinear vibration of flexible rotors," Trans. of JSME, 446(49), pp. 1862-1868.

[71] NOAH, S., and CHOI, Y. S., 1987, "Nonlinear steady-state response of a rotor-support system," ASME, Transactions, Journal of Vibration, Acoustics, Stress, and Reliability in Design, 109, pp. 255-261.

[72] Ehrich, F. F., 1987, "High order subharmonic response of high speed rotors in bearing clearance," Rotating machinery dynamics, pp. 167-174.

[73] Holmes, A., Ettles, C., and Mayes, I., 1978, "The aperiodic behaviour of a rigid shaft in short journal bearings," International Journal for Numerical Methods in Engineering, 12(4), pp. 695-702.

[74] Nikolajsen, J., and Holmes, R., 1979, "Investigation of squeeze-film isolators for the vibration control of a flexible rotor," Journal of Mechanical Engineering Science, 21(4), pp. 247-252.

[75] Muszynska, A., 1986, "Whirl and whip—rotor/bearing stability problems," Journal of Sound and Vibration, 110(3), pp. 443-462.

[76] Hassard, B. D., Kazarinoff, N. D., and Wan, Y. H., 1981, Theory and applications of Hopf bifurcation, CUP Archive.

[77] Ding, Q., Cooper, J., and Leung, A., 2002, "Hopf bifurcation analysis of a rotor/seal system," Journal of Sound and Vibration, 252(5), pp. 817-833.

[78] Kapitaniak, T., 1992, Chaotic oscillators: theory and applications, World Scientific Publishing Company Incorporated.

[79] Nayfeh, A. H., and Balachandran, B., 2008, Applied nonlinear dynamics: analytical, computational, and experimental methods, Wiley-VCH.

[80] Hori, Y., "Anti-earthquake considerations in rotordynamics," pp. 1-8.

[81] Hori, Y., and Kato, T., 1990, "Earthquake-induced instability of a rotor supported by oil film bearings," Journal of vibration, acoustics, stress, and reliability in design, 112(2), pp. 160-165.

[82] Khonsari, M., and Chang, Y., 1993, "Stability boundary of non-linear orbits within clearance circle of journal bearings," Journal of vibration and acoustics, 115(3), pp. 303-307.

[83] Wang, J., and Khonsari, M., 2006, "Prediction of the stability envelope of rotor-bearing system," Journal of vibration and acoustics, 128(2), pp. 197-202.

[84] Childs, D., 1993, "Turbomachinery rotordynamics- Phenomena, modeling, and analysis(Book)," New York: John Wiley & Sons, Inc, 1993.

[85] Childs, D., Moes, H., and Van Leeuwen, H., "Journal bearing impedance descriptions for rotordynamic applications," p. 1976.

[86] Deepak, J., and Noah, S., 1998, "Experimental verification of subcritical whirl bifurcation of a rotor supported on a fluid film bearing," Journal of tribology, 120(3), pp. 605-609.
[87] Muszynska, A., and Bently, D., 1990, "Frequency-swept rotating input perturbation techniques and identification of the fluid force models in rotor/bearing/seal systems and fluid handling machines," Journal of Sound and Vibration, 143(1), pp. 103-124.
[88] Poore, A., 1976, "On the theory and application of the Hopf-Friedrichs bifurcation theory," Archive for Rational Mechanics and Analysis, 60(4), pp. 371-393.
[89] Namachchivaya, N. S., and Ariaratnam, S., 1987, "Periodically perturbed Hopf bifurcation," SIAM Journal on Applied Mathematics, 47(1), pp. 15-39.
[90] Wang, J., and Khonsari, M., 2006, "Bifurcation analysis of a flexible rotor supported by two fluid-film journal bearings," Journal of tribology, 128(3), pp. 594-603.
[91] Raimondi, A. A., and Szeri, A. Z., 1984, "Journal and Thrust Bearings," CRC Handbook of Lubrication (Theory and Practice of Tribology), E. R. Booser, ed., pp. 413-462.
[92] Lund, J., 1964, "Spring and damping coefficients for the tilting-pad journal bearing," ASLE transactions, 7(4), pp. 342-352.
[93] Miraskari, M., Hemmati, F., Jalali, A., AlQaradawi, M., and Gadala, M. S., 2016, "A Robust Modification to the Universal Cavitation Algorithm in Journal Bearings," Journal of Tribology.
[94] Sawicki, J. T., and Rao, T., 2004, "A nonlinear model for prediction of dynamic coefficients in a hydrodynamic journal bearing," International Journal of Rotating Machinery, 10(6), pp. 507-513.
[95] Vijayaraghavan, D., and Keith Jr, T., 1989, "Development and evaluation of a cavitation algorithm," Tribology Transactions, 32(2), pp. 225-233.
[96] Ståhl, J., and Jacobson, B. O., 2003, "Compressibility of lubricants at high pressures," Tribology Transactions, 46(4), pp. 592-599.
[97] Guy, B., 2014, "From a compressible fluid model to new mass conserving cavitation algorithms," Tribology International, 71, pp. 38-49.
[98] Rao, T., and Sawicki, J. T., 2002, "Linear stability analysis for a hydrodynamic journal bearing considering cavitation effects," Tribology Transactions, 45(4), pp. 450-456.
[99] Ceze, M., and Fidkowski, K. J., 2015, "Constrained pseudo-transient continuation," International Journal for Numerical Methods in Engineering, 102(11), pp. 1683-1703.

[100] Fesanghary, M., and Khonsari, M., 2011, "A modification of the switch function in the Elrod cavitation algorithm," Journal of tribology, 133(2), p. 024501.

[101] Celik, I. B., Ghia, U., and Roache, P. J., 2008, "Procedure for estimation and reporting of uncertainty due to discretization in {CFD} applications," Journal of fluids {Engineering-Transactions} of the {ASME}, 130(7).

[102] Jalali, A., Sharbatdar, M., and Ollivier-Gooch, C., 2014, "Accuracy analysis of unstructured finite volume discretization schemes for diffusive fluxes," Computers & Fluids, 101, pp. 220-232.

[103] DiPrima, R., 1963, "A note on the stability of flow in loaded journal bearings," ASLE transactions, 6(3), pp. 249-253.

[104] Taylor, C., and Dowson, D., 1974, "Turbulent lubrication theory—application to design," Journal of Lubrication Technology, 96(1), pp. 36-46.

[105] Constantinescu, V., 1959, "On turbulent lubrication," Proceedings of the Institution of Mechanical Engineers, 173(1), pp. 881-900.

[106] Elrod, H., and Ng, C., 1967, "A theory for turbulent fluid films and its application to bearings," Journal of Lubrication Technology, 89(3), pp. 346-362.

[107] Gertzos, K., Nikolakopoulos, P., and Papadopoulos, C., 2008, "CFD analysis of journal bearing hydrodynamic lubrication by Bingham lubricant," Tribology International, 41(12), pp. 1190-1204.

[108] Hopf, E., 1942, "Abzweigung einer periodischen Lösung von einer stationären Lösung eines Differentialsystems," Ber. Math.-Phys. Kl Sächs. Akad. Wiss. Leipzig, 94, pp. 1-22.

[109] Marsden, J. E., and McCracken, M., 2012, The Hopf bifurcation and its applications, Springer Science & Business Media.

[110] Hassard, B., and Wan, Y., 1978, "Bifurcation formulae derived from center manifold theory," Journal of Mathematical Analysis and Applications, 63(1), pp. 297-312.

[111] Andronov, A. A., and Fishwick, W., 1966, Theory of oscillators, Courier Corporation.

[112] Dai, R., Dong, Q., and Szeri, A., 1992, "Approximations in hydrodynamic lubrication," Journal of tribology, 114(1), pp. 14-25.

[113] Miraskari, M., Hemmati, F., AlQaradawi, M., and Gadala, M. S., 2016, "Linear Stability Analysis of Finite Length Journal bearings in Laminar and Turbulent Regimes."

[114] Kelley, C. T., and Keyes, D. E., 1998, "Convergence analysis of pseudo-transient continuation," SIAM Journal on Numerical Analysis, 35(2), pp. 508-523.

[115] Childs, D., Moes, H., and Van Leeuwen, H., 1977, "Journal bearing impedance descriptions for rotordynamic applications," Journal of lubrication technology, 99(2), pp. 198-210.
[116] Seydel, R., 2009, Practical bifurcation and stability analysis, Springer Science & Business Media.
[117] Hale, J. K., 1969, "Ordinary differential equations," Pure and Applied Mathematics, 21.
[118] Reithmeier, E., 1991, Periodic solutions of nonlinear dynamical systems, Springer.
[119] Seydel, R., 1985, "Calculating the loss of stability by transient methods, with application to parabolic partial differential equations," Numerical Boundary Value ODEs, Springer, pp. 261-270.
[120] Muszynska, A., 1995, "Vibrational diagnostics of rotating machinery malfunctions," International Journal of Rotating Machinery, 1(3-4), pp. 237-266.
[121] Dimarogonas, A. D., 1996, "Vibration of cracked structures: a state of the art review," Engineering Fracture Mechanics, 55(5), pp. 831-857.
[122] Muszynska, A., 1989, "Rotor-to-stationary element sub-related vibration phenomena in rotating machinery: literature survey," The Shock and Vibration Digest, 21(3), pp. 3-11.
[123] Fan, C.-C., Syu, J.-W., Pan, M.-C., and Tsao, W.-C., 2011, "Study of start-up vibration response for oil whirl, oil whip and dry whip," Mechanical Systems and Signal Processing, 25(8), pp. 3102-3115.

Appendices

Appendix A : Discretized Reynolds Equation for the Cavitation Problem

To simplify notation it is useful to define:

$$H_{i+1/2,j} = \frac{H_{i+1,j} + H_{i,j}}{2};\ and\ \ H_{i,j+1/2} = \frac{H_{i,j+1} + H_{i,j}}{2}$$
$$H_{i-1/2,j} = \frac{H_{i-1,j} + H_{i,j}}{2};\ and\ \ H_{i,j-1/2} = \frac{H_{i,j-1} + H_{i,j}}{2} \qquad (A.1)$$
$$g_{i+1/2,j} = \frac{g_{i+1,j} + g_{i,j}}{2};\ and\ \ g_{i-1/2,j} = \frac{g_{i-1,j} + g_{i,j}}{2}$$

Recall from Eq. (2.23):

$$u = \alpha H$$
$$F = \frac{u}{4\pi} - \frac{\beta}{48\pi^2}\ H^3 \frac{\partial g(\alpha - 1)}{\partial x} - (1 - g)\left(\frac{\partial^2 u}{\partial x^2}\ \frac{\Delta x^2}{3} - \frac{\partial^3 u}{\partial x^3}\ \frac{\Delta x^3}{4}\right) \qquad (A.2)$$
$$G = \frac{\beta}{48\ (L/D)^2} H^3 \frac{\partial g(\alpha - 1)}{\partial z}$$

Hence, the fluxes at control surface boundaries using a central differencing formulation can be written as:

$$F_{i+\frac{1}{2},j} = \frac{1}{4\pi}\left(\frac{\alpha_{i,j}H_{i,j} + \alpha_{i+1,j}H_{i+1,j}}{2}\right) - \frac{\beta H_{i+\frac{1}{2},j}{}^3}{48\pi^2}\left(\frac{(\alpha_{i+1,j} - 1)g_{i+1,j} - (\alpha_{i,j} - 1)g_{i,j}}{\Delta x}\right) - \frac{1 - g_{i+1/2,j}}{4\pi}\left(\frac{\alpha_{i-1,j}H_{i-1,j} - 2\alpha_{i,j}H_{i,j} + \alpha_{i+1,j}H_{i+1,j}}{2}\right)$$
$$F_{i-\frac{1}{2},j} = \frac{1}{4\pi}\left(\frac{\alpha_{i-1,j}H_{i-1,j} + \alpha_{i,j}H_{i,j}}{2}\right) - \frac{\beta H_{i-\frac{1}{2},j}{}^3}{48\pi^2}\left(\frac{(\alpha_{i,j} - 1)g_{i,j} - (\alpha_{i-1,j} - 1)g_{i-1,j}}{\Delta x}\right) - \frac{1 - g_{i-1/2,j}}{4\pi}\left(\frac{\alpha_{i-2,j}H_{i-2,j} - 2\alpha_{i-1,j}H_{i-1,j} + \alpha_{i,j}H_{i,j}}{2}\right) \qquad (A.3)$$

$$G_{i,j+\frac{1}{2}} = \frac{-\beta H_{i,j+\frac{1}{2}}^{\ 3}}{48\,(L/D)^2}\left(\frac{(\alpha_{i,j+1}-1)g_{i,j+1}-(\alpha_{i,j}-1)g_{i,j}}{\Delta z}\right)$$

$$G_{i,j-\frac{1}{2}} = \frac{-\beta H_{i,j-\frac{1}{2}}^{\ 3}}{48\,(L/D)^2}\left(\frac{(\alpha_{i,j}-1)g_{i,j}-(\alpha_{i,j-1}-1)g_{i,j-1}}{\Delta z}\right)$$

The higher order artificial viscosity terms in $F_{i+\frac{1}{2},j}$ and $F_{i-\frac{1}{2},j}$ of Eq. (A.3) are chosen such that by substituting $g = 0$ in the shear term at cavitation zone, the second order accurate centrally differenced derivative be reduced to a second order upwind difference:

$$\frac{\partial u}{\partial x} = \left.\frac{F_{i+\frac{1}{2},j} - F_{i-\frac{1}{2},j}}{\Delta x}\right|_{g=0} = \frac{1}{4\pi}\frac{\alpha_{i-2,j}H_{i-2,j} - 4\alpha_{i-1,j}H_{i-1,j} + 3\alpha_{i,j}H_{i,j}}{2\,\Delta x} \tag{A.4}$$

And hence it satisfies the upwind differencing in the hyperbolic cavitation zone as proposed by Vijayaraghavan and Keith [36, 95]. The values of the fluxes at the control surface boundaries in Eq. (A.3) is then to be substituted in the space-time discretized system of Eq. (2.21); dropping all the superscripts knowing that all the terms are evaluated at the current time-step we can write:

$$\begin{aligned}\delta\bar{u}_{i,j}\left(\frac{1}{\Delta t} + \frac{1}{\Delta x}\frac{\partial F_{i+\frac{1}{2},j}}{\partial \bar{u}_{i,j}} - \frac{1}{\Delta x}\frac{\partial F_{i-\frac{1}{2},j}}{\partial \bar{u}_{i,j}} + \frac{1}{\Delta z}\frac{\partial G_{i,j+\frac{1}{2}}}{\partial \bar{u}_{i,j}} - \frac{1}{\Delta z}\frac{\partial G_{i,j-\frac{1}{2}}}{\partial \bar{u}_{i,j}}\right)& \\ + \frac{1}{\Delta x}\frac{\partial F_{i+\frac{1}{2},j}}{\partial \bar{u}_{i+1,j}}\delta\bar{u}_{i+1,j} - \frac{1}{\Delta x}\frac{\partial F_{i-\frac{1}{2},j}}{\partial \bar{u}_{i-1,j}}\delta\bar{u}_{i-1,j} + \frac{1}{\Delta z}\frac{\partial G_{i,j+\frac{1}{2}}}{\partial \bar{u}_{i,j+1}}\delta\bar{u}_{i,j+1}& \\ - \frac{1}{\Delta z}\frac{\partial G_{i,j-\frac{1}{2}}}{\partial \bar{u}_{i,j-1}}\delta\bar{u}_{i,j-1} = -\frac{F_{i+\frac{1}{2},j} - F_{i-\frac{1}{2},j}}{\Delta x} - \frac{G_{i,j+\frac{1}{2}} - G_{i,j-\frac{1}{2}}}{\Delta z}&\end{aligned} \tag{A.5}$$

Where the RHS (right hand side) of Eq. (A.5) is the flux integral and can be written in its final form as:

$$RHS = FI = -\frac{\beta g_{-1+i,j}H_{i-\frac{1}{2},j}^3}{48\pi^2\Delta x^2} + \frac{\beta g_{i,j}H_{i-\frac{1}{2},j}^3}{48\pi^2\Delta x^2} - \frac{\beta g_{i,-1+j}H_{i,j-\frac{1}{2}}^3}{48\left(\frac{L}{D}\right)^2\Delta z^2} + \frac{\beta g_{i,j}H_{i,j-\frac{1}{2}}^3}{48\left(\frac{L}{D}\right)^2\Delta z^2} \tag{A.6}$$

$$+\frac{\beta g_{i,j}H^3_{i,j+\frac{1}{2}}}{48\left(\frac{L}{D}\right)^2\Delta z^2}-\frac{\beta g_{i,1+j}H^3_{i,j+\frac{1}{2}}}{48\left(\frac{L}{D}\right)^2\Delta z^2}+\frac{\beta g_{i,j}H^3_{i+\frac{1}{2},j}}{48\pi^2\Delta x^2}-\frac{\beta g_{1+i,j}H^3_{i+\frac{1}{2},j}}{48\pi^2\Delta x^2}$$

$$+\left(-\frac{H_{i-2,j}}{8\pi\Delta x}+\frac{g_{i-\frac{1}{2},j}H_{i-2,j}}{8\pi\Delta x}\right)\alpha_{i-2,j}$$

$$+\left(\frac{H_{i-1,j}}{2\pi\Delta x}-\frac{g_{i-\frac{1}{2},j}H_{i-1,j}}{4\pi\Delta x}-\frac{g_{i+\frac{1}{2},j}H_{i-1,j}}{8\pi\Delta x}+\frac{\beta g_{i-1,j}H^3_{i-\frac{1}{2},j}}{48\pi^2\Delta x^2}\right)\alpha_{i-1,j}$$

$$+\left(-\frac{\beta g_{i,j}H^3_{i-\frac{1}{2},j}}{48\pi^2\Delta x^2}-\frac{\beta g_{i,j}H^3_{i,j-\frac{1}{2}}}{48\left(\frac{L}{D}\right)^2\Delta z^2}-\frac{3H_{i,j}}{8\pi\Delta x}+\frac{g_{i-\frac{1}{2},j}H_{i,j}}{8\pi\Delta x}+\frac{g_{i+\frac{1}{2},j}H_{i,j}}{4\pi\Delta x}\right.$$

$$\left.-\frac{\beta g_{i,j}H^3_{i,j+\frac{1}{2}}}{48\left(\frac{L}{D}\right)^2\Delta z^2}-\frac{\beta g_{i,j}H^3_{i+\frac{1}{2},j}}{48\pi^2\Delta x^2}\right)\alpha_{i,j}$$

$$+\left(\frac{\beta g_{i+1,j}H^3_{i+\frac{1}{2},j}}{48\pi^2\Delta x^2}-\frac{g_{i+\frac{1}{2},j}H_{1+i,j}}{8\pi\Delta x}\right)\alpha_{i+1,j}$$

$$+\frac{\beta g_{i,j-1}H^3_{i,-\frac{1}{2}+j}}{48\left(\frac{L}{D}\right)^2\Delta z^2}\alpha_{i,j-1}+\frac{\beta g_{i,j+1}H^3_{i,j+\frac{1}{2}}}{48\left(\frac{L}{D}\right)^2\Delta z^2}\alpha_{i,j+1}$$

Carrying out the partial derivations in the LHS (left hand side) of Eq. (A.5) we will have:

$$\frac{\partial F_{i+\frac{1}{2},j}}{\partial \bar{u}_{i,j}}=\frac{\partial F_{i+\frac{1}{2},j}}{\partial \alpha_{i,j}H_{i,j}}=\frac{6\pi\Delta x\left(3-2g_{i+\frac{1}{2},j}\right)H_{i,j}+\beta g_{i,j}H^3_{i+\frac{1}{2},j}}{48\pi^2\Delta x\,H_{i,j}} \tag{A.7}$$

And similarly for all the other partial derivative terms. Hence the LHS in its final form can be written as

$$LHS=X_{-2}\,\delta u_{i-2,j}+X_{-1}\,\delta u_{i-1,j}+XZ_0\,\delta u_{i,j}+X_{+1}\,\delta u_{i+1,j}+Y_{-1}\,\delta u_{i,j-1}+Y_{-2}\,\delta u_{i,j+1} \tag{A.8}$$

where:

$$X_{-2} = -\frac{\left(-1 + g_{i-\frac{1}{2},j}\right)}{8\pi\ \Delta\mathrm{x}}$$

$$X_{-1} = \left(\frac{-1 + g_{i+\frac{1}{2},j}}{8\pi\ \Delta\mathrm{x}} - \frac{6\pi\Delta\mathrm{x}\left(3 - 2g_{i-\frac{1}{2},j}\right) H_{-1+i,j} + \beta g_{-1+i,j}\, H^3_{i-\frac{1}{2},j}}{48\,\pi^2\Delta\mathrm{x}^2\, H_{i-1,j}}\right)$$

$$XZ_0 = \left(\frac{1}{\Delta\mathrm{t}} + \frac{\beta g_{i,j}\, H^3_{i,j-\frac{1}{2}}}{48\left(\frac{L}{D}\right)^2 \Delta\mathrm{z}^2 H_{i,j}} - \frac{-\beta g_{i,j} H^3_{i-\frac{1}{2},j} + 6\pi\ \Delta\mathrm{x}\, g_{i-\frac{1}{2},j} H_{i,j}}{48\pi^2\Delta\mathrm{x}^2 H_{i,j}}\right.$$

$$\left. + \frac{\beta g_{i,j}\, H^3_{i,j+\frac{1}{2}}}{48\left(\frac{L}{D}\right)^2 \Delta\mathrm{z}^2 H_{i,j}} + \frac{6\pi\ \Delta\mathrm{x}\left(3 - 2g_{i+\frac{1}{2},j}\right) H_{i,j} + \beta g_{i,j} H^3_{i+\frac{1}{2},j}}{48\pi^2\Delta\mathrm{x}^2 H_{i,j}}\right) \quad \text{(A.9)}$$

$$X_{+1} = \frac{\left(-\beta g_{i+1,j}\, H^3_{i+\frac{1}{2},j} + 6\pi\ \Delta\mathrm{x}\, g_{i+\frac{1}{2},j} H_{1+i,j}\right)}{48\,\pi^2\Delta\mathrm{x}^2\, H_{i+1,j}}$$

$$Z_{-1} = -\frac{\beta g_{i,j-1}\, H^3_{i,j-\frac{1}{2}}}{48\left(\frac{L}{D}\right)^2 \Delta\mathrm{z}^2 H_{i,j-1}}$$

$$Z_{+1} = -\frac{\beta g_{i,j+1}\, H^3_{i,j+\frac{1}{2}}}{48\,(L/D)^2\,\Delta\mathrm{z}^2\, H_{i,j+1}}$$

And hence the final fully discretized Reynolds equation can be written as:

$$X_{-2}\,\delta\Phi_{i-2,j} + X_{-1}\,\delta\Phi_{i-1,j} + XZ_0\,\delta\Phi_{i,j} + X_{+1}\,\delta\Phi_{i+1,j} + Z_{-1}\,\delta\Phi_{i,j-1} + Z_{-2}\,\delta\Phi_{i,j+1} = FI \quad \text{(A.10)}$$

Now, as an example, considering a 2D mesh of size 4×4 as a subset of a bigger mesh as shown in Figure 1-1.

(1,1)	(1,2)	(1,3)	(1,4)
(2,1)	(2,2)	(2,3)	(2,4)
(3,1)	(3,2)	(3,3)	(3,4)
(4,1)	(4,2)	(4,3)	(4,4)

Figure 1-1. A 4×4 mesh

One can form the full linear system for a 4×4 mesh as:

$$[A][\delta u] = [FI] \tag{A.11}$$

where

$$[A] = \begin{bmatrix}
XZ_0 & X_{+1} & & & Z_1 & & & & & & & & & & & \\
X_{-1} & XZ_0 & X_{+1} & & & Z_1 & & & & & & & & & & \\
X_{-2} & X_{-1} & XZ_0 & X_{+1} & & & Z_1 & & & & & & & & & \\
 & X_{-2} & X_{-1} & XZ_0 & & & & Z_1 & & & & & & & & \\
Z_{-1} & & & & XZ_0 & X_{+1} & & & Z_1 & & & & & & & \\
 & Z_{-1} & & & X_{-1} & XZ_0 & X_{+1} & & & Z_1 & & & & & & \\
 & & Z_{-1} & & X_{-2} & X_{-1} & XZ_0 & X_{+1} & & & Z_1 & & & & & \\
 & & & Z_{-1} & & X_{-2} & X_{-1} & XZ_0 & & & & Z_1 & & & & \\
 & & & & Z_{-1} & & & & XZ_0 & X_{+1} & & & Z_1 & & & \\
 & & & & & Z_{-1} & & & X_{-1} & XZ_0 & X_{+1} & & & Z_1 & & \\
 & & & & & & Z_{-1} & & X_{-2} & X_{-1} & XZ_0 & X_{+1} & & & Z_1 & \\
 & & & & & & & Z_{-1} & & X_{-2} & X_{-1} & XZ_0 & & & & Z_1 \\
 & & & & & & & & Z_{-1} & & & & XZ_0 & X_{+1} & & \\
 & & & & & & & & & Z_{-1} & & & X_{-1} & XZ_0 & X_{+1} & \\
 & & & & & & & & & & Z_{-1} & & X_{-2} & X_{-1} & XZ_0 & X_{+1} \\
 & & & & & & & & & & & Z_{-1} & & X_{-2} & X_{-1} & XZ_0
\end{bmatrix} \tag{A.12}$$

and,

$$[\delta u] = \begin{bmatrix} \delta u_{1,1} \\ \delta u_{2,1} \\ \delta u_{3,1} \\ \delta u_{4,1} \\ \delta u_{1,2} \\ \delta u_{2,2} \\ \delta u_{3,2} \\ \delta u_{4,2} \\ \delta u_{1,3} \\ \delta u_{2,3} \\ \delta u_{3,3} \\ \delta u_{4,3} \\ \delta u_{1,4} \\ \delta u_{2,4} \\ \delta u_{3,4} \\ \delta u_{4,4} \end{bmatrix} ; [FI] = \begin{bmatrix} FI_{1,1} \\ FI_{2,1} \\ FI_{3,1} \\ FI_{4,1} \\ FI_{1,2} \\ FI_{2,2} \\ FI_{3,2} \\ FI_{4,2} \\ FI_{1,3} \\ FI_{2,3} \\ FI_{3,3} \\ FI_{4,3} \\ FI_{1,4} \\ FI_{2,4} \\ FI_{3,4} \\ FI_{4,4} \end{bmatrix} \quad \text{(A.13)}$$

Appendix B : The Hopf Bifurcation Algorithm

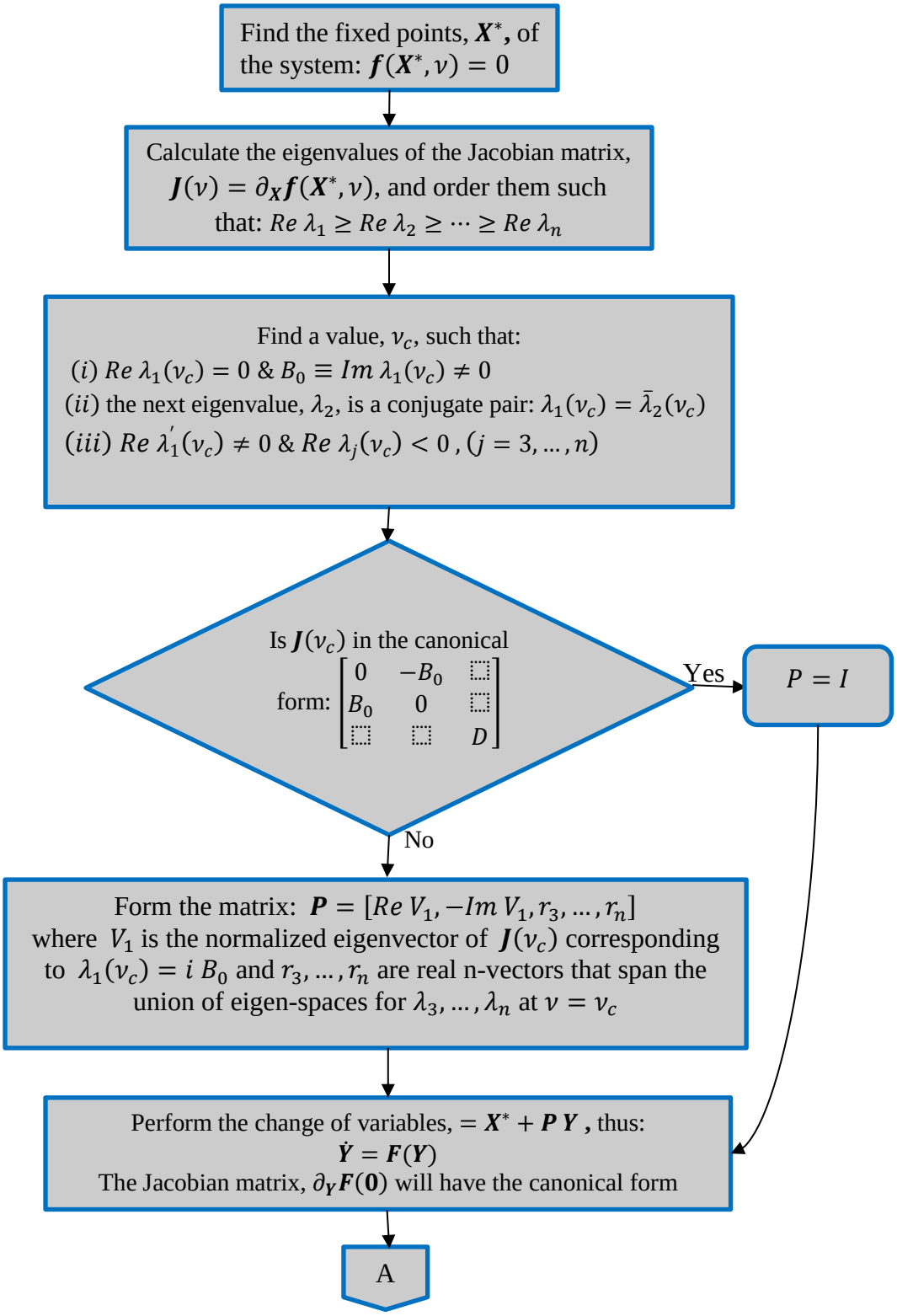

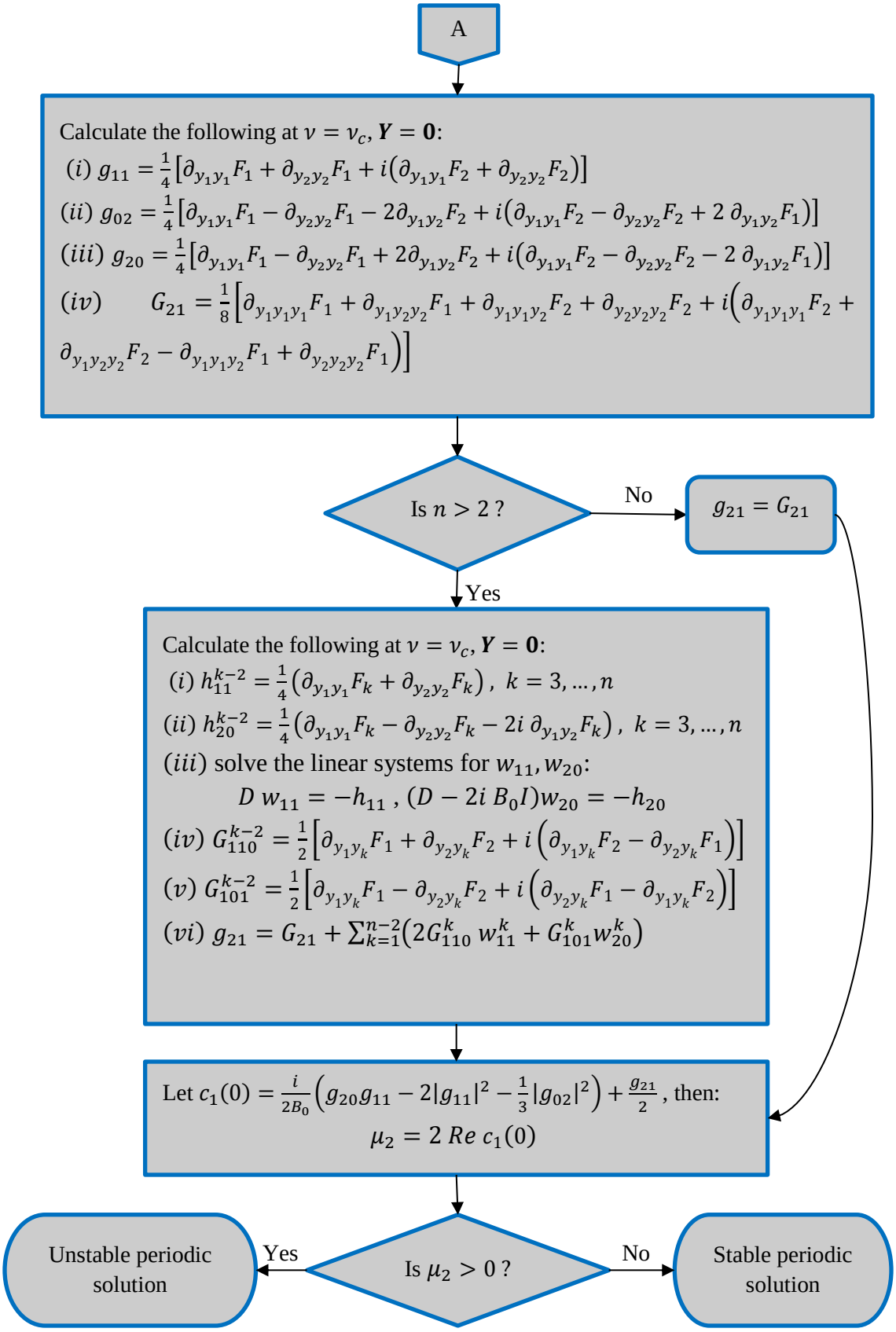
A
Calculate the following at $\nu = \nu_c$, $\boldsymbol{Y} = \mathbf{0}$:
$(i)\ g_{11} = \frac{1}{4}[\partial_{y_1y_1}F_1 + \partial_{y_2y_2}F_1 + i(\partial_{y_1y_1}F_2 + \partial_{y_2y_2}F_2)]$
$(ii)\ g_{02} = \frac{1}{4}[\partial_{y_1y_1}F_1 - \partial_{y_2y_2}F_1 - 2\partial_{y_1y_2}F_2 + i(\partial_{y_1y_1}F_2 - \partial_{y_2y_2}F_2 + 2\,\partial_{y_1y_2}F_1)]$
$(iii)\ g_{20} = \frac{1}{4}[\partial_{y_1y_1}F_1 - \partial_{y_2y_2}F_1 + 2\partial_{y_1y_2}F_2 + i(\partial_{y_1y_1}F_2 - \partial_{y_2y_2}F_2 - 2\,\partial_{y_1y_2}F_1)]$
$(iv)\quad G_{21} = \frac{1}{8}\left[\partial_{y_1y_1y_1}F_1 + \partial_{y_1y_2y_2}F_1 + \partial_{y_1y_1y_2}F_2 + \partial_{y_2y_2y_2}F_2 + i\left(\partial_{y_1y_1y_1}F_2 + \partial_{y_1y_2y_2}F_2 - \partial_{y_1y_1y_2}F_1 + \partial_{y_2y_2y_2}F_1\right)\right]$
Is $n > 2$?
No
$g_{21} = G_{21}$
Yes
Calculate the following at $\nu = \nu_c$, $\boldsymbol{Y} = \mathbf{0}$:
$(i)\ h_{11}^{k-2} = \frac{1}{4}\left(\partial_{y_1y_1}F_k + \partial_{y_2y_2}F_k\right),\ k = 3, \dots, n$
$(ii)\ h_{20}^{k-2} = \frac{1}{4}\left(\partial_{y_1y_1}F_k - \partial_{y_2y_2}F_k - 2i\,\partial_{y_1y_2}F_k\right),\ k = 3, \dots, n$
(iii) solve the linear systems for w_{11}, w_{20}:
$D\,w_{11} = -h_{11}\ ,\ (D - 2i\,B_0 I)w_{20} = -h_{20}$
$(iv)\ G_{110}^{k-2} = \frac{1}{2}\left[\partial_{y_1y_k}F_1 + \partial_{y_2y_k}F_2 + i\left(\partial_{y_1y_k}F_2 - \partial_{y_2y_k}F_1\right)\right]$
$(v)\ G_{101}^{k-2} = \frac{1}{2}\left[\partial_{y_1y_k}F_1 - \partial_{y_2y_k}F_2 + i\left(\partial_{y_2y_k}F_1 - \partial_{y_1y_k}F_2\right)\right]$
$(vi)\ g_{21} = G_{21} + \sum_{k=1}^{n-2}\left(2G_{110}^k\,w_{11}^k + G_{101}^k w_{20}^k\right)$
Let $c_1(0) = \frac{i}{2B_0}\left(g_{20}g_{11} - 2|g_{11}|^2 - \frac{1}{3}|g_{02}|^2\right) + \frac{g_{21}}{2}$, then:
$\mu_2 = 2\,Re\,c_1(0)$
Unstable periodic solution
Yes
Is $\mu_2 > 0$?
No
Stable periodic solution

Appendix C : Analytical Dynamic Coefficients

C.1 Linear Coefficients

The general form of the linear dynamic stiffness coefficients in the *X*-*Y* coordinate system can be written as:

$$\begin{aligned}
\bar{K}_{xx} = {} & \frac{\partial f_{\epsilon}}{\partial \epsilon}\cos(\phi)^2 - \frac{\partial f_{\varphi}}{\partial \epsilon}\cos(\phi)\sin(\phi) - \frac{\partial f_{\epsilon}}{\epsilon \partial \varphi}\cos(\phi)\sin(\phi) + \frac{\partial f_{\varphi}}{\epsilon \partial \varphi}\sin(\phi)^2 \\
& + \frac{f_{\epsilon 0}}{\epsilon}\sin(\phi)^2 + \frac{f_{\phi 0}}{\epsilon}\cos(\phi)\sin(\phi) \\
\bar{K}_{xy} = {} & \frac{\partial f_{\epsilon}}{\epsilon \partial \varphi}\cos(\phi)^2 + \frac{\partial f_{\epsilon}}{\partial \epsilon}\cos(\phi)\sin(\phi) - \frac{\partial f_{\varphi}}{\epsilon \partial \varphi}\cos(\phi)\sin(\phi) - \frac{\partial f_{\varphi}}{\partial \epsilon}\sin(\phi)^2 \\
& - \frac{f_{\epsilon 0}}{\epsilon}\cos(\phi)\sin(\phi) - \frac{f_{\phi 0}}{\epsilon}\cos(\phi)^2 \\
\bar{K}_{yx} = {} & \frac{\partial f_{\varphi}}{\partial \epsilon}\cos(\phi)^2 + \frac{\partial f_{\epsilon}}{\partial \epsilon}\cos(\phi)\sin(\phi) - \frac{\partial f_{\varphi}}{\epsilon \partial \varphi}\cos(\phi)\sin(\phi) - \frac{\partial f_{\epsilon}}{\epsilon \partial \varphi}\sin(\phi)^2 \\
& - \frac{f_{\epsilon 0}}{\epsilon}\cos(\phi)\sin(\phi) + \frac{f_{\phi 0}}{\epsilon}\sin(\phi)^2 \\
\bar{K}_{yy} = {} & \frac{\partial f_{\varphi}}{\epsilon \partial \varphi}\cos(\phi)^2 + \frac{\partial f_{\varphi}}{\partial \epsilon}\cos(\phi)\sin(\phi) + \frac{\partial f_{\epsilon}}{\epsilon \partial \varphi}\cos(\phi)\sin(\phi) + \frac{\partial f_{\epsilon}}{\partial \epsilon}\sin(\phi)^2 \\
& + \frac{f_{\epsilon 0}}{\epsilon}\cos(\phi)^2 - \frac{f_{\phi 0}}{\epsilon}\cos(\phi)\sin(\phi)
\end{aligned} \tag{C.1}$$

It shall be noted again that all the derivatives are to be evaluated at the steady state where $\dot{e} = \dot{\varphi} = 0$. Since a clockwise rotation can transform the forces to the *X*-*Y* coordinate, we can write:

$$f_x = f_{\epsilon}\cos\varphi - f_{\varphi}\sin\varphi \text{ and } f_y = f_{\epsilon}\sin\varphi + f_{\varphi}\cos\varphi \tag{C.2}$$

Combining Eq. (C.1) with Eq. (C.2) will yield the identical form as in references [25, 92]. Similarly, linear dynamic damping coefficients in the *X*-*Y* coordinate are found as follows:

$$\begin{aligned}
\bar{C}_{xx} = {} & \omega\frac{\partial f_{\epsilon}}{\partial \dot{\epsilon}}\cos(\phi)^2 - \omega\frac{\partial f_{\varphi}}{\partial \dot{\epsilon}}\cos(\phi)\sin(\phi) - \omega\frac{\partial f_{\epsilon}}{\epsilon \partial \dot{\varphi}}\cos(\phi)\sin(\phi) \\
& + \omega\frac{\partial f_{\varphi}}{\epsilon \partial \dot{\varphi}}\sin(\phi)^2
\end{aligned} \tag{C.3}$$

$$\bar{C}_{xy} = \omega \frac{\partial f_\epsilon}{\epsilon \partial \dot{\varphi}} \cos(\phi)^2 + \omega \frac{\partial f_\epsilon}{\partial \dot{\epsilon}} \cos(\phi)\sin(\phi) - \omega \frac{\partial f_\varphi}{\epsilon \partial \dot{\varphi}} \cos(\phi)\sin(\phi) - \omega \frac{\partial f_\varphi}{\partial \dot{\epsilon}} \sin(\phi)^2$$

$$\bar{C}_{yx} = \omega \frac{\partial f_\varphi}{\partial \dot{\epsilon}} \cos(\phi)^2 + \omega \frac{\partial f_\epsilon}{\partial \dot{\epsilon}} \cos(\phi)\sin(\phi) - \omega \frac{\partial f_\varphi}{\epsilon \partial \dot{\varphi}} \cos(\phi)\sin(\phi) - \omega \frac{\partial f_\epsilon}{\epsilon \partial \dot{\varphi}} \sin(\phi)^2$$

$$\bar{C}_{yy} = \omega \frac{\partial f_\varphi}{\epsilon \partial \dot{\varphi}} \cos(\phi)^2 + \omega \frac{\partial f_\varphi}{\partial \dot{\epsilon}} \cos(\phi)\sin(\phi) + \omega \frac{\partial f_\epsilon}{\epsilon \partial \dot{\varphi}} \cos(\phi)\sin(\phi) + \omega \frac{\partial f_\epsilon}{\partial \dot{\epsilon}} \sin(\phi)^2$$

Noting that $\omega \frac{\partial f_\epsilon}{\partial \dot{\varphi}} = -2 f_\epsilon$ and $\omega \frac{\partial f_\varphi}{\partial \dot{\varphi}} = -2 f_\varphi$ [25] and the form of Eq. (C.2), the result of linear damping coefficients is again in complete agreement with the literature [25, 92]. The linear dynamic coefficients are calculated for the special case of a π-film short bearing and are tabulated in Table C-1 and Table C-2.

Table C-1. Linear stiffness coefficients for a short bearing (π film) in X-Y coordinate system

Linear Stiffness Coefficients	Short Bearing (π film)
$\bar{K}_{xx}$	$-\frac{\pi L^2 \epsilon(-3\pi\epsilon(\epsilon^2-1)sin(2\phi) + 4\sqrt{1-\epsilon^2}(3\epsilon^2+1)cos(2\phi) + 4\sqrt{1-\epsilon^2}(\epsilon^2+3))}{2D^2(1-\epsilon^2)^{7/2}}$
$\bar{K}_{xy}$	$-\frac{\pi L^2 (4\sqrt{1-\epsilon^2}(3\epsilon^2+1)\epsilon\, sin(2\phi) + 3\pi(\epsilon^2-1)\epsilon^2 cos(2\phi) - \pi(\epsilon^4+\epsilon^2-2))}{2D^2(1-\epsilon^2)^{7/2}}$
$\bar{K}_{yx}$	$-\frac{\pi L^2 (4\sqrt{1-\epsilon^2}(3\epsilon^2+1)\epsilon\, sin(2\phi) + 3\pi(\epsilon^2-1)\epsilon^2 cos(2\phi) + \pi(\epsilon^4+\epsilon^2-2))}{2D^2(1-\epsilon^2)^{7/2}}$
$\bar{K}_{yy}$	$-\frac{\pi L^2 \epsilon(3\pi\epsilon(\epsilon^2-1)sin(2\phi) - 4\sqrt{1-\epsilon^2}(3\epsilon^2+1)cos(2\phi) + 4\sqrt{1-\epsilon^2}(\epsilon^2+3))}{2D^2(1-\epsilon^2)^{7/2}}$

Table C-2. Linear damping coefficients for a short bearing (π film) in X-Y coordinate system

Linear Damping Coefficients	Short Bearing (π film)
$\bar{C}_{xx}$	$-\frac{\pi L^2(8\sqrt{1-\epsilon^2}\epsilon\, sin(2\phi)+3\pi\epsilon^2 cos(2\phi)+\pi(\epsilon^2+2))}{D^2(1-\epsilon^2)^{5/2}}$
$\bar{C}_{xy}$	$\frac{\pi L^2\epsilon(8\sqrt{1-\epsilon^2}cos(2\phi)-3\pi\epsilon\, sin(2\phi))}{D^2(1-\epsilon^2)^{5/2}}$
$\bar{C}_{yx}$	$\frac{\pi L^2\epsilon(8\sqrt{1-\epsilon^2}cos(2\phi)-3\pi\epsilon\, sin(2\phi))}{D^2(1-\epsilon^2)^{5/2}}$
$\bar{C}_{yy}$	$\frac{\pi L^2(8\sqrt{1-\epsilon^2}\epsilon\, sin(2\phi)+3\pi\epsilon^2 cos(2\phi)-\pi(\epsilon^2+2))}{D^2(1-\epsilon^2)^{5/2}}$

C.2 Nonlinear Second Order Coefficients

The general form for six nonlinear stiffness coefficients can be expressed as:

$$\begin{aligned}\overline{K}_{xxx} = \frac{1}{2\epsilon^2}\Bigg\{&\frac{\partial^2 f_\epsilon}{\partial\epsilon^2}\cos^3(\phi) - \epsilon\sin(\phi)\cos^2(\phi)\left(2\frac{\partial^2 f_\epsilon}{\partial\epsilon\partial\varphi}+\frac{\partial^2 f_\varphi}{\partial\epsilon^2}\epsilon-2\frac{\partial f_\varphi}{\partial\epsilon}\right)\\&+\left(\frac{\partial^2 f_\epsilon}{\partial\varphi^2}-2\frac{\partial f_\varphi}{\partial\varphi}\right)\sin^2(\phi)\cos(\phi)\\&+\epsilon\left(\frac{\partial^2 f_\varphi}{\partial\epsilon\partial\varphi}+\frac{\partial f_\epsilon}{\partial\epsilon}\right)\sin(\phi)\sin(2\phi)-\left(\frac{\partial^2 f_\varphi}{\partial\varphi^2}+2\frac{\partial f_\epsilon}{\partial\varphi}\right)\sin^3(\phi)\\&-\sin^2(\phi)\left(f_{\epsilon 0}\cos(\phi)-f_{\phi 0}\sin(\phi)\right)\Bigg\}\end{aligned} \tag{C.4}$$

$$\begin{aligned}\overline{K}_{yxx} = \frac{1}{2\epsilon^2}\Bigg\{&\frac{\partial^2 f_\varphi}{\partial\epsilon^2}\epsilon^2\cos^3(\phi)+\epsilon\sin(\phi)\cos^2(\phi)\left(\frac{\partial^2 f_\epsilon}{\partial\epsilon^2}\epsilon-2\frac{\partial^2 f_\varphi}{\partial\epsilon\partial\varphi}-2\frac{\partial f_\epsilon}{\partial\epsilon}\right)\\&+\sin^2(\phi)\cos(\phi)\left(\frac{\partial^2 f_\varphi}{\partial\varphi^2}-2\frac{\partial^2 f_\epsilon}{\partial\epsilon\partial\varphi}\epsilon\right)+\left(\frac{\partial^2 f_\epsilon}{\partial\varphi^2}-2\frac{\partial f_\varphi}{\partial\varphi}\right)\sin^3(\phi)\\&+\sin(\phi)\sin(2\phi)\left(\frac{\partial f_\epsilon}{\partial\varphi}+\frac{\partial f_\varphi}{\partial\epsilon}\epsilon\right)-\sin^2(\phi)\left(f_{\epsilon 0}\sin(\phi)+f_{\phi 0}\cos(\phi)\right)\Bigg\}\end{aligned}$$

and,

$$\bar{K}_{xyy} = \frac{1}{2\epsilon^2}\left\{-\frac{\partial^2 f_{\varphi}}{\partial\epsilon^2}\epsilon^2\sin^3(\phi) + \epsilon\sin^2(\phi)\cos(\phi)\left(\frac{\partial^2 f_{\epsilon}}{\partial\epsilon^2}\epsilon - 2\frac{\partial^2 f_{\epsilon}}{\partial\epsilon\partial\varphi} - 2\frac{\partial f_{\epsilon}}{\partial\epsilon}\right)\right.$$
$$- \sin(\phi)\cos^2(\phi)\left(-2\frac{\partial^2 f_{\epsilon}}{\partial\epsilon\partial\varphi}\epsilon + \frac{\partial^2 f_{\varphi}}{\partial\varphi^2} + 2\frac{\partial f_{\epsilon}}{\partial\varphi} + 2\frac{\partial f_{\varphi}}{\partial\epsilon}\epsilon\right)$$
$$\left. + \left(\frac{\partial^2 f_{\epsilon}}{\partial\varphi^2} - 2\frac{\partial f_{\varphi}}{\partial\varphi}\right)\cos^3(\phi) - f_{\epsilon 0}\cos^3(\phi) + f_{\phi 0}\sin(\phi)\cos^2(\phi)\right\}$$
$$\bar{K}_{yyy} = \frac{1}{2\epsilon^2}\left\{\frac{\partial^2 f_{\epsilon}}{\partial\epsilon^2}\epsilon^2\sin^3(\phi) + \epsilon\sin^2(\phi)\cos(\phi)\left(2\frac{\partial^2 f_{\epsilon}}{\partial\epsilon\partial\varphi} + \frac{\partial^2 f_{\varphi}}{\partial\epsilon^2}\epsilon - 2\frac{\partial f_{\varphi}}{\partial\epsilon}\right)\right.$$
$$+ \sin(\phi)\cos^2(\phi)\left(\frac{\partial^2 f_{\epsilon}}{\partial\varphi^2} + 2\epsilon\frac{\partial^2 f_{\varphi}}{\partial\epsilon\partial\varphi} + 2\epsilon\frac{\partial f_{\epsilon}}{\partial\epsilon} - 2\frac{\partial f_{\varphi}}{\partial\varphi}\right)$$
$$\left. + \left(\frac{\partial^2 f_{\varphi}}{\partial\varphi^2} + 2\frac{\partial f_{\epsilon}}{\partial\varphi}\right)\cos^3(\phi) - \cos^2(\phi)\left(f_{\epsilon 0}\sin(\phi) + f_{\phi 0}\cos(\phi)\right)\right\} \quad \text{(C.5)}$$

and,

$$\bar{K}_{xxy} = \frac{1}{\epsilon^2}\left\{\cos(\phi)^3\left(\frac{\partial^2 f_{\epsilon}}{\partial\epsilon\partial\varphi}\epsilon - \frac{\partial f_{\varphi}}{\partial\epsilon}\epsilon\right)\right.$$
$$+ \cos(\phi)^2\sin(\phi)\left(\frac{\partial^2 f_{\epsilon}}{\partial\epsilon^2}\epsilon^2 - \frac{\partial^2 f_{\epsilon}}{\partial\varphi^2} + \frac{\partial f_{\varphi}}{\partial\varphi} - \frac{\partial^2 f_{\varphi}}{\partial\epsilon\partial\varphi}\epsilon - \frac{\partial f_{\epsilon}}{\partial\epsilon}\epsilon + f_{\epsilon 0}\right)$$
$$+ \cos(\phi)\sin(\phi)^2\left(-\frac{\partial^2 f_{\varphi}}{\partial\epsilon^2}\epsilon^2 + \frac{\partial^2 f_{\varphi}}{\partial\varphi^2} - \frac{\partial^2 f_{\epsilon}}{\partial\epsilon\partial\varphi}\epsilon + \frac{\partial f_{\varphi}}{\partial\epsilon}\epsilon - f_{\phi 0}\right)$$
$$\left. + \sin(\phi)^3\left(\frac{\partial^2 f_{\varphi}}{\partial\epsilon\partial\varphi}\epsilon + \frac{\partial f_{\epsilon}}{\partial\epsilon}\epsilon\right) + \frac{\partial f_{\epsilon}}{\partial\varphi}\sin(\phi)\sin(2\phi)\right\}$$
$$\bar{K}_{yxy} = \frac{1}{\epsilon^2}\left\{\cos(\phi)^3\left(\frac{\partial^2 f_{\epsilon}}{\partial\epsilon\partial\varphi}\epsilon + \frac{\partial f_{\epsilon}}{\partial\epsilon}\epsilon\right)\right. \quad \text{(C.6)}$$
$$+ \cos(\phi)^2\sin(\phi)\left(\frac{\partial^2 f_{\varphi}}{\partial\epsilon^2}\epsilon^2 - \frac{\partial^2 f_{\varphi}}{\partial\varphi^2} - \frac{\partial f_{\epsilon}}{\partial\varphi} + \frac{\partial^2 f_{\epsilon}}{\partial\epsilon\partial\varphi}\epsilon - \frac{\partial f_{\varphi}}{\partial\epsilon}\epsilon + f_{\phi 0}\right)$$
$$+ \cos(\phi)\sin(\phi)^2\left(+\frac{\partial^2 f_{\epsilon}}{\partial\epsilon^2}\epsilon^2 - \frac{\partial^2 f_{\epsilon}}{\partial\varphi^2} - \frac{\partial^2 f_{\varphi}}{\partial\epsilon\partial\varphi}\epsilon - \frac{\partial f_{\epsilon}}{\partial\epsilon}\epsilon + f_{\epsilon 0}\right)$$
$$\left. + \sin(\phi)^3\left(-\frac{\partial^2 f_{\epsilon}}{\partial\epsilon\partial\varphi}\epsilon + \epsilon\frac{\partial f_{\varphi}}{\partial\epsilon}\right) + \frac{\partial f_{\varphi}}{\partial\varphi}\sin(\phi)\sin(2\phi)\right\}$$

The eight nonlinear second-order damping coefficients can be found in a similar fashion and are given in their final simplified form:

$$\bar{C}_{xxx} = \frac{\omega}{\epsilon^2}\left\{\frac{\partial^2 f_\epsilon}{\partial\dot{\epsilon}\partial\epsilon}\epsilon^2\cos^3(\phi) - \epsilon\sin(\phi)\cos^2(\phi)\left(\frac{\partial^2 f_\epsilon}{\partial\dot{\epsilon}\partial\varphi} + \frac{\partial^2 f_\epsilon}{\partial\dot{\varphi}\partial\epsilon} + \frac{\partial^2 f_\varphi}{\partial\dot{\epsilon}\partial\epsilon}\epsilon - \frac{\partial f_\varphi}{\partial\dot{\epsilon}}\right)\right.$$
$$+ \sin^2(\phi)\cos(\phi)\left[\frac{\partial^2 f_\epsilon}{\partial\dot{\varphi}\partial\varphi} + \epsilon\left(\frac{\partial^2 f_\varphi}{\partial\dot{\epsilon}\partial\varphi} + \frac{\partial^2 f_\varphi}{\partial\dot{\varphi}\partial\epsilon} + \frac{\partial f_\epsilon}{\partial\dot{\epsilon}}\right) - \frac{\partial f_\varphi}{\partial\dot{\varphi}}\right]$$
$$\left. - \left(\frac{\partial^2 f_\varphi}{\partial\dot{\varphi}\partial\varphi} + \frac{\partial f_\epsilon}{\partial\dot{\varphi}}\right)\sin^3(\phi)\right\}$$

$$\bar{C}_{yxx} = \frac{\omega}{\epsilon^2}\left\{\frac{\partial^2 f_\varphi}{\partial\dot{\epsilon}\partial\epsilon}\epsilon^2\cos^3(\phi)\right. \tag{C.7}$$
$$- \epsilon\sin(\phi)\cos^2(\phi)\left(-\frac{\partial^2 f_\epsilon}{\partial\dot{\epsilon}\partial\epsilon} + \frac{\partial^2 f_\varphi}{\partial\dot{\epsilon}\partial\varphi} + \frac{\partial^2 f_\varphi}{\partial\dot{\varphi}\partial\epsilon}\epsilon + \frac{\partial f_\epsilon}{\partial\dot{\epsilon}}\right)$$
$$+ \sin^2(\phi)\cos(\phi)\left[-\epsilon\left(\frac{\partial^2 f_\epsilon}{\partial\dot{\epsilon}\partial\varphi} + \frac{\partial^2 f_\epsilon}{\partial\dot{\varphi}\partial\epsilon} - \frac{\partial f_\varphi}{\partial\dot{\epsilon}}\right) + \frac{\partial^2 f_\varphi}{\partial\dot{\varphi}\partial\varphi} + \frac{\partial f_\epsilon}{\partial\dot{\varphi}}\right]$$
$$\left. + \left(\frac{\partial^2 f_\epsilon}{\partial\dot{\varphi}\partial\varphi} - \frac{\partial f_\varphi}{\partial\dot{\varphi}}\right)\sin^3(\phi)\right\}$$

and,

$$\bar{C}_{xyx} = \frac{\omega}{\epsilon^2}\left\{\frac{\partial^2 f_\epsilon}{\partial\dot{\varphi}\partial\epsilon}\epsilon\cos^3(\phi)\right.$$
$$+ \sin(\phi)\cos^2(\phi)\left(\frac{\partial^2 f_\epsilon}{\partial\dot{\epsilon}\partial\epsilon}\epsilon^2 - \frac{\partial^2 f_\epsilon}{\partial\dot{\varphi}\partial\epsilon} - \frac{\partial^2 f_\varphi}{\partial\dot{\varphi}\partial\epsilon}\epsilon + \frac{\partial f_\varphi}{\partial\dot{\varphi}}\right)$$
$$+ \sin^2(\phi)\cos(\phi)\left[-\epsilon\left(\frac{\partial^2 f_\epsilon}{\partial\dot{\epsilon}\partial\varphi} + \frac{\partial^2 f_\varphi}{\partial\dot{\epsilon}\partial\epsilon}\epsilon - \frac{\partial f_\varphi}{\partial\dot{\epsilon}}\right) + \frac{\partial^2 f_\varphi}{\partial\dot{\varphi}\partial\varphi} + \frac{\partial f_\epsilon}{\partial\dot{\varphi}}\right]$$
$$\left. + \epsilon\left(\frac{\partial^2 f_\varphi}{\partial\dot{\epsilon}\partial\varphi} + \frac{\partial f_\epsilon}{\partial\dot{\epsilon}}\right)\sin^3(\phi)\right\}$$

$$\bar{C}_{yyx} = \frac{\omega}{\epsilon^2}\left\{\frac{\partial^2 f_\varphi}{\partial\dot{\varphi}\partial\epsilon}\epsilon\cos^3(\phi)\right. \tag{C.8}$$
$$- \sin(\phi)\cos^2(\phi)\left(-\frac{\partial^2 f_\epsilon}{\partial\dot{\varphi}\partial\epsilon}\epsilon - \frac{\partial^2 f_\varphi}{\partial\dot{\epsilon}\partial\epsilon}\epsilon^2 + \frac{\partial^2 f_\varphi}{\partial\dot{\varphi}\partial\varphi} + \frac{\partial f_\epsilon}{\partial\dot{\varphi}}\right)$$
$$- \sin^2(\phi)\cos(\phi)\left[\epsilon\left(-\frac{\partial^2 f_\epsilon}{\partial\dot{\epsilon}\partial\epsilon}\epsilon + \frac{\partial^2 f_\varphi}{\partial\dot{\epsilon}\partial\varphi} + \frac{\partial f_\epsilon}{\partial\dot{\epsilon}}\right) + \frac{\partial^2 f_\epsilon}{\partial\dot{\varphi}\partial\varphi} - \frac{\partial f_\varphi}{\partial\dot{\varphi}}\right]$$
$$\left. + \epsilon\left(\frac{\partial f_\varphi}{\partial\dot{\epsilon}} - \frac{\partial^2 f_\epsilon}{\partial\dot{\epsilon}\partial\varphi}\right)\sin^3(\phi)\right\}$$

and:

$$\bar{C}_{xxy} = \frac{\omega}{\epsilon^2}\left\{\epsilon\left(\frac{\partial^2 f_\epsilon}{\partial\dot{\epsilon}\partial\varphi} - \frac{\partial f_\varphi}{\partial\dot{\epsilon}}\right)\cos^3(\phi) + \frac{\partial^2 f_\varphi}{\partial\dot{\phi}\partial\epsilon}\epsilon\sin^3(\phi)\right.$$
$$- \sin(\phi)\cos^2(\phi)\left[\epsilon\left(-\frac{\partial^2 f_\epsilon}{\partial\dot{\epsilon}\partial\epsilon}\epsilon + \frac{\partial^2 f_\varphi}{\partial\dot{\epsilon}\partial\varphi} + \frac{\partial f_\epsilon}{\partial\dot{\epsilon}}\right) + \frac{\partial^2 f_\epsilon}{\partial\dot{\phi}\partial\varphi} - \frac{\partial f_\varphi}{\partial\dot{\phi}}\right]$$
$$\left. + \sin^2(\phi)\cos(\phi)\left(-\frac{\partial^2 f_\epsilon}{\partial\dot{\phi}\partial\epsilon}\epsilon - \frac{\partial^2 f_\varphi}{\partial\dot{\epsilon}\partial\epsilon}\epsilon^2 + \frac{\partial^2 f_\varphi}{\partial\dot{\phi}\partial\varphi} + \frac{\partial f_\epsilon}{\partial\dot{\phi}}\right)\right\}$$
$$\bar{C}_{yxy} = \frac{\omega}{\epsilon^2}\left\{\epsilon\left(\frac{\partial^2 f_\varphi}{\partial\dot{\epsilon}\partial\varphi} + \frac{\partial f_\epsilon}{\partial\dot{\epsilon}}\right)\cos^3(\phi) - \frac{\partial^2 f_\epsilon}{\partial\dot{\phi}\partial\epsilon}\epsilon\sin^3(\phi)\right. \quad \text{(C.9)}$$
$$- \sin(\phi)\cos^2(\phi)\left[-\epsilon\left(\frac{\partial^2 f_\epsilon}{\partial\dot{\epsilon}\partial\varphi} + \frac{\partial^2 f_\varphi}{\partial\dot{\epsilon}\partial\epsilon}\epsilon - \frac{\partial f_\varphi}{\partial\dot{\epsilon}}\right) + \frac{\partial^2 f_\varphi}{\partial\dot{\phi}\partial\varphi} + \frac{\partial f_\epsilon}{\partial\dot{\phi}}\right]$$
$$\left. + \sin^2(\phi)\cos(\phi)\left(\frac{\partial^2 f_\epsilon}{\partial\dot{\epsilon}\partial\epsilon}\epsilon^2 - \frac{\partial^2 f_\epsilon}{\partial\dot{\phi}\partial\varphi} - \frac{\partial^2 f_\varphi}{\partial\dot{\phi}\partial\epsilon}\epsilon + \frac{\partial f_\varphi}{\partial\dot{\phi}}\right)\right\}$$

and finally,

$$\bar{C}_{xyy} = \frac{\omega}{\epsilon^2}\left\{\left(\frac{\partial^2 f_\epsilon}{\partial\dot{\phi}\partial\varphi} - \frac{\partial f_\varphi}{\partial\dot{\phi}}\right)\cos^3(\phi) - \frac{\partial^2 f_\varphi}{\partial\dot{\epsilon}\partial\epsilon}\epsilon^2\sin^3(\phi)\right.$$
$$- \sin(\phi)\cos^2(\phi)\left[-\epsilon\left(\frac{\partial^2 f_\epsilon}{\partial\dot{\epsilon}\partial\varphi} + \frac{\partial^2 f_\epsilon}{\partial\dot{\phi}\partial\epsilon} - \frac{\partial f_\varphi}{\partial\dot{\epsilon}}\right) + \frac{\partial^2 f_\varphi}{\partial\dot{\phi}\partial\varphi} + \frac{\partial f_\epsilon}{\partial\dot{\phi}}\right]$$
$$\left. - \epsilon\sin^2(\phi)\cos(\phi)\left(-\frac{\partial^2 f_\epsilon}{\partial\dot{\epsilon}\partial\epsilon}\epsilon + \frac{\partial^2 f_\varphi}{\partial\dot{\epsilon}\partial\varphi} + \frac{\partial^2 f_\varphi}{\partial\dot{\phi}\partial\epsilon} + \frac{\partial f_\epsilon}{\partial\dot{\epsilon}}\right)\right\}$$
$$\bar{C}_{yyy} = \frac{\omega}{\epsilon^2}\left\{\left(\frac{\partial^2 f_\varphi}{\partial\dot{\phi}\partial\varphi} + \frac{\partial f_\epsilon}{\partial\dot{\phi}}\right)\cos^3(\phi) + \frac{\partial^2 f_\epsilon}{\partial\dot{\epsilon}\partial\epsilon}\epsilon^2\sin^3(\phi)\right. \quad \text{(C.10)}$$
$$+ \sin(\phi)\cos^2(\phi)\left[\epsilon\left(\frac{\partial^2 f_\varphi}{\partial\dot{\epsilon}\partial\varphi} + \frac{\partial^2 f_\varphi}{\partial\dot{\phi}\partial\epsilon} + \frac{\partial f_\epsilon}{\partial\dot{\epsilon}}\right) + \frac{\partial^2 f_\epsilon}{\partial\dot{\phi}\partial\varphi} - \frac{\partial f_\varphi}{\partial\dot{\phi}}\right]$$
$$\left. + \epsilon\sin^2(\phi)\cos(\phi)\left(\frac{\partial^2 f_\epsilon}{\partial\dot{\epsilon}\partial\varphi} + \frac{\partial^2 f_\epsilon}{\partial\dot{\phi}\partial\epsilon} + \frac{\partial^2 f_\varphi}{\partial\dot{\epsilon}\partial\epsilon}\epsilon - \frac{\partial f_\varphi}{\partial\dot{\epsilon}}\right)\right\}$$

The nonlinear second order dynamic coefficients are calculated for the special case of a π-film short bearing and are tabulated in Table C-3 and Table C-4.

Table C-3. Nonlinear stiffness coefficients for a short bearing (π film) in X-Y coordinate system

$\bar{K}_{xxx}$	$\frac{\pi L^2}{4D^2\epsilon(1-\epsilon^2)^{9/2}}\{\pi(\epsilon^2-1)sin(\phi)[9\epsilon^4+9\epsilon^2+(11\epsilon^4+5\epsilon^2-1)cos(2\phi)-3] - 2\epsilon\sqrt{1-\epsilon^2}(13\epsilon^4+50\epsilon^2+9)cos(\phi) - 2\epsilon\sqrt{1-\epsilon^2}(11\epsilon^4+14\epsilon^2-1)cos(3\phi)\}$
$\bar{K}_{yxx}$	$\frac{-\pi L^2}{8D^2\epsilon(1-\epsilon^2)^{9/2}}\{8\epsilon\sqrt{1-\epsilon^2}sin(\phi)[9\epsilon^4+18\epsilon^2+(11\epsilon^4+14\epsilon^2-1)cos(2\phi)-3]+\pi(13\epsilon^6+18\epsilon^4 - 30\epsilon^2-1)cos(\phi)+\pi(11\epsilon^6-6\epsilon^4-6\epsilon^2+1)cos(3\phi)\}$
$\bar{K}_{xyy}$	$\frac{\pi L^2}{8D^2\epsilon(1-\epsilon^2)^{9/2}}\{\pi(\epsilon^2-1)[(13\epsilon^4+31\epsilon^2+1)sin(\phi)+(-11\epsilon^4-5\epsilon^2+1)sin(3\phi)] - 4\epsilon\sqrt{1-\epsilon^2}(7\epsilon^4+22\epsilon^2-5)cos(\phi)+4\epsilon\sqrt{1-\epsilon^2}(11\epsilon^4+14\epsilon^2-1)cos(3\phi)\}$
$\bar{K}_{yyy}$	$\frac{-\pi L^2}{8D^2\epsilon(1-\epsilon^2)^{9/2}}\{8\epsilon\sqrt{1-\epsilon^2}sin(\phi)[\epsilon^4+18\epsilon^2+(-11\epsilon^4-14\epsilon^2+1)cos(2\phi)+5]+\pi(7\epsilon^6+6\epsilon^4 - 18\epsilon^2+5)cos(\phi)+\pi(-11\epsilon^6+6\epsilon^4+6\epsilon^2-1)cos(3\phi)\}$
$\bar{K}_{xxy}$	$\frac{-\pi L^2}{D^2\epsilon(1-\epsilon^2)^{9/2}}\{\pi(2\epsilon^6-3\epsilon^4+1)cos^3(\phi)-8\epsilon\sqrt{1-\epsilon^2}(\epsilon^4-1)sin^3(\phi) + 4\epsilon\sqrt{1-\epsilon^2}(9\epsilon^4+14\epsilon^2+1)sin(\phi)cos^2(\phi) + 3\pi\epsilon^2(-3\epsilon^4+\epsilon^2+2)sin^2(\phi)cos(\phi)\}$
$\bar{K}_{yxy}$	$\frac{-\pi L^2}{D^2\epsilon(1-\epsilon^2)^{9/2}}\{\pi(2\epsilon^6-3\epsilon^4+1)sin^3(\phi)+8\epsilon\sqrt{1-\epsilon^2}(\epsilon^4-1)cos^3(\phi) + 3\pi\epsilon^2(-3\epsilon^4+\epsilon^2+2)sin(\phi)cos^2(\phi) - 4\epsilon\sqrt{1-\epsilon^2}(9\epsilon^4+14\epsilon^2+1)sin^2(\phi)cos(\phi)\}$

Table C-4. Nonlinear damping coefficients for a short bearing (π film) in *X-Y* coordinate system

$\bar{C}_{xxx}$	$\frac{-\pi L^2}{2D^2\epsilon(1-\epsilon^2)^{7/2}}\{8\epsilon\sqrt{1-\epsilon^2}sin(\phi)[(7\epsilon^2+1)cos(2\phi)+5\epsilon^2+3]+\pi(13\epsilon^4+31\epsilon^2+1)cos(\phi) + \pi(11\epsilon^4+5\epsilon^2-1)cos(3\phi)\}$
$\bar{C}_{yxx}$	$\frac{-\pi L^2}{2D^2\epsilon(1-\epsilon^2)^{7/2}}\{2\pi sin(\phi)[(11\epsilon^4+5\epsilon^2-1)cos(2\phi)+9(\epsilon^4+\epsilon^2)-3]-4\epsilon\sqrt{1-\epsilon^2}(5\epsilon^2 + 3)cos(\phi)-4\epsilon\sqrt{1-\epsilon^2}(7\epsilon^2+1)cos(3\phi)\}$
$\bar{C}_{xyy}$	$\frac{-\pi L^2}{2D^2\epsilon(1-\epsilon^2)^{7/2}}\{\sqrt{1-\epsilon^2}(3\epsilon^2+1)\epsilon sin^3(\phi)-\frac{\pi}{4}(\epsilon^2-1)^2cos^3(\phi) - \frac{\pi}{4}(-10\epsilon^4-7\epsilon^2+2)sin^2(\phi)\,cos(\phi)-4\sqrt{1-\epsilon^2}\epsilon^3sin(\phi)cos^2(\phi)\}$

$\bar{C}_{yyy}$	$\frac{-\pi L^2}{2D^2\epsilon(1-\epsilon^2)^{7/2}}\{-4\epsilon\sqrt{1-\epsilon^2}(3\epsilon^2+5)cos(\phi)+4\epsilon\sqrt{1-\epsilon^2}(7\epsilon^2+1)cos(3\phi)$ $+\pi(13\epsilon^4+31\epsilon^2+1)sin(\phi)+\pi(-11\epsilon^4-5\epsilon^2+1)sin(3\phi)\}$
$\bar{C}_{xxy}$	$\frac{-\pi L^2}{2D^2\epsilon(1-\epsilon^2)^{7/2}}\{4\epsilon\sqrt{1-\epsilon^2}(3\epsilon^2+5)cos(\phi)-4\epsilon\sqrt{1-\epsilon^2}(7\epsilon^2+1)cos(3\phi)$ $+3\pi(\epsilon^4+3\epsilon^2+1)sin(\phi)+\pi(11\epsilon^4+5\epsilon^2-1)sin(3\phi)\}$
$\bar{C}_{yxy}$	$\frac{-\pi L^2}{2D^2\epsilon(1-\epsilon^2)^{7/2}}\{-8\epsilon\sqrt{1-\epsilon^2}\,sin(\phi)\,(7\epsilon^2\,cos(2\phi)+3\epsilon^2+cos(2\phi)-3)$ $+3\pi(\epsilon^4+3\epsilon^2+1)\,cos(\phi)-\pi(11\epsilon^4+5\epsilon^2-1)cos(3\phi)\}$
$\bar{C}_{xyx}$	$\frac{-\pi L^2}{2D^2\epsilon(1-\epsilon^2)^{7/2}}\{-4\epsilon\sqrt{1-\epsilon^2}(\epsilon^2+7)cos(\phi)-4\epsilon\sqrt{1-\epsilon^2}(7\epsilon^2+1)cos(3\phi)$ $+3\pi(\epsilon^4+3\epsilon^2+1)sin(\phi)+\pi(11\epsilon^4+5\epsilon^2-1)sin(3\phi)\}$
$\bar{C}_{yyx}$	$\frac{-\pi L^2}{2D^2\epsilon(1-\epsilon^2)^{7/2}}\{-8\epsilon\sqrt{1-\epsilon^2}\,sin(\phi)\,((7\epsilon^2+1)\,cos(2\phi)+5\epsilon^2+3)+3\pi(\epsilon^4+3\epsilon^2+1)\,cos(\phi)$ $-\pi(11\epsilon^4+5\epsilon^2-1)cos(3\phi)\}$

C.3 Nonlinear Third Order Coefficients

The third order coefficients can be found in a similar fashion. For instance, $\bar{K}_{xxxx}$ and $\bar{C}_{xxxx}$ are found for a π-film short bearing as:

$$\begin{aligned}\bar{K}_{xxxx} = \frac{\pi L^2}{6D^2\epsilon^2(1-\epsilon^2)^{11/2}}\{&-\pi(\epsilon^2-1)^3(7\epsilon^2+2)sin^3(\phi)cos(\phi)\\ &-2\epsilon(1-\epsilon^2)^{3/2}sin^2(\phi)[23\epsilon^4+50\epsilon^2+(25\epsilon^4+46\epsilon^2+1)cos(2\phi)-1]\\ &+3\pi\epsilon^2(14\epsilon^6+13\epsilon^4-33\epsilon^2+6)sin(\phi)cos^3(\phi)-96\epsilon^3\sqrt{1-\epsilon^2}(\epsilon^4\\ &+5\epsilon^2+2)cos^4(\phi)\}\\ \bar{C}_{xxxx} = \frac{-\pi L^2}{D^2\epsilon^2(1-\epsilon^2)^{9/2}}\{&-6\pi\epsilon^6sin^2(2\phi)+\pi(\epsilon^2-1)^3sin^4(\phi)\\ &+3\pi\epsilon^2[8(\epsilon^2+3)\epsilon^2+3]cos^4(\phi)+3\pi(9\epsilon^2-1)sin^2(\phi)cos^2(\phi)\\ &+8\sqrt{1-\epsilon^2}(-3\epsilon^4+2\epsilon^2+1)\epsilon sin^3(\phi)cos(\phi)+96\sqrt{1-\epsilon^2}(\epsilon^2\\ &+1)\epsilon^3sin(\phi)cos^3(\phi)\}\end{aligned} \tag{C.11}$$

The rest of the third order coefficients are calculated similarly.

Appendix D : Estimating the Fixed Points of the System $\dot{X} = \boldsymbol{f}(\boldsymbol{X}, \boldsymbol{\nu})$

Algorithm.

Provide an estimate for ν_1 as the critical parameter value

Provide an estimate for $X_0^1 = \boldsymbol{X}^*(\nu_1)$

$\nu_0 = \nu_1 + \Delta\nu = \nu_1 + \sqrt{u}(\nu_{ref})$

$X_1^1 = X_0^1 - [\partial_{\boldsymbol{X}}\boldsymbol{f}(X_0^1, \nu_1)]^{-1}\boldsymbol{f}(X_0^1, \nu_1)$

$X_1^1 \to X_1^*$, $X_1^* \to X_0^0$

$X_1^0 = X_0^0 - [\partial_{\boldsymbol{X}}\boldsymbol{f}(X_0^0, \nu_0)]^{-1}\boldsymbol{f}(X_0^0, \nu_0)$

$X_1^0 \to X_0^*$

$A(\nu_1) = Re\ (eig[\partial_{\boldsymbol{X}}\boldsymbol{f}(X_1^*, \nu_1)])$

$A(\nu_0) = Re\ (eig[\partial_{\boldsymbol{X}}\boldsymbol{f}(X_0^*, \nu_0)])$

$$\gamma_1 = \frac{A(\nu_1)}{A(\nu_1) - A(\nu_0)}$$

$\nu_2 = \nu_1 - \gamma_1(\nu_1 - \nu_0)$

$X_0^2 = X_1^* - \gamma_1(X_1^* - X_0^*)$

$X_1^2 = X_0^2 - [\partial_{\boldsymbol{X}}\boldsymbol{f}(X_0^2, \nu_2)]^{-1}\boldsymbol{f}(X_0^2, \nu_2)$

$k = 1$

while $|A(\nu_k)| > \varepsilon$ & $|\nu_{k+1} - \nu_k| > 10^{-N_{sig}}$

$k = k + 1$, $j = 0$

while $\sum_{i=1}^{N}\left(\frac{X_j^k - X_{j-1}^k}{X_{ref}}\right)^2 > 10^{(-2N_{sig})}$ & $\left\|\boldsymbol{f}\left(X_j^k, \nu_k\right)\right\| > \varepsilon$

$X_{j+1}^k = X_j^k - \left[\partial_{\boldsymbol{X}}\boldsymbol{f}\left(X_j^k, \nu_k\right)\right]^{-1}\boldsymbol{f}\left(X_j^k, \nu_k\right)$

$j = j + 1$

end

$X_{j+1}^k \to X_k^*$

$A(\nu_k) = Re\ (eig[\partial_{\boldsymbol{X}}\boldsymbol{f}(X_k^*, \nu_k)])$

$\gamma_k = \frac{A(\nu_k)}{A(\nu_k) - A(\nu_{k-1})}$

$\nu_{k+1} = \nu_k - \gamma_k(\nu_k - \nu_{k-1})$

$X_0^{k+1} = X_k^* - \gamma_k(X_k^* - X_{k-1}^*)$

end